FLOW AROUND A CYLINDER IN A SCOURED CHANNEL BED

THÈSE N^{O} 2368 (2001)

PRÉSENTÉE AU DÉPARTEMENT DE GÉNIE CIVIL

ÉCOLE POLYTECHNIQUE FÉDÉRALE DE LAUSANNE

POUR L'OBTENTION DU GRADE DE DOCTEUR ÈS SCIENCES TECHNIQUES

PAR

Istiarto ISTIARTO

Insinyur (civil), Gadjah Mada University, Yogyakarta, Indonésie
M.Eng., Asian Institute of Technology, Bangkok, Thaïlande
de nationalité indonésienne

acceptée sur proposition du jury :

Prof. W.H. Graf, Directeur de thèse
Dr. M.S. Altinakar, rapporteur
Dr. M. Cellino, rapporteur
Dr. R. Monti, rapporteur
Prof. Y. Zech, rapporteur

Lausanne, EPFL
2001

Flow around a Cylinder in a scoured Channel Bed

Abstract

The flow pattern around a cylinder protruding vertically on a scoured channel bed was experimentally and numerically investigated. Flow in an equilibrium scour hole (the scouring has ceased) under a clear water regime (no sediment supply into the scour hole) was considered.

Detailed measurements were obtained with a non-intrusive instrument, the **A**coustic **D**oppler **V**elocity **P**rofiler (ADVP), which measures the profiles of the 3D instantaneous velocity vectors. The measurements were done in different vertical planes positioned around the cylinder. From the measured data, the spatial distributions of the mean (time-averaged) velocities and its turbulence components could be deduced.

The numerical simulations of the flow were performed by using a 3D model, which is developed based on the approximate solution of the time-averaged equations of motion and of continuity for incompressible flows by using a finite-volume method. The model uses the k-ε turbulence closure model to compute the turbulence stresses and the **S**emi-**I**mplicit **M**ethod for **P**ressure-**L**inked **E**quation (SIMPLE) method to link the velocity to the pressure. The discretisation of the equations were done following the hybrid and power-law schemes on a structured, collocated, hexahedral, body-fitted grid. While the essentials of the model are relatively standard, some detailed derivations and clarifications were elucidated about the boundary conditions and the pressure-velocity coupling.

The measured velocity data show that a three-dimensional flow establishes itself, which is characterized by a rotating flow inside the scour hole upstream of the cylinder formed by a strong downward flow along the cylinder face and a reversed flow along the scour bed. This structure, which is known as horseshoe vortex, disappears behind the cylinder where a flow reversal towards the water surface is observed immediately behind the cylinder. These observations are supported by the numerical simulation.

The measured turbulence intensities show a considerable increase inside the scour hole and in regions close to the cylinder. The turbulent kinetic energy increases on entering the scour hole, on approaching the cylinder, and on moving towards downstream regions. The profiles of the turbulent kinetic energy are characterized by bulges below the original bed level. Similar observations can be made for the Reynolds stresses.

The numerical simulation under-predicted the turbulent kinetic energy, notably in the wake region immediately behind the cylinder. It appears that this problem is related to the

computation of the turbulent kinetic-energy generation at the solid boundaries. This problem was identified and discussed.

Estimates on the bed shear-stresses along the plane of symmetry, based on the measured velocity and Reynolds stress, disclose a diminishing value upon entering the scour hole and upon approaching the cylinder. Negative values are observed in the upstream scour bed, which is in accordance with the reversed flow in that region. Moving downstream and leaving the scour hole, the bed shear-stresses recover towards their value in the approach flow. Values obtained from the numerical simulation show a similar trend, having a satisfactory agreement with the ones obtained from the measurements.

The computation of the water surface profile produced results that are in agreement with the measured one, with the exception for those along the side circumference of the cylinder. The discrepancy in this region is apparently due to the inaccuracy of the computation in regions of a strong pressure gradient, such as the case along the cylinder circumference. Another method of positioning the water surface, employing kinematic boundary conditions, was proposed and discussed.

Écoulement à Surface Libre autour d'un Cylindre dans une Fosse d'Érosion Locale

Résumé

L'écoulement autour d'un cylindre dans une fosse d'érosion a été étudié en effectuant des mesures dans un modèle réduit et des simulations numériques avec un modèle hydrodynamique tridimensionnel. Les mesures et les simulations se limitent à un écoulement avec une profondeur de fosse qui est en équilibre (il n'y a plus d'érosion) et sans transport solide.

Le travail expérimental s'effectue principalement par des mesures de vitesses d'écoulement. Un **P**rofileur **V**élocimétrique **A**coustique **D**oppler (PVAD) a été utilisé ; ce dispositif très puissant est capable de mesurer les vecteurs de vitesse instantanés en plusieurs points de mesures. À partir de ces mesures, les profils des vitesses (moyennées sur les temps), des intensités de turbulence et des tensions de Reynolds sont obtenus. La plupart des mesures a été faite sur des plans verticaux autour du cylindre.

Pour faciliter le travail numérique, un modèle hydrodynamique tridimensionnel a été développé. Ce modèle est basé sur la représentation en volumes finis des équations de Reynolds. Il emploie un maillage structuré dont les variables primitives sont définies au centre des volumes de contrôle. Les flux convectif et diffusif sont calculés par deux méthodes (*hybride* et *loi de puissance*) avec des corrections des termes non orthogonaux. La méthode SIMPLE (***S**emi-**I**mplicit **M**ethod for **P**ressure-**L**inked **E**quation*) établit le couplage de la pression avec la vitesse ; elle permet le calcul du champ de pression. La viscosité turbulente est calculée à l'aide du modèle k-ε. Le modèle est relativement standard ; néanmoins, quelques dérivations et clarifications ont été abordées sur les conditions aux bords et le calcul de pression.

Les données des vitesses mesurées montrent que l'écoulement dans le plan de symétrie amont s'organise dans un tourbillon créé par l'arrêt de l'écoulement arrivant au cylindre. La pression due à l'arrêt d'écoulement augmente et, par conséquent, conduit l'écoulement vers le bas près du cylindre avec une vitesse croissante ; près du fond, l'écoulement se dirige vers l'amont. Ce tourbillon est le départ de ce qui est appelé le *vortex de fer-à-cheval*. Il se propage vers l'aval et son intensité devient faible voire presque invisible. Derrière le cylindre, un autre courant de retour est observé alors que celui prés de la surface se dirige vers le cylindre. Ces phénomènes ont été également vérifiés par les résultats de la simulation numérique.

Les intensités de turbulence s'accroissent vers, en entrant la fosse, en approchant le cylindre et en allant vers l'aval. Les intensités de turbulence sont caractérisés par des pics

qui se trouvent au dessous de la ligne du fond original. La même tendance a été observée sur les profils des tensions de Reynolds.

L'énergie cinétique turbulente obtenue par la simulation numérique a pu être comparée avec les mesures. Le modèle a sous-estimé les valeurs mesurées. Il paraît que ce problème provient de la difficulté du calcul de la génération d'énergie cinétique turbulente près du bord solide. Ce problème a été identifié et discuté en détail.

Les mesures de vitesse et de tensions de Reynolds près du fond permettent d'estimer la force de frottement au fond de la fosse ; celle ci a été faite aux plans de symétrie amont et aval. Elle montre que la force de frottement décroît en entrant dans la fosse et en s'approchant du cylindre. Des valeurs négatives sont obtenues au plan amont où le courant de retour est observé. Derrière le cylindre, la force de frottement décroît en sortant de la fosse. La même tendance a été démontrée par les résultats de la simulation numérique.

Le profil de la surface d'eau en amont du cylindre concorde avec les mesures. Vers les plans aval, le résultat de la simulation est moins satisfaisant ; le modèle a sous-estimé la profondeur de l'eau dans le plan normal de l'écoulement. Ce problème pourrait être dû à l'imprécision de la méthode de calcul aux endroits ayant un gradient de pression forte. Une proposition d'amélioration du calcul de la surface libre, en utilisant la condition cinématique, a été élaborée.

Acknowledgements

I wish to express my deepest gratitude and appreciation to my supervisor, Prof. W.H. Graf, Director of the Laboratoire de Recherches Hydrauliques (LRH) of the École Polytechnique Fédérale de Lausanne (EPFL), for admitting me to undertake the research work leading to this dissertation. I consider it as a privilege to work under his supervision. It is through his inexhaustible guidance, advice, and encouragement that this work could be accomplished.

I am deeply indebted to Prof. Y. Zech from the Université Catholique de Louvain, Louvain-la-Neuve, Belgium, with whom I had fruitful discussions during his many stays at EPFL as a visiting professor and a member of the examination committee. His constructive ideas and suggestions have certainly contributed a lot to the work, particularly for the numerical part. I appreciate his careful reading of the manuscript and the verification he did to all mathematical expressions.

Sincere thanks go to all the members of LRH for their friendships and unconditional readiness to help. Special appreciation is due to Dr. M.S. Altinakar for the many rewarding discussions and his willingness to serve as a member of the examination committee, to Dr. U. Lemmin for providing the experimental facilities, and to C. Perrinjaquet for his invaluable help in the computer logistic support. Thanks go also to my fellow (past and present) doctoral students at the LRH: P. Hamm, B. Yulistiyanto, R. Jiang, C. Shen, M. Cellino, K. Blanckaert, D. Hurther, I. Fer, A. Kurniawan, Z. Qu, Y. Guan, and I. Schoppe. I thank Dr. M. Cellino for serving as the member of the examination committee.

I express my thanks to Dr. R. Monti from the Terr@A Hydraulic Research Centre for the Environment, Departement of IIAR, Politecnico di Milano, Italy, for her constructive comments while serving as a member of the examination committee. Prof. P. Egger is acknowledged for his willingness to serve as the chairman of the examination committee.

My special thanks go to Dr. Budi Wignyosukarto and Dr. Djoko Legono from the Civil Engineering Department, Gadjah Mada University, Indonesia, for their support and encouragement in my decision to go abroad to undertake this study. Their continuous help offered to me and to my family is sincerely acknowledged.

Finally, I wish to convey my gratitude to the Swiss Federal Commission on Scholarships for Foreign Students for providing the financial support during the early phase of the work.

To all of you, I say a most heartfelt thank you.

Table of Contents

Chapter 1

1 Introduction

1.1 Flow around a cylinder

Local scour around a pier is a result of the interaction amongst the pier, the approach flow and the erodible bed. The presence of a pier results in a stagnation pressure build-up in front of the pier and a three-dimensional turbulent flow —characterized by the downward flow ahead of the pier and the so-called horseshoe vortex along the base of the pier— forms itself. The flow modifies the erodible bed in the vicinity of the pier when local scour takes place. It has been generally agreed upon that this scour is initiated by the downward flow and further provoked by the horseshoe vortex. The scour process can be either a clear-water one when there is no general sediment transport, or a live-bed one when a sediment transport takes place along the channel. Local scour is a complex phenomenon due to the interplay among various parameters, namely the fluid, the flow, the time, the bed material, and the pier. Two particular interests in the study of local scour around a pier are the development of the equilibrium scour hole as a function of those parameters and the alteration of the flow field around the pier. This second aspect has been selected as the object in the present work. The flow field around a cylindrical pier is studied numerically and experimentally, in which a clear-water flow in an equilibrium (maximum) scour-depth is considered. This work is a continuation and an extension of the previous study conducted at the *Laboratoire de recherches hydrauliques* (LRH) of EPFL (*Yulistiyanto*, 1997).

In the work previously conducted at LRH, extensive velocity data of flow around a cylinder on a flat channel bed were reported (*Yulistiyanto*, 1997; *Graf and Yulistiyanto*, 1998). The three-dimensional instantaneous velocities are measured by using an *A*coustic *D*oppler *V*elocity *P*rofile*r* (ADVP) conceived and developed at LRH (*Lhermitte and Lemmin*, 1994). The data are presented as the vertical distributions of velocities, Reynolds stresses, and turbulence intensities in different vertical planes around the cylinder. It is reported that the horseshoe vortex manifests itself, which depends largely on the approaching flow; it has the strongest rotation at the plane of symmetry upstream of the cylinder. Its strength weakens as it travels downstream along the perimeter of the cylinder. Their measurements show that, as the flow passes the cylinder from upstream up to the side of the cylinder, the turbulent kinetic energy decreases, but further downstream the turbulent kinetic energy increases. Upstream of the cylinder, the maximum energy is concentrated at the bottom corner of the cylinder. This region of maximum energy at the other planes shifts away from the bed and from the cylinder. In addition to the laboratory measurements, a numerical simulation of the flow is also reported (*Yulistiyanto*, 1997; *Yulistiyanto et al.*, 1998). The depth-averaged velocity field

was computed by using a numerical model which takes into account the dispersion stresses, evaluated from the velocity distributions along the curved streamlines. The simulation compares favorably with the measurements.

In the light of the previous study results, the work is continued and extended in the present investigation to embody a scour hole around the cylinder. A similar path is followed, i.e. by performing numerical flow simulations and by conducting velocity measurements. The first is aimed at obtaining the general pattern of the velocity alteration by the cylinder while the second is directed at getting detail pictures of the velocity and its turbulence structure around the cylinder.

The depth-averaged numerical simulation approach used in the preceding study is not suitable for the present case since the three-dimensional features of the geometry, i.e. the scour hole, and the flow are significant. A three-dimensional numerical model is thus opted. The model is developed based on the approximate solution of the time-averaged equations of motion and continuity for incompressible flows by using finite-volume method. The closure model is achieved by using the k-ε model (*Launder and Spalding*, 1974). Non-orthogonal hexahedral cell-centered grid arrangements are used and all variables are defined in the Cartesian coordinate system. The classical hybrid and power-law schemes (*Patankar*, 1980) are applied to discretise the convective-diffusive fluxes, combined with the so-called *S*emi-*I*mplicit *M*ethod for *P*ressure-*L*inked *E*quation (SIMPLE) method to compute the pressure (*Patankar and Spalding*, 1972).

The ADVP, as in the preceding study, is used to measure the three-dimensional instantaneous velocity. The measurements are conducted in the equilibrium (maximum) scour-depth condition which is established under a clear-water scour regime. Vertical distributions of the three-dimensional instantaneous velocities are measured at radial planes around the cylinder, from which the vertical distributions of the (time-averaged) velocities, the turbulence intensities, and the Reynolds stresses are deduced.

A number of works on local scour around cylindrical piers, both numerical simulations and experiments, have been reported. Herein a brief summary of those previous works is presented.

Most of the experimental works on flow around a cylinder so far concern with the development of the scour depth. Few work have focused on the flow field (see for example *Hjorth*, 1975; *Melville*, 1975; *Dargahi*, 1987; *Dey et al.*, 1995; *Ahmed and Rajaratnam*, 1998; *Graf and Yulistiyanto*, 1998). *Melville* (1975) was the first who conducted velocity measurements around a cylinder in the scour hole. He measured the flow velocity and its turbulent structure near the bottom and inside the scour hole by using hot-film anemometer and pitot tube. From the measurements, he was able to describe the horseshoe vortex as it travels along the perimeter of the cylinder; the strength of the horseshoe vortex was evaluated. *Hjorth* (1975) and *Dargahi* (1987) did a thorough investigation by measurements, but concern mostly the flat channel-bed case. *Dey et al.* (1995) proposed an analytical flow model to analyze the mean flow velocity in the scour hole based on the velocity data obtained from measurements using a 5-yaw and a 3-yaw

pitot tubes. *Ahmed and Rajaratnam* (1998) attempted to describe the velocity profiles in the upstream plane of symmetry by using a Clauser-type defect scheme. It was also reported that, rather than separating from the bed, the approach flow accelerates on entering the scour hole; a downward velocity up to 95% of the approach velocity was reported.

Simulations of three-dimensional flow around a cylinder have been reported (see for example *Ali et al.*, 1997, *Olsen and Kjellesvig*, 1998). Up to recently, however, there has not been any comparison of the results to detailed measurements. This is mostly due to the fact that such data are not always available to modelers. A comparison of the computed and measured flow, not only the time-averaged velocities but also the turbulence, would help to define clearly the limitations of a mathematical modeling approach and, in a broader perspective, to evidence the need for further developments or refinements of the computational techniques. In this aspect, therefore, the contribution of the present work shall be considered.

1.2 Objective and scope of the work

The objective of the present work is focused on the obtaining of better understanding to the flow and turbulence structures around the cylinder as they are altered by the cylinder and the scour hole. The investigation is limited to the flow in an equilibrium scour-depth under a clear-water scour regime. The work is implemented through laboratory experiments by conducting detailed measurements on the three-dimensional velocity and through numerical modeling by performing three-dimensional flow simulations.

The detailed measurements of the vertical distributions of the three-dimensional instantaneous velocities are conducted in vertical planes around the cylinder by using ADVP, a non-intrusive acoustic velocity profiler (see Chapter 2). From those measurements the distributions of the (time-averaged) velocities, of the vorticities, of the turbulence intensities, and of the Reynolds stresses can be constructed and investigated (see Chapter 3). The velocity measurements are performed only for a single run with a given set of flow parameters and one cylinder diameter. Four observations of scour depth developments under different flow conditions and cylinder diameters, nevertheless, are conducted.

The numerical simulations are performed by using a three-dimensional model developed in the present work (see Chapter 4). The model is based on the approximate solution of the time-averaged equations of motion and continuity for incompressible flows by using finite-volume method. The model uses the k-ε turbulence closure model to compute the turbulence stresses and the SIMPLE method to link the velocity to the pressure. The water surface boundary is determined according to the pressure along the surface boundary. The model, even though solves the transient flow equations, is applicable only for steady flow problems. The model is tested to simulate a simple uniform flow to verify its basic performance. The tested model is then applied to simulate flow around a cylinder. Two cases of flow around a cylinder are considered, namely flat channel bed

and scoured channel bed (see Chapter 5). The simulation results for the flat channel bed case are compared to the Yulistiyanto's measurements (*Yulistiyanto*, 1997). The results of the scoured channel bed case are compared to the present measurements.

References

Ahmed, F., and Rajaratnam, N. (1998). "Flow around bridge piers." *ASCE, J. Hydr. Engrg.*, 124(3), 288-300.

Ali, K. H. M., Karim, O. A., and O'Connor, B. A. (1997). "Flow patterns around bridge piers and offshore structures." *Proc. 27th Congress of the IAHR*, San Francisco, California, Theme A, 208-213.

Dargahi, B. (1987). "Flow Field and Local Scouring around a Cylinder." *Bulletin No. TRITA-VBI-137*, Hydraulic Laboratory, The Royal Inst. of Technology, Stockholm, Sweden.

Dey, S., Bose, S. K., and Sastry, G. L. N. (1995). "Clear water scour at circular piers: a model." *ASCE, J. Hydr. Engrg.*, 121(12), 869-876.

Graf, W. H., and Yulistiyanto, B. (1998). "Experiments on flow around a cylinder; the velocity and vorticity fields." *IAHR, J. Hydr. Res.*, 36(4), 637-653.

Hjorth, P. (1975). *Studies on the Nature of Local Scour.*, Dept. of Water Res. Engrg., Lund Inst. of Technology, Sweden.

Launder, B. E., and Spalding, D. B. (1974). "The numerical computation of turbulent flows." *Computer Methods in Applied Mechanics and Engineering*, 3, 269-289.

Lhermitte, R., and Lemmin, U. (1994). "Open-channel flow and turbulence measurement by high-resolution Doppler sonar." *J. Atm. Ocean. Tech.*, 11, 1295-1308.

Melville, B. W. (1975). "Local scour at bridge sites." *Report No. 117*, Univ. of Auckland, School of Engrg., New Zealand.

Olsen, N. R. B., and Kjellesvig, H. M. (1998). "Three-dimensional numerical flow modeling for estimation of maximum local scour depth." *IAHR, J. of Hydr. Res.*, 36(4), 1670-1681.

Patankar, S. V. (1980). *Numerical Heat Transfer and Fluid Flow.*, Hemisphere Publishing Corp., New York, USA.

Patankar, S. V., and Spalding, D. B. (1972). "A calculation procedure for heat, mass and momentum transfer in three-dimensional parabolic flows." *Int. J. Heat Mass Transfer*, 15, 1787-1806.

Yulistiyanto, B. (1997). *Flow around a cylinder installed in a fixed-bed open channel.*, *Doctoral Dissertation*, No. 1631, EPFL, Lausanne, Switzerland.

Yulistiyanto, B., Zech, Y., and Graf, W. H. (1998). "Flow around a cylinder: shallow-water modeling with diffusion-dispersion." *ASCE, J. Hydr. Engrg.*, 124(4), 419-429.

Chapter 2

2 Flow Measurements

Abstract

Measured three-dimensional flow fields around a vertical cylinder, in an established (equilibrium) scour hole under a clear-water regime, are reported. An acoustic Doppler velocity profiler (ADVP) was used to measure instantaneously the vertical distributions of the three velocity components in vertical planes around the cylinder. The flow field is presented as the vertical distributions of the (time averaged) velocities, of the turbulence intensities, and of the Reynolds stresses in the planes $\alpha = 0°$, 45°, 90°, 135° and 180°.

The flow in plane of symmetry upstream of the cylinder, $\alpha = 0°$, is characterized by a reversed flow along the scour bed and a strong downward flow close to the cylinder. This structure remains, but with diminishing strength, in the other planes, $\alpha = 45°$, 90°, and 135°. In these three planes, the downward flow has a decreasing magnitude. In the plane $\alpha = 180°$, there is a flow reversal close to the surface. As the flow moves downstream, leaving the scour hole, the flow reversal diminishes; the flow is recovering to the approach flow condition. Measurements in all planes show that the flow in the far region, outside the scour hole, does not change with the presence of the cylinder. The flow is altered only in the scour-hole region.

The turbulence intensities get stronger in the downstream planes. The increase is notably important from the plane $\alpha = 90°$ to $\alpha = 135°$ and further downstream to $\alpha = 180°$. Approaching the cylinder, in all planes except in the plane $\alpha = 180°$, the turbulence intensifies within the scour hole, $z < 0$, but remains more or less unchanged outside the scour hole, $z > 0$. Downstream of the cylinder, in the plane $\alpha = 180°$, the turbulence gets its strongest intensities. It is interesting that the three components of the intensity, $\sqrt{\overline{u'u'}}$, $\sqrt{\overline{v'v'}}$, and $\sqrt{\overline{w'w'}}$, in the plane $\alpha = 180°$ indicate a tendency of being isotropic.

The vertical distributions of the Reynolds stresses in the planes $\alpha = 0°$ to 135° have an almost linear distribution in the upper layer, $z > 0$, while in the lower layer, they exhibit a strong peak. From the plane $\alpha = 0°$ to $\alpha = 135°$, the Reynolds stresses inside the scour hole get increasingly stronger. In all planes, the $-\overline{u'w'}$ is always dominant compared to the $-\overline{v'w'}$. Downstream of the cylinder in the plane $\alpha = 180°$, however, the vertical distributions of the Reynolds stresses do not show any conclusive trend.

Presented also are the vertical distributions of the uniform approach flow, i.e. the flow without the cylinder being installed. The approach flow is uniform, but shows a slight tendency of being decelerated; the bed is hydraulically (incomplete) rough.

Résumé

Le champ des vitesse mesuré autour d'un cylindre dans un affouillement est présenté. Un profileur vélocimétrique acoustique Doppler est utilisé pour effectuer les mesures ; ce dispositif mesure les trois composantes de vitesse instantanée en plusieurs points de mesure au long d'un vertical. A partir de ces mesures, les profils des vitesses (moyennées), des turbulences et des tensions de Reynolds sont obtenues.

Les données des vitesses mesurées montrent que l'écoulement dans le plan de symétrie amont s'organise dans un tourbillon créé par l'arrêt de l'écoulement arrivant au cylindre. La pression due à l'arrêt d'écoulement augmente et, par conséquent, conduit l'écoulement vers le bas près du cylindre avec une vitesse croissante (un maximum de $0.6U_\infty$) ; près du fond, l'écoulement se dirige vers l'amont. Ce tourbillon est le départ de ce qui est appelé le *vortex de fer-à-cheval*. Il se propage vers l'aval et son intensité devient faible voire presque invisible. Derrière le cylindre, un autre courant de retour est observé alors que celui prés de la surface se dirige vers le cylindre.

Les intensités de turbulence s'accroissent vers les plans aval. Cette augmentation est plus significative au plan $\alpha = 90°$ au $\alpha = 135°$, et également au plan $\alpha = 180°$. Les turbulences dans la fosse, d'après les mesures sur tous les plans, s'intensifient quand l'écoulement s'approche du cylindre. Les intensités de turbulence sont au maximum au plan $\alpha = 180°$. Il est intéressant de noter que dans ce plan la turbulence ait une tendance à être isotropique. Les profils de l'énergie cinétique turbulente sont caractérisés par des pics qui se trouvent à la ligne de séparation.

Les profils des tensions de Reynolds, $-\overline{u'w'}$ et $-\overline{v'w'}$, sont à peu près linéaires dans la partie supérieure, $z > 0$, alors que dans la fosse, $z < 0$, ils montrent une forte croissante vers le maximum. Du plan $\alpha = 0°$ aux plans $\alpha = 45°$, 90° et 135°, les tensions de Reynolds dans la fosse augmentent. Dans tous les plans, la composante $-\overline{u'w'}$ est toujours supérieure par rapport au $-\overline{v'w'}$. Derrière le cylindre, la répartition des tensions de Reynolds ne donne pas de tendance concluante.

Des mesures ont été aussi effectuées dans l'écoulement à fond plat sans cylindre ; celles-ci représentent les conditions d'approche. Les profils mesurés indiquent que l'écoulement d'approche est uniforme et a une tendance à décélérer et hydrauliquement en transition-rugueux.

2.1 Measurement design

The flow measurement is aimed at collecting detailed data of the three-dimensional velocity fields around the cylinder, from which a close investigation can be made to characterize the alteration of the flow around the cylinder. A series of measurements shall be performed around the cylinder in an equilibrium scour-depth under a clear-water scour regime. An equilibrium scour-depth is defined as the depth of scour hole in front of the cylinder that has no longer changed appreciably under a continuous (steady) flow. A clear-water scour regime prevails when the scouring process is due solely to the interaction of the flow with the obstruction (the cylinder) and that the sediment transport does not exist in the approach flow. A live-bed scour prevails otherwise.

The ADVP shall be used to obtain the vertical distributions of the instantaneous three-dimensional velocities. The measurements are to be performed at stations distributed along vertical planes around the cylinder, outside and inside the scour hole. The hydraulic parameters of the experiment are selected according to certain criteria relating to the scouring mechanism and the available laboratory facilities and instrumentation. In terms of the scouring process, the flow has to maintain a clear-water scour and result in a maximum scour depth for the given sediment and cylinder diameter. This can be achieved with flows having a velocity close to but less than the sediment entrainment velocity. From the instrument point of view, the scour-hole depth shall be small to keep the entire flow depth in the range of the instrument measuring capability.

Given in the following sections are the detailed aspects of the measurements, from the setup to the results of the measurements.

2.2 Experimental setup

2.2.1 Laboratory channel

The experiments were conducted in a 29 [m] long and 2.45 [m] wide rectangular erodible-bed channel. This wide channel allows for flows with sufficiently large aspect ratio in terms of the flow depth and cylinder diameter. Large ratios of channel width, B, to cylinder diameter, D_p, guarantee that the flow around the cylinder is a manifestation of the interaction between the approaching flow and the cylinder. In the present work, this ratio is $B/D_p = 16$, being sufficiently higher than the generally agreed minimum ratio of $B/D_p > 8$. The large ratios of the channel width to the flow depth, h_∞, ensure the approaching flow to be a quasi two-dimensional one where the side wall does not influence the flow. In the present work, the ratio is $B/h = 13.6$; this is higher than the minimum value usually taken as the criterion, $B/h > 7$. The general view of the channel is shown in Fig. 2.1 and its principal elements are presented in the following paragraphs.

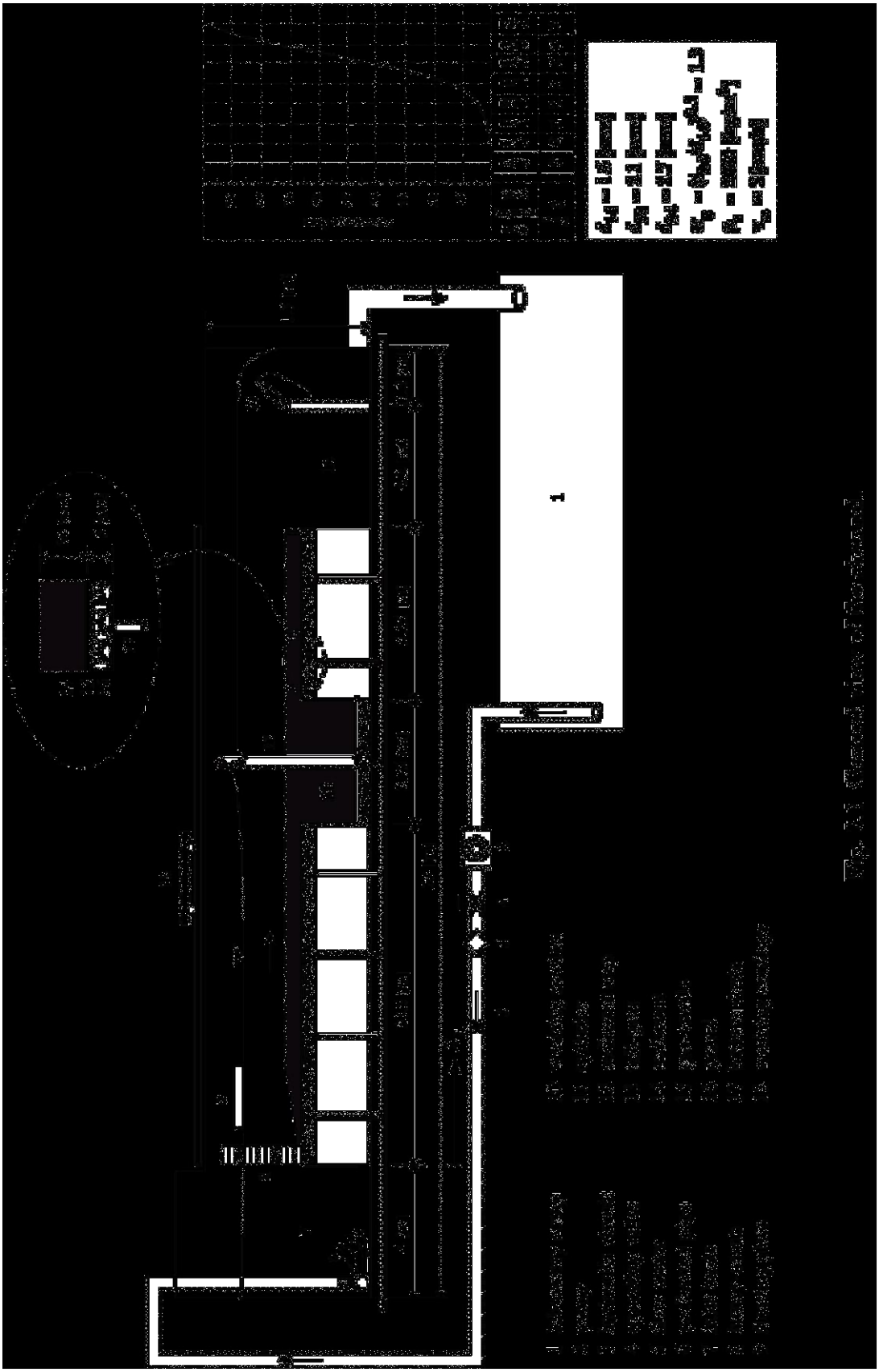

The *water circuit* is a closed loop in which clear water is circulated. The flow is generated from the general sump (1) by a 0.250[m^3/s]-capacity pump (2), flowing through the hydraulic circuit (3), passing the operating valve (4) and the electro-magnetic flow-meter (5), entering the channel through the perforated pipe (6) and the channel inlet-basin (7). After the inlet basin, a type of honeycomb (8) is provided to distribute evenly the flow over the upstream section of the channel. At the downstream of the honeycomb, a floating plate (9) is installed to stabilize the water surface. The water flows along the channel, passes through the *working reach* (10) at 10.5 [m] $\leq x_L \leq$ 14.25 [m] (x_L is the distance from the entrance) where the cylinder (11) is vertically installed at x_L = 11 [m]. A basin (12) is provided at the downstream reach to trap the transported sediment. Before leaving the channel and going back to the general sump, the water passes through a motor-regulated tailgate (13), which is used to control the water-depth in the channel.

The *mobile-bed* is made of a uniform sand (14) having a mean diameter of d_{50} = 2.1 [mm] and a distribution ratio of σ_g = 1.3. The sand layer is 50 [cm] in the working reach and 10 [cm] along the rest of the channel. The sand layer is separated from the bottom of the channel by a geotextile-sheet (15) and a layer of gravel (16). These layers avoid the deformation of the sand layer when the channel is being slowly filled (at the beginning of the experiment) or drained (at the end of the experiment) through the bottom pipes (17).

The *measuring instrument*, ADVP, is mounted on a measuring carriage (18) having a three-axis positioning equipment allowing the instrument to be positioned at any point along and across the channel.

2.2.2 Acoustic Doppler Velocity Profiler (ADVP)

Working principles

The **A**coustic **D**oppler **V**elocity **P**rofiler (ADVP) conceived and developed at LRH (*Lhermitte and Lemmin*, 1994) is the main measuring instrument in the present work. This non-intrusive instrument measures the instantaneous velocity vector at a number of layers within the water column. The ADVP has been extensively exploited in the research works conducted at LRH. Its modular installation allows a high flexibility in its use. Several different configurations have been used in different measurements conducted previously at LRH. This section describes the one used in the present work; given also are the procedures of the measurement and of the velocity abstraction. Detail technical descriptions of the instrument can be found in reports and publications elsewhere (*Lhermitte and Lemmin*, 1994; *Rolland*, 1994; *Hurther et al.*, 1996).

The ADVP measures the velocities in a water column based on the back-scattered acoustic wave information. An emitting transducer sends an acoustic wave across the water column. Upon hitting a target moving with the flow, the wave is reflected and captured by one or several receiving transducers. The target can be air bubbles, suspended particles, or density fronts due to temperature differences. Knowing the frequency difference between the emitted and reflected ones, the so-called Doppler

frequency, the velocity of the moving target can be deduced. To obtain profiles of the velocity across the water depth, the recording time of the reflected waves is gated according to a predetermined interval. This time gate determines the height of the measured target. The diameter of the target is obviously determined by the diameter of the acoustic beam from the emitting transducer.

Instantaneous velocity

The derivation of the instantaneous velocity from the measured Doppler frequency depends, among others, on the configuration and/or the placement of the emitter and receivers. Several configurations have been used in the measurement works at LRH; they are largely determined by the geometry of the measurement fields. For the present work, the set-up consists of one conical emitter, T_3, and four plane receivers, T_1^-, T_1^+, T_2^-, T_2^+, which are arranged according to Fig. 2.2.

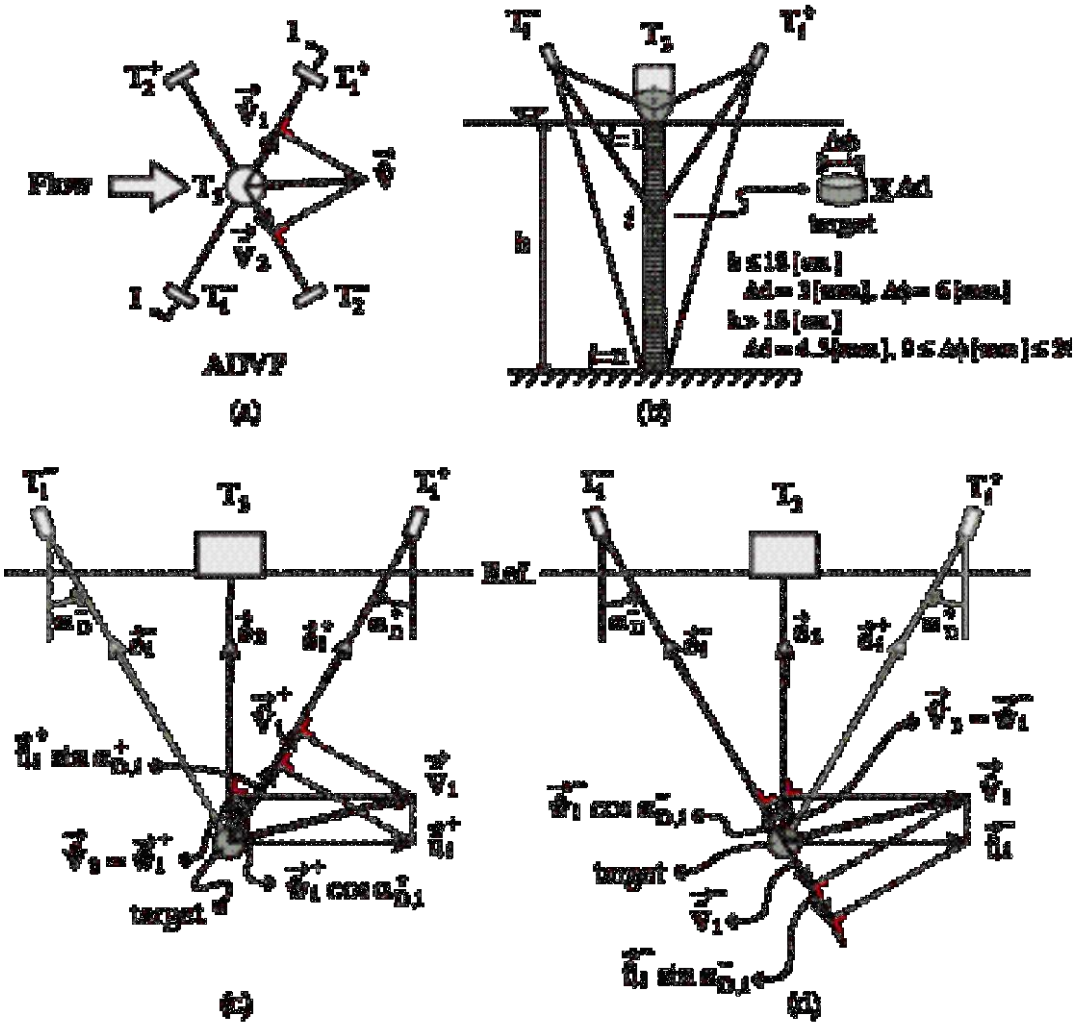

Fig. 2.2 Configuration of the ADVP instrument used in the velocity measurement: (a) top view, (b) side view along section I-I, (c) velocity derivation along the tristatic plane $T_3T_1^+$, and (d) velocity derivation along the tristatic plane $T_1^-T_3$.

Consider a target "*i*" moving with the flow, passing the acoustic beam emitted from the ADVP as shown in Fig. 2.2a,b where the vertical plane $T_1^- T_3 T_1^+$ is shown (the vertical plane $T_2^- T_3 T_2^+$ is analogous). The dimension of the target constitutes the measuring volume which depends on the diameter of the acoustic beam (determined by the type of the emitter T_3), its distance from the emitter, and the recording time-gate interval. This will be described in the later section.

The three-dimensional instantaneous velocity, $\vec{\mathbf{V}}(\hat{u}, \hat{v}, \hat{w})$, is measured by the ADVP as a pair of two-dimensional instantaneous velocities, $\vec{\mathbf{V}}_1(\hat{u}_1, \hat{w}_1)$ and $\vec{\mathbf{V}}_2(\hat{u}_2, \hat{w}_2)$, i.e. the projections of the target velocity on the vertical planes $T_1^- T_3 T_1^+$ and $T_2^- T_3 T_2^+$, respectively. Both velocities are identified by their components along the longitudinal direction, $\hat{u}_1$ or $\hat{u}_2$, and along the vertical direction, $\hat{w}_1$ or $\hat{w}_2$, of the respective planes. The system of one emitter and a pair of receivers $T_1^- T_3 T_1^+$ or $T_2^- T_3 T_2^+$ is called a *tristatic mode* measurement and the vertical plane formed by the system is called a *tristatic plane*. By geometrical relationships, the two measured velocity components, $\vec{\mathbf{V}}_1(\hat{u}_1, \hat{w}_1)$ and $\vec{\mathbf{V}}_2(\hat{u}_2, \hat{w}_2)$, can be combined to give the target velocity, $\vec{\mathbf{V}}(\hat{u}, \hat{v}, \hat{w})$. The following paragraphs describe the derivation of the target's velocity; the procedure follows the one given by *Rolland* (1994). Details are given for the derivation of the velocity component $\vec{\mathbf{V}}_1(\hat{u}_1, \hat{w}_1)$ by referring to Fig. 2.2c,d; an analogy applies to the other component.

The instantaneous velocity component along the tristatic plane $T_1^- T_3 T_1^+$, $\vec{\mathbf{V}}_1(\hat{u}_1, \hat{w}_1)$, is obtained from the Doppler frequency measurement by $T_3 T_1^+$ (Fig. 2.2c) and $T_1^- T_3$ (Fig. 2.2d) transducers. The frequency difference recorded by the $T_3 T_1^+$ transducers can be related to the target velocity "seen" by this couple of transducers according to the following expression (*Rolland*, 1994):

$$f_D^+ = \frac{f_e}{c_s}\left(\vec{\mathbf{V}}_1^+ \cdot \mathbf{e}_1^+ + \vec{\mathbf{V}}_3 \cdot \mathbf{e}_3\right) \tag{2.1}$$

where f_D^+ is the Doppler frequency recorded by the $T_3 T_1^+$, f_e is the emitted frequency, c_s is the speed of acoustic wave in water, and $\mathbf{e}_1^+$ and $\mathbf{e}_3$ are the unit directional vectors of T_1^+ and T_3, respectively. From the geometrical relationships (see Fig. 2.2c), one can write:

$$\begin{aligned} \vec{\mathbf{V}}_1^+ \cdot \mathbf{e}_1^+ &= \hat{V}_1^+ = \hat{u}_1^+ \sin\alpha_{D,1}^+ + \hat{w}_1^+ \cos\alpha_{D,1}^+ \\ \vec{\mathbf{V}}_3 \cdot \mathbf{e}_3 &= \hat{V}_3^+ = \hat{w}_1^+ \end{aligned} \tag{2.2}$$

in which $\hat{u}_1^{i+}$ and $\hat{w}_1^{i+}$ are the longitudinal and vertical components, respectively, along the tristatic plane $T_1^- T_3 T_1^+$ as measured by the $T_3 T_1^+$ transducers. Inserting the above relation into Eq. 2.1 yields:

$$f_{D,1}^{+} = \frac{f_e}{c_s}\left[\hat{u}_1^{+}\sin\alpha_{D,1}^{+} + \hat{w}_1^{+}\left(1+\cos\alpha_{D,1}^{+}\right)\right] \tag{2.3}$$

By analogy, similar relations as Eqs. 2.1 to 2.3 exist for the Doppler frequency recorded by the transducer $T_1^- T_3$ (see Fig. 2.2d). The analogy of Eq. 2.1 for the transducers $T_1^- T_3$ reads:

$$f_D^- = \frac{f_e}{c_s}\left(\vec{\hat{V}}_1^{-} \cdot \mathbf{e}_1^{-} + \vec{\hat{V}}_3 \cdot \mathbf{e}_3\right) \tag{2.4}$$

and by using geometrical relationships (see Fig. 2.2d), it can be shown that:

$$\begin{aligned} \vec{\hat{V}}_1^{-} \cdot \mathbf{e}_1^{-} &= \hat{V}_1^{-} = \hat{u}_1^{-}\sin\alpha_{D,1}^{-} + \hat{w}_1^{-}\cos\alpha_{D,1}^{-} \\ \vec{\hat{V}}_3 \cdot \mathbf{e}_3 &= \hat{V}_3^{-} = \hat{w}_1^{-} \end{aligned} \tag{2.5}$$

Thus, one can rewrite Eq. 2.4 as:

$$f_{D,1}^{-} = \frac{f_e}{c_s}\left[\hat{u}_1^{-}\sin\alpha_{D,1}^{-} + \hat{w}_1^{-}\left(1+\cos\alpha_{D,1}^{-}\right)\right] \tag{2.6}$$

If the systems of $T_1^- T_3$ and $T_3 T_1^+$ are symmetrical about the T_3-axis and the measuring volume of the two systems is the same, one may write:

$$\alpha_{D,1}^{+} = \alpha_{D,1}^{-} = \alpha_{D,1}, \quad \hat{u}_1^{+} = \hat{u}_1^{-} = \hat{u}_1, \quad \text{and} \quad \hat{w}_1^{+} = \hat{w}_1^{-} = \hat{w}_1$$

Therefore, the instantaneous velocity component $\hat{u}_1$ and $\hat{w}_1$ can be extracted from Eqs. 2.3 and 2.6, obtained from the $T_1^- T_3 T_1^+$ system as follows:

$$\hat{u}_1 = \frac{c_s\left(f_{D,1}^{+} - f_{D,1}^{-}\right)}{2\, f_e \sin\alpha_{D,1}} \quad \text{and} \quad \hat{w}_1 = \frac{c_s\left(f_{D,1}^{+} + f_{D,1}^{-}\right)}{2\, f_e\left(1+\cos\alpha_{D,1}\right)} \tag{2.7}$$

The above relations give the two-dimensional velocity component, $\vec{V}_1(\hat{u}_1, \hat{w}_1)$, of the three-dimensional velocity of the target, $\vec{\hat{V}}^{i}(\hat{u},\hat{v},\hat{w})$; this is the projection of $\vec{\hat{V}}^{i}(\hat{u},\hat{v},\hat{w})$ on the tristatic plane formed by the $T_1^- T_3 T_1^+$ transducers. The other two-dimensional velocity component, $\vec{V}_2(\hat{u}_2, \hat{w}_2)$, can be worked out by analogy to Eq. 2.7 for the tristatic plane $T_2^- T_3 T_2^+$. This yields the following expressions:

$$\hat{u}_2 = \frac{c_s\left(f_{D,2}^{+} - f_{D,2}^{-}\right)}{2\, f_e \sin\alpha_{D,2}} \quad \text{and} \quad \hat{w}_2 = \frac{c_s\left(f_{D,2}^{+} + f_{D,2}^{-}\right)}{2\, f_e\left(1+\cos\alpha_{D,2}\right)} \tag{2.8}$$

Obtaining the velocity components along the two planes, $\vec{V}_1(\hat{u}_1, \hat{w}_1)$ and $\vec{V}_2(\hat{u}_2, \hat{w}_2)$, it is possible to deduce the three-dimensional instantaneous velocity, $\vec{V}^i(\hat{u}, \hat{v}, \hat{w})$. In order to do this, however, it is necessary that the two velocity components be measured from the same measuring volume. This can only be guaranteed if the four receivers, T_1^-, T_2^+, T_2^-, and T_2^+ are placed at the same radial distance with respect to the emitter T_3 and at the same plane (co-planar) that is parallel to the reference plane (see Fig. 2.2c). If, in addition, the emitter T_3 is vertical, one may write for the vertical velocity component:

$$\hat{w}_1 = \hat{w}_2 = \hat{w} \tag{2.9}$$

To obtain the horizontal velocity components, (the $\hat{u}$- and $\hat{v}$-components), the measured velocities along the two tristatic planes, $\vec{V}_1(\hat{u}_1, \hat{w}_1)$ and $\vec{V}_2(\hat{u}_2, \hat{w}_2)$, are first projected on the horizontal plane to give a resultant horizontal velocity, $\vec{V}_h(\hat{u}, \hat{v})$, whose direction is α_V with respect to the $T_1^- T_1^+$ (see Fig. 2.3). Using geometrical relationships, one writes:

- for the triangle ACA′: $\overline{AC} = \dfrac{\overline{AA'}}{\sin\alpha_T} = \dfrac{\hat{u}_2 - \hat{u}_1 \cos\alpha_T}{\sin\alpha_T}$
- for the triangle OAC: $\hat{V}_h = \left[(\hat{u}_1)^2 + \overline{AC}^2\right]^{1/2}$

where α_T is the angle of the tristatic-plane $T_2^- T_2^+$ with respect to $T_1^- T_1^+$.

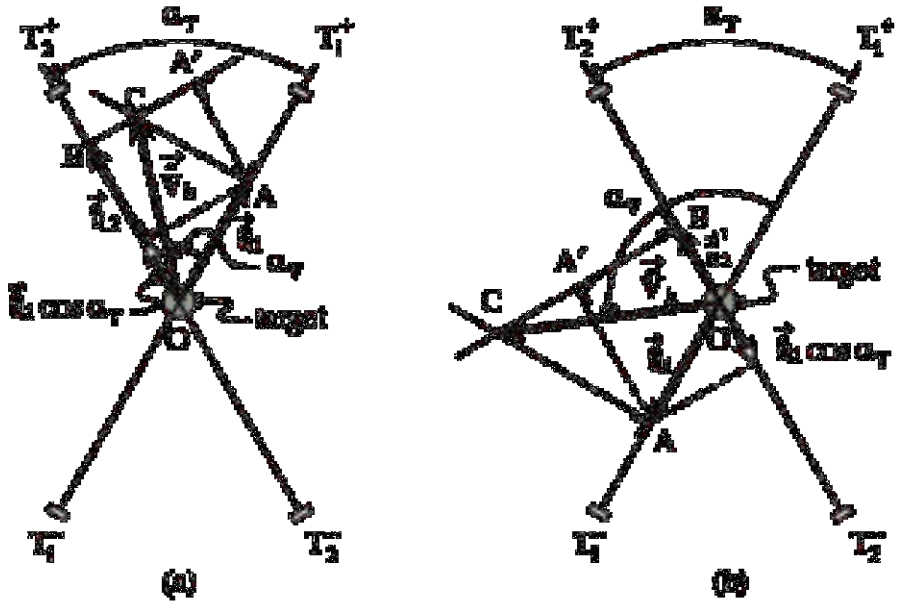

Fig. 2.3 Derivation of the instantaneous horizontal velocity component, $\vec{V}_h(\hat{u}, \hat{v})$, along the tristatic planes: (a) for $\hat{u}_1 \geq 0$, and (b) for $\hat{u}_1 < 0$.

The horizontal velocity component is thus:

$$\hat{V}_h = \left[(\hat{u}_1)^2 + \left(\frac{\hat{u}_2 - \hat{u}_1 \cos\alpha_T}{\sin\alpha_T} \right)^2 \right]^{1/2} \tag{2.10}$$

The velocity direction, α_V, is given by the relations below:

$$\begin{aligned} \alpha_V &= \arcsin\left(\frac{\hat{u}_2 - \hat{u}_2 \cos\alpha_T}{\hat{V}_h \sin\alpha_T} \right), && \text{if} \quad \hat{u}_1 \geq 0 \\ \alpha_V &= 180^\circ - \arcsin\left(\frac{\hat{u}_2 - \hat{u}_2 \cos\alpha_T}{\hat{V}_h \sin\alpha_T} \right), && \text{if} \quad \hat{u}_2 < 0 \end{aligned} \tag{2.11}$$

The three relations, Eqs. 2.9, 2.10, and 2.11, are the ones required to describe the three-dimensional instantaneous velocity of the moving target. It is, however, more convenient to describe the velocity by its components along the Cartesian or cylindrical coordinate system. The following section discusses the decomposition of the velocity into those components.

Cartesian and cylindrical velocity components

The Cartesian coordinate axes are defined as *x*, *y*, and *z* for the horizontal, transversal, and vertical directions, respectively. The cylindrical coordinate axes are defined as *r*, α ($\alpha = \theta - 180°$), and *z* for the radial, angular, and vertical directions, respectively (see Fig. 2.4). The origin of the two coordinate systems is defined at the center of the cylinder, at the original (uneroded) bed level.

The decomposition of the velocity into its components along the Cartesian and cylindrical coordinate systems depends on the orientation of the ADVP with respect to the coordinate system. In the measurements, the instrument is positioned along radial planes around the cylinder. Fig. 2.4 shows a typical placement of the ADVP and the decomposition of the velocity into its components along the Cartesian and cylindrical coordinate systems.

By using geometrical relationships, the Cartesian velocity components can be obtained from the following expressions:

$$\begin{aligned} \hat{u} &= \hat{V}_h \cos(\alpha + \alpha_R + \alpha_V) \\ \hat{v} &= \hat{V}_h \sin(\alpha + \alpha_R + \alpha_V) \\ \hat{w} &= \hat{w}_1 = \hat{w}_2 \end{aligned} \tag{2.12}$$

where the definitions of the angles are given in Fig. 2.4.

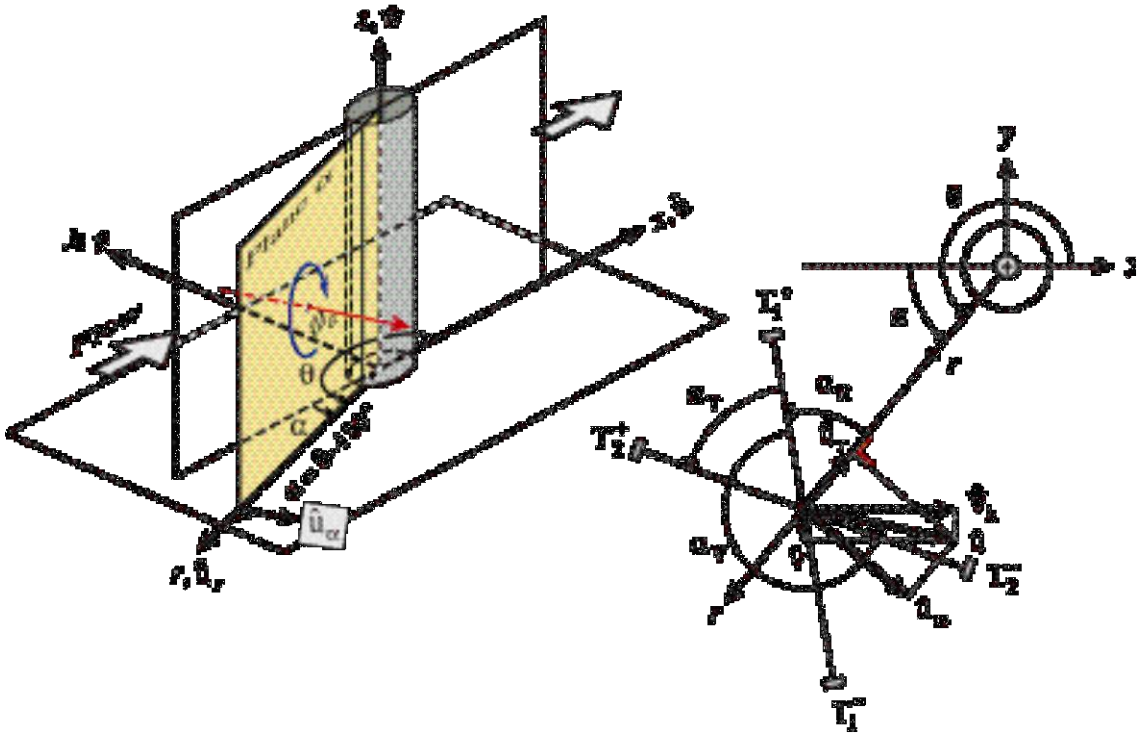

Fig. 2.4 Cartesian and cylindrical coordinate systems and the decomposition of the measured instantaneous velocity into its components in these coordinate systems.

The velocity components along the Cartesian and the cylindrical coordinate systems are interchangeable by using transformation functional expression as follows:

$$\begin{Bmatrix} \hat{u}_r \\ \hat{u}_\alpha \\ \hat{w} \end{Bmatrix} = \begin{bmatrix} \cos\theta & \sin\theta & 0 \\ -\sin\theta & \cos\theta & 0 \\ 0 & 0 & 1 \end{bmatrix} \begin{Bmatrix} \hat{u} \\ \hat{v} \\ \hat{w} \end{Bmatrix} = \begin{bmatrix} -\cos\alpha & -\sin\alpha & 0 \\ \sin\alpha & -\cos\alpha & 0 \\ 0 & 0 & 1 \end{bmatrix} \begin{Bmatrix} \hat{u} \\ \hat{v} \\ \hat{w} \end{Bmatrix} \tag{2.13a}$$

$$\begin{Bmatrix} \hat{u} \\ \hat{v} \\ \hat{w} \end{Bmatrix} = \begin{bmatrix} \cos\theta & -\sin\theta & 0 \\ \sin\theta & \cos\theta & 0 \\ 0 & 0 & 1 \end{bmatrix} \begin{Bmatrix} \hat{u}_r \\ \hat{u}_\alpha \\ \hat{w} \end{Bmatrix} = \begin{bmatrix} -\cos\alpha & \sin\alpha & 0 \\ -\sin\alpha & -\cos\alpha & 0 \\ 0 & 0 & 1 \end{bmatrix} \begin{Bmatrix} \hat{u}_r \\ \hat{u}_\alpha \\ \hat{w} \end{Bmatrix} \tag{2.13b}$$

where $\hat{u}_r, \hat{u}_\alpha$, and $\hat{w}$ are the radial, angular, and vertical velocity components, respectively, along the cylindrical coordinate system, (r,α,z), whose origin is defined at the center of the cylinder.

Time-averaged and fluctuating velocity components

Obtaining the instantaneous velocity data over the measurement period, the statistical parameters can be found. Three quantities are computed, i.e. the mean (the time-averaged velocities), the variance (the squared values of the turbulent intensities), and the covariance (the Reynolds stresses).

The time-averaged velocity components are obtained by:

$$u = \bar{\hat{u}} = \frac{1}{N_V}\sum_{j=1}^{N_V}(\hat{u})_j,$$

$$v = \bar{\hat{v}} = \frac{1}{N_V}\sum_{j=1}^{N_V}(\hat{v})_j, \qquad (2.14)$$

$$w = \bar{\hat{w}} = \frac{1}{N_V}\sum_{j=1}^{N_V}(\hat{w})_j$$

where N_V is the number of instantaneous velocities obtained from the measurement. Having the time-averaged velocity, the fluctuating components, defined as the deviation of the instantaneous velocity with respect to the time-averaged value, can be computed by:

$$u' = \hat{u} - u, \qquad v' = \hat{v} - v, \qquad \text{and} \qquad w' = \hat{w} - w \qquad (2.15)$$

The turbulence (the Reynolds) stresses can thus be obtained by:

$$\overline{u'u'} = \frac{1}{N_V - 1}\sum_{j=1}^{N_V}\left[(\hat{u} - u)_j^{\,2}\right] \approx \overline{(\hat{u})^2} - u^2 \qquad (2.16a)$$

$$\overline{v'v'} = \frac{1}{N_V - 1}\sum_{j=1}^{N_V}\left[(\hat{v} - v)_j^{\,2}\right] \approx \overline{(\hat{v})^2} - v^2 \qquad (2.16b)$$

$$\overline{w'w'} = \frac{1}{N_V - 1}\sum_{j=1}^{N_V}\left[(\hat{w} - w)_j^{\,2}\right] \approx \overline{(\hat{w})^2} - w^2 \qquad (2.16c)$$

$$-\overline{u'w'} = -\frac{1}{N_V - 1}\sum_{j=1}^{N_V}\left[(\hat{u} - u)_j(\hat{w} - w)_j\right] \approx -\overline{(\hat{u}\hat{w})} + uw \qquad (2.16d)$$

$$-\overline{v'w'} = -\frac{1}{N_V - 1}\sum_{j=1}^{N_V}\left[(\hat{v} - v)_j(\hat{w} - w)_j\right] \approx -\overline{(\hat{v}\hat{w})} + vw \qquad (2.16e)$$

Measuring volume, frequency, and duration of velocity acquisition

The derivation of the Doppler frequency by the ADVP is implemented by recording the emitted and reflected wave frequencies. The emitting transducer, T_3, sends a series of short trains sinusoidal acoustic waves (pulse) repetitively at a regular time interval (the *pulse repetition frequency*, PRF). Between two successive pulses, the receiving transducers, T_1^-, T_1^+, T_2^-, and T_2^+ receive the back-scattered signals. The electronic system of the ADVP detects and records the intensity and the phase of the incoming signals at every receiver. The recording process is gated in time in which one *time-gate*, T_g, corresponds to one target. The instantaneous velocity is deduced from the velocity of the target, the volume of which, therefore, represents the measuring volume. The diameter of the target is determined by that of the acoustic beam emitted from the transducer T_3, where as its thickness is defined by the time-gate, T_g. Two types of

transducer were used, a focused-type and a plane-type transducers. The focused-type transducer was used for measurements at depth $h \leq 18$ [cm] where the time-gate was specified to $T_g = 4$ [μs]. The measuring volume has a dimension of (see Fig. 2.2b): thickness $\Delta d = 3$ [mm], diameter $\Delta\phi = 6$ [mm]. The plane-type transducer was used for measurements at depth $h > 18$ [cm] with the time-gate fixed at $T_g = 6$ [μs]. In these measurements the measuring volume has a dimension of: thickness $\Delta d = 4.5$ [mm], diameter $9 \leq \Delta\phi\,[\text{mm}] \leq 26$.

To obtain the time series of the instantaneous velocities of a target, the recorded intensities and phases of the signals are grouped in which each group contains a number of intensity-phase data-pairs obtained from several pulses (the *number of pulse-pairs*, NPP). A value of NPP of 32 is used in the present work. From each group, one Doppler frequency is obtained at each receiver. The instantaneous velocity can then be derived from the Doppler frequency according to Eqs. 2.7 and 2.8. There exists, therefore, a relation between the pulse frequency, PRF, the number of pulse-pairs, NPP, and the frequency of the data acquisition, f_V:

$$f_V = \text{PRF}/\text{NPP} \tag{2.17}$$

If the acquisition is done within the duration of T_{acq}, the number of instantaneous velocities, N_V, for one measurement is:

$$N_V = f_V \times T_{acq} \tag{2.18}$$

The measurements in the present work were conducted with a data acquisition frequency of $f_V = 20.8$ to 28.4 [Hz] (PRF = 667 to 909 [Hz]). The duration of the acquisition was $T_{acq} = 150$ [s] for measurements at the uniform approach flow and was $T_{acq} = 60$ [s] for measurements around the cylinder. There are thus 3,140 instantaneous velocity data at every gate (measurement point) for the measurements at the uniform approach flow, while for the measurements around the cylinder there are 1,250 to 1,700 data.

2.2.3 Other measuring instruments

Besides the ADVP, some other measuring equipment were employed for different purposes:

- Point-gauge limnimeter: to map the water surface and the channel bed.
- Periscope: to measure the scour depth. The equipment is inserted in the cylinder, which is transparent. The scour bed can be easily viewed through the mirror provided at the periscope.
- Electro-magnetic discharge meter: to detect the discharge passing through the circuit.
- Theodolite: to measure the slope of the channel bed.

2.2.4 Flow parameters

The experiment is designed such that the scour hole is at its maximum depth for a given diameter of the cylinder, but a clear-water scour is still maintained. This can be achieved if the flow velocity is lower than but close to the sediment entrainment velocity. Given the available sediment size of $d_{50} = 2.1$ [mm] and a predetermined bed slope of $S_o = 0.00055$, a preliminary run without the cylinder was performed. The discharge and the flow depth were regulated such that the sediment particles were about to move and a uniform flow depth was maintained along the working reach. It was found that the discharge is of $Q = 0.2$ [m^3/s], the flow depth is of $h_\infty = 0.18$ [m] and the average velocity is of $U_\infty = 0.45$ [m/s].

The diameter of the cylinder is dictated by the measurement's technical factors. The present configuration of the ADVP cannot measure the zone closer than 3 [cm] from the leading edge of the cylinder and the zone deeper than 50 [cm] from the water surface. The first constraint suggests that big cylinders are preferred to small ones since the closest measured profile will be very close with respect to the diameter of the cylinder. The second constraint, on the other hand, limits the diameter of the cylinder since the bigger the cylinder, the deeper the scour will be. From those criteria, and after conducting some preliminary test runs, the diameter of the cylinder was determined as $D_p = 15$ [cm]. Table 2.1 summarizes the pertinent hydraulic parameters of the present measurement.

Table 2.1 Hydraulic parameters of the experiment

B [m]	S_O [10^{-4}]	Q [m^3/s]	h_∞ [cm]	B/h_∞ [cm]	U_∞ [m/s]	Fr [–]	Re_h [–]	d_{50} [mm]	D_P [cm]	Re_{Dp} [–]	B/D_P [–]	h_∞/D_p [–]	D_P/d_{50} [–]
2.45	5.5	0.2	18	13.6	0.45	0.34	81,000	2.1	15	67,500	16.3	1.2	70

2.2.5 Experimental procedures

The experimental procedures basically consist of three major steps.

(1) *Measurements of velocity of the uniform (approaching) flow*. Without the cylinder, a uniform flow was established in the channel; measurement of the corresponding velocity was then carried out. This step is aimed at obtaining velocity data of the flow "unperturbed" by the cylinder. The data serve as the reference data with which the measured data around the cylinder shall be compared.

(2) *Establishment of the scour hole*. The cylinder was vertically mounted in the working reach of the channel, at 11 [m] from the entrance. Starting with a flat bed, the flow was released and allowed to erode the sediment around the cylinder. The time development of the scour depth at the leading edge of the cylinder was monitored. The flow was maintained until the equilibrium scour depth was obtained, that is when it has no longer appreciably changed. A 5-to-7 day run was

typically needed for this purpose. The channel was drained and the scour geometry, considered as the (near) equilibrium one, was mapped by point-gauge measurement.

(3) *Measurements of the flow fields around the cylinder*. Vertical distributions of the velocity vector were measured at radial planes of $\alpha = n \times 15^{\circ}$, n = 0, 1, 2, ..., 12. A number of 15 to 25 profiles were obtained at each plane. Due to technical reasons, the flow had to be occasionally stopped between measurements. In such a case, care was taken in restarting the flow such that the scour geometry was not disturbed. When a run was stopped, the water in the channel was slowly evacuated through the bottom pipes. To restart the run, the water was carefully supplied into the channel from the same pipes until a sufficient water depth was obtained in the channel. The supply was then replaced by pump through the hydraulic circuit. The discharge was regulated, starting with a small one and being gradually increased until the designed one. The flow depth at the channel was, at the same time, adjusted by regulating the tailgate.

2.3 Preliminary experiments

2.3.1 Scour depth measurements

Before arriving to the flow parameters selected for the velocity measurements (see Table 2.1 in Sect. 2.2.4) a series of preliminary experiments had been carried out. These experiment tests provided also knowledge of the scour processes, notably the time development of the scour depth. Four preliminary runs were performed, namely Test 1, 2, 3 and 4, with the cylinder diameters of D_p = 11, 10, 15, and 20 [cm]. The hydraulic parameters of these test runs are listed in Table 2.2. During the test runs, some modifications were made to the experimental installation to get the best hydraulic performance, such as improvements made to the inlet and the outlet sections.

Table 2.2 Hydraulic parameters of the preliminary experiment

Test	d_{50} [mm]	Q [m^3/s]	h_∞ [m]	D_p [m]	d_s [m]	D_p/d_{50} [–]	h_∞/D_p [–]	d_s/D_p [–]
1	2.1	0.220	0.170	0.11	0.174	52.38	1.54	1.55
2	2.1	0.250	0.232	0.10	0.195	47.62	2.32	1.95
3	2.1	0.250	0.232	0.15	0.259	71.43	1.55	1.73
4	2.1	0.250	0.232	0.20	0.319	95.24	1.16	1.60

In the test runs only the time development of the scour depth was measured; the velocity was not measured. Visual observation, however, suggested that the bed particles were about to move, thus $U/U_{cr} \approx 1$, where U_{cr} is the critical velocity for particle entrainment. The scour depth measurements were made at the leading edge of the cylinder where the

maximum depth was observed. The cylinder was transparent allowing the measurements be made from inside the cylinder with the help of a periscope. The equilibrium scour depths obtained after about 120 [hours] for all tests are shown in Table 2.2.

2.3.2 Time evolution of scour depth

The time histories of the scour depth are depicted in Fig. 2.5a,b plotted in normal and logarithmic scales.

Observation of the scour development within the first 3 to 5 [minutes] revealed that the scouring process was very active. The scour initiated at two points approximately 90° to the right and left off the centerline. The initial scouring propagated upstream along the perimeter of the cylinder and the two scours met at the leading edge of the cylinder. The scour depth increased rapidly that at the end of the first hour it reached 50% of the equilibrium depth. The rate of scour slowed down during the next 48 [hours], after which the scour depth did not show a significant increase. In the fifth day the scour depth did not change appreciably; the scour geometry thus obtained was considered as a near equilibrium one.

The equilibrium scour depths from the four test runs are in the range of $1.55 \le d_s/D_p \le 1.95$, which are in the range of the measurements reported in the literature (see Fig. 2.6 and the discussion given in the next section).

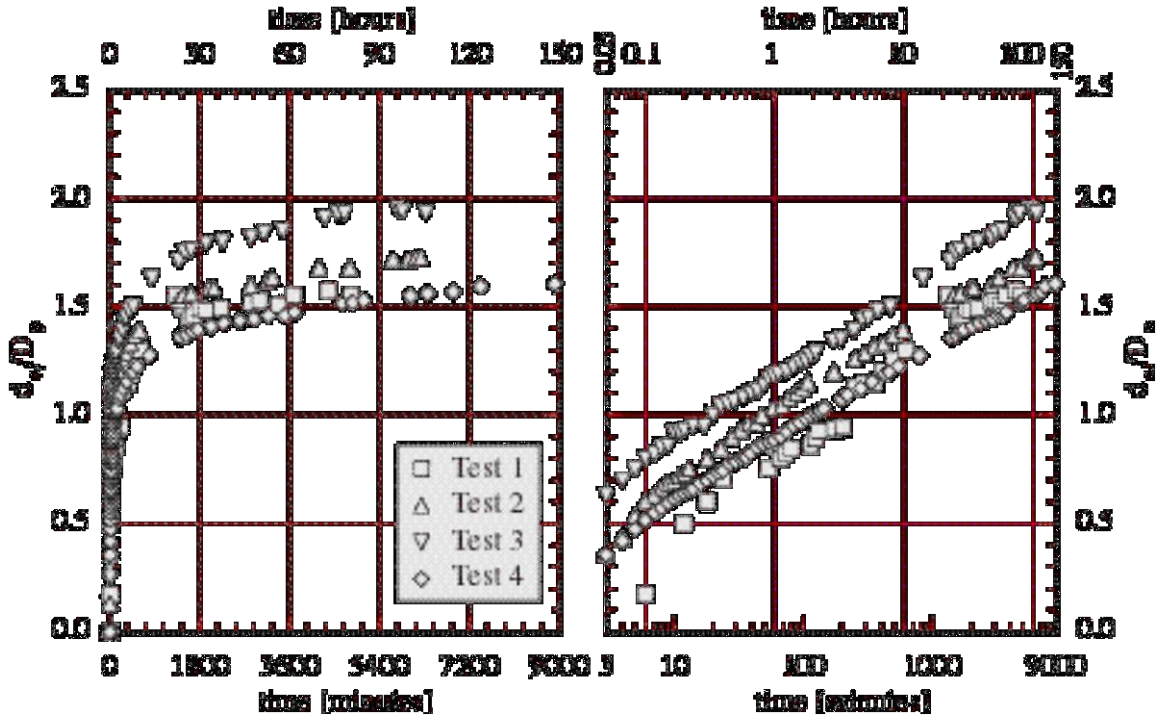

Fig. 2.5 Relative scour depth at clear water scour versus time in (a) the normal scale and (b) the logarithmic scale

2.3.3 Comparison to other measurements

Various factors affect the scour depth; those are the fluid, the flow, the sediment, and the cylinder itself (*Breusers* et *al*., 1977; *Breusers* and *Raudkivi*, 1991; *Graf* and *Altinakar*, 1996). The time may also have an effect (*Melville*, 1975). A general function relating the relative scour depth, d_s/D_p, to the dimensionless parameters is given as follows (*Graf* and *Altinakar,* 1996):

$$\frac{d_s}{D_p} = f\left(\frac{U}{U_{cr}}, \frac{h}{D_p}, \frac{d}{D_p}; \xi_g, \xi_s, \xi_\alpha\right) \tag{2.19}$$

in which d is the sediment diameter, ξ_g, ξ_s and ξ_α are dimensionless correction coefficients due to the sediment grading, pier shape, and pier alignment, respectively. The influence of those coefficients on the relative scour depth is given in graphical forms based on various measurement data (see *Graf* and *Altinakar,* 1996); it is reproduced here in Fig. 2.6. For a cylindrical pier aligned with the flow as in the present experiment, there is not any correction due to neither the shape nor alignment of the pier, $\xi_s = \xi_\alpha = 1$. Putting the results of the present measurements on these graphs, it can be seen that the effect of the flow velocity and flow depth agrees reasonably with the other measurements (see Fig. 2.6a,b). The effect of the sediment diameter in the present measurements, however, underestimates the scour depth when compared with the other measurements (see Fig. 2.6c). The coefficient of sediment grading, ξ_g, —taking as $\xi_g = 0.9$ (see Fig. 2.6d)— may explain partially this underestimation.

2.3.4 Selected cylinder diameter

Based on those preliminary experiments and technical considerations relating to the ADVP configuration, the $D_p = 15$ [cm] cylinder was selected for the experiment with the velocity measurements (see Sect. 2.2.4). The flow parameters were modified slightly, by selecting a smaller discharge, $Q = 0.200$ [m^3/s], and accordingly a lower flow depth, $h_\infty = 18$ [cm] (see Table 2.1). The maximum scour depth with this selected flow parameters is $d_s = 25$ [cm] ($d_s/D_p = 1.7$), which was obtained after a 5-day of continuous run. Fig. 2.7 shows the geometry of this scour hole. The ridge formed by the deposition of the bed material in the downstream section extends up to 5 [m] from the cylinder; the original bed level was found 0.5 [m] further downstream.

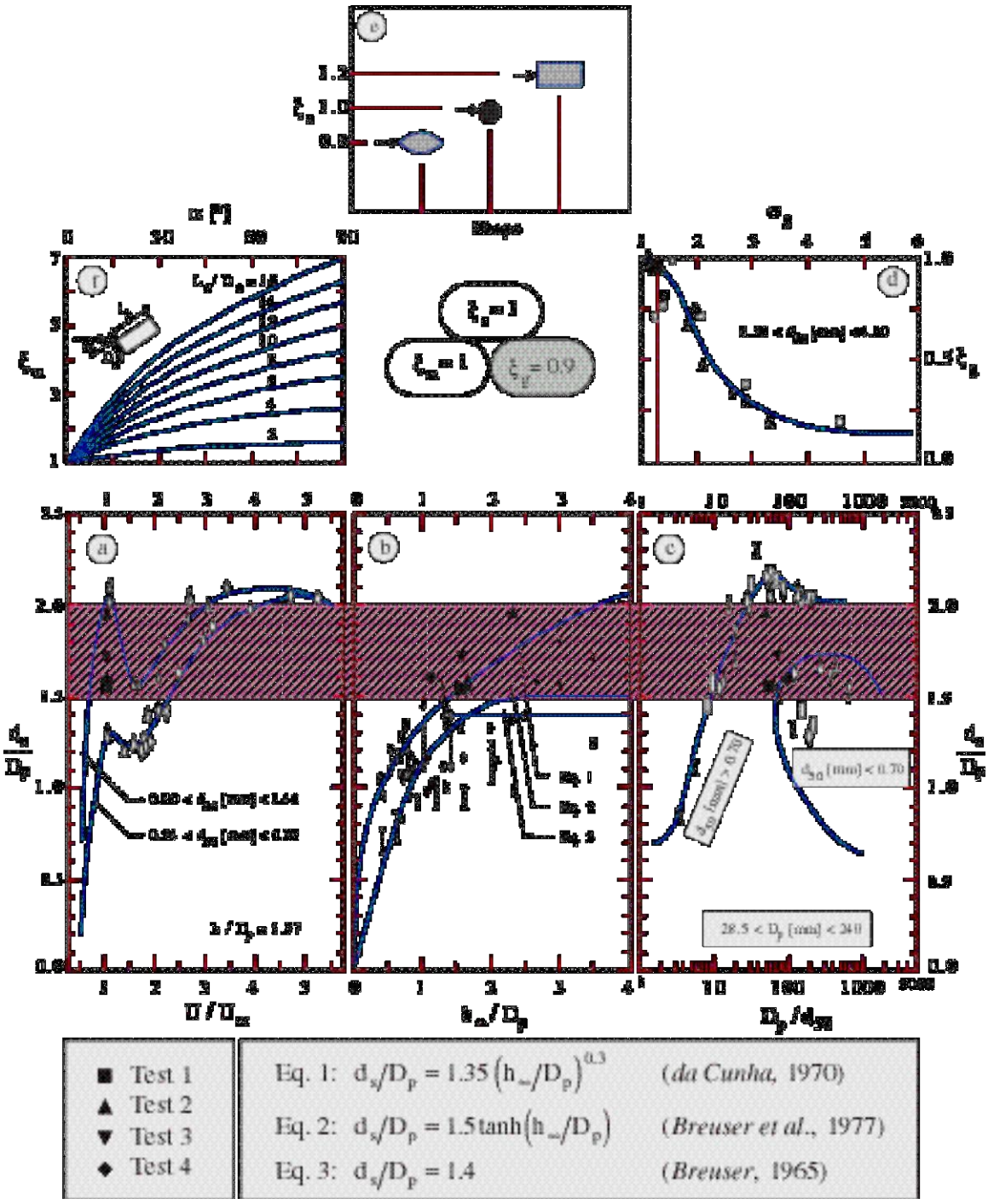

Fig. 2.6 Comparison of the measured relative scour depth with other measurements (see *Graf* and *Altinakar*, 1996)

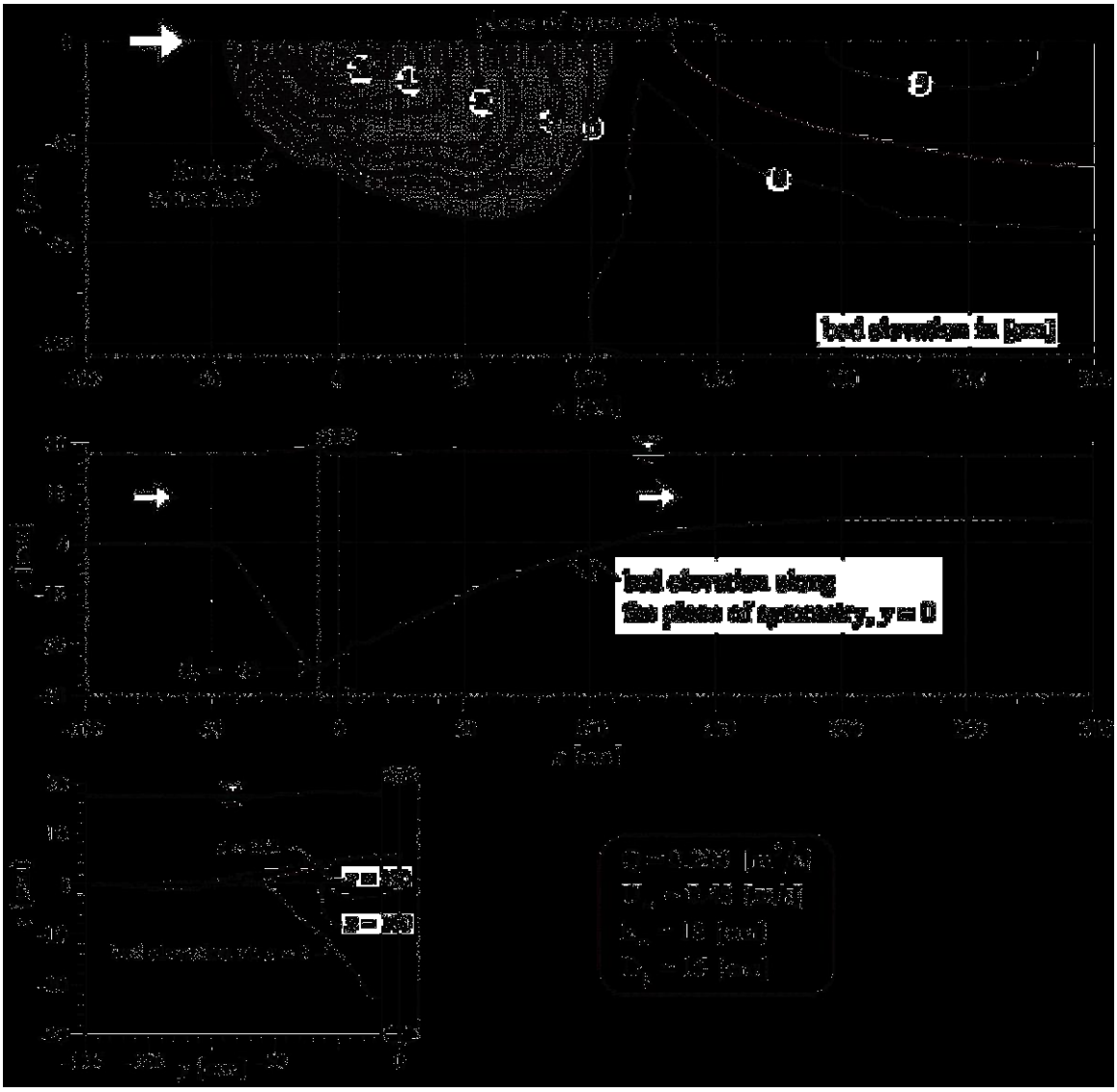

Fig. 2.7 Scour hole geometry obtained with the selected flow configuration, $Q = 0.200$ [m^3/s], $U_\infty = 0.45$ [m/s], $h_\infty = 18$ [cm], and $D_p = 15$ [cm].

2.4 Velocity measurements in the uniform approach flow (without cylinder)

2.4.1 Measurement stations

The measurement of velocity in the uniform flow (it will be the approach flow when the cylinder is installed) is intended to provide the reference flow data, which shall be useful later in analyzing the flow data from the measurements around the cylinder.

Six vertical distributions of velocity were measured at stations x_L [m] = 9, 10, 11, 12, 13, and 14 along the centerline of the channel. At each station, 52 data points are obtained

throughout the flow depth. The velocity was measured at a frequency of 20.8 [Hz] during 150 [s]; this produces a total number of instantaneous velocities of 3140 at each data point. The measurement data are presented in the form of vertical distributions of the time-averaged velocity, of the turbulence intensity, and of the Reynolds stress. The Cartesian coordinate system is used.

2.4.2 Vertical distribution of the (time-averaged) velocity

Fig. 2.8 shows the vertical distributions of the time-averaged velocities measured at the six stations. For writing simplicity the term "velocity", otherwise explicitly stated, will be used to describe the time-averaged velocity. In uniform flows, the vertical distribution of the longitudinal velocity, u(z), can be described by the universal law-of-the-wall, for the so-called inner region, $z/h \le 0.2$, and by the Coles law-of-the-wake for the entire flow depth, except within the viscous layer, $0.1 \le z/h \le 1$.

Assuming the flow is hydraulically rough, the law-of-the-wall reads (*Graf and Altinakar*, 1998, p. 56):

$$\frac{u(z)}{u_*} = \frac{1}{\kappa} \ln\left(\frac{z}{k_s}\right) + B_R \tag{2.20}$$

where u_* is the friction velocity, k_s is the equivalent standard roughness of the bed ($k_s = d_{50} = 2.1\,[\text{mm}]$), B_R is a constant of integration, and κ is the Karman constant ($\kappa = 0.4$). The origin of the vertical distance, $z = 0$, is defined at a level $0.2k_s$ below the peaks of the bed roughness. By using the best fit method of Eq. 2.20 to the logarithmic plot of the measured longitudinal velocity data for $z \le 0.2h$ (see Fig. 2.8a), the friction velocity, u_*, and the constant of integration, B_R, can be obtained and are presented in Table 2.3 The average values from the six measurements are $\bar{u}_* = 2.7\,[\text{cm/s}]$ and $\bar{B}_R = 8.75\,[-]$. The average value of $\bar{B}_R$ falls in the range of values reported in the literature, i.e. 8.5 ± 15% (see *Graf and Altinakar*, 1998, p. 56).

Using the friction velocity, $\bar{u}_* = 2.7\,[\text{cm/s}]$, and taking the viscosity of water, $\nu = 10^{-6}$ [m^2/s], the Reynolds number computed based on the bed standard-roughness is found as $\text{Re}_{k_s} = u_* k_s/\nu = 57$. This value, being less than 70, suggests that the bed is not completely rough.

The vertical distribution of the velocity can be expressed by the Coles law-of-the-wake which is valid for the inner and outer regions (except within the viscous layer). For the hydraulically rough uniform flow, the Coles equation can be written in the following form (see *Song et al.*, 1994):

$$\frac{u(z)}{u_*} = \frac{1}{\kappa} \ln\left(\frac{z}{k_s}\right) + B_R + \frac{2\Pi}{\kappa} \sin^2\left(\frac{\pi z}{2h}\right) \tag{2.21}$$

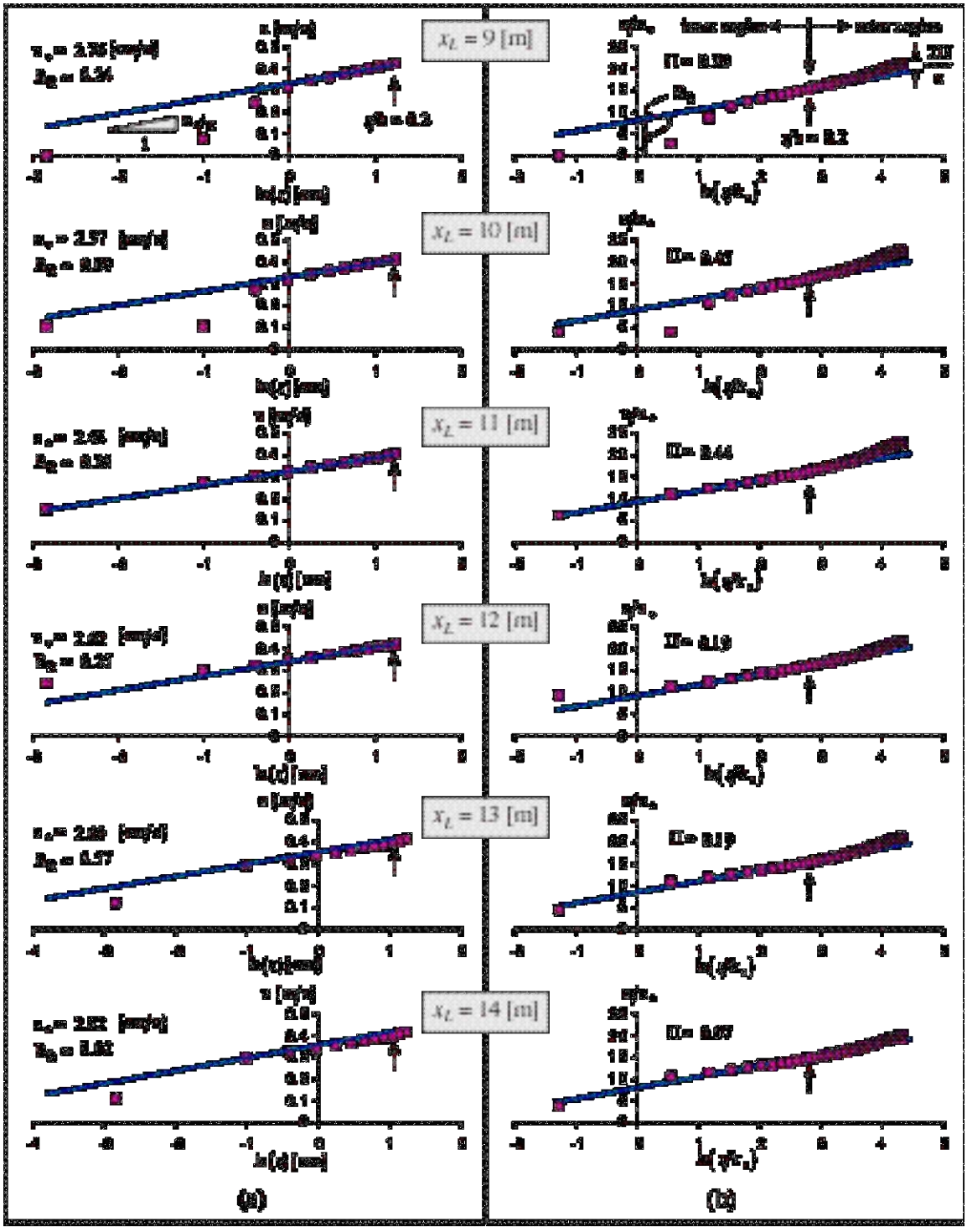

Fig. 2.8 Distributions of the longitudinal velocity, u(z), of the approach flow: (a) in the inner region according to the law-of-the-wall, and (b) in the inner- and outer-regions according to the Coles law-of-the-wake.

where Π is the wake-strength parameter. Using the friction velocity previously obtained and the measured u-component data for the inner and outer regions (see Fig. 2.8b), the Π-value at every station can be determined from the difference between the measured value and the theoretical one at the water surface, which is equal to $2\Pi/\kappa$. Since the velocity data at the surface is not available, the upper most value was selected as an approximation; these are presented in Table 2.3 The average Π-value obtained from this operation, being $\Pi = 0.28$, is in the range of the values reported in the literature, i.e. $0.1 \leq \Pi \leq 0.3$ (see *Graf and Altinakar*, 1996, p. 58).

Table 2.3 Parameters of the vertical distributions of u-velocities and the Reynolds shear-stresses of the approach flow.

Station	From the u-profile			From the $-\overline{u'w'}$-profile	
	Π	B_R	u_* [cm/s]	u_* [cm/s]	τ_o/ρ [m^2/s^2]
$x_L = 9$ [m]	0.29	8.24	2.76	2.64	6.94×10^{-4}
$x_L = 10$ [m]	0.44	9.09	2.57	2.57	6.60×10^{-4}
$x_L = 11$ [m]	0.44	9.35	2.48	2.80	7.84×10^{-4}
$x_L = 12$ [m]	0.20	9.25	2.62	2.39	5.70×10^{-4}
$x_L = 13$ [m]	0.20	8.57	2.69	2.93	8.58×10^{-4}
$x_L = 14$ [m]	0.09	8.02	2.82	2.52	6.33×10^{-4}
Average	0.28	8.75	2.70	2.60	7.00×10^{-4}

2.4.3 Vertical distribution of the turbulence intensities

The intensity of turbulence is defined as the root mean square of the fluctuating velocities, $\sqrt{\overline{u'u'}}$, $\sqrt{\overline{v'v'}}$, and $\sqrt{\overline{w'w'}}$. Fig. 2.9 shows the vertical distributions of the turbulence intensities measured at the six stations. The data have been normalized by the friction velocity, $u_* = 2.7$ [cm/s]. As can be seen in Fig. 2.9, all three components of the turbulence intensities decrease with an increase in depth. Close to the bed, however, there is a decreasing tendency in the longitudinal, $\sqrt{\overline{u'u'}}$, and vertical, $\sqrt{\overline{w'w'}}$, components which is not observed for the transversal component, $\sqrt{\overline{v'v'}}$. The measured turbulence intensities shall be compared with the expressions of the turbulence intensities proposed by Nezu and Nakagawa (see *Nezu and Nakagawa*, 1993, p. 24) which are given in the following form:

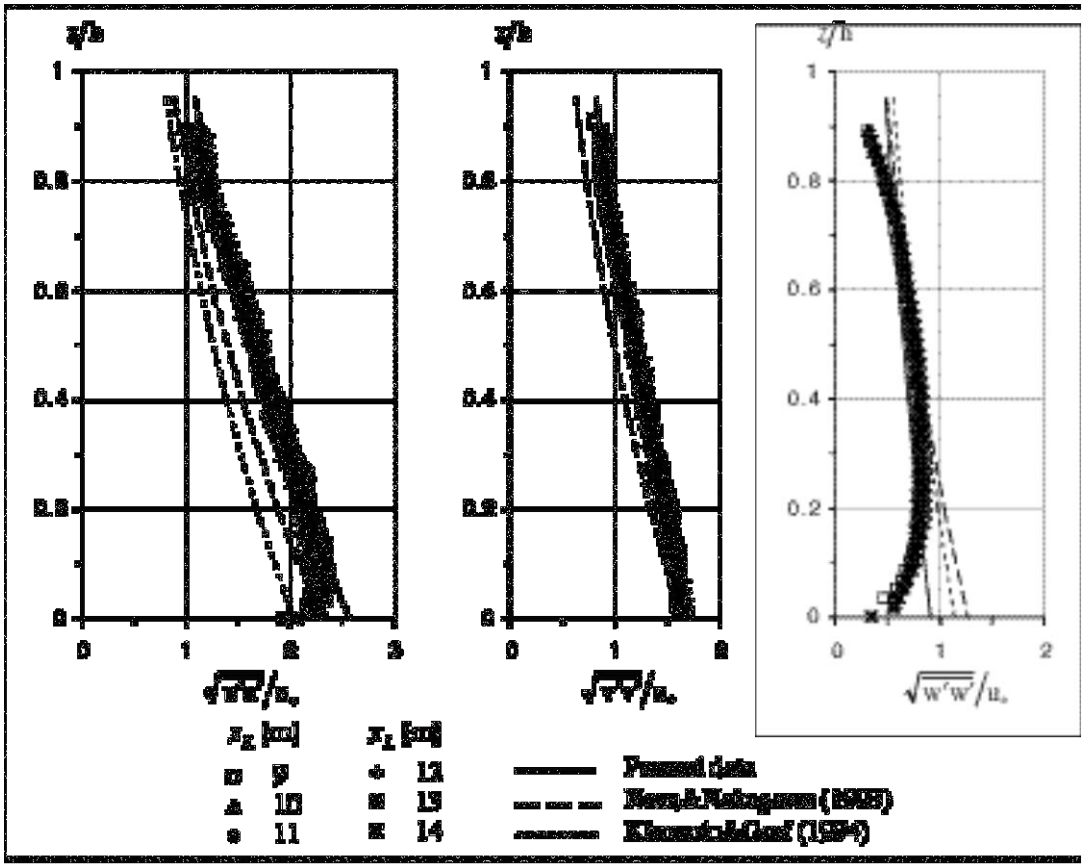

Fig. 2.9 Turbulence intensities of the approach flow.

$$\sqrt{\overline{u'u'}}/u_* = D_u \exp\left(-C_u z/h\right)$$
$$\sqrt{\overline{v'v'}}/u_* = D_v \exp\left(-C_v z/h\right) \qquad (2.22)$$
$$\sqrt{\overline{w'w'}}/u_* = D_w \exp\left(-C_w z/h\right)$$

where, C_u, C_v, C_w, and, D_u, D_v, D_w, are empirical constants. These constants are supposedly independent of the Reynolds and Froude numbers with the values of: $D_u = 2.30$, $D_v = 1.63$, $D_w = 1.27$, and $C_u = C_v = C_w = 1$ (see *Nezu and Nakagawa*, 1993, p. 24). Slightly different values were reported from measurements in hydraulically rough flows: $D_u = 2.04$ with $C_u = 0.97$ and $D_w = 1.14$ with $C_w = 0.76$ (see *Kironoto and Graf*, 1994). By applying regression method to the present data and using Eq. 2.22, the constants D and C, and their correlation coefficient R^2, are as follows:

$D_u = 2.57$ (2.04) [2.30], $C_u = 0.90$ (0.97) [1.0], $R^2 = 0.97$,
$D_v = 1.74$ (—) [1.63], $C_v = 0.79$ (—) [1.0], $R^2 = 0.98$,
$D_w = 0.91$ (1.14) [1.27], $C_w = 0.67$ (0.76) [1.0], $R^2 = 0.50$.

The values inside the parentheses are according to *Kironoto and Graf* (1994) and those in the square brackets are according to *Nezu and Nakagawa* (1993). As can be seen, the vertical component of the turbulence intensity has the least correlation coefficient. The

plot of $\sqrt{\overline{w'w'}}$ indicates that it is not exponentially distributed. It is not clearly known what may cause this deviation of the measured and theoretical distributions of $\sqrt{\overline{w'w'}}$; other measurements at LRH have also the same phenomenon (see *Cellino*, 1998; *Yulistiyanto*, 1997).

2.4.4 Vertical distribution of the Reynolds shear-stresses

Fig. 2.10 shows the vertical distributions of the Reynolds stresses measured at the six stations. The transversal component of the Reynolds stress, $-\overline{v'w'}$, is always negligible compared to the longitudinal component, $-\overline{u'w'}$.

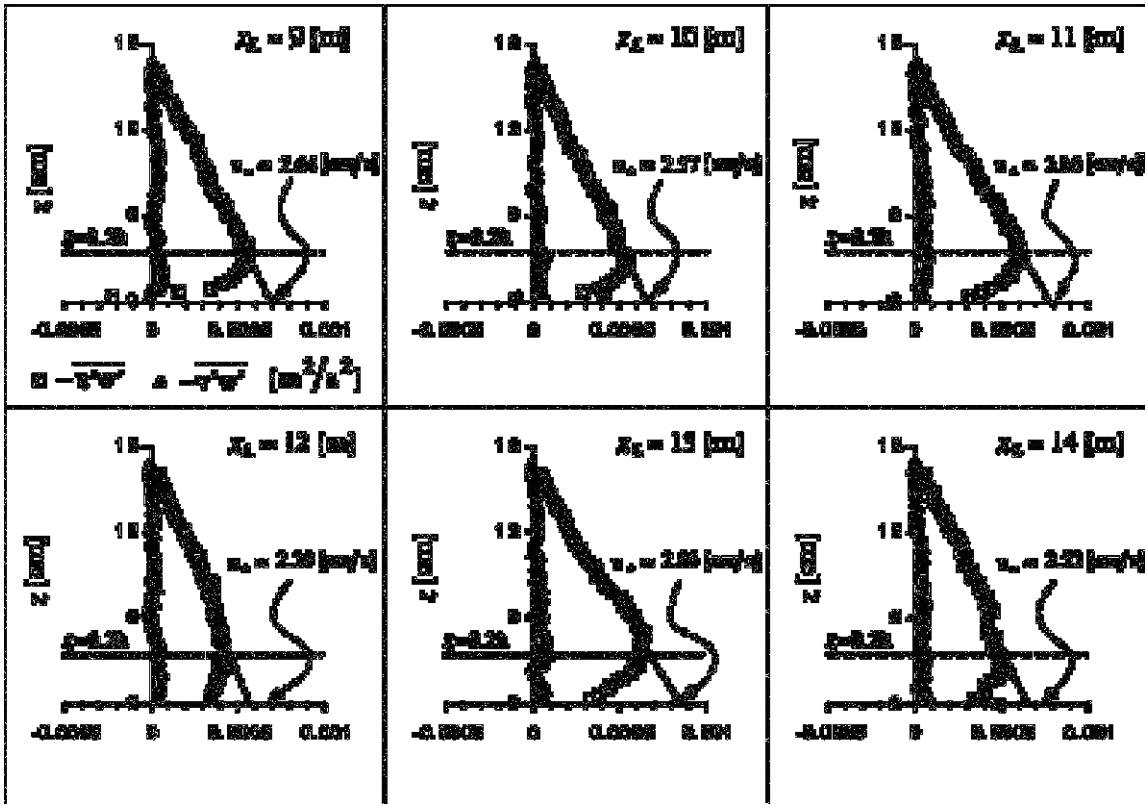

Fig. 2.10 Reynolds shear-stresses of the approach flow.

The Reynolds stress, $-\rho\overline{v'w'}$, can be interpreted as the total shear stress since the viscous component of the shear stress is negligible compared to the turbulence stress in the most part of the flow depth. Its vertical distribution is linear with a zero stress at the water surface and a maximum at the bed. It is given by (*Graf and Altinakar*, 1998, p. 64):

$$\tau_{zx}/\rho = -\overline{u'w'} = \tau_o/\rho(1 - z/h) = u_*^2(1 - z/h) \tag{2.23}$$

in which the origin of the vertical distance, $z = 0$, is defined at a level $0.2k_s$ below the peaks of the bed roughness. The above relation can be used to obtain the bed shear stress,

τ_o, and accordingly the friction velocity, u_*, from the measured distribution of $-\overline{u'w'}$. The measured Reynolds stress shows that it is linearly distributed in the outer region (see Fig. 2.10). However, within the inner region and towards the bed, the distribution swings and diminishes. The reason of this phenomenon is not yet been known. It is suspected that an inherent characteristic of the measuring instrument, due most probably to the difficulty in obtaining clear acoustic back-scattered signals at regions close to the bed, might have contributed to this phenomenon (see also *Cellino*, 1998; *Yulistiyanto*, 1997). For that reason, the bed shear stress is obtained by best fitting of Eq. 2.23 to the measured data at the outer region, $z/h \geq 0.2$, and extrapolating the fitted line to the bed, $z = 0$, to get τ_o and u_* (see Fig. 2.10). The bed shear stress and the friction velocity obtained at the six stations are presented in Table 2.3. The average u_*-value, being $\bar{u}_* = 2.60\,[\mathrm{cm/s}]$, is rather close to the one computed previously from the velocity profile.

2.5 Velocity measurements around the cylinder

2.5.1 Measurement strategy

The flow along the channel is assumed to be symmetrical about the line passing through the center of the cylinder. This assumption was taken for practical reasons since the flow in the scour hole along the plane of symmetry is not completely two-dimensional as will be evidenced from the measurements. The measurements were performed at the one-half area around the cylinder. Vertical distributions of the instantaneous velocities were obtained at the measuring stations located at P(r,α,z) (see Fig. 2.11), where r [cm] is the radial distance ($r = 0$ is the center of the cylinder), α [°] is the angular direction of the plane ($\alpha = \theta - 180°$), and z [cm] is the vertical direction ($z = 0$ is in the original uneroded-bed level). While the positioning of the measurement stations was expressed according to the cylindrical coordinate system, (r,α,z), the velocities were decomposed into its components along the Cartesian coordinate system, (u,v,w). The coordinate transformation (see Fig. 2.4 and Eq. 2.13) provides the relation between these two coordinate systems. Five main radial-planes: $\alpha = 0°$, 45°, 90°, 135° and 180° (see Fig. 2.11a) were selected in which about 15 to 25 verticals were obtained for each plane. Additional measurements, with fewer verticals (8 to 10 verticals), were performed at 6 planes: $\alpha = 15°$, 30°, 60°, 75°, 105° and 120°. These measurements provide supplementary data that may be necessary in the analyses of the flow pattern (this will be treated in Chapter 5). For technical reasons, each plane was divided into three zones: A($r \geq 20, \alpha, z \geq 5$), B($r, \alpha, z < 5$) and C($r < 20, \alpha, z \geq 5$) (see Fig. 2.11b). Measurements were possible in the zones A and B, but technical difficulties hinder the measurement in zone C, being a “blank zone” where data cannot be obtained. The measurements in zones A and B were performed such that the data obtained from the two measurements overlap. The overlap is generally made at $7 \geq z\,[\mathrm{cm}] \geq -2$, that is, the measurements at zone A penetrate up to $z = -2$ [cm] and those in zone B start at $z = 7$ [cm] (see Fig. 2.11c).

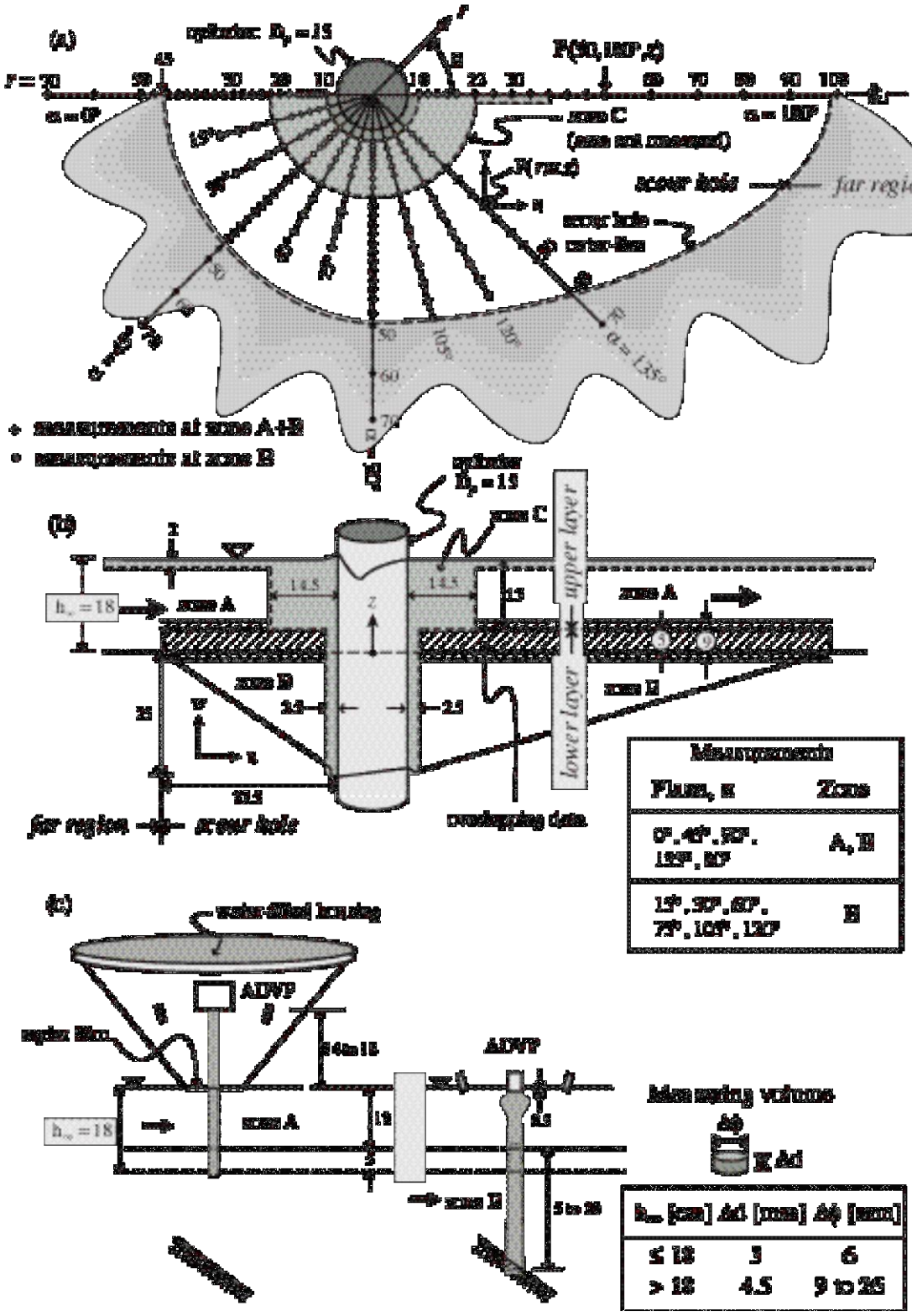

Fig. 2.11 Measurement stations around the cylinder and ADVP positioning (scale in [cm]).

Measurements in zone A. The emitter and the receivers of the ADVP-instrument were placed in a water-filled housing at the water surface (see Fig. 2.11c). A mylar film was provided as the contact medium between the housing and the water surface. Precautions were taken in positioning the housing so that least contact between the mylar and the water surface was maintained to minimize flow perturbation. Nevertheless, the data within 2 [cm] from the water surface are considered not to be reliable and are excluded. A focused-type emitter was used which has the advantage of having a small-diameter acoustic-beam of 6 [mm], which is also the diameter of the measurement volume (a 4 [μs] time-gate was used which corresponds to a thickness of the measuring volume of 3 [mm], see Sect. 2.2.2). The transducer was positioned several centimeters, 14 to 18 [cm], above the water surface; this distance is required to avoid the parasite acoustic signals reflected by the mylar. The measurements, however, were not possible for the depth of more than 20 [cm] (zone B) due to the limit of the effective distance of the emitted wave. The instrument housing hinders, furthermore, measurements at radial distance closer than 20 [cm] (zone C). Some of the measurement data at zone A downstream of the cylinder (plane $\alpha = 180°$), at $r \leq 38$, have to be interpreted with caution. The measurements at that part was difficult, the acoustic signals recorded by the ADVP-instrument were not clean, and thus the data quality is less good than that of the other part. This problem is due to a fluctuating water surface, that makes the placement of the instrument housing difficult, and the air entrainment into the flow, that frequently blocks and disturbs the acoustic waves. The fluctuating water surface and the air entrainment are provoked by the wake-vortices downstream of the cylinder.

Measurements in zone B. The ADVP was put directly at the water surface, penetrating about 0.5 [cm] into the flow (see Fig. 2.11c). To minimize the perturbation of the instrument to the flow, a small emitter, of diameter 28 [mm], was used. This allows also the measurements close to the cylinder, up to $r = 10$ [cm] (2.5 [cm] from the leading edge of the cylinder). The configuration, however, cannot measure area closer than 10 [cm] from the emitter (zones A and C). The measuring volume with this type of emitter is of 9 to 26 [mm] (diameter) and of 4.5 [mm] (thickness).

2.5.2 Data presentations

The results of the measurements are presented as the vertical distributions (z profiles) of the velocities, turbulence intensities, and Reynolds stresses in their Cartesian coordinate components at different measuring verticals, P(r,α,z). The measurements are presented in the following figures, Fig. 2.12 to Fig. 2.16; they are classed first for each radial plane ($\alpha = 0°$, $\alpha = 45°$, etc.) and subsequently according to the radial position in the order of approaching the cylinder. Brief discussions are given to the data in each plane. Measured data from the additional planes ($\alpha = 15°$, 30°, etc.) will be presented in the succeeding chapter (see Chapter 5) where more detailed analyses of the data will be elaborated. The terms *upper layer* and *lower layer* (see Fig. 2.11) are frequently used in the following presentation to distinguish the regions above and below the original uneroded-bed level, $z = 0$, respectively. Other terms, the *far region* and the *scour-hole region* are used to

identify the uneroded area beyond the outer line of the scour hole and the one inside the scour-hole perimeter, respectively (see Fig. 2.11).

2.5.3 Measurements in the plane $\alpha = 0°$

The scour hole in the plane $\alpha = 0°$ starts at $r \approx 45$ [cm] ($3D_p$) with the maximum scour depth of $d_s = 25$ [cm] ($1.67h_\infty$) at the leading edge of the cylinder; the downward incline into the scour-hole is thus $\Theta = 35°$. At 26 stations, vertical distributions of velocities, Reynolds stresses, and turbulence intensities are obtained from the measurements in the plane $\alpha = 0°$, being the plane of symmetry upstream of the cylinder. The data were obtained in the radial distance of $10 \le r$ [cm] ≤ 80, which cover the far region (the approach flow) and the scour hole region. For $r \ge 20$ [cm], the data cover almost the entire flow depth (zones A and B), while for $r < 20$ [cm], the data are only available at $z \le 5$ [cm] (zone B). The measured distributions are plotted and presented in Fig. 2.12; here the data at $r = 80$ [cm], being very much similar to those at $r = 70$ [cm], are not shown.

Velocities in the plane $\alpha = 0°$. The u-component is dominant along the most part of this plane of symmetry. In the far region, $r \ge 45$ [cm], the v- and w-components are practically negligible. Entering the scour-hole region, $r \le 45$ [cm], the u-component remains important up to close to the cylinder, notably within the upper layer, $z \ge 0$. This component does not show the effect of the cylinder until as close as $r = 20$ [cm]. Taking the u-component at $z = 0$, one observes that it is almost constant at $u \approx 0.4$ [m/s] ($0.9U_\infty$) before decreasing to $u \approx 0.2$ [m/s] ($0.45U_\infty$) approaching the cylinder. From $r = 30$ [cm], at the lower layer and approaching the cylinder, the w-component, being a downward component, becomes important. It usually reaches a negative maximum value in the upper layer of the scour hole, $w \approx -0.27$ [m/s] ($-0.6U_\infty$) and tends towards zero or slightly positive values at the solid boundary of the scour hole. Close to the solid boundary of the scour hole and notably at the range of $16 \le r$ [cm] ≤ 32, noticeable is a return flow formed by a negative u-component and a positive w-component. The v-component shows a noticeable deviation from zero at the lower layer and approaching the cylinder; it has a tendency of being biased towards one side. Close to the cylinder, the v-component shows non zero values (positive and negative ones) with a maximum value of $v = -0.045$ [m/s] ($0.1U_\infty$) at the lower layer. This suggests that the flow along the plane of symmetry, notably at the lower layer, is not completely two-dimensional.

Turbulence intensities in the plane $\alpha = 0°$. The measured turbulence intensities, presented as the root-mean-square (rms) of the fluctuating components of the velocity, $\sqrt{\overline{u'u'}}$, $\sqrt{\overline{v'v'}}$, and $\sqrt{\overline{w'w'}}$, are shown in the second column of Fig. 2.12. In the far region, $r \ge 45$ [cm], their vertical distributions are similar to those of the uniform approach flow. Within the scour-hole region, the distributions show little effect of the cylinder within the upper layer and be particularly characterized by a sharp turn towards a peak underneath the $z = 0$. The peak becomes noticeable at $r = 36$ [cm] and remains so up to $r = 10$ [cm]. The $\sqrt{\overline{u'u'}}$-peak is more or less constant of about $\sqrt{\overline{u'u'}} \approx 0.08$ to 0.09 [m/s]. The peaks of the other components are always smaller, being about $0.5\sqrt{\overline{u'u'}}$

and $0.3\sqrt{\overline{u'u'}}$ for the $\sqrt{\overline{v'v'}}$ and $\sqrt{\overline{w'w'}}$, respectively. Close to the solid boundary of the scour hole, there is a strong tendency that the $\sqrt{\overline{u'u'}}$ and $\sqrt{\overline{v'v'}}$ increase; this increase becomes important approaching the cylinder where maximum values of $\sqrt{\overline{u'u'}} \approx 0.20$ [m/s] and of $\sqrt{\overline{v'v'}} \approx 0.10$ [m/s] are observed. Close to the cylinder, the vertical component has a maximum value of $\sqrt{\overline{w'w'}} \approx 0.04$ [m/s].

Reynolds stresses in the plane $\alpha = 0°$. The measured Reynolds shear-stresses, presented by the $-\overline{u'w'}$ and $-\overline{v'w'}$ components, are shown in the third column of Fig. 2.12. The linear distribution of the $-\overline{u'w'}$, similar to that in the uniform approach flow, is observed within the far region, $r \geq 45$ [cm], and remains so within the upper layer of the scour-hole region, $z \geq 5$ [cm] and $r \leq 45$ [cm]. Within the scour-hole region and at the lower layer, $z \leq 5$ [cm] and $r \leq 45$ [cm], the distribution sharply turns towards a peak $-\overline{u'w'}$ underneath the $z = 0$. The peak moves downward as the scour hole becomes deeper approaching the cylinder. The peak becomes pronounce at $34 \geq r$ [cm] ≥ 28 with values ranging at $0.0015 \leq -\overline{u'w'}$ [m^2/s^2] ≤ 0.002. Below the peak, the $-\overline{u'w'}$ decreases with increasing scour hole. Approaching the cylinder, there are negative $-\overline{u'w'}$-values near the solid boundary of the scour hole. Approaching the cylinder, the negative $-\overline{u'w'}$ constantly increases from –0.005 at $r = 18$ [cm] to –0.002 [m^2/s^2] at $r = 10$ [cm]. The negative values correspond with the return flow component as previously described. The $-\overline{v'w'}$ remains essentially insignificant and is much smaller than the $-\overline{u'w'}$ up to $r = 13$ [cm]. The $-\overline{v'w'}$ becomes comparable with the $-\overline{u'w'}$ only close to the cylinder and within the lower layer where the distribution of the two components is similar, being characterized by a noticeable peak.

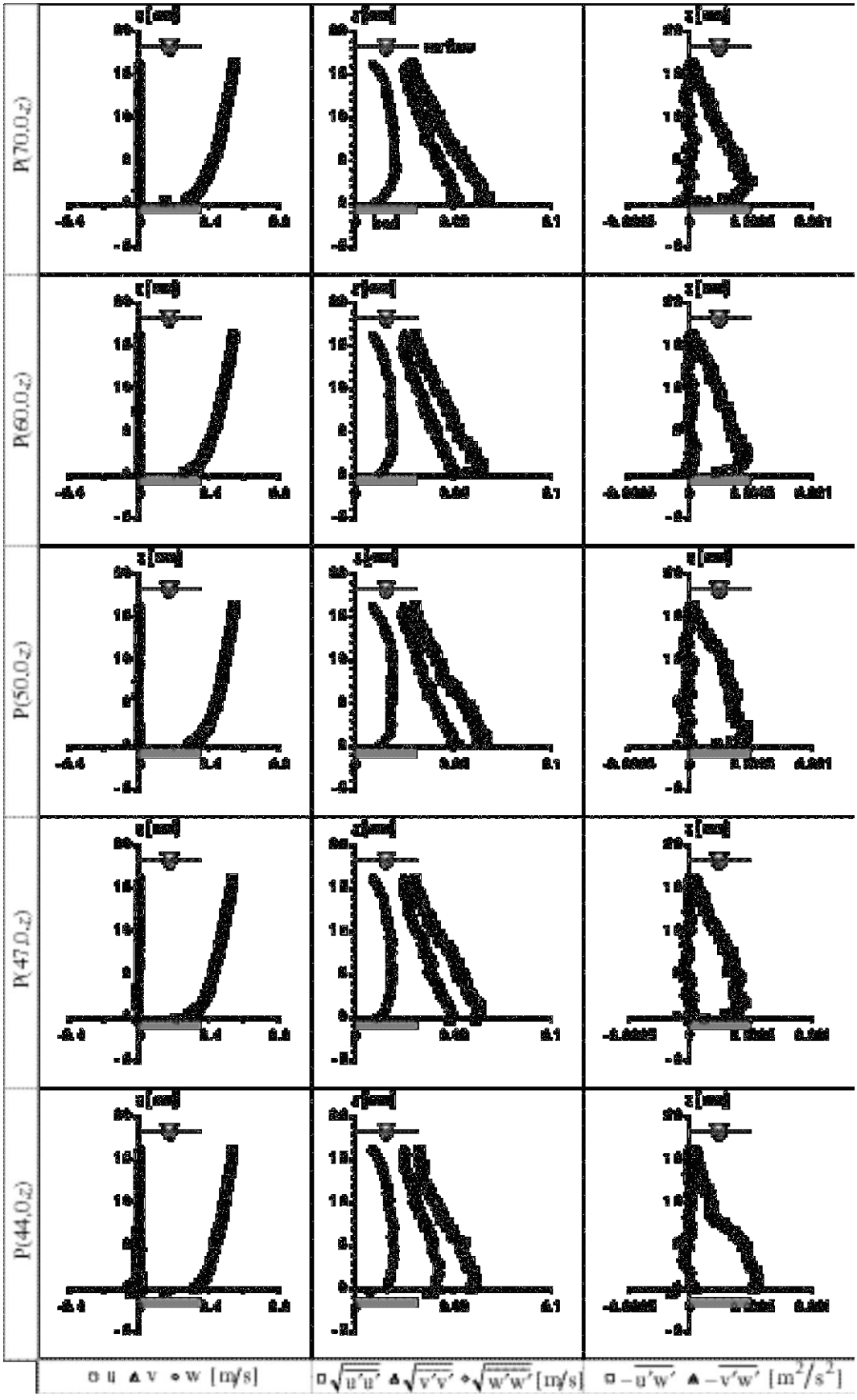

Fig. 2.12a Vertical distributions of the measured velocities, turbulence intensities, and Reynolds stresses in the plane $\alpha = 0°$.

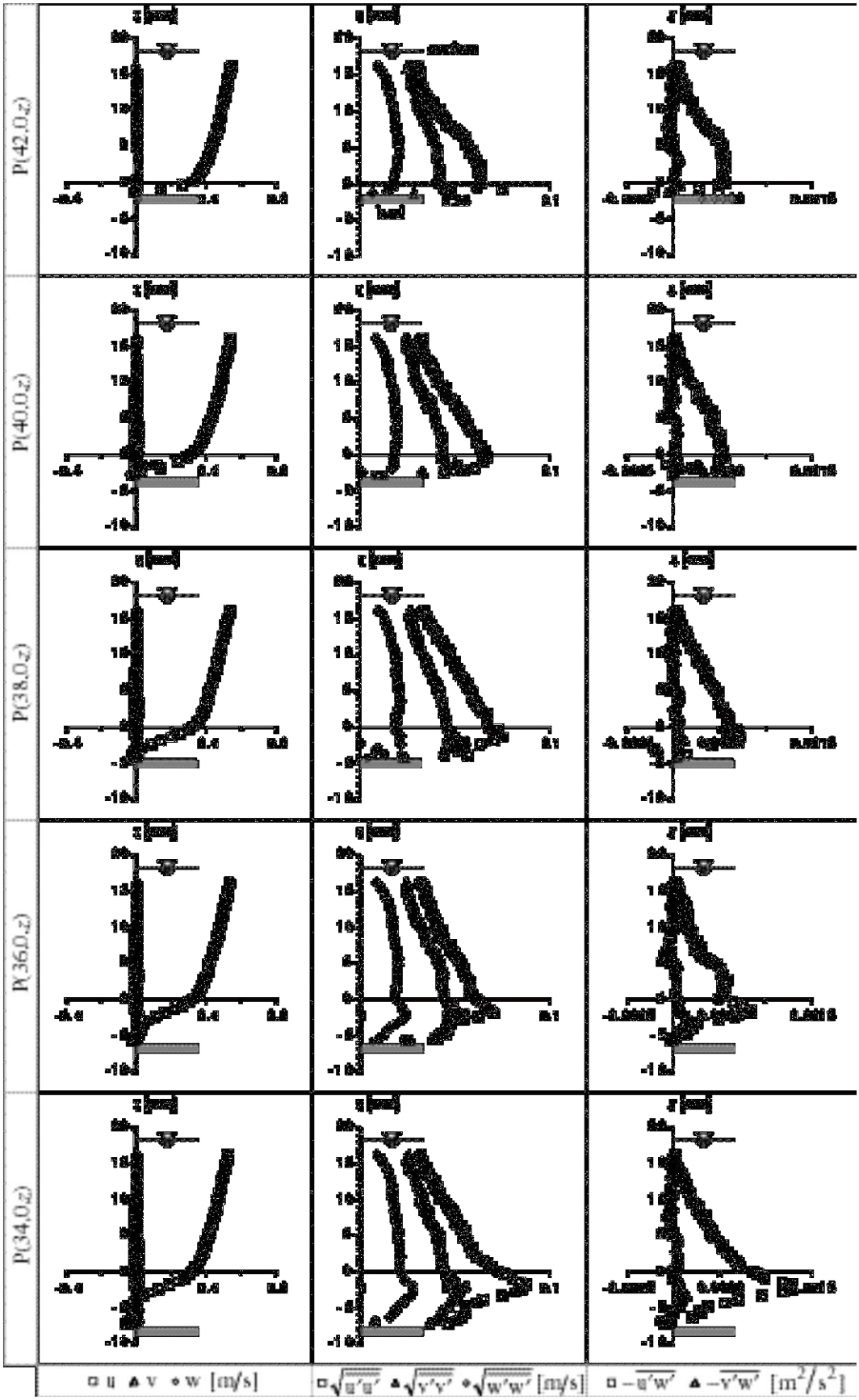

Fig. 2.12b Cont'd.

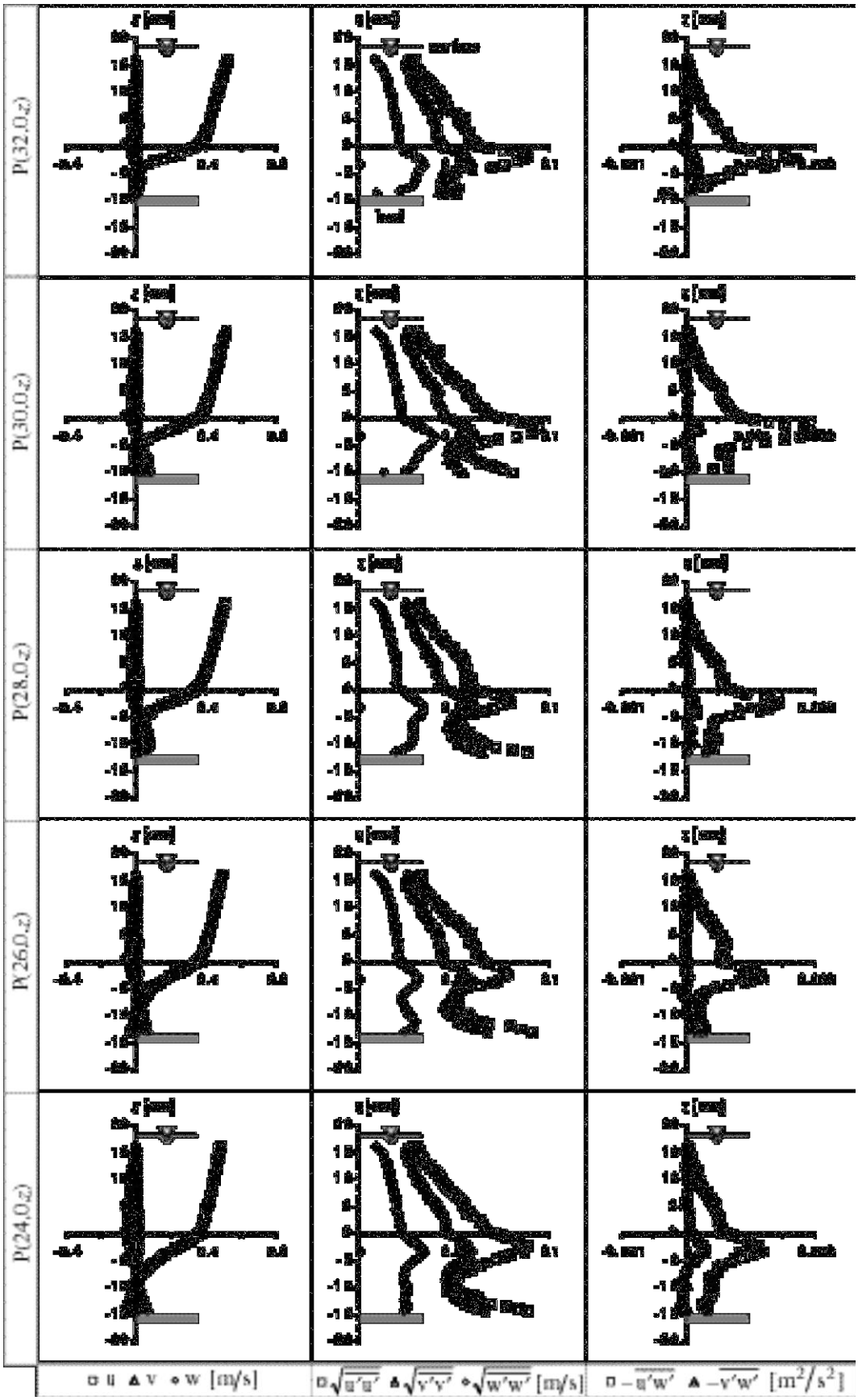

Fig. 2.12c Cont'd.

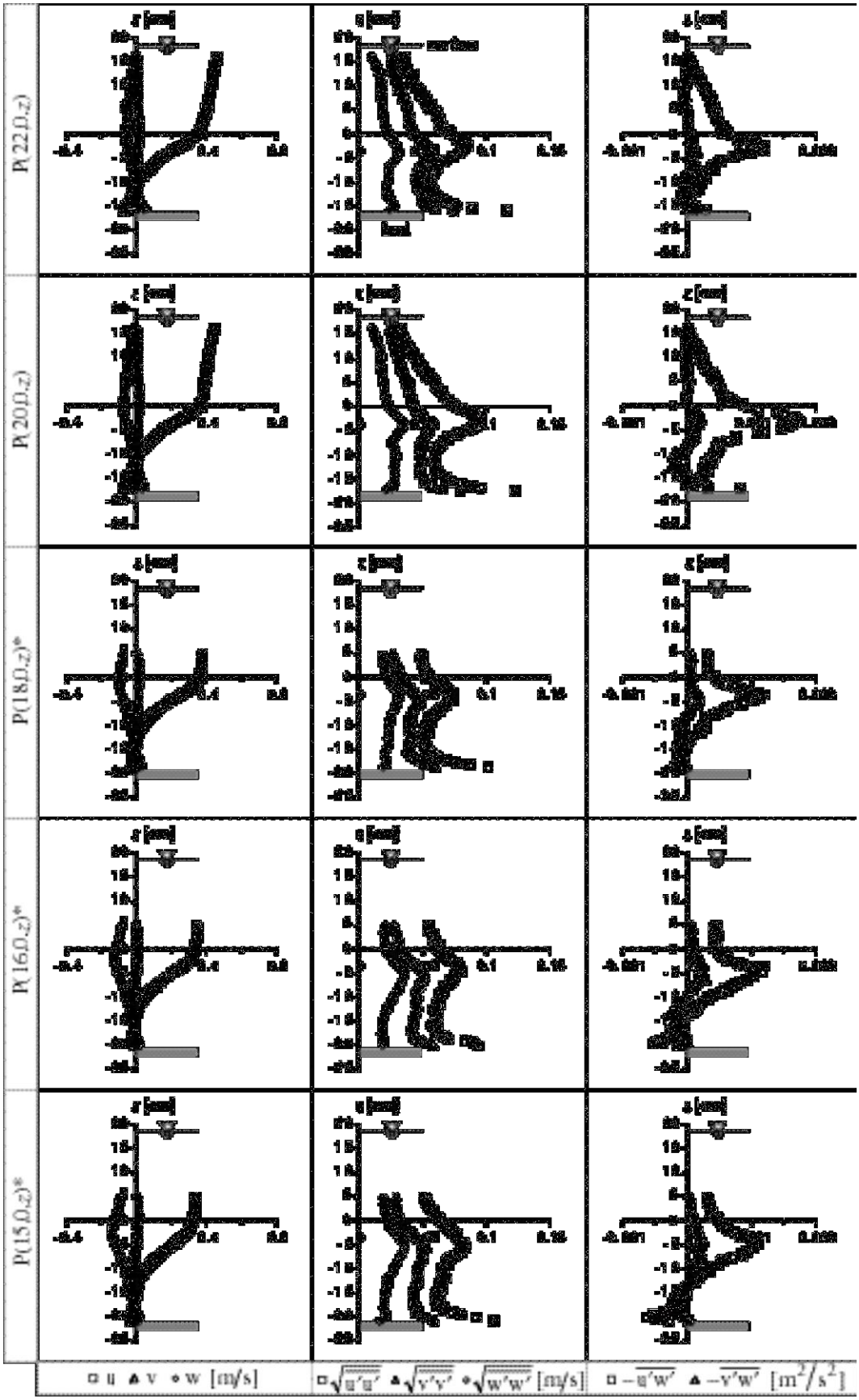

*Note: P(r≤ 18.0, z ≥ 5) data not available.

Fig. 2.12d Cont'd.

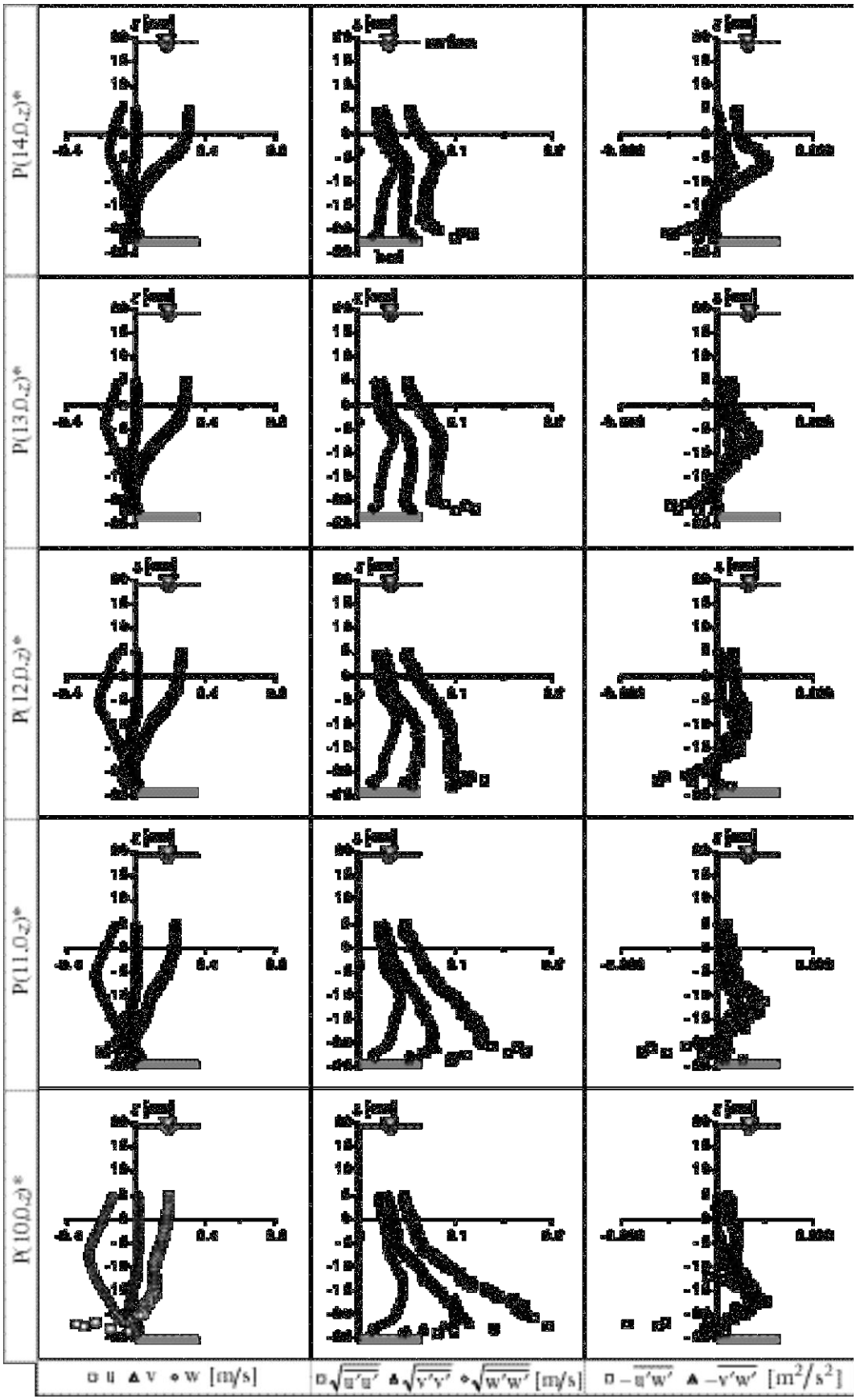

Fig. 2.12e Cont'd.

2.5.4 Measurements in the plane $\alpha = 45°$

The scour hole in the plane $\alpha = 45°$ starts at $r = 45$ [cm] ($3D_p$) with the maximum depth of $d_s = 25$ [cm] ($1.67h_\infty$) at the leading edge of the cylinder; the downward incline into the scour hole is thus $\Theta = 35°$. The measurements in the plane $\alpha = 45°$ were performed at $10 \le r$ [cm] ≤ 80; for $r \ge 22$ [cm] the data were obtained from almost the entire depth (zones A and B), while for $r \le 20$ [cm], the data were taken from $z \le 5$ [cm] (zone B). There are 26 vertical distributions of the velocities, the turbulence intensities, and the Reynolds stresses obtained. The measured distributions are presented in Fig. 2.13, which are plotted in the order of approaching the cylinder. The data at $r = 80$ [cm], being very much similar to those at $r = 70$ [cm], are not shown.

Velocities in the plane $\alpha = 45°$. The vertical distributions of the u-, v-, and w-velocities in the far region, $r \ge 45$ [cm], as have also been observed in the far region of the plane $\alpha = 0°$, have little indication of the cylinder effect. Their distributions are very much similar to those of the uniform approach flow. At the approach region, the u-component is dominant over the other components and this remains so throughout the upper layer of the scour hole region. The u-component is always positive at the upper layer. At the lower layer and at $24 \le r$ [cm] ≤ 36, there is a weak tendency of negative u-velocities, having a magnitude of $u \approx 0.045$ [m/s] ($0.1U_\infty$). The v- and w-components are negligible in the far region, but entering the scour-hole region and approaching the cylinder, they become pronounced; at the lower layer they are comparable to the u-component. In the scour-hole region, the flow is skewed, having negative v-components at the upper layer (the flow deflects away from the cylinder) and positive v-values at the lower layer (the flow skews towards the cylinder). Approaching the cylinder, the negative v-component becomes more important than the positive one, reaching the maximum value of $v \approx -0.18$ [m/s] ($-0.4U_\infty$) at $r \le 14$ [cm]. Similar observation can be made to the w-component; it appears as a downward flow that becomes more significant when approaching the cylinder. This downward flow is less strong compared to that in the plane $\alpha = 0°$. The maximum downward flow here is $w \approx -0.22$ [m/s] ($-0.5U_\infty$) at $r = 10$ [cm], which is 80% of that in the plane $\alpha = 0°$. At $16 \le r$ [cm] ≤ 34 and close to the solid boundary of the scour hole, where there is a tendency of negative u-component, the w-component shows a positive value with the maximum value of $w \approx 0.06$ [m/s] ($0.13U_\infty$).

Turbulence intensities in the plane $\alpha = 45°$. In the far region, $r \ge 45$ [cm], similar observations as those for the velocities can be made to the turbulence intensities; the intensities of the turbulence remain unaffected by the presence of the cylinder. Their distribution resembles that of the uniform approach flow. This is also the case at the upper layer of the scour-hole region. At the lower layer of the scour-hole region, the $\sqrt{\overline{u'u'}}$, $\sqrt{\overline{v'v'}}$, $\sqrt{\overline{w'w'}}$ components have a sharp turn towards the peak underneath the $z = 0$ [cm]. Far from the cylinder, the $\sqrt{\overline{u'u'}}$ is always dominant than the other components, but approaching the cylinder and at the lower layer, the $\sqrt{\overline{u'u'}}$ and $\sqrt{\overline{v'v'}}$ become comparable. The two components have a strong tendency of increasing close to

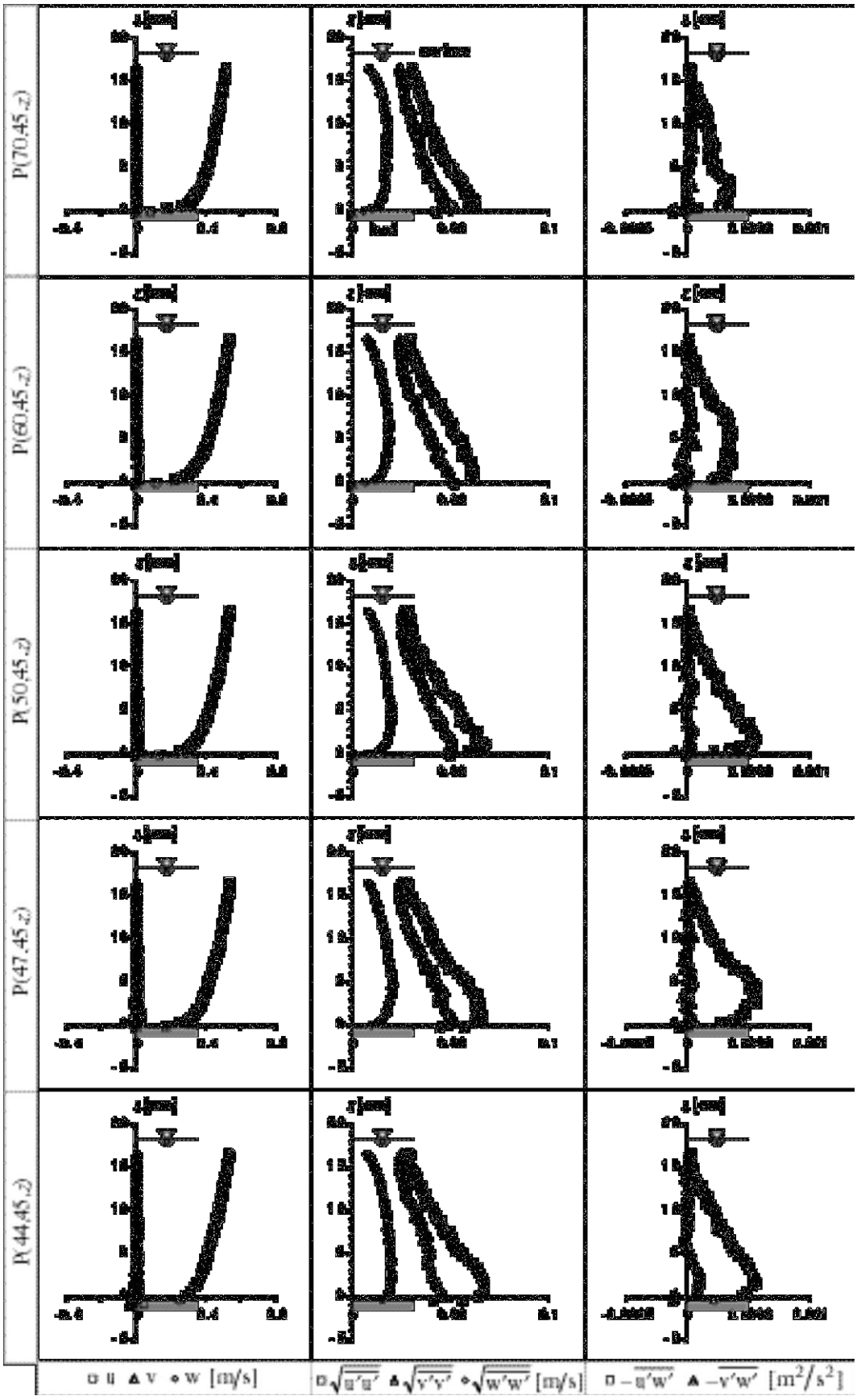

Fig. 2.13a Vertical distributions of the measured velocities, turbulence intensities, and Reynolds stresses in the plane $\alpha = 45°$.

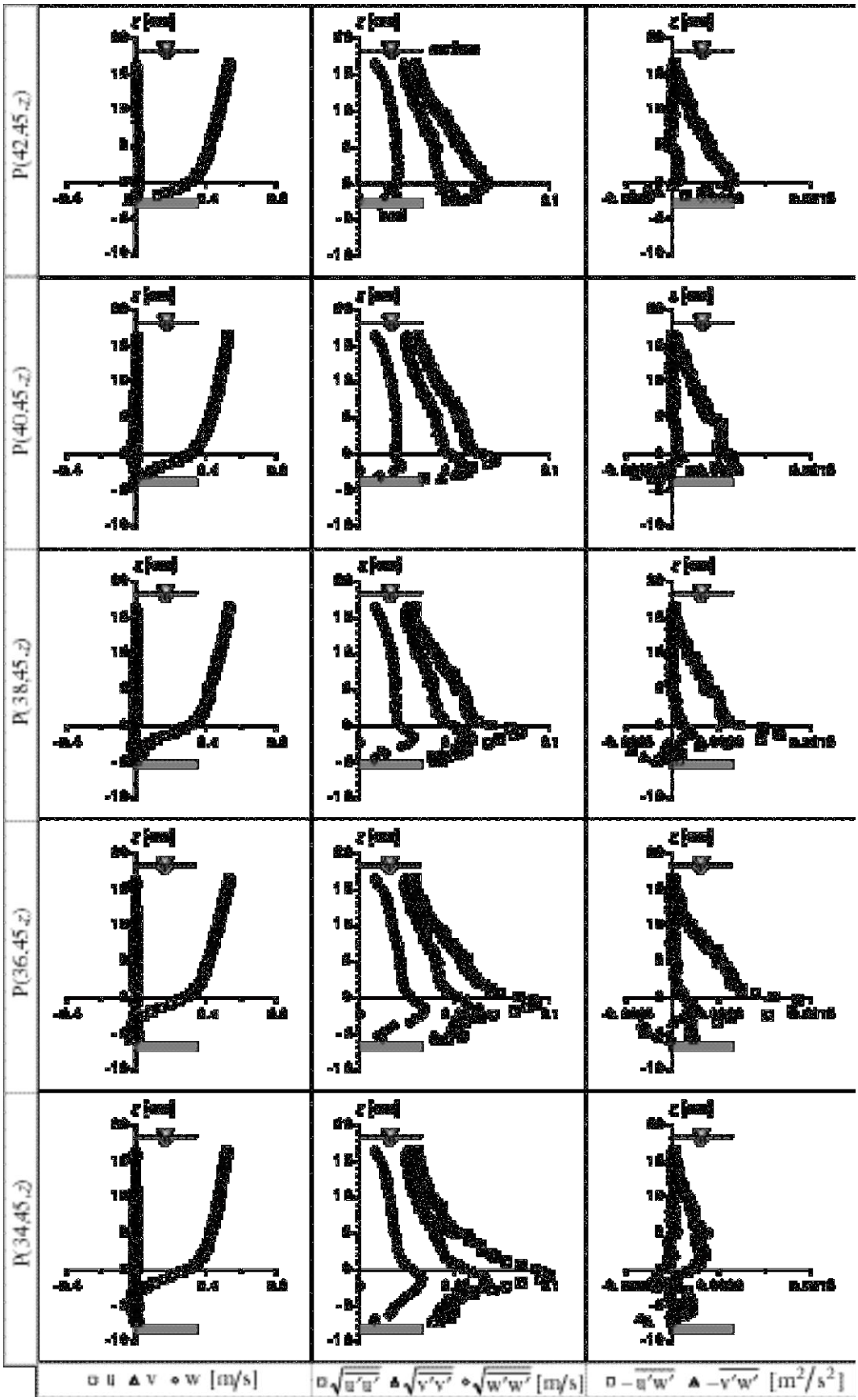

Fig. 2.13b Cont'd.

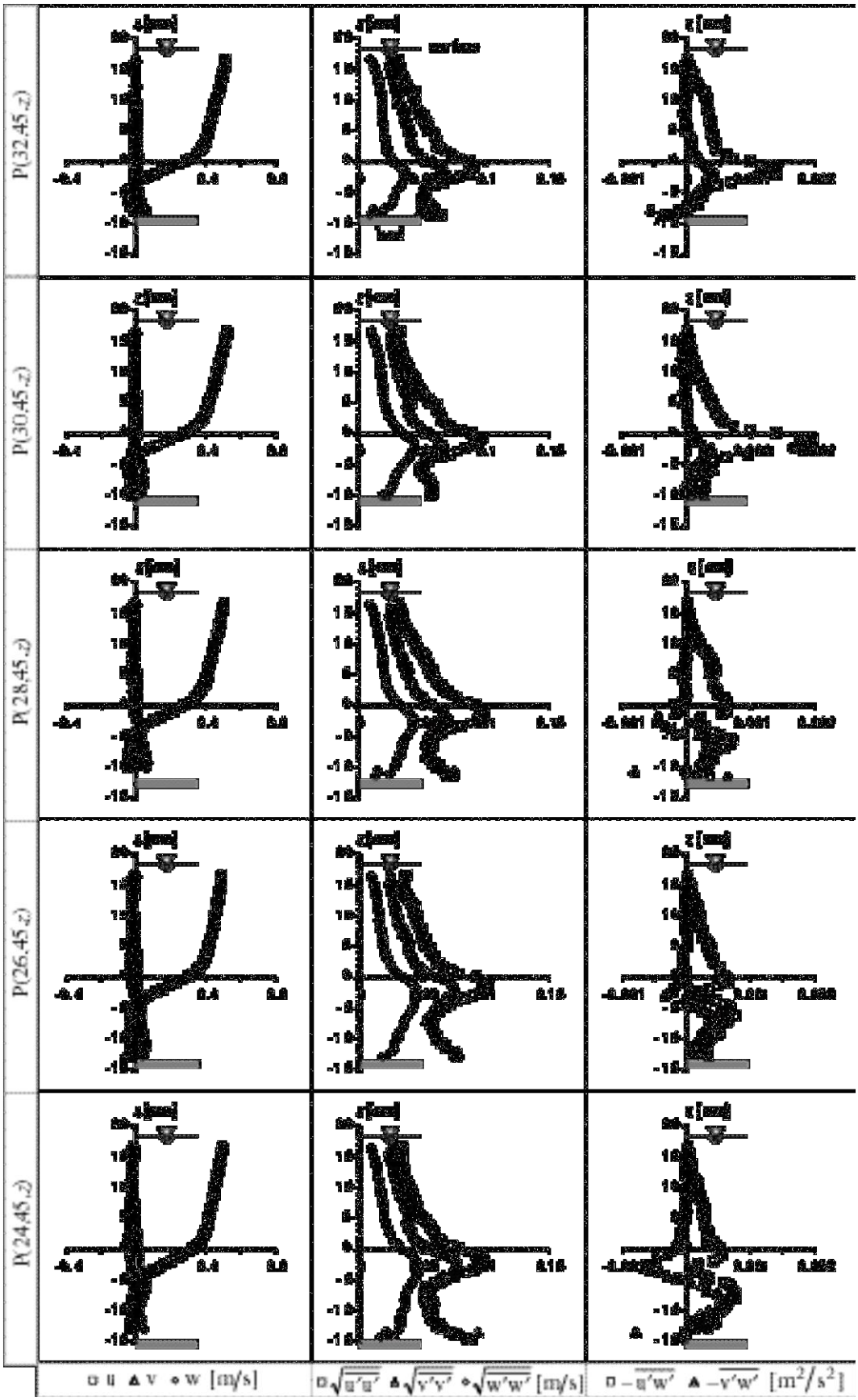

Fig. 2.13c Cont'd.

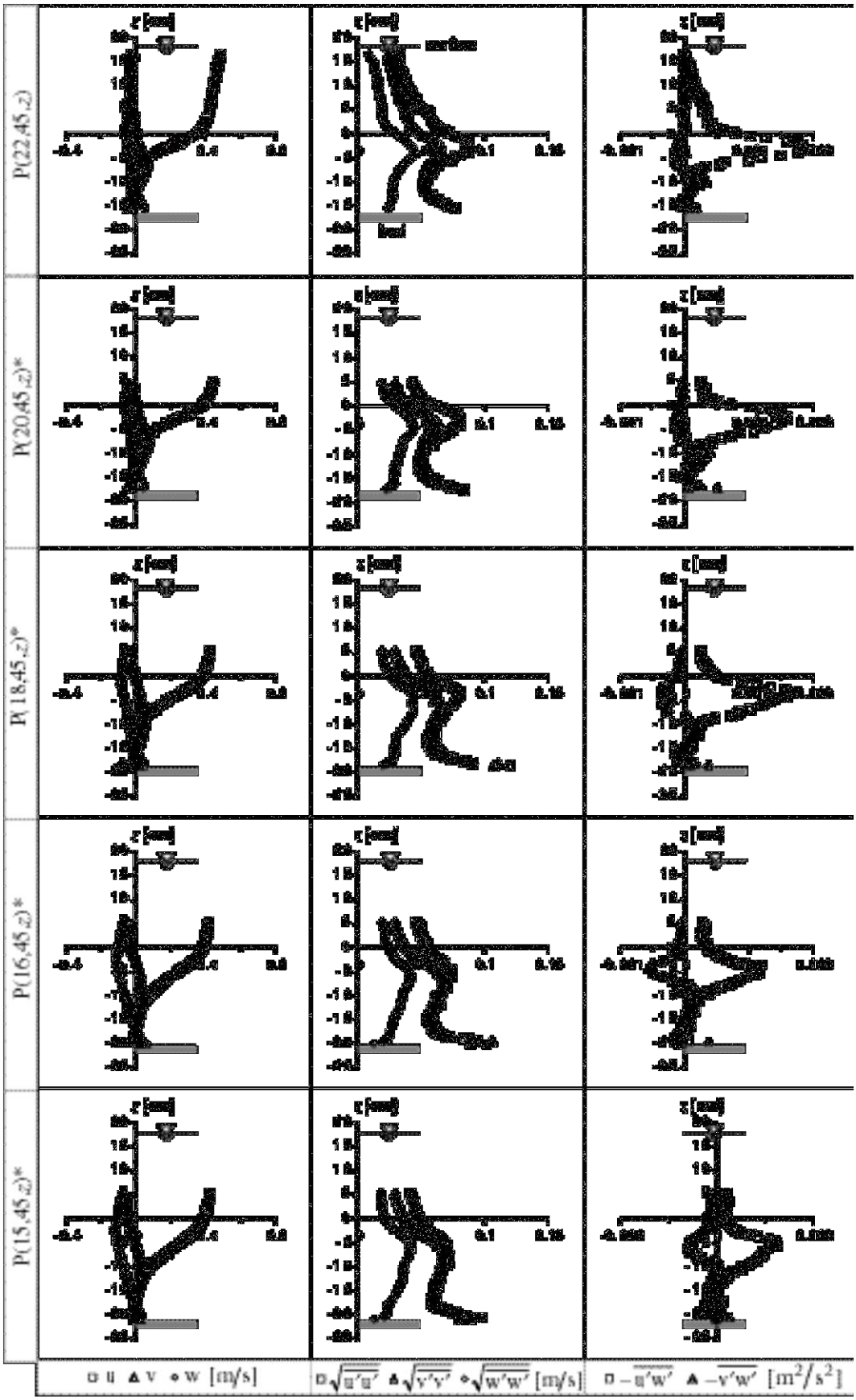

*Note: P(x≤ 20, 45, z ≥ 5) data not available.

Fig. 2.13d Cont'd.

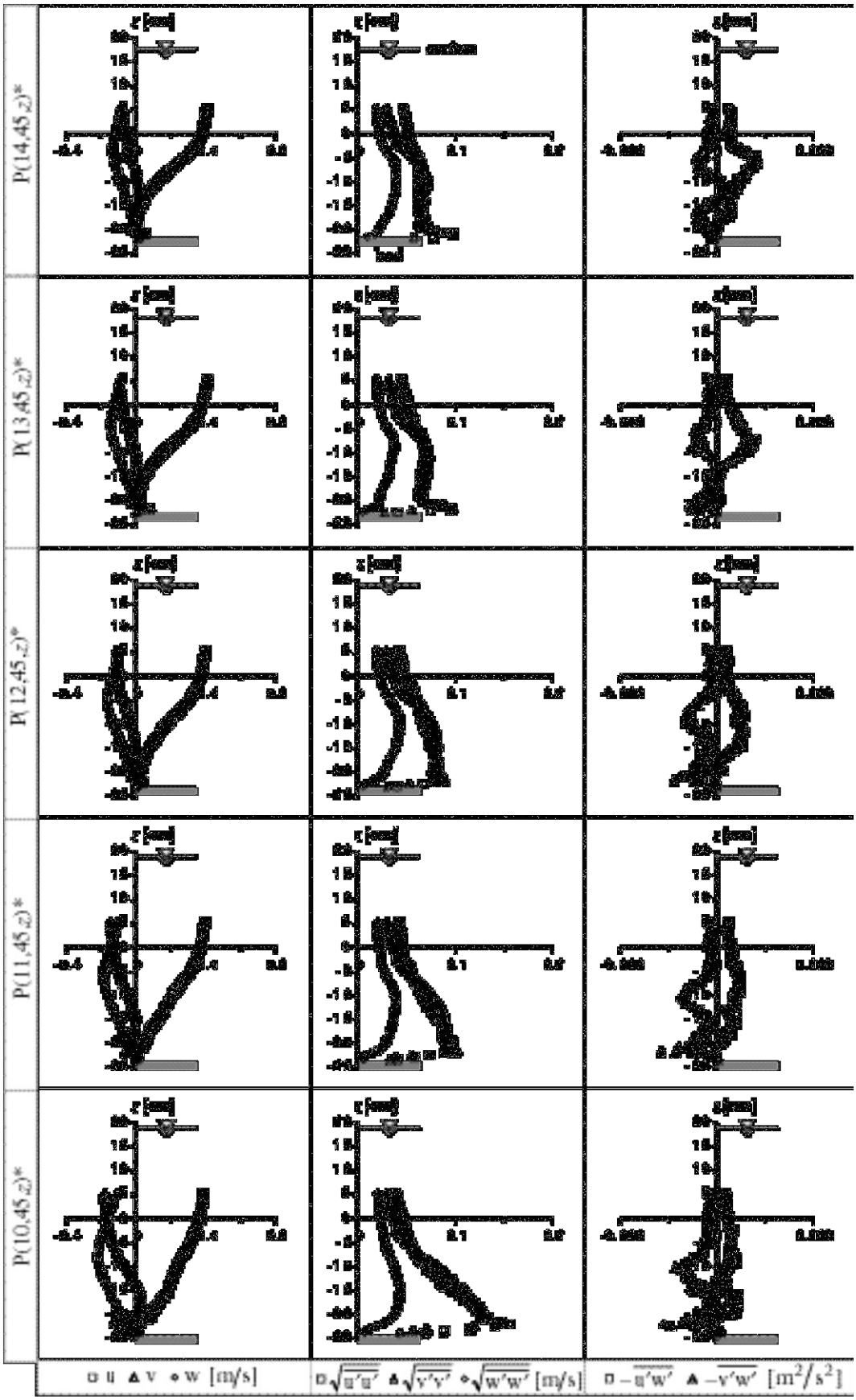

*Note: P(x=20, 45, z≥5) data not available.

Fig. 2.13e Cont'd.

the solid boundary of the scour hole, particularly at $15 \le r\,[\text{cm}] \le 32$. The $\sqrt{\overline{w'w'}}$ component, on the other hand, does not show this kind of tendency. Further close to the cylinder, the $\sqrt{\overline{u'u'}}$ and $\sqrt{\overline{v'v'}}$ are monotonically distributed with the maximum value at the bed. Compared to the plane $\alpha = 0°$, there is a moderate increase in the $\sqrt{\overline{v'v'}}$, while the other components, $\sqrt{\overline{u'u'}}$ and $\sqrt{\overline{w'w'}}$ remain essentially equivalent.

Reynolds stresses in the plane $\alpha = 45°$. In the far region, $r \ge 45$ [cm], there is no clear sign of the effect of the cylinder as also evidenced from the velocity and turbulence intensity data. The $-\overline{u'w'}$ is linearly distributed over the entire depth and the $-\overline{v'w'}$ is essentially insignificant. This phenomenon continues into the upper layer of the scour-hole region and remains so up to close to the cylinder. The $-\overline{u'w'}$ in general behaves like in the plane $\alpha = 0°$. At the lower layer, the $-\overline{u'w'}$ shows a sharp turn toward a peak (positive) value which, at $24 \le r\,[\text{cm}] \le 28$, is interrupted by a negative peak. Close to the cylinder, $r \le 14$ [cm], the peak disappears and the $-\overline{u'w'}$ turns toward negative values close to the bed. For the $-\overline{v'w'}$, there are two peaks of negative or positive magnitudes of $-\overline{v'w'} = \pm 0.0005$ [m²/s²]. Approaching the cylinder, the $-\overline{v'w'}$ is at the negative magnitude; this seems to correspond with the negative v observed at this region.

2.5.5 Measurements in the plane $\alpha = 90°$

The scour hole in the plane $\alpha = 90°$ starts at $r = 52$ [cm] $(3.5D_p)$ with the maximum depth of $d_s = 24$ [cm] $(1.33h_\infty)$ at the leading edge of the cylinder. The measurements in the plane $\alpha = 90°$ were performed at $10 \le r\,[\text{cm}] \le 80$. For $r \ge 22$ [cm] the data were obtained from the entire depth (zones A and B), while for $r \le 20$ [cm], the data were taken from $z \le 5$ [cm] (zone B). There are 26 vertical distributions of the velocities, the turbulence intensities, and the Reynolds stresses obtained. The measured distributions are shown in Fig. 2.14; the data at $r = 80$ [cm] are not shown.

Velocities in the plane $\alpha = 90°$. The velocities in the far region, $r \ge 50$ [cm], as the measurements in the two previous planes have shown, are not altered by the presence of the cylinder. The distributions of the three velocity components, u, v and w, remain basically similar to those of the uniform approach flow. In the scour-hole region and approaching the cylinder, the u-component moderately increases and is always dominant compared to the other components. In the scour-hole region the v-component, which is negligible in the plane $\alpha = 0°$ and pronounced in the plane $\alpha = 45°$, is important but diminishing; at $r = 10$ [cm] this component is of $v \approx -0.11$ [m/s] $(-0.23U_\infty)$ which is 60% of that in the plane $\alpha = 45°$. The w-component, like in the previous planes, manifests itself as a downward velocity that gets stronger approaching the cylinder. Close to the cylinder, $r = 10$ [cm], the downward velocity is of $w \approx -0.16$ [m/s] $(-0.35U_\infty)$, which is 60% of that in the plane $\alpha = 0°$ and is 70% of that in the plane $\alpha = 45°$. The v and w components, demonstrate a weak rotating flow going away from the cylinder at the upper layer (v and w are negative) and towards the cylinder at the lower layer (v and w are positive). That rotating flow has also a tangential component, which is evidenced by the negative u close to the bed, at $18 \le r\,[\text{cm}] \le 30$, coinciding with the positive w.

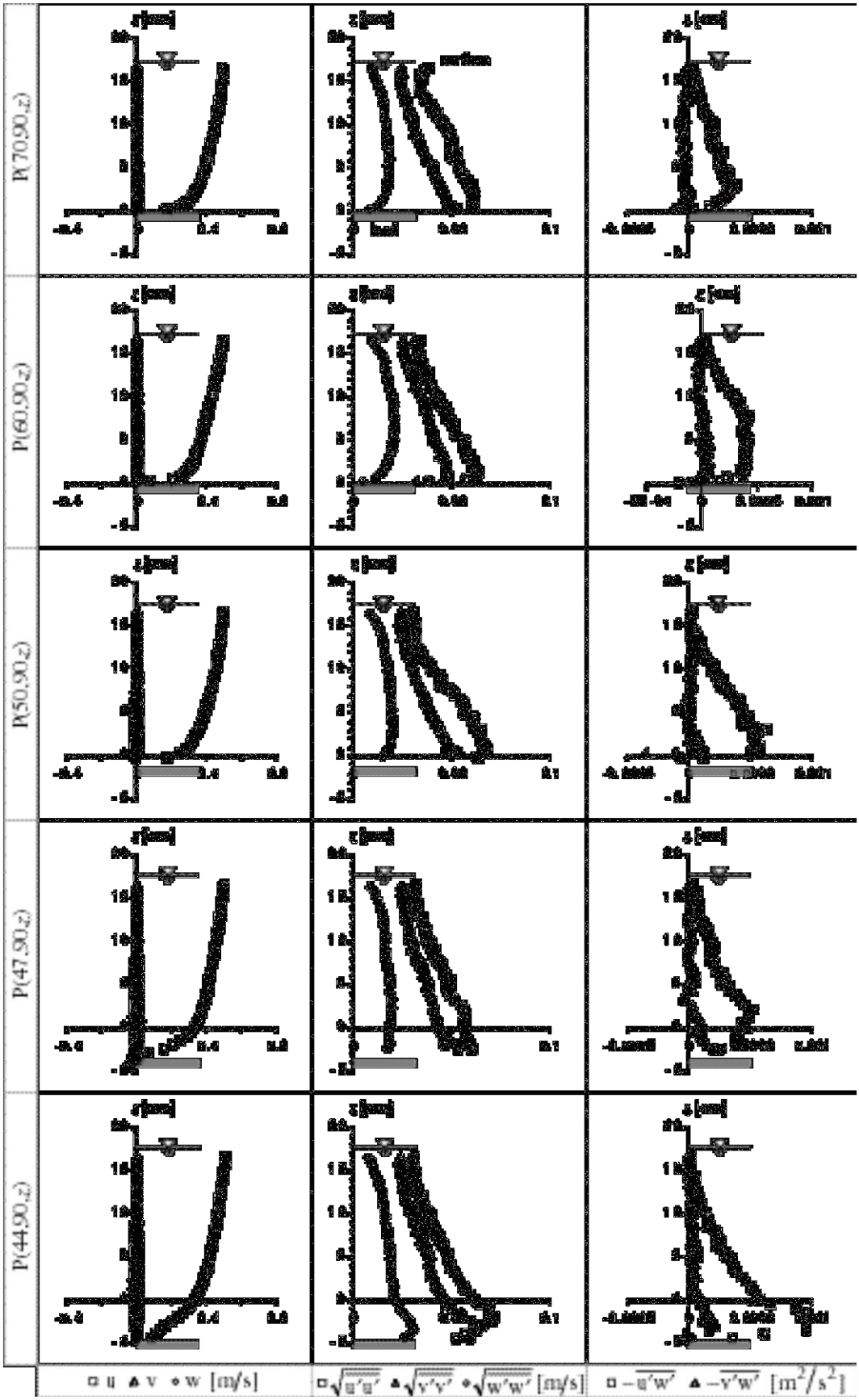

Fig. 2.14a Vertical distributions of the measured velocities, turbulence intensities, and Reynolds stresses in the plane $\alpha = 90°$.

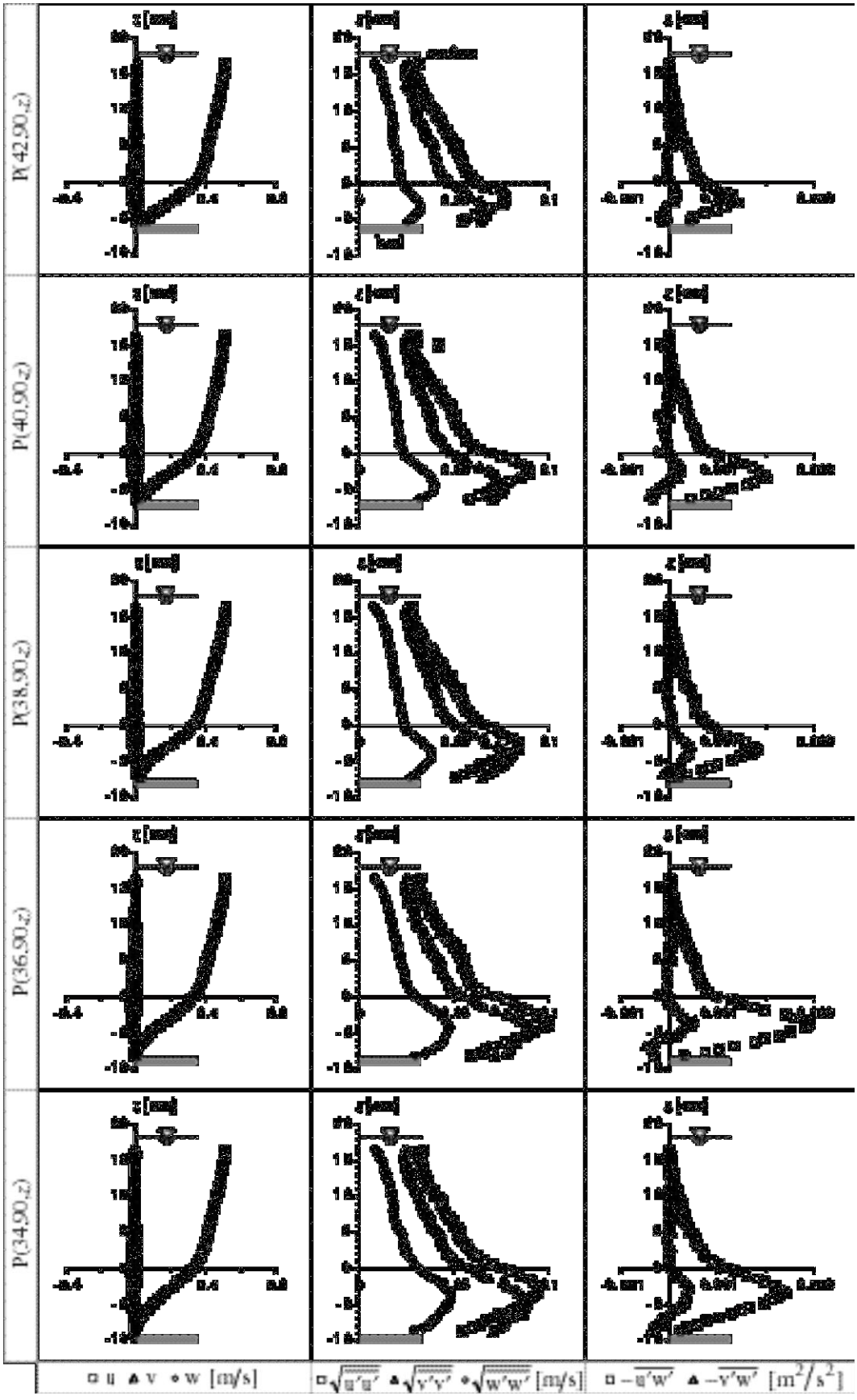

Fig. 2.14b Cont'd.

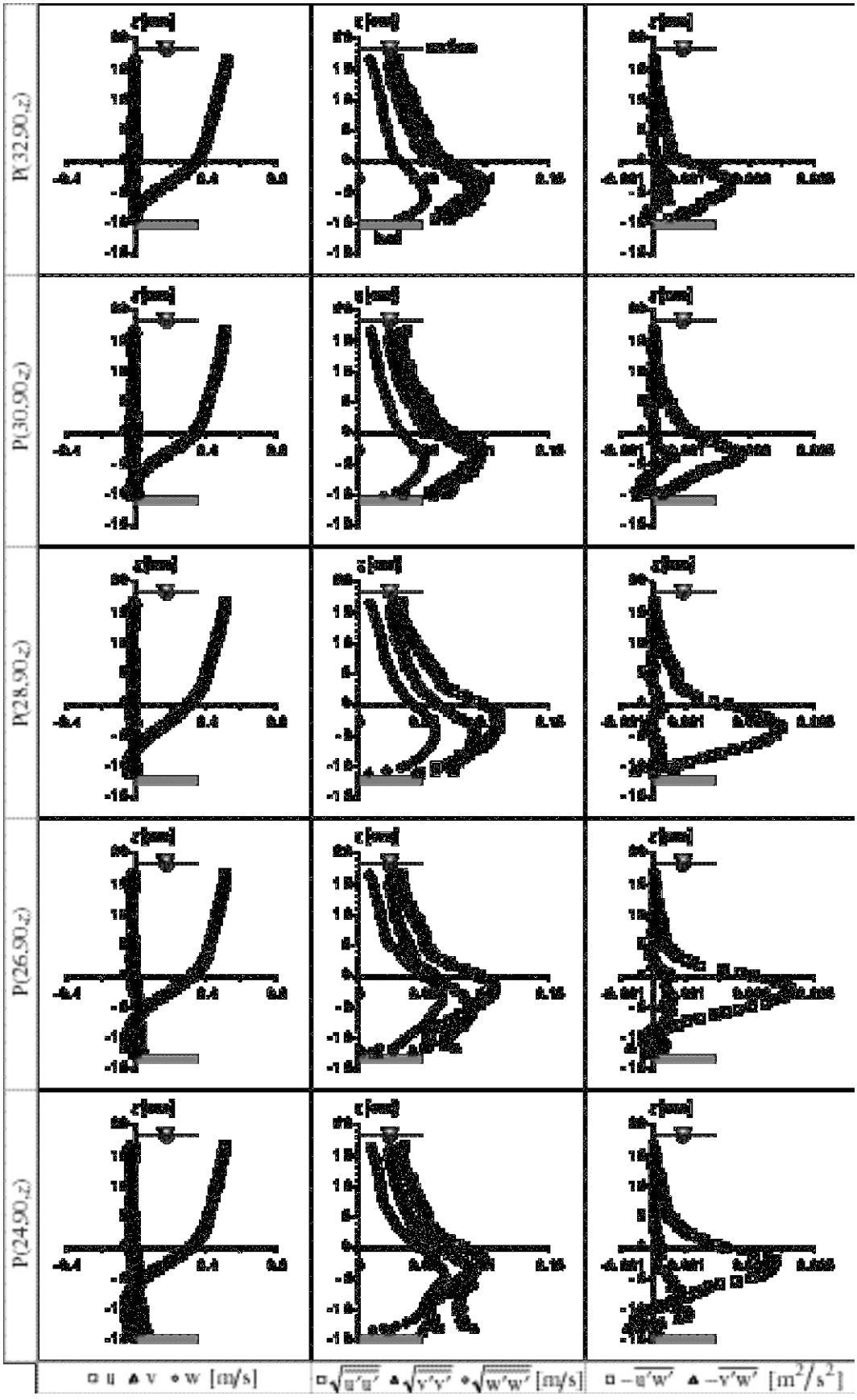

Fig. 2.14c Cont'd.

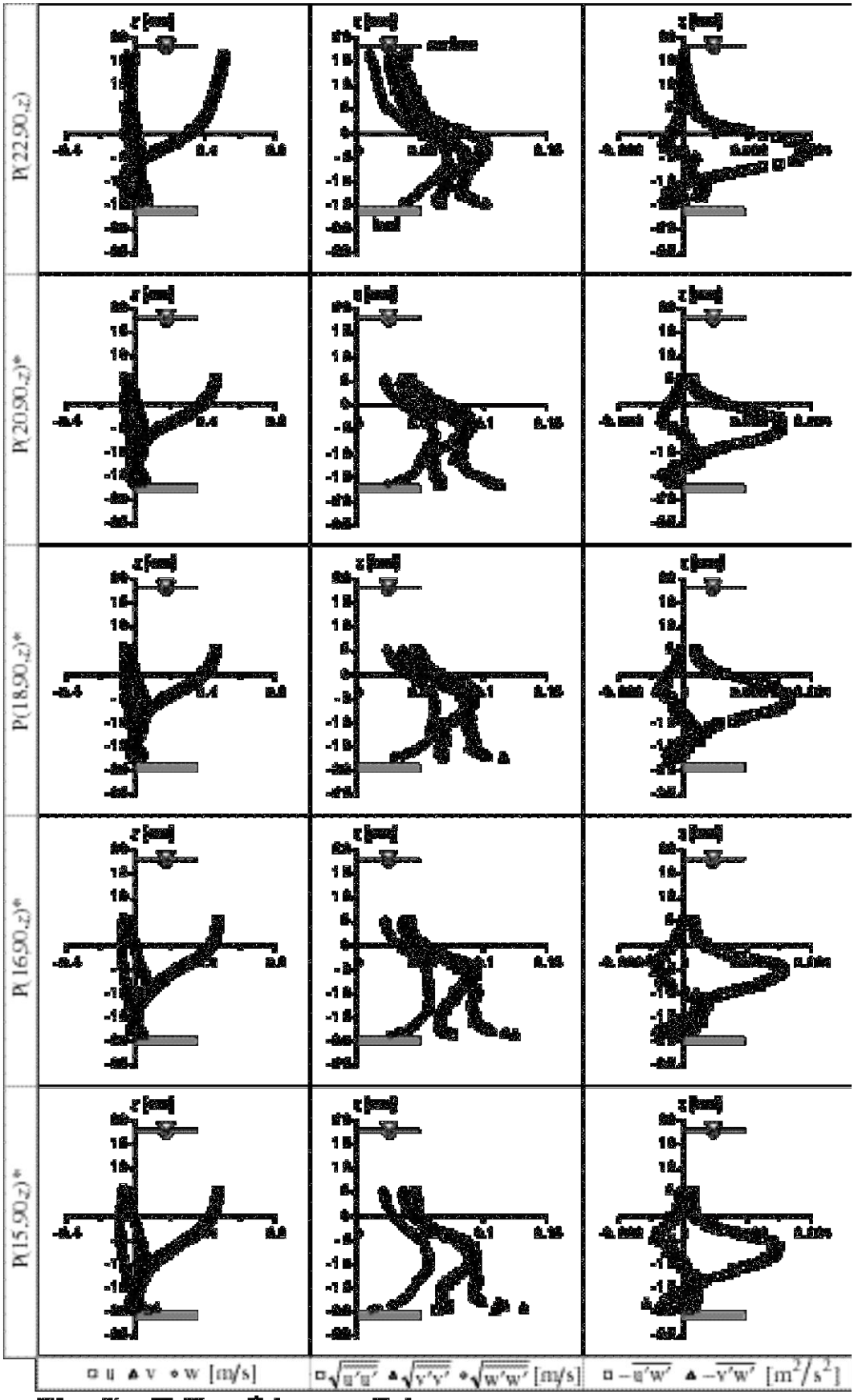

*Note: P(r≤20,50, z≥5) data not available.

Fig. 2.14d Cont'd.

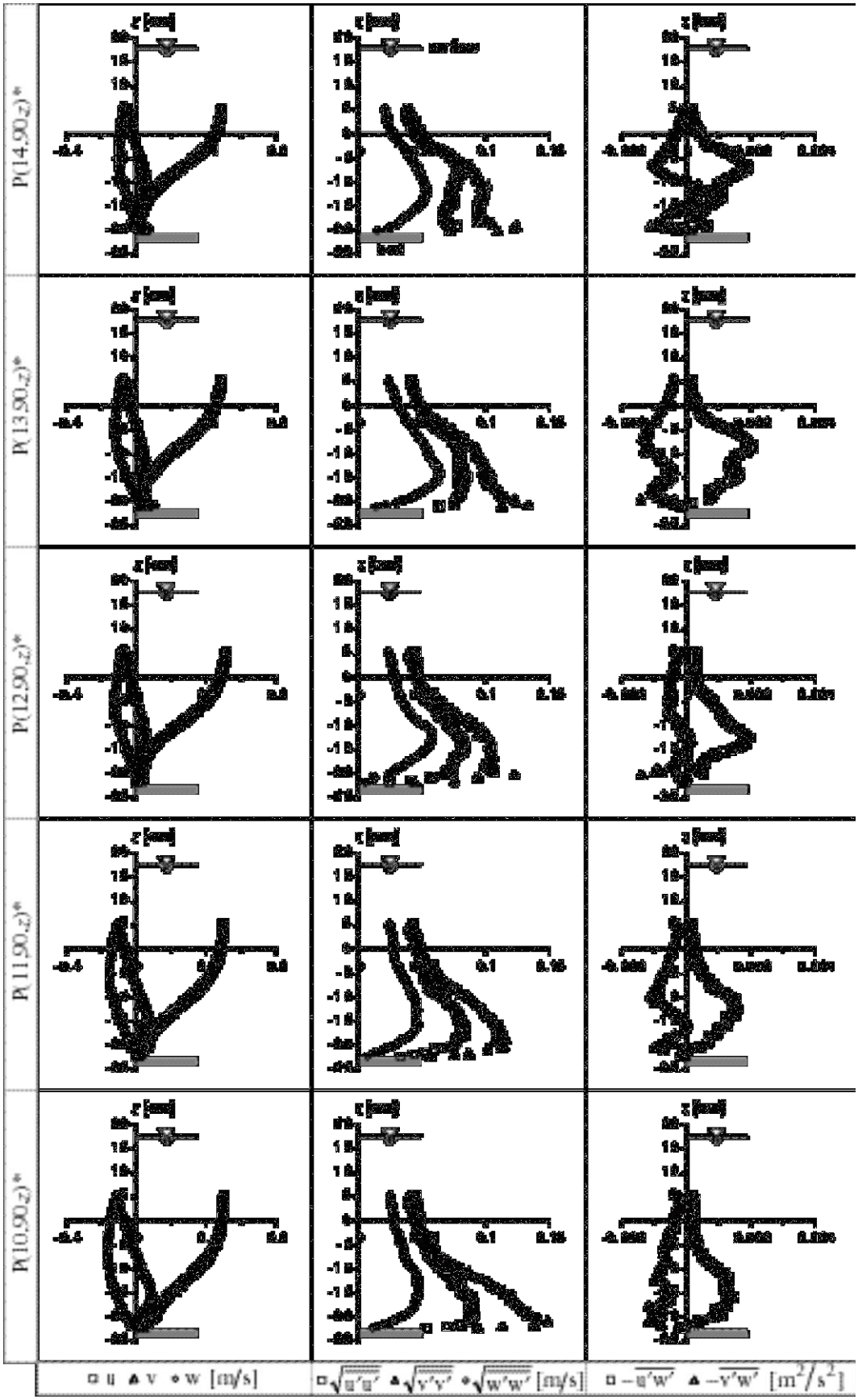

*Note: P(r=[0, 90], z ≥ 5) data not available.

Fig. 2.14e Cont'd.

Turbulence intensities in the plane 90°. In the far region, the turbulence intensity distributions resemble the one in the uniform approach flow. In the scour-hole region and approaching the cylinder, the distributions keep constant within the upper layer and increase within the lower layer. At the upper layer, the $\sqrt{\overline{u'u'}}$ is always dominant, followed by, successively, the $\sqrt{\overline{v'v'}}$ and $\sqrt{\overline{w'w'}}$. At the lower layer, however, the $\sqrt{\overline{v'v'}}$ eventually exceeds the $\sqrt{\overline{u'u'}}$ and becomes the most prominent; at $r = 10$ [cm], the values are $\sqrt{\overline{v'v'}} \approx 0.15$ [m/s] and $\sqrt{\overline{u'u'}} \approx 0.09$ [m/s]. Compared to the planes $\alpha = 0°$ and 45°, the $\sqrt{\overline{u'u'}}$ component shows similar tendency, except at $r = 10$ [cm] where it exhibits a decrease. For the other two components, there is a modest increase.

Reynolds stresses in the plane $\alpha = 90°$. The Reynolds stress in the far region, as in the case of the velocity, does not show any noticeable change due to the cylinder. In the scour-hole region and approaching the cylinder, the $-\overline{u'w'}$ stays more or less constant at the upper layer and increases at the lower layer, while the $-\overline{v'w'}$ becomes more pronounced. The $-\overline{u'w'}$ at the lower layer shows a sharp turn towards a peak underneath $z = 0$, as also in the case of the planes $\alpha = 0$ and 45° but with considerably higher values. Approaching the cylinder from $r = 44$ to 22 [cm], this peak increases from $-\overline{u'w'} \approx 0.001$ to 0.004 [m^2/s^2], but further approaching the cylinder, this peak decreases to $-\overline{u'w'} \approx 0.0015$ [m^2/s^2] at $r = 10$ [cm]. There is a negative $-\overline{u'w'}$-value at $15 \le r$ [cm] ≤ 26 and close to the bed; this corresponds with the negative u-component and the upward w-component previously presented. The $-\overline{v'w'}$ has a distribution in alternating negative-positive-negative values with the depth. Closer to the cylinder, the negative value becomes dominant and at $r = 10$ [cm], the $-\overline{v'w'}$ all takes the negative value. Compared to the planes $\alpha = 0°$ and 45°, the $-\overline{v'w'}$ is generally higher.

2.5.6 Measurements in the plane $\alpha = 135°$

The scour hole in the plane $\alpha = 135°$ extends up to $r = 90$ [cm] ($6D_p$) with the maximum scour depth of $d_s = 21.3$ [cm] ($1.4h_\infty$) at the leading edge of the cylinder. Unlike the previous planes, there is no single, but a double inclination of the scour hole. The measurements at this plane were performed at $10 \le r$ [cm] ≤ 80, from which 16 vertical distributions of the velocities, the turbulence intensities, and Reynolds stresses were obtained. The data are available in the entire depth (zones A and B) for $r \ge 22$ [cm] but are only available at $z \le 5$ [cm] (zone B) for $r \le 18$ [cm]. Shown in Fig. 2.15 are the measured distributions for $10 \le r$ [cm] ≤ 70; the data at $r = 80$ [cm] are not shown.

Velocities in the plane $\alpha = 135°$. The u-component is always dominant among the other components, v and w. Approaching the cylinder, the u-component gradually increases and is always positive. At the same time, the v- and w-components get more important but remain smaller than the u-component. The v-component is vertically distributed in an alternating negative-positive value, but close to the cylinder, it shifts towards the positive side. At $r = 10$ [cm], it is positive along the entire depth of measurement with the maximum value of $v \approx 0.15$ [m/s] ($0.33U_\infty$). The w-component manifests itself as a downward velocity, except close to the bed where there is an upward component. The

maximum downward flow is $w \approx -0.13$ [m/s] ($0.29U_\infty$) which is much weaker (about 50%) than that in the plane $\alpha = 0°$ and is slightly weaker (80%) than that in the plane $\alpha = 90°$.

Turbulence intensities in the plane $\alpha = 135°$. The three components of the turbulence show an increasing intensity compared to those of the previous planes, $\alpha = 0°$, 45° and 90°. The turbulence intensifies closer to the cylinder, notably at the lower layer. At the upper layer, it is more or less constant. The three components, the $\sqrt{\overline{u'u'}}$, $\sqrt{\overline{v'v'}}$, and $\sqrt{\overline{w'w'}}$, are well organized and their profiles have a similar shape. The $\sqrt{\overline{u'u'}}$ and the $\sqrt{\overline{w'w'}}$ components are the most and the least dominant, respectively, with an exception close to the bed where the $\sqrt{\overline{v'v'}}$ is comparable to the $\sqrt{\overline{u'u'}}$. The $\sqrt{\overline{u'u'}}$, notably at the lower layer, increases from the maximum value of $\sqrt{\overline{u'u'}} \approx 0.065$ [m/s] at $r = 70$ [cm] to $\sqrt{\overline{u'u'}} \approx 0.12$ [m/s] at $r = 10$ [cm]. The $\sqrt{\overline{v'v'}}$ behaves like the $\sqrt{\overline{u'u'}}$. It is lower than the $\sqrt{\overline{u'u'}}$, but close to the bed, the two components become comparable. The $\sqrt{\overline{w'w'}}$ is always the least important. Approaching the cylinder, it only slightly increases; the maximum $\sqrt{\overline{w'w'}}$ increases from 0.04 to 0.06 [m/s].

Reynolds stresses in the plane $\alpha = 135°$. The Reynolds stresses in this plane continue to increase compared with those in the previous planes; they are about 2.8 times higher than those in the plane $\alpha = 0°$. The Reynolds stresses, both at the upper layer and lower layer, increase as they are approaching the cylinder. The $-\overline{u'w'}$ is always positive, whereas the $-\overline{v'w'}$ has positive and negative values. The $-\overline{u'w'}$ has a peak at the lower layer whose magnitude increases from $-\overline{u'w'} = 0.001$ [m^2/s^2] at $r = 70$ [cm] to $-\overline{u'w'} = 0.005$ [m^2/s^2] at $r = 22$ [cm]. As it further approaches the cylinder, the peak slightly diminishes to $-\overline{u'w'} \approx 0.004$ [m^2/s^2] at $r = 10$ [cm]. The $-\overline{v'w'}$ has a negative value at the upper layer, a positive value at the lower layer, and tends to a negative value close to the bed. The magnitude increases as it approaches the cylinder. At the two profiles closest to the cylinder, at $r = 12$ and 10 [cm], the $-\overline{v'w'}$ has an alternating positive-negative value.

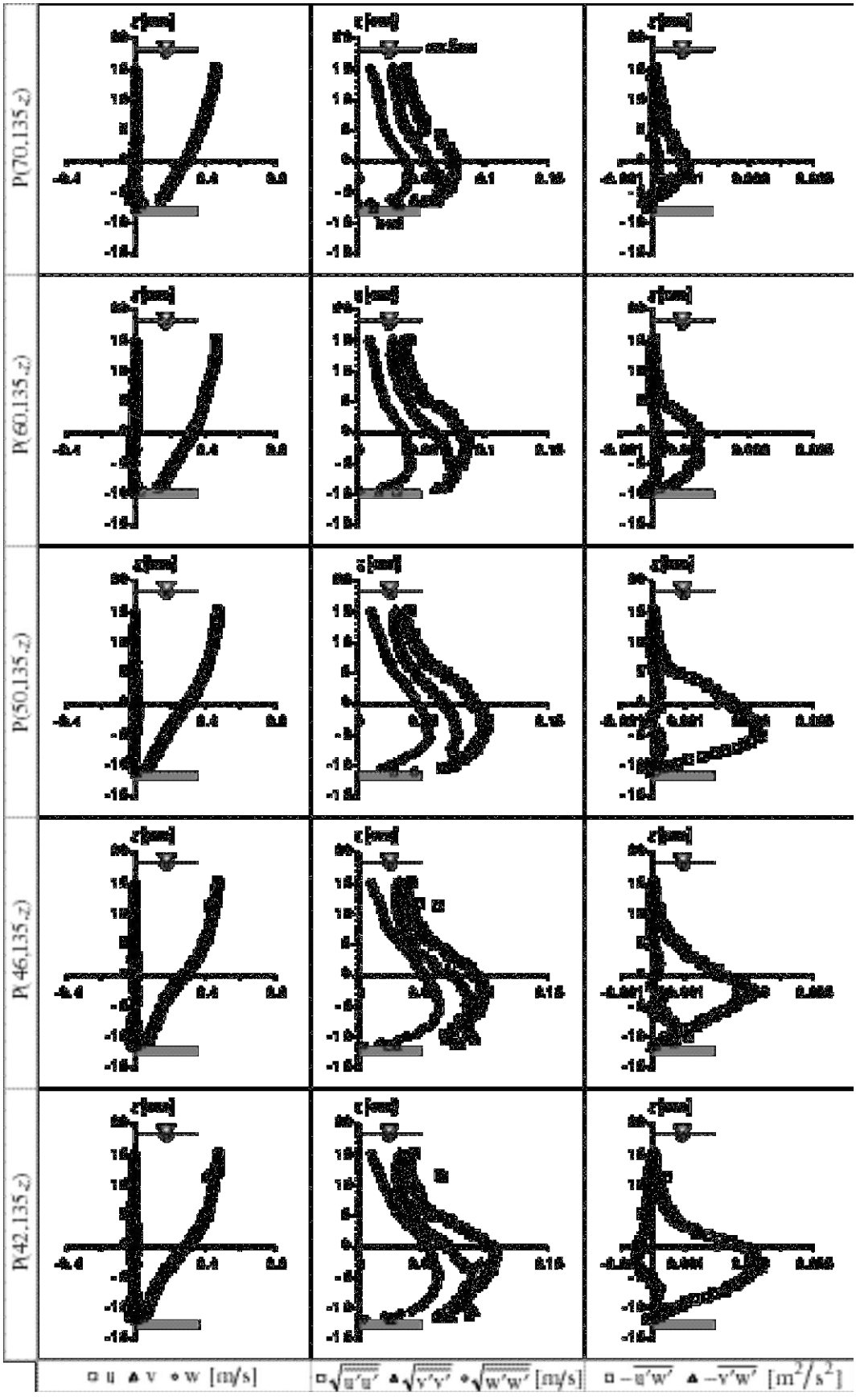

Fig. 2.15a Vertical distributions of the measured velocities, turbulence intensities, and Reynolds stresses in the plane $\alpha = 135°$.

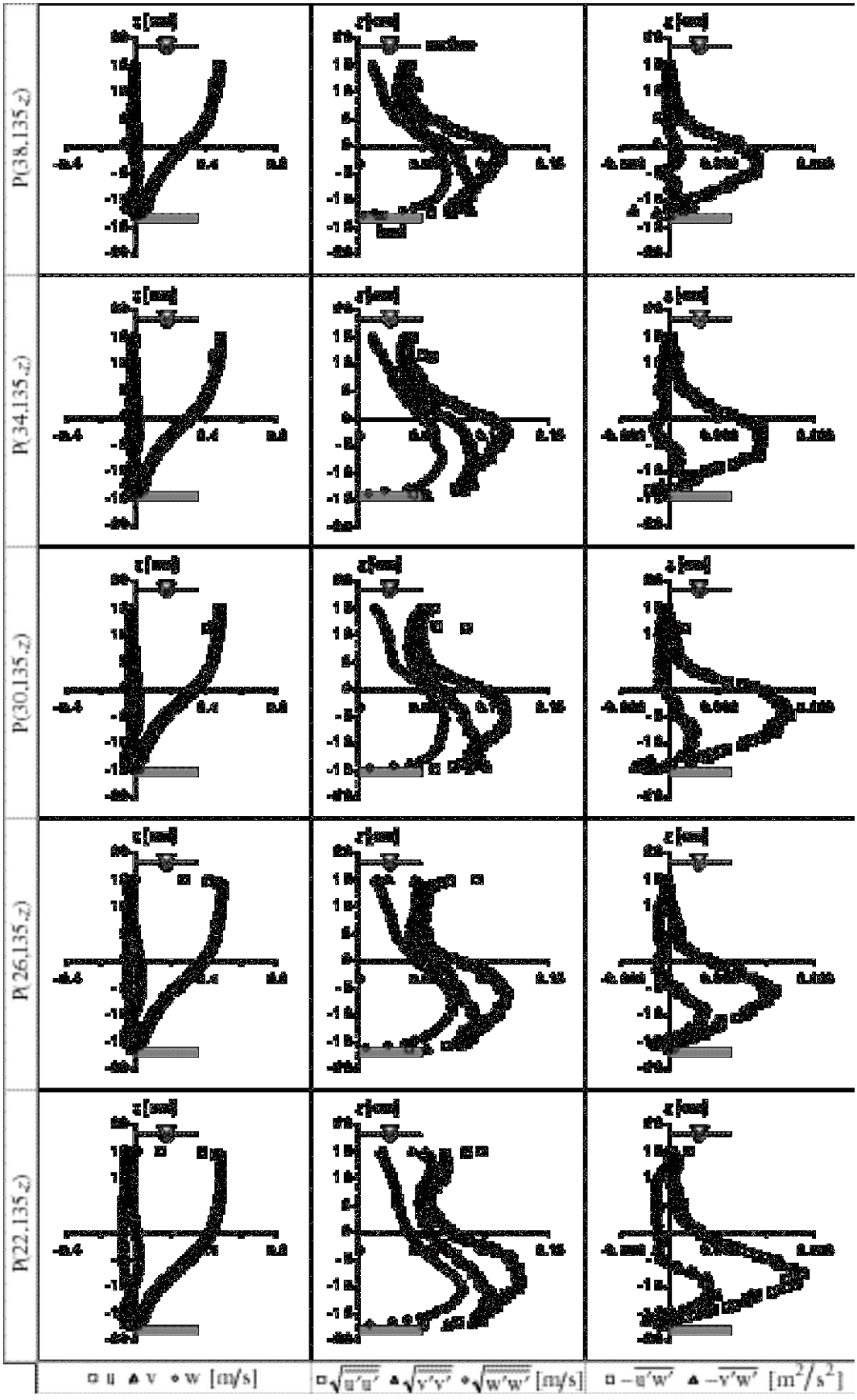

Fig. 2.15b Cont'd.

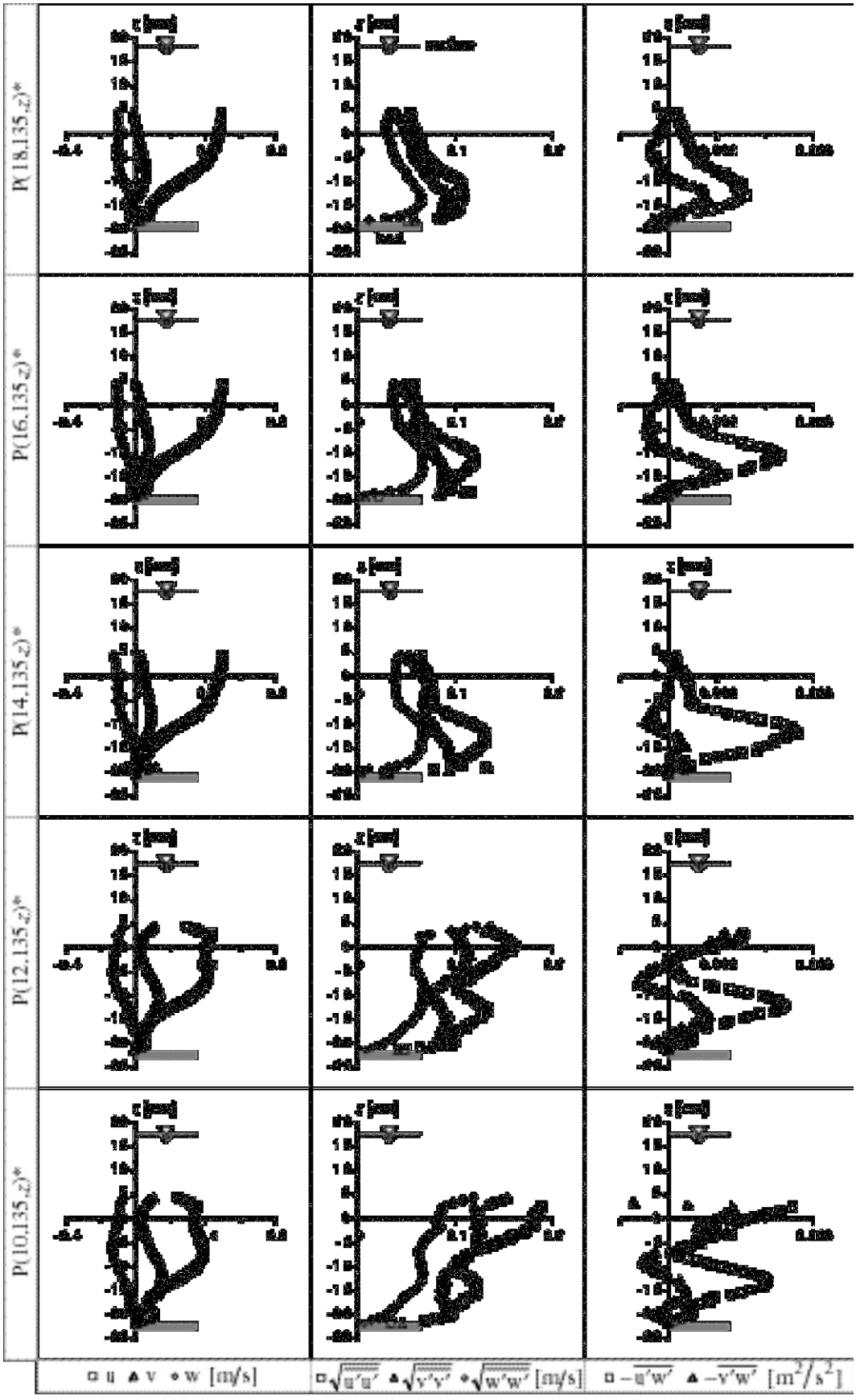

*Note: P(x=18, 135, z in 5) data not available.

Fig. 2.15c Cont'd.

2.5.7 Measurements in the plane $\alpha = 180°$

The scour hole in the downstream of the cylinder ($\alpha = 180°$) extends far to the downstream, $r = 105$ [cm] ($7D_p$), with the maximum scour depth of $d_s = 19$ [cm] ($1.3h_\infty$); the upward incline of the scour hole is thus $\Theta = 11°$. Further downstream, up to $r = 300$ [cm] ($20D_p$), the bed continues with a deposition. The ADVP measurements were performed at $10 \le r\,[\text{cm}] \le 100$, from which 18 vertical distributions of the velocities, the turbulence intensities, and the Reynolds stresses were obtained. The data for the region close to the cylinder, $r < 22$ [cm], are available only at $z \le 5$ [cm], while those for the rest, $r \ge 22$ [cm], cover almost the entire flow depth. The 18 vertical distributions are presented in Fig. 2.16

The flow in the wake of the cylinder is characterized by the so-called wake vortices that are formed by the shear-layers as a result of the flow separation detaching from the cylinder surface. At the surface and notably near the cylinder, the vortex is strong, the surface considerably fluctuates, and an air entrainment frequently takes place, generating air bubbles in the flow. These air bubbles, being of important dimensions, made the measurements very difficult by blocking the acoustic signal. This was particularly so in the case of measurements in zone A where the air bubbles stick to the mylar film of the instrument housing. The positioning of the ADVP-instrument was also difficult due to the fluctuating surface. For that reason, some of the measurement data from the zone A ($z > 5$ [cm]) and $r \le 38$ [cm] have to be interpreted with care.

Velocities in the plane $\alpha = 180°$. Close and behind the cylinder, $r \le 38$ [cm], the u- and w-components indicate a flow reversal towards the water surface. The u-component is small close to the cylinder, being $u \approx 0.1$ [m/s] ($0.22U_\infty$) at $r = 10$ [cm]. Moving outward from the scour hole the u-component increases and the flow reversal diminishes. The u-component is quasi-uniformly distributed along the depth with the value of $u \approx 0.3$ [m/s] ($0.67U_\infty$) at $r = 70$ [cm]; further downstream, it is recovering towards a logarithmic distribution, nevertheless up to $r = 100$ [cm], the logarithmic distribution has not been completely attained. The w-component is always in the upward direction, which is on the contrary to that in the plane $\alpha = 0°$. Its maximum value is $w \approx 0.16$ [m/s] ($0.33U_\infty$) at $r = 10$ [cm], which constantly diminishes as the flow leaves the scour hole. The v-component is usually small; immediately behind the cylinder, however, it has larger values of $v \approx 0.04$ [m/s] ($0.09U_\infty$), which is an indication of three-dimensional flow.

Turbulence intensities in the plane $\alpha = 180°$. The intensity of the turbulence at the plane $\alpha = 180°$ is considerably strong. Close to the cylinder, the three components show magnitudes of approximately $\sqrt{\overline{u'u'}} \approx \sqrt{\overline{v'v'}} \approx 0.2$ [m/s] and $\sqrt{\overline{w'w'}} \approx 0.15$ [m/s], which are more than twice higher than those at the plane $\alpha = 0°$. The maximum intensity is found at $r = 18$ [cm], which is unlike the case for the other planes where the maximum is found at the measured vertical closest to the cylinder, $r = 10$ [cm]. As the flow moves away from the cylinder, the turbulence intensities decrease. Along the range of the measurements, the $\sqrt{\overline{u'u'}}$ and $\sqrt{\overline{v'v'}}$ are comparable with the one occasionally exceeds the other, where as the $\sqrt{\overline{w'w'}}$ is always the least dominant.

Reynolds stresses in the plane $\alpha = 180°$. There is little that can be deduced from the Reynolds stress data in this plane. The data do not give any conclusive trend. Nevertheless, at $26 \geq r \geq 10$ one may notice that the $-\overline{u'w'}$ and $-\overline{v'w'}$ components are comparable with the $-\overline{v'w'}$ component; the latter occasionally exceeds the $-\overline{u'w'}$. Their distributions have a positive peak underneath $z = 0$, ranging from 0.003 to 0.004 [m²/s²]. Near the solid boundary of the scour hole, the stresses have the tendency to diminish towards zero.

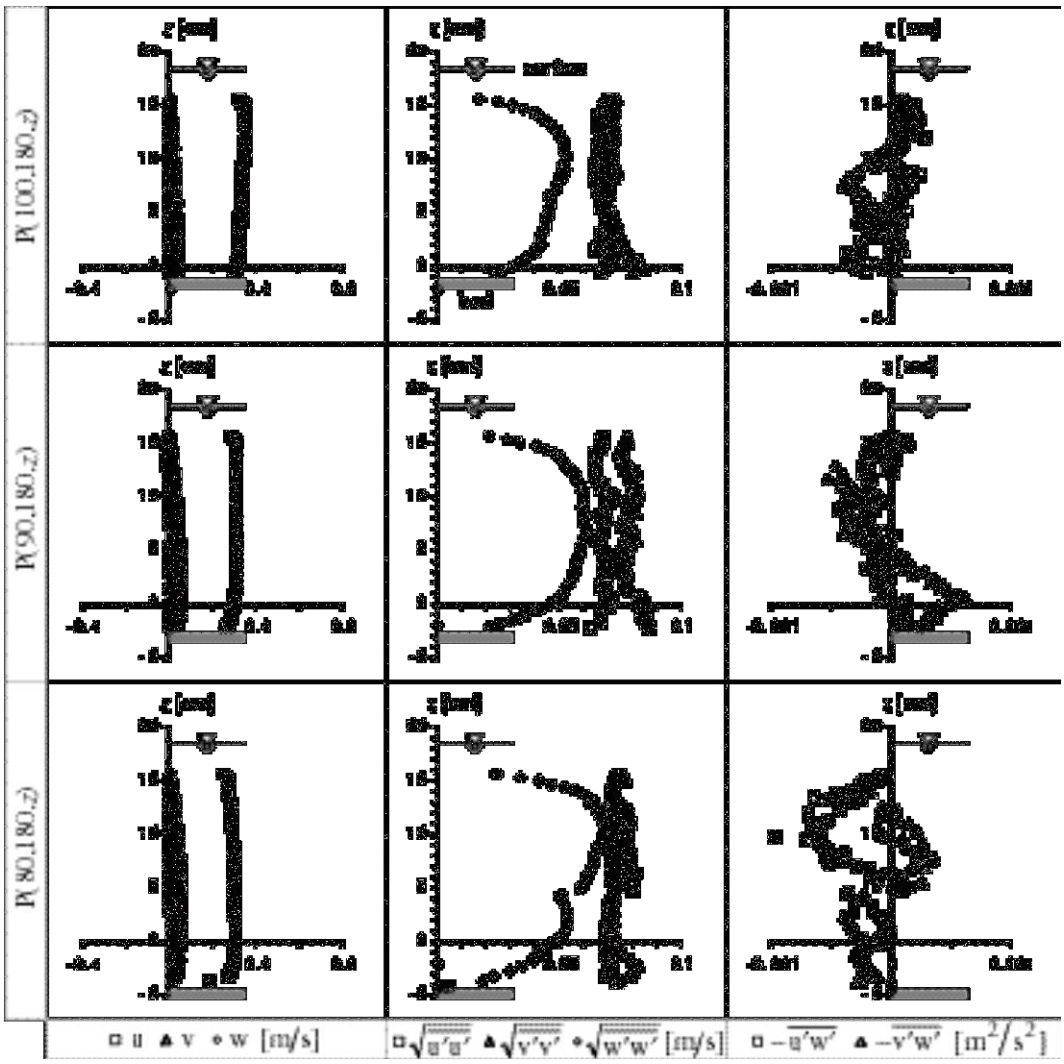

Fig. 2.16a Vertical distributions of the measured velocities, turbulence intensities, and Reynolds stresses in the plane $\alpha = 180°$.

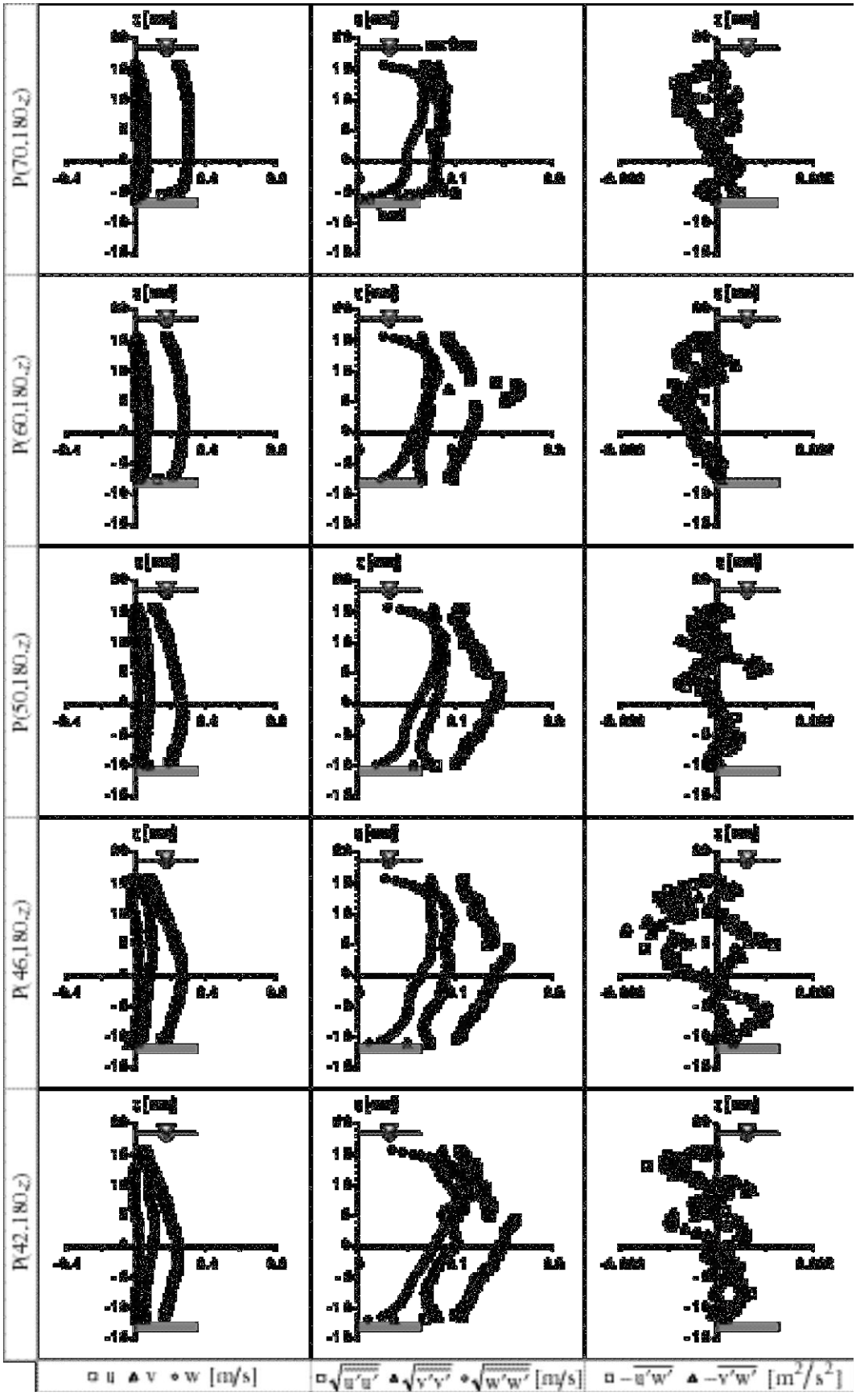

Fig. 2.16b Cont'd.

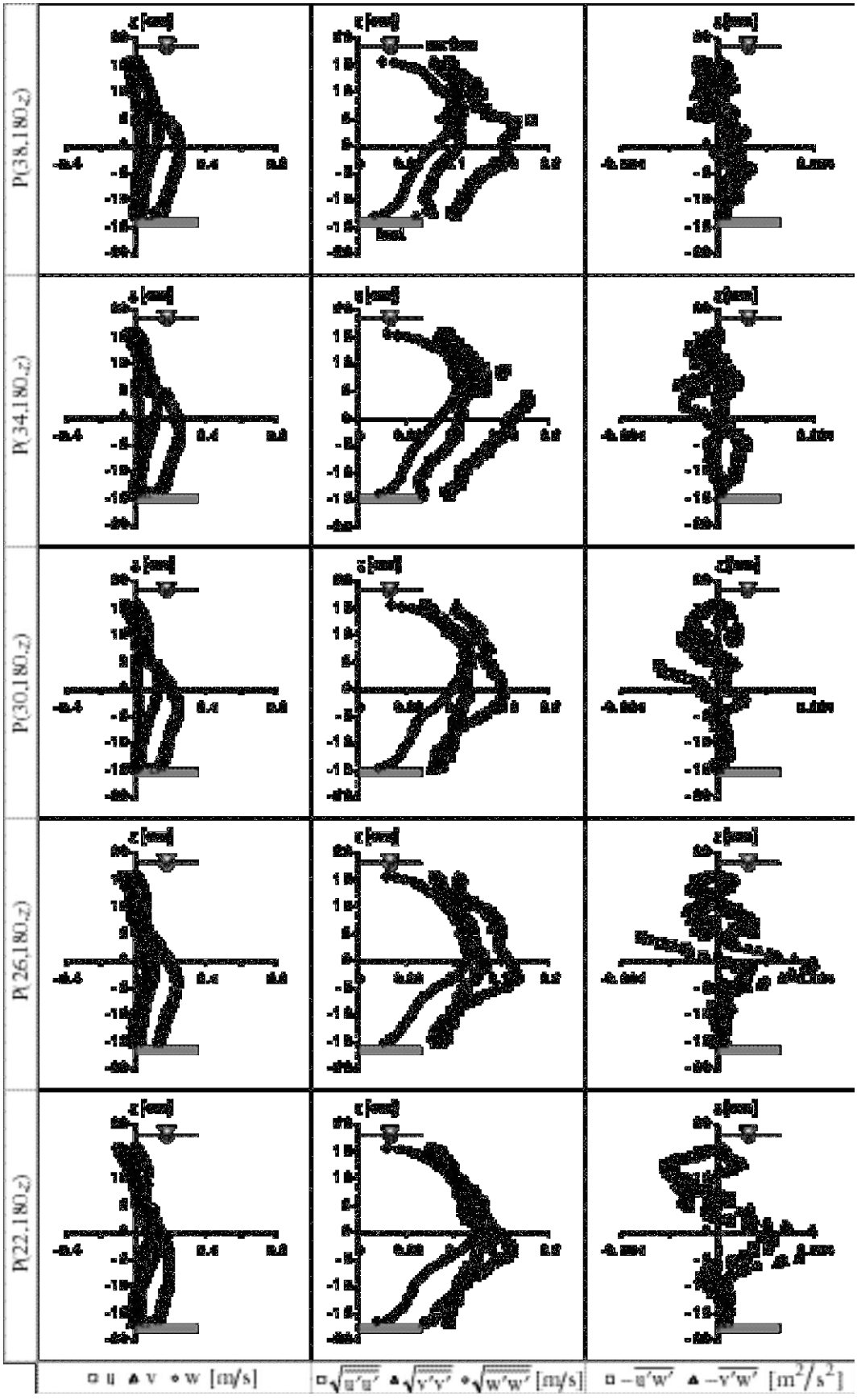

Fig. 2.16c Cont'd.

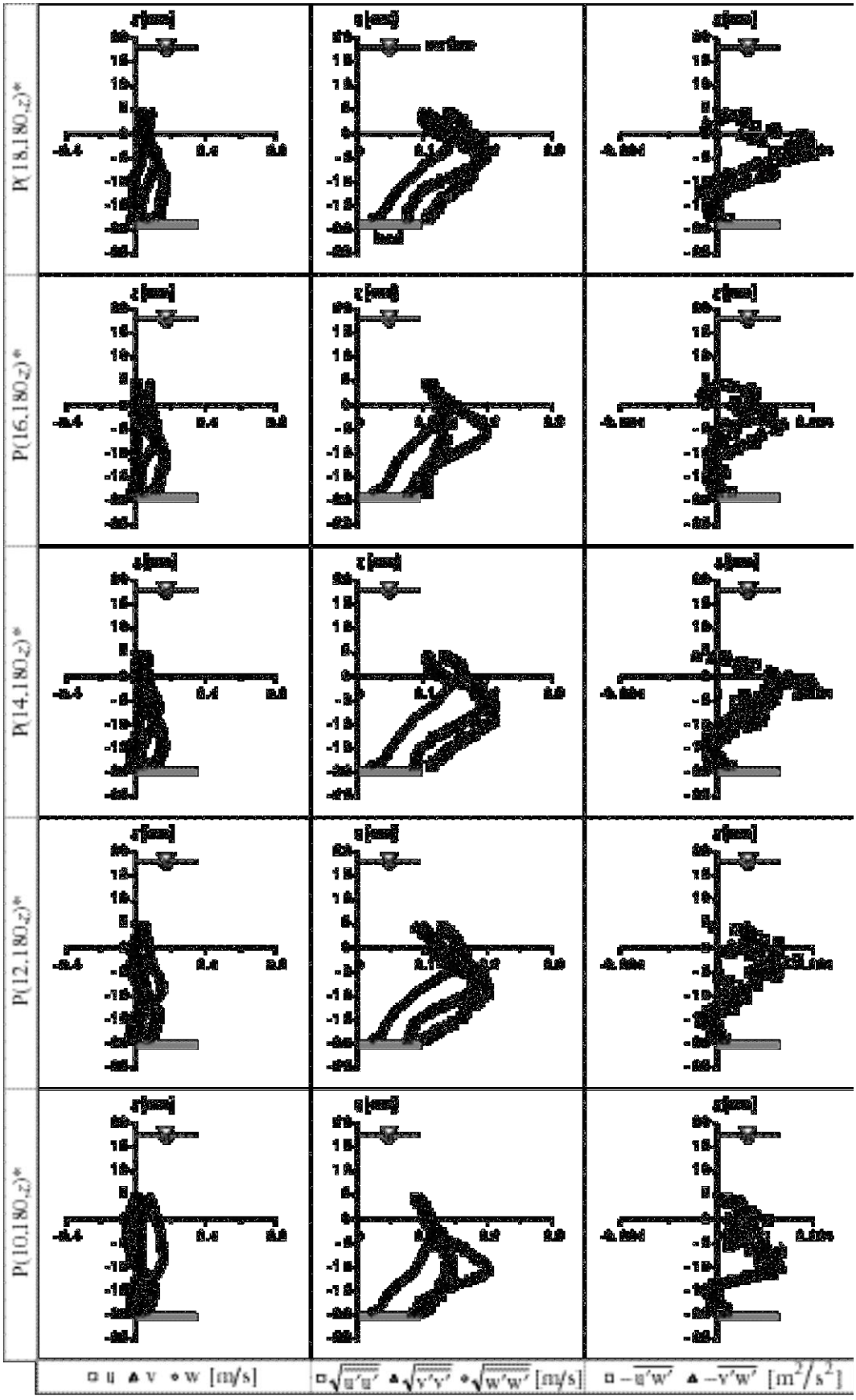

*Note: P(r ≤ 18, 180, z ≥ 5) data not available.

Fig. 2.16d Cont'd.

2.6 Summary and conclusions

Presented in this chapter are the measured data of the three-dimensional flow fields around a vertical cylinder, installed in an established (equilibrium) scour depth, under a clear-water regime. The acoustic-Doppler velocity profiler (ADVP) was used to measure instantaneously the vertical distributions of the three velocity components in vertical planes around the cylinder. The ADVP, conceived and developed at LRH, is a non-intrusive instrument, capable of measuring the three components of the instantaneous velocity in a number of points (in a 3 to 5 [mm] interval) over a vertical. The measured flow field is presented as the vertical distributions of the (time-averaged) velocities, the turbulence intensities, and the Reynolds shear-stresses in the planes $\alpha = 0°$, 45°, 90°, 135°, and 180°. Presented also are the vertical distributions for the uniform approach flow, i.e. the flow without the cylinder being installed.

The measurement in the approach flow, without the cylinder being installed, reveals that the approach flow is uniform, with a slight tendency of being a decelerated one, and is hydraulically (incomplete) rough. The vertical distribution of its longitudinal velocity component, $u(z)$, can be well explained by the logarithmic law-of-the-wall for the inner region, $z/h \le 0.2$, and by the Coles law-of-the-wake for the entire depth. The vertical distributions of the longitudinal component of the turbulence intensities can be satisfactorily presented by the semi-empirical expression in the form of $\sqrt{\overline{u'u'}}/u_* = D_u \exp(-C_u z/h)$ (see *Nezu and Nakagawa*, 1993). A similar expression, with slightly different values of the constants D and C, describes the transverse component. The vertical component of the turbulence intensities, however, cannot be satisfactorily described by that type of expression. The vertical distribution of the Reynolds shear-stresses shows a linear distribution as expected, being zero at the water surface and increasing towards the bed. The profiles, however, indicates diminishing values in the inner layer, $z \le 0.2h$.

The velocity measurements, with the cylinder in the scour hole, have confirmed the complex picture of the three-dimensional pattern of flow around a cylinder. The flow in the plane $\alpha = 0°$, being the plane of symmetry (confirmed by negligible v-component except close to the cylinder and the bed where a weak transverse velocity is detected), is characterized by a flow circulation and a strong downward flow at region close to the cylinder. Towards the downstream planes, $\alpha = 45°$, 90° and 135°, the flow circulation remains, but with a diminishing strength. Similarly, the downward flow close to the cylinder also remains and shows a decreasing intensity. Downstream of the cylinder, in the plane $\alpha = 180°$, there is a flow reversal towards the cylinder close to the surface. The v-component, as in the plane $\alpha = 0°$, is always negligible except at regions close to the cylinder and to the bed where small values are detected. As the flow moves downstream, leaving the scour hole, the flow reversal diminishes and the flow is recovering to the approach flow condition. In all planes the measurements show that the flow in the far region, beyond the scour-hole circumference, does not change with the presence of the cylinder. The flow is practically altered only in the scour-hole region.

As the flow advances to the downstream passing the scour hole, the intensity of the turbulence gets stronger. The increase of the turbulence level is notably noticeable from the plane $\alpha = 90°$ to $\alpha = 135°$. This increase continues, but with diminishing rate, in the plane $\alpha = 180°$. In this downstream plane, the turbulence demonstrates its peak intensity. It is interesting to observe that, in this plane, the three components of the intensity, $\sqrt{\overline{u'u'}}$, $\sqrt{\overline{v'v'}}$ and $\sqrt{\overline{w'w'}}$, indicate a tendency of being isotropic. Observing the intensity of the turbulence in each plane, one can notice that, approaching the cylinder, the turbulence inside the scour hole intensifies. In the upper layer, on the other hand, the turbulence level remains more or less constant.

Approaching the cylinder, in all planes except in the plane $\alpha = 180°$, the turbulence intensifies within the scour hole, $z < 0$, but remains more or less unchanged outside the scour hole, $z > 0$. Downstream of the cylinder, in the plane $\alpha = 180°$, the turbulence gets its strongest intensities.

The Reynolds shear-stresses inside the scour hole gets increasingly stronger as the flow moves towards downstream from the plane $\alpha = 0°$ to $\alpha = 135°$. In the plane $\alpha = 135°$, the stresses are about 3 times higher than those in the plane $\alpha = 0°$. In the upper layers, $z > 0$, the profiles of the Reynolds stresses exhibit a nearly linear distribution. Underneath, $z \leq 0$, the profiles of the Reynolds stresses turn towards a strong peak. In all planes, the $-\overline{u'w'}$ is always dominant compared to the $-\overline{v'w'}$. Downstream of the cylinder, $\alpha = 180°$, the vertical distributions of the Reynolds stresses do not show any conclusive trend.

References

Cellino, M. (1998). *Experimental study of suspension flow in open channels*., *Doctoral Dissertation*, No. 1824, EPFL, Lausanne, Switzerland.

Graf, W. H., and Altinakar, M. S. (1996). *Hydraulique Fluviale, Tome 2*., P.P.U.R., Lausanne, Switzerland.

Graf, W. H., and Altinakar, M. S. (1998). *Fluvial Hydraulics*., John Wiley & Sons, Ltd., Chichester, England.

Hurther, D., Lemmin, U., and Arditi, M. (1996). "Using an annular curved array transducer for bistatic ADVP application." *Rapport Annuel, Laboratoire de recherches hydrauliques, EPFL*, 1996, B.201.1-B.201.19.

Kironoto, B. A., and Graf, W. H. (1994). "Turbulence characteristics in rough uniform open-channel flow." *Proc. Instn. Civ. Engrs. Wat., Marit. & Energy*, 106, 333-344.

Lhermitte, R., and Lemmin, U. (1994). "Open-channel flow and turbulence measurement by high-resolution Doppler sonar." *J. Atm. Ocean. Tech.*, 11, 1295-1308.

Nezu, I., and Nakagawa, H. (1993). *Turbulence in open-channel flows*., A.A. Balkema, Rotterdam, NL.

Rolland, T. (1994). *Developpement d'une instrumentation Doppler ultrasonore adapteé à l'etude hydraulique de la turbulence dans les canaux.*, *Doctoral Dissertation*, No. 1281, EPFL, Lausanne, Switzerland.

Song, T., Graf, W. H., and Lemmin, U. (1994). "Uniform flow in open channels with movable gravel bed." *IAHR, J. Hydr. Res.*, 32(6), 861-876.

Yulistiyanto, B. (1997). *Flow around a cylinder installed in a fixed-bed open channel.*, *Doctoral Dissertation*, No. 1631, EPFL, Lausanne, Switzerland.

Notations

A, B, C		measurement zones.
B_R		constant of integration of the logarithmic law-of-the-wall.
$C_u, C_v, C_w,$		coefficients in the semi-empirical relation of the turbulence
D_u, D_v, D_w		intensity.
D_p	[cm]	diameter of the cylinder.
N_V		number of the measured instantaneous-velocity data.
NPP		number of the pulse pairs.
$P(r,\alpha,z)$		measurement section.
PRF	[Hz]	frequency of the pulse emission.
Q	[m^3/s]	discharge.
Re		Reynolds number.
S_o		channel bed slope.
T_{acq}	[s]	duration of the velocity data acquisition.
T_g	[s]	time gate of the velocity data acquisition.
$T_1^-, T_1^+, T_2^-, T_2^+, T_3$		ADVP transducers.
$\vec{\mathbf{V}}, V$	[m/s]	velocity.
$\vec{\hat{\mathbf{V}}}, \hat{V}$	[m/s]	instantaneous velocity.
$\vec{\hat{\mathbf{V}}}_h, \hat{V}_h$	[m/s]	instantaneous horizontal velocity component.
c_s	[m/s]	acoustic wave speed in water.
d_{50}	[mm]	mean diameter of the sediment.
d_s	[m]	equilibrium (maximum) scour depth.
f_D	[Hz]	Doppler frequency.
f_V	[Hz]	frequency of the velocity data acquisition.
h, h_∞	[m]	flow depth, flow depth of the approach flow.
k_s	[mm]	equivalent (standard) uniform roughness.
r	[m]	radial direction.
u_*	[m/s]	friction velocity.
u_r	[m/s]	radial velocity component.
u_α	[m/s]	tangential (angular) velocity component.
u,v,w	[m]	time average velocity components.
$\hat{u}, \hat{v}, \hat{w}$	[m/s]	instantaneous velocity components.
$\hat{u}_1, \hat{v}_1, \hat{w}_1$	[m/s]	instantaneous velocity components along the tristatic plane 1.

x,y,z	[m]	longitudinal, transversal, and vertical directions.
α	[°]	angular direction.
α_D	[°]	Doppler angle.
α_T	[°]	angle of the tristatic plane.
α_V	[°]	direction of the instantaneous velocity vector.
κ		Karman constant.
Π		wake-strength parameter.
Θ	[°]	scour bed inclination.
θ	[°]	angular direction of the cylindrical coordinate.
ρ	[kg/m^3]	water density.
σ_g		uniformity index of the sediment.
τ, τ_o	[N/m^2]	shear stress, bed shear stress.

Chapter 3

3 Elaboration of the measured Flow

Abstract

The measured three-dimensional flow field in an equilibrium scour hole presented in the preceding chapter (see Chapter 2) is here further investigated. The analyses are focused on the alteration of the flow structure due to the combined effect of the cylinder and the scour hole. Spatial distributions of the time-averaged velocities, of the vorticities, of the turbulence intensities, and of the Reynolds stresses in vertical planes around the cylinder are investigated. The measured velocity data show that a three-dimensional flow establishes itself, being characterized by notably a rotating flow inside the scour hole upstream of the cylinder and a downward flow in the upstream close vicinity of the cylinder. This is know as the horseshoe vortex. This structure disappears behind the cylinder, and a flow reversal towards the water surface is observed. The intensity of the turbulence increases considerably inside the scour hole, and particularly close to the cylinder. The turbulent kinetic energy increases on entering the scour hole, on approaching the cylinder, and on moving towards downstream regions. Its profiles are characterized by bulges below the original bed level. A similar observation can be made on the Reynolds stresses. Estimates on the bed shear-stresses along the plane of symmetry disclose a diminishing value of the bed shear-stresses upon entering the scour hole and approaching the cylinder. Moving downstream and leaving the scour hole, the bed shear-stresses are recovering towards their value in the approach flow.

Résumé

Le champ des vitesses tridimensionnelles mesuré dans une fosse autour d'un cylindre vertical présenté auparavant (voir Chapitre 2) est ici étudié plus en détail. Le but de cette étude est de connaître l'effet apporté par la fosse et le cylindre au changement de l'écoulement. L'analyse se fait par des répartitions spatiales de vitesses (moyennées dans le temps), vorticité, intensité des turbulences et des tensions de Reynolds dans différents plans verticaux autour du cylindre. L'analyse des vitesses montre que l'écoulement est tridimensionnel et caractérisé notamment par un tourbillon dans les plans amont et par le courant vers le bas qui se trouve à proximité du cylindre. Ce system est appelé le *vortex de fer-à-cheval*. Il se propage vers l'aval et son intensité devient faible voire presque invisible. Derrière le cylindre, un autre courant de retour est observé alors que celui près de la surface se dirige vers le cylindre. La turbulence s'amplifie dans la fosse et notamment dans la proximité du cylindre. L'énergie cinétique de turbulence croît en

entrant dans la fosse en s'approchant le cylindre ; sa valeur aux régions de sillage est très élevée. Les profils de l'énergie cinétique turbulente sont caractérisés par des pics qui se trouvent au dessous de la ligne du fond original. Les tensions de Reynolds augmentent de la même façon. L'estimation de la valeur de cisaillement au fond, à partir des donnée des vitesses et des tensions de Reynolds, met en évidence sa décroissance due à la fosse et au cylindre.

3.1 Introduction

Presented in the previous chapter are the velocity fields measured in five vertical planes radiating from the cylinder, $\alpha = 0°$, 45°, 90°, 135°, and 180°. Brief discussions on the velocities, turbulence intensities, and Reynolds stresses were given following the presentation of the measurements in each plane. Detailed discussions are presented in this chapter where more emphasize is put rather on the (time-averaged) velocity. Most of the discussions are associated with the flow pattern in radial planes around the cylinder. A comparison with other relevant data in the available literature is also presented.

3.2 (Time-averaged) velocity fields

Vertical distributions of measured (time-averaged) velocities in planes around the cylinder have been presented in Chapter 2. It has been shown that the flow outside the scour hole is not altered by the presence of the cylinder. The vertical distribution of the velocity outside the scour hole is very much similar to the one of the undisturbed flow. In the scour hole region, notably in the upper layer, $z > 0$, the effect of the cylinder is noticealbe in a region that is relatively close to the cylinder, $r/D_p \leq 1.3$. In the lower layer, $z < 0$, and notably in the upstream planes, $\alpha \leq 90°$, the flow is characterized by a *rotating flow* and a *downward flow*, better known as the *horseshoe vortex*. This vortex is a result of interaction among the incoming flow, the scour hole, and the cylinder.

It has also been presented that the velocity field is dominated by the u component in all measurement planes. Only very close to the cylinder the u component is exceeded by the vertical velocity. The w-velocity component manifests itself as a *downward flow* that reaches its strongest magnitude at the circumference of the cylinder. This downward flow gets weaker along the angular distance, $\alpha > 0°$, and becomes *upward flow* in the rear of the cylinder, $\alpha = 180°$. In the upstream planes, $\alpha \leq 90°$, it is through this downward flow that the incoming flow-momentum is transferred into the scour hole. The behavior of the downward flow in the upstream planes, $\alpha \leq 90°$, notably close to the cylinder, $r = 10$ [cm], will be further investigated (see Sect. 3.2.4).

The dominance of the u-velocity component over the v component over all planes, notably in the upstream planes, $\alpha \leq 90°$, is an interesting phenomenon. Measurements on a flat channel bed (see *Graf and Yulistiyanto*, 1998) show that in the plane $\alpha = 45°$ close to the cylinder, the u- and v-velocity components are comparable, indicating that the flow is directed tangentially with respect to the cylinder. This is not the case in the present measurements where the v component is persistently less pronounced. The dominant u-velocity component suggests that the incoming flow be directed straightforwardly to the downstream. This is most likely due to either the attraction of the scour hole to pull the flow or the momentum of the incoming flow. The incoming flow-momentum is strong enough to overcome any flow alteration by the cylinder. The spatial evolution of the v-velocity component will be discussed in Sect. 3.2.3.

3.2.1 Vertical distribution of the velocity

Shown in Fig. 5.1 are some selected velocity profiles, u(z), v(z), and w(z), measured in the planes $\alpha = 0°$, 45°, 90°, 135°, and 180°. Indicated also in the figure are the normalized axes, u/U_∞ and z/h_∞, where $U_\infty = 0.45$ [m/s] and $h_\infty = 18$ [cm] are the cross sectional velocity and flow depth of the (far-field) approach flow. Observing individually the three velocity components in each plane, the following is to be remarked:

- In the plane $\alpha = 0°$, approaching the cylinder. The u component hardly changes its magnitude until $r = 42$ [cm], slightly decreases until $r = 30$ [cm], and progressively diminishes over the entire flow depth closer to the cylinder. Noticeable is the negative u-component at the lower layer of $r \leq 30$ [cm], indicating a reversed flow. The v component is practically negligible in all measured profiles, showing that the flow is practically symmetrical about the center line. The w component considerably grows into a *downward flow* (negative values) with a maximum value of $w/U_\infty = -0.6$ close to the cylinder. A similar magnitude of downward velocity was reported by Melville (see *Melville and Raudkivi*, 1977). In the flat channel bed measurement, however, a lower downward peak was obtained, $w/U_\infty = -0.3$ (see *Graf and Yulistiyanto*, 1998).

- In the plane $\alpha = 45°$, approaching the cylinder. The u component slightly decreases in the upper layer, but progressively increases in the lower layer; negative u-component is observed close to the bed, but with a lower intensity than that in the plane $\alpha = 0°$. The v component remains nearly constant until $r = 30$ [cm], and afterwards shows decreasing positive values in the lower layer, $v/U_\infty = 0.1$, and increasing negative values in the upper layer, $v/U_\infty = -0.4$. The w component exhibits a similar pattern as that in the plane $\alpha = 0°$ where an increasing downward flow is observed, but with a slightly lower intensity. A maximum downward flow of $w/U_\infty = -0.5$ was measured close to the cylinder.

- In the plane $\alpha = 90°$, approaching the cylinder. The u component moderately grows, notably after $r \leq 30$ [cm]; a weak negative velocity is observed close to the bed. The v component is small in $r > 30$ [cm], shows afterwards increasing negative values (the flow is away from the cylinder) in the upper layer and increasing positive values (the flow is towards the cylinder) in the lower layer. An important v component is observed close to the bed and next to the cylinder. The w component always exhibits an increasing downward flow, but in a smaller intensity than that in the planes $\alpha = 0°$ and 45°, being $w/U_\infty = -0.35$. The w(z) profiles show concave distribution with zero values at the bed and surface. This is unlike in the flat channel bed measurement where the w velocity is maximum near the surface and is decreasing towards zero at the bed (see *Graf and Yulistiyanto*, 1998). The concave w(z) profiles are also observed in the previous planes ($\alpha = 0°$ and 45°).

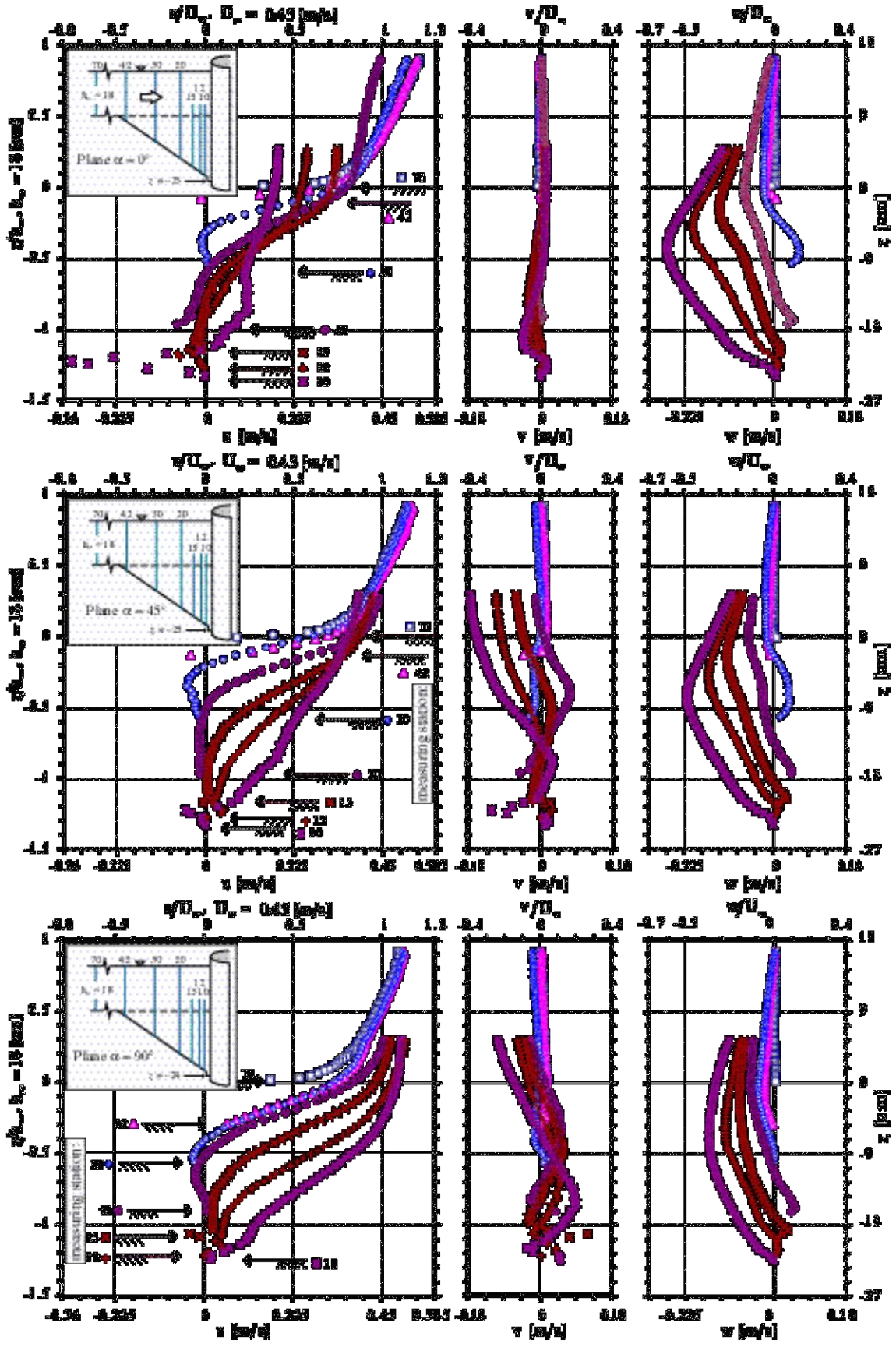

Fig. 3.1 Measured velocity profiles, u(z), v(z), w(z), around the cylinder.

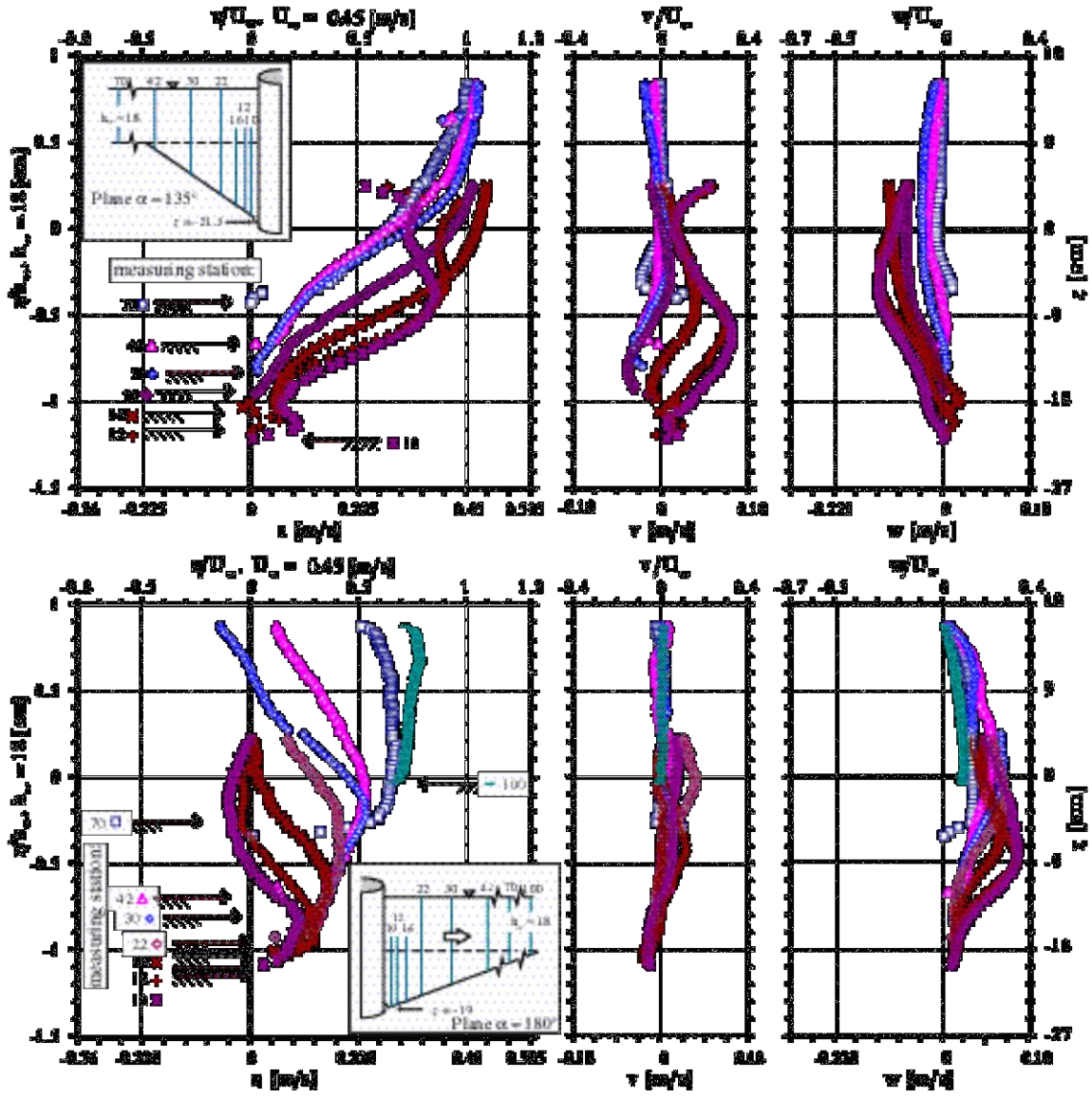

Fig. 3.1 Cont'd.

- In the plane $\alpha = 135°$, leaving the cylinder. The u component diminishes over the entire depth, but has always positive values. The v component remains negligible in the upper layer, but decreases in the lower layer where it becomes negative for $r > 22$ [cm]. The w component exhibits a rather weaker downward flow than in the previous planes, being $w/U_\infty = -0.3$. This component looses its strength and becomes negligible for $r > 70$ [cm].

- In the plane $\alpha = 180°$, leaving the cylinder. The u component shows a flow reversal towards the surface, its profile shows a recovery towards the one of uniform flow. The v component is generally small, but is rather noticeable, $v/U_\infty = \pm 0.1$, close to the cylinder. The w component is, contrary to that in the other planes, always directed upward and diminishing.

3.2.2 Flow pattern around the cylinder

A further investigation on the flow field can be made by presenting the measured velocity data in vector plots as depicted in Fig. 3.2. The plots, however, offer only a 2D picture of the flow field. In order to obtain a better observation on the flow structure around the cylinder, isoline contours of the velocity magnitude in different planes are plotted in Fig. 3.3. The velocity magnitude is normalized by the velocity of the approach flow, V/U_∞, where $V = \sqrt{u^2 + v^2 + w^2}$ and $U_\infty = 0.45\,[m/s]$. This can be interpreted as the flow intensity. These two figures together give a clear idea about the flow pattern around the cylinder. In the following paragraphs, the flow pattern around the cylinder is discussed, firstly for the plane of symmetry upstream of the cylinder ($\alpha = 0°$) and secondly for the other planes ($\alpha = 45°$, 90°, 135°, and 180°).

Flow in the plane $\alpha = 0°$

- The (far-field) approach flow, being essentially uni-directional, undergoes a separation upon encountering the sloping bed of the scour hole (see Fig. 3.2a). This process is similar to that of flow over a back-facing step (see *Nakagawa and Nezu*, 1987), except that the separation does not take place immediately at the tip of the bed change but at a point further downstream. By visual observation, the separation starts approximately at 5 [cm] after the sloping bed starts. Underneath the separation line, a weak clockwise rotating flow forms itself.

- Above the separation line, the flow is decelerating notably in the region $r > 30$ [cm]. Within a short distance $20 \geq r\,[\text{cm}] \geq 14$, the flow intensity decreases from V/U_∞ = 0.8 to 0.6 (see Fig. 3.3a). This decelerating flow is associated with a reverse pressure gradient created by the cylinder, which develops into a stagnation pressure at the cylinder face. In the vertical direction, the (dynamic) pressure diminishes with increasing depth (decreasing z). Consequently, the flow is down-deflected that becomes more pronounced approaching the cylinder. A strong downward flow develops along the cylinder face.

- The downward flow gets stronger with increasing depth, reaches a peak value of $-w/U_\infty = 0.6$ (Fig. 3.1) somewhere below the original bed level (Sect. 3.2.4 will discuss further the distribution of the maximum downward velocity). Below the peak, the (downward) flow looses its intensity from V/U_∞ = 0.6 to 0.2 (see Fig. 3.3a) when it encounters the separation zone and interacts with the rotating flow already exists there. The downward flow enhances the rotating flow and, conversely, the rotating flow attenuates the downward flow. At the bed, the flow is reversed back towards upstream by the cylinder and the bed; this further strengthening the rotating flow. This system of rotating and downward flows, which continues to exist as one follows the angular direction around the cylinder, is better known as the ***horseshoe vortex***.

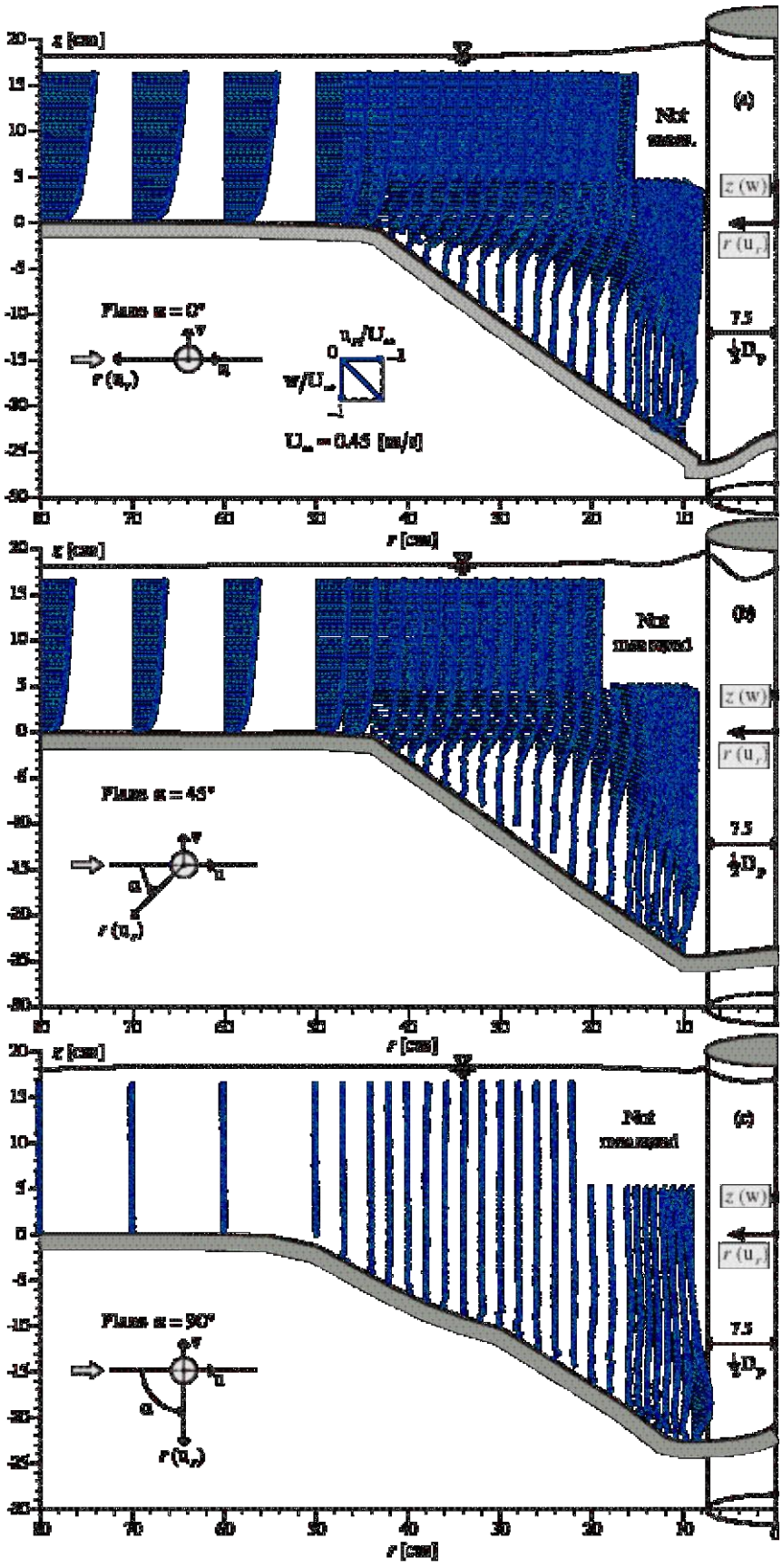

Fig. 3.2 Measured velocity fields in vertical planes, $\vec{\mathbf{V}}(u_r, w)$, around the cylinder.

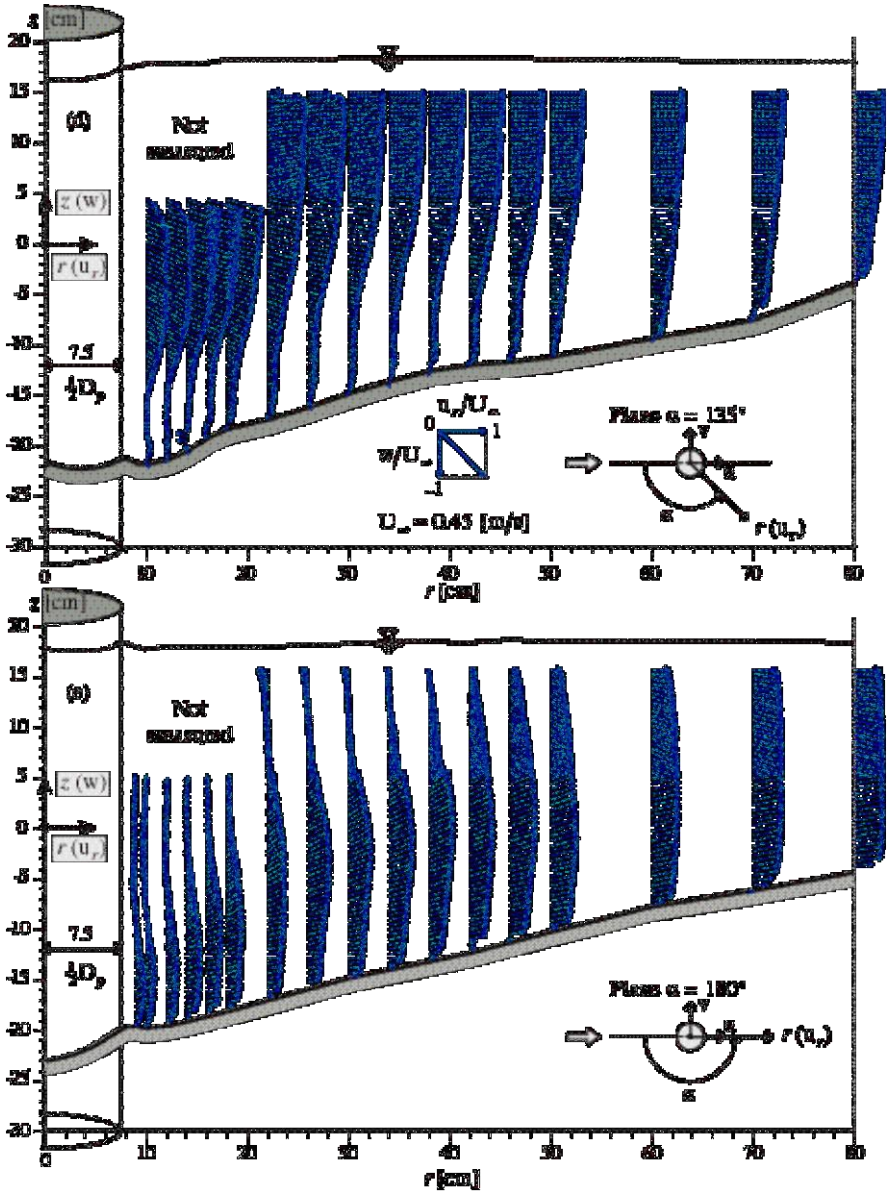
[cm]
(g)
Not measured
z (W)
r (u_r)
7.5
½D_p
u_r/U_∞
w/U_∞
U_∞ = 0.45 [m/s]
Plane α = 135°
r (u_r)
r [cm]
[cm]
(g)
Not measured
z (W)
r (u_r)
7.5
½D_p
Plane α = 180°
r (u_r)
r [cm]

Fig. 3.2 Cont'd.

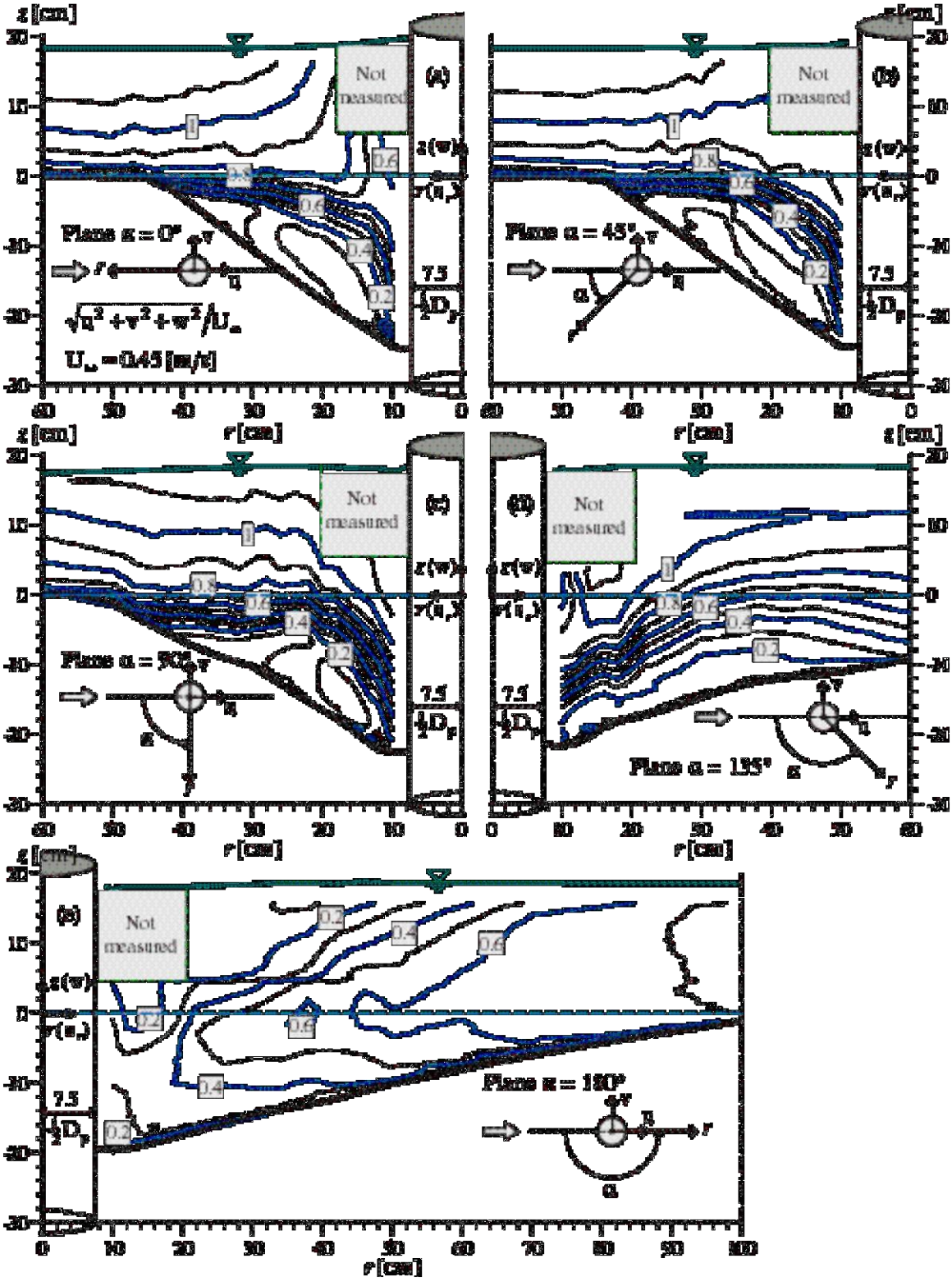

Fig. 3.3 Contours of the measured flow intensity, V/U_∞, where $V = \sqrt{u^2 + v^2 + w^2}$ and $U_\infty = 0.45\,[m/s]$.

Flow in the plane $\alpha = 45°$ and 90°

- In the plane $\alpha = 45°$, a similar observation as in the previous plane ($\alpha = 0°$) can be made, notably on the downward flow close to the cylinder and the rotating flow inside the scour hole, the horseshoe vortex, (see Fig. 3.2b). The velocity contour plot (see Fig. 3.3b), however, indicates a diminishing flow intensity compared to the one in the plane $\alpha = 0°$. Similarly, the downward velocity along the cylinder face is also less pronounced as has been shown previously (see Fig. 3.1). In the context of the horseshoe vortex, it can be concluded that this vortex is diminishing.
- In the plane $\alpha = 90°$, the radial velocity components are very weak (see Fig. 3.2c). The flow intensity (see Fig. 3.3c), on the other hand, is high and comparable with the one in the plane $\alpha = 45°$. This shows that much of the flow is dominated by the downstream velocity components, $u_\alpha >> u_r$ ($u_\alpha = u$, $u_r = -v$), as has also been evidenced in the velocity profiles discussed in the previous section (see Sect. 3.2.1, Fig. 3.1). Close to the cylinder (Fig. 3.3c), nevertheless, there is a noticeable radial velocity component, showing a flow direction away from the cylinder in the upper layer, $z > 0$, and vice versa in the lower layer, $z \leq 0$. The horseshoe vortex is practically not detected in this plane.

Flow in the plane $\alpha = 135°$ and 180°

- In the downstream planes ($\alpha = 135°$ and 180°), the flow is directed away from the cylinder (see Fig. 3.2d,e). The downward flow is weak in the plane $\alpha = 135°$ and is no longer noticeable in the plane $\alpha = 180°$. Behind the cylinder, a wake flow, characterized by a flow reversal towards the surface, takes over. Leaving the scour hole, the flow is recovering into a unidirectional one; at $r = 100$ [cm] it has not, however, entirely reached the (far-field) approach flow condition.

3.2.3 Transverse velocity

The alteration of the flow pattern due to the cylinder and the scour hole can also be investigated by looking into the directional change (deviation) of the flow with respect to the far-field approach flow. The vertical flow deviation can be readily illustrated by the vertical velocity component; this will be discussed in the next section. The horizontal flow deviation could be manifested by the skewed velocity profiles; this was experimentally investigated, for example, by *Ahmed and Rajaratnam* (1997). From the measured data obtained outside the scour hole, they defined the skewed profiles by making use of the normal (cross flow) velocity component and the streamwise velocity at the surface. In the present work, since the surface velocity is not measured, the transverse velocity component, v, is chosen as a measure of the horizontal deviation of the flow with respect to the main direction of the far-field approach flow. It has been shown in the preceding sections that the v component is always less prominent than the u component, meaning that the flow deviation (in the horizontal direction) is low. The evolution of the v-velocity component around the cylinder is here investigated, whereas that of the w component will be discussed in the following section.

The spatial evolution of the v-velocity component in the planes $\alpha = 45°$, 90°, and 135°, is displayed in Fig. 3.4. Shown on the left are the scalar values of the v velocity, normalized by the velocity in the approach flow, v/U_∞. Shown on the right are the direction (in degrees) of the local velocity vector, $\vec{V}_h(u,v)$, with respect to the plane of symmetry, such as $\beta = \arctan(v/|u|)$ with $-90 \le \beta\,[°] \le 90$. The negative values (indicated by the dashed contour lines) denote flow being deflected away from the plane of symmetry.

- In the plane $\alpha = 45°$, outside the scour hole the v-velocity component remains negligible, implying that the flow is unaltered either by the cylinder or the scour hole. Beginning at $r = 35$ [cm], it starts to show negative values (the flow deviates away from the plane of symmetry) and vice versa inside the scour hole. Approaching the cylinder, the negative deviation grows stronger in magnitude, $v/U_\infty \approx 0.35$, in direction, $\beta \approx -20$ [°], and in area, $z \ge -11$ [cm] (see Fig. 3.4a,b). Inside the scour hole, a weak flow, $v/U_\infty \approx 0.1$ to 0.15, deviates strongly, $\beta \approx 80$ [°], towards the plane of symmetry.

- In the plane $\alpha = 90°$, a weak flow deviation, $v/U_\infty \approx \pm 0.1$, is observed away from the cylinder at the upper layer, $z > 0$, and towards the cylinder inside the scour hole (see Fig. 3.4c,d). A small area, confined near the bed, of negative deviation is noticed. In the rest of the scour hole, $r > 30$ [cm], the flow is not deviated at all. Compared to the measurements on the flat channel bed (*Yulistiyanto*, 1997), this flow deviation is much less pronounced; the scour hole hinders the cylinder-induced deviating flow from developing.

- In the plane $\alpha = 135°$, a weak flow deviation is observed; although the maximum value is $v/U_\infty \approx 0.2$, but it is largely around $v/U_\infty \approx 0.1$. The deviation here is very much similar to that in the plane $\alpha = 90°$.

From the above observation on the transverse velocity component, it can be concluded that influence of the cylinder and the scour hole in deviating horizontally the approach flow is limited inside the scour hole and close to the cylinder. Outside the scour hole, the horizontal flow-direction remains the same as that of the far-field approach flow. This is supported further by the vector plots of the horizontal velocity, $\vec{V}_h(u,v)$, around the cylinder at different elevations z depicted in Fig. 3.5.

Fig. 3.5 also reveals the horizontal component of a rotating flow inside the scour hole; at $z = -10$ [cm] a clockwise rotating flow is noticeable on the side of the cylinder, $0° < \alpha \le 105°$, with a weaker counter-clockwise one next to it (see Fig. 3.5c). Deeper inside the scour hole, $z = -15$ [cm], this structure remains but has become very weak (see Fig. 3.5d). Downstream, $\alpha > 90°$, and close to the cylinder, the flow is accelerated and directed towards the wake behind the cylinder (see Fig. 3.5c,d). Immediately behind the cylinder, the flow meets the one coming from the other side of the symmetry plane; both together form an upward flow.

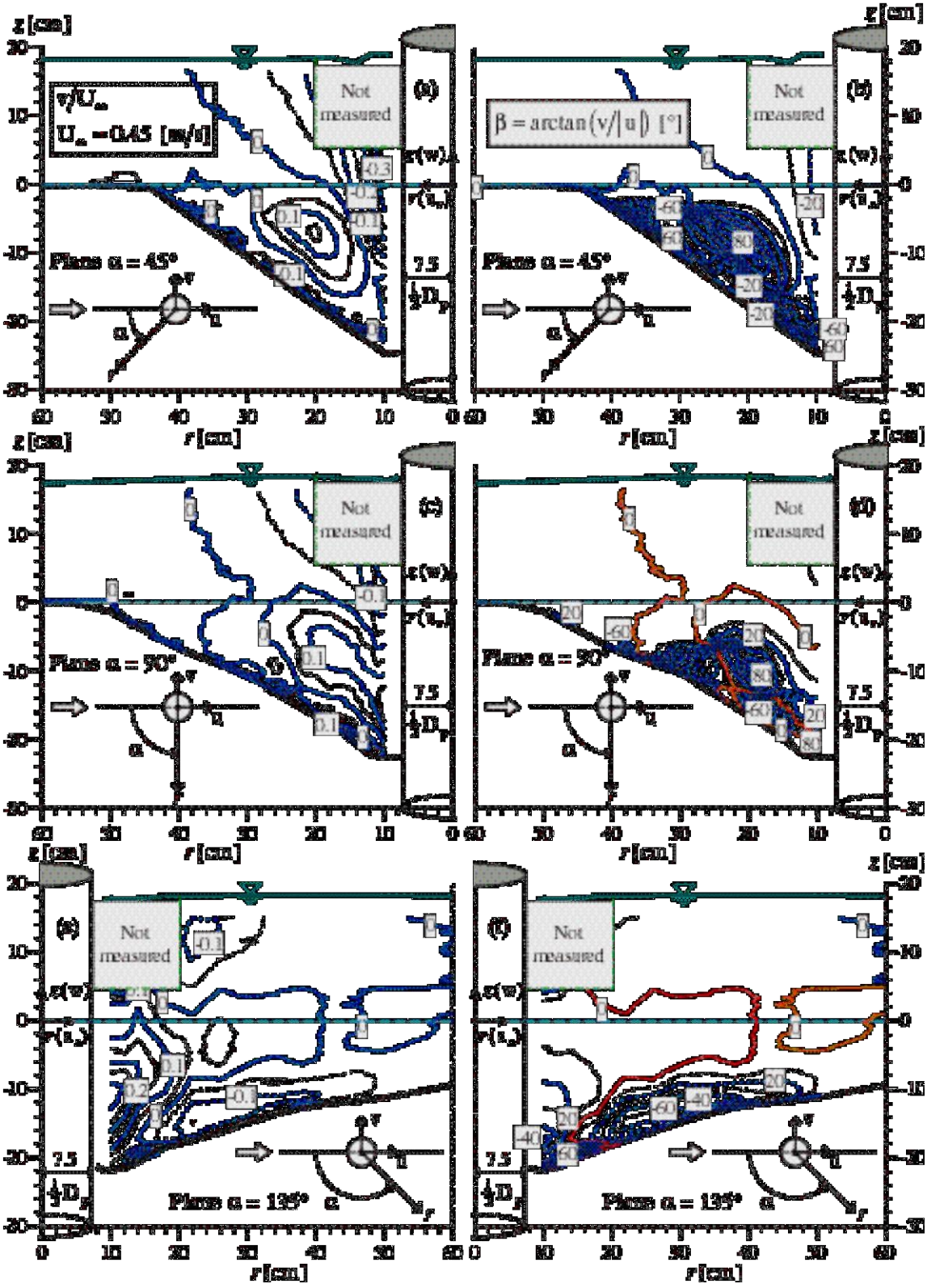

Fig. 3.4 Contours of the measured transverse velocity, v/U_∞, (on the left) and of the angles formed by the transverse velocity and the longitudinal velocity, $\arctan(v/|u|)$ in degrees, (on the right)

Fig. 3.5 Measured horizontal velocity vectors, $\vec{\mathbf{V}}_{\mathrm{h}}(\mathrm{u},\mathrm{v})$, at different elevations *z*.

3.2.4 Vertical velocity (downward flow)

The vertical velocity component manifests itself as a downward flow, notably in the upstream planes close to the cylinder. The downward flow along the cylinder face is driven by the pressure gradient in the vertical (z) and angular (α) directions. It is one of the important signatures of the flow around the cylinder; together with the reversed flow, they are usually referred to as the horseshoe vortex.

It has been previously shown (see Fig. 3.1) that the downward velocity has its maximum value near the cylinder (at the cylinder face). The variation of this downward velocity along the cylinder face (at $r = 10$ [cm]) observed in the upstream planes ($\alpha \leq 90°$), is shown Fig. 3.6a. The data are normalized by the maximum value, w_m, attained in the corresponding plane. Note that the data from the additional measurements in the planes $\alpha = 15°$, 30°, 60°, and 75° (see Chapter 2) have been included in the figure. It is interesting to see that the maximum values in all planes fall at 40% of the local depth measured from the bed, $(z - z_{bed})/h = 0.4$. Their profile, notably below the maximum value, falls in a narrow band, showing a near similarity.

A different result was reported by *Dey et al.* (1995), who found that the maximum downward flow was at the original bed level, $z \approx 0$, irrespective of the plane α.

In the case of flat channel bed (see *Graf and Yulistiyanto*, 1998), a somewhat different result was reported. In the plane $\alpha = 0°$ the downward velocity is increasing with depth, in the plane $\alpha = 45°$ it is almost uniformly distributed over the depth, and in the plane $\alpha = 90°$ it is diminishing with depth. The downward flow peak, in the plane $\alpha = 0$, is found at $z/h = 0.15$, which is much closer to the bed than what is observed in the present case with scoured channel bed. This is due partly to the lower depth (less friction loss by the cylinder) and, to a lesser extent, to the smaller separation zone. Consequently, the horseshoe vortex in the flat channel bed case is squeezed to the bottom corner of the cylinder.

A similar observation was reported by *Ahmed and Rajaratnam* (1998). The maximum downward flow is attained near or at the bed in the absence of scour hole, and below the original bed level in the presence of a scour hole.

Fig. 3.6b depicts the distribution of the maximum downward velocity in the radial direction for $\alpha \leq 90°$. Plotted in the figure are the maximum values of downward velocity attained at any particular distance, denoted by $\tilde{w}_m$, which are normalized by the largest of these values, w_m. What is interesting here is that the profiles fall in a narrow band, notably for $r/D_p \leq 1.8$ where a similarity can be observed. Regression through all data points yields an exponential relation:

$$\tilde{w}_m / w_m = 2.9683 \exp\left[-1.6736 \left(r/D_p \right)\right] \tag{3.1}$$

which is indicated by the solid line in Fig. 3.6b. The figure confirms also that the maximum downward velocity is observed at the cylinder face (at $r = 10$ [cm] or $r/D_p = 0.67$ as the available data closest to the cylinder). This maximum downward velocity diminishes with angular distance around the cylinder, from $w/U_\infty = -0.6$ at $\alpha = 0°$ to $w/U_\infty = -0.3$ at $\alpha = 135°$, and becomes upward velocity, $w/U_\infty = 0.35$ at $\alpha = 180°$, as displayed in Fig. 3.6c. The figure shows also the angular variation of the downward velocity at the original bed level, $z = 0$ [cm]; it varies in a similar manner as the maximum value, from $w/U_\infty \approx -0.4$ in $\alpha = 0°$ to $w/U_\infty \approx -0.2$ at $\alpha = 135°$, and $w/U_\infty = 0.25$ in $\alpha = 180°$.

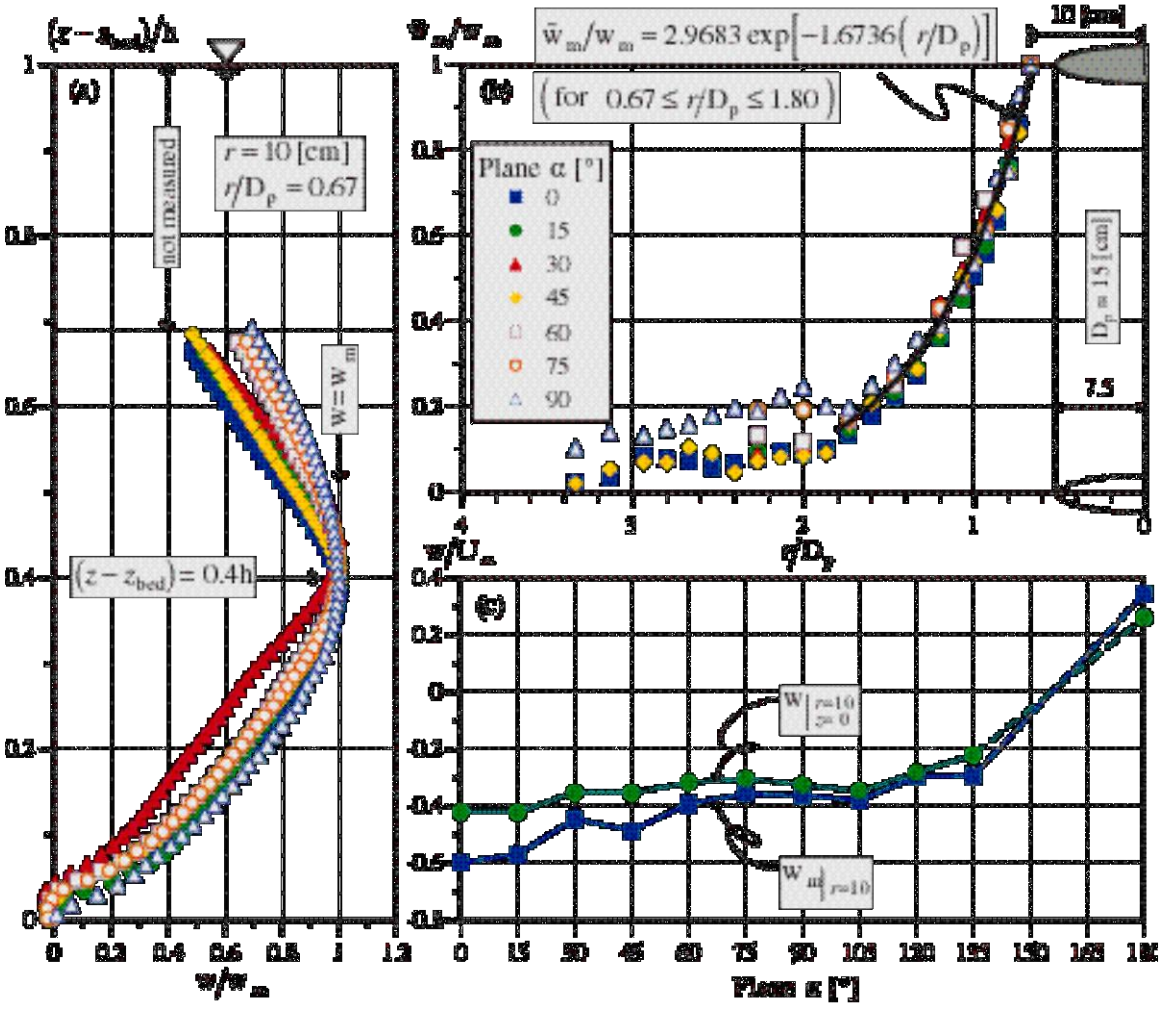

Fig. 3.6 Measured downward velocity around the cylinder: (**a**) vertical distribution along the cylinder face ($r = 10$ [cm]) in different planes, (**b**) radial distribution of the maximum values in different planes, and (**c**) angular distribution of the maximum values and of the values at the original bed level, $z = 0$.

The fact that the vertical velocity component has largely negative values, except in the plane $\alpha = 180°$, suggests that the scour hole attracts the flow. Inside the scour hole, the

flow may undergo a rotating mechanism; the rotation yet takes place and remains inside the scour hole. It seems that the flow out of the scour hole exits through the wake behind the cylinder, where the w component has positive values.

Fig. 3.7 shows the velocity vectors $\vec{\mathbf{V}}(u_\alpha, w)$ along vertical planes around the cylinder at a fixed radial distance from the cylinder, r = 10, 16, 22, and 30 [cm]. This figure clearly shows that the flow is deflected towards the bed due to the attraction of the scour hole to pull the flow; this holds even in the plane $\alpha = 135°$, which is near the wake region. The rotating flow, which is seen from the velocity vectors in Fig. 3.2, has an angular component notably at a distance of r = 22 [cm] as seen from Fig. 3.7c. At this distance and behind the cylinder, transverse components can be seen, indicating a weak 3D flow.

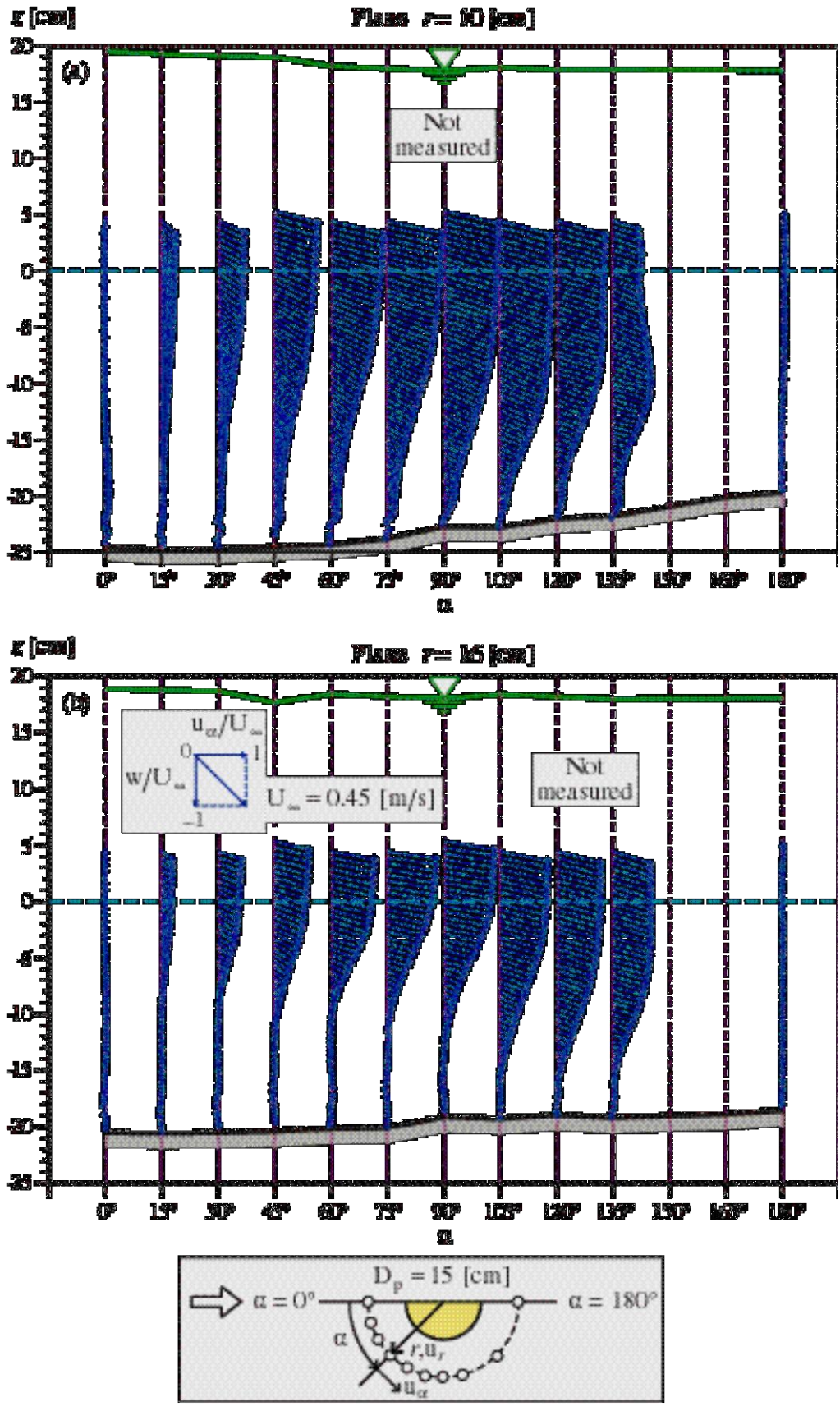

Fig. 3.7 Measured velocity fields in vertical planes at a constant distance r from the cylinder, $\vec{\mathbf{V}}(u_\alpha, w)$.

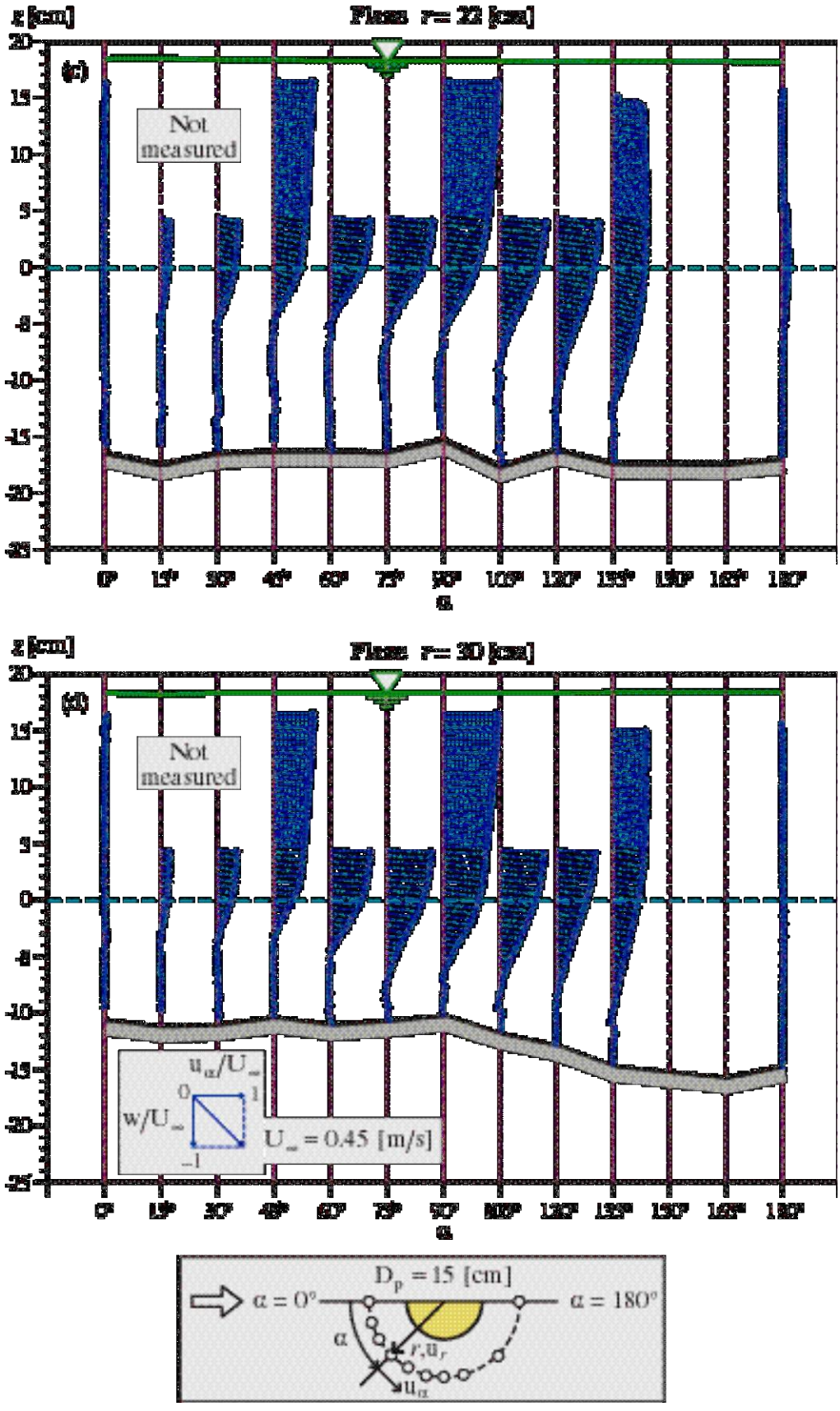
z [cm]
Plane r= 22 [cm]
(c)
Not measured
α
z [cm]
Plane r= 30 [cm]
(d)
Not measured
u_α/U_∞
w/U_∞
U_∞ = 0.45 [m/s]
D_p = 15 [cm]
α = 0°
α = 180°
α
r,u_r
u_α

Fig. 3.7 Cont'd.

3.2.5 Vorticity fields

The data of the velocity fields (see Fig. 3.1 and Fig. 3.2) can readily be used to generate the vorticity contours; this is shown in Fig. 3.8, where only the region of significant vorticity, $z \leq 2$ [cm], is displayed. The vorticity in a vertical plane, ω_ξ, is computed by:

$$\omega_\xi = \frac{\partial u_\xi}{\partial z} - \frac{\partial w}{\partial \xi} \tag{3.2}$$

where ξ is the x-axis rotated by α and u_ξ the corresponding velocity component. The transformation of the Cartesian coordinate axes and velocities is obtained by: $\xi = x\cos\alpha + y\sin\alpha$ and $u_\xi = u\cos\alpha + v\sin\alpha$. The central finite-difference technique was applied to the velocity data from all measuring stations in each plane. The following is to be observed:

- In the plane $\alpha = 0°$, a strong positive vorticity is seen at the upstream edge of the scour hole, which is due to a change in the bed slope; this is possibly related to the start of a separating flow (Fig. 3.8a). Similarly, a countour line of $\omega_\xi = 5$ [m^{-1}], which extends towards the cylinder bottom corner, is most likely related to the separation line. A weak negative vorticity is observed at $\xi = –35$ [cm]. Another strong positive vorticity is created in the downstream edge of the scour hole, $\xi = –10$ [cm], caused by the adverse pressure gradient due to the flow obstruction of the cylinder. This positive vorticity is accompanied by another strong (negative) vorticity underneath. In the remaining part of the scour-hole, the vorticity is rather weak, being of the same order as the vorticity in the approach flow. Behind the cylinder, the positive vorticity seen at the vicinity of the bed is probably due to the boundary-layer flow. The negative vorticity in the upper layer is related to the rotating flow as seen in the velocity fields; this disappears when the flow moves away from the cylinder and out of the scour hole.

- In the plane $\alpha = 45°$, a rather similar picture as in the plane $\alpha = 0°$ is observed; a strong positive vorticity is created on entering the scour hole, subsequently a weak negative one is seen at $\xi = –35$ [cm]. Another strong positive one is found at the bottom corner close to the cylinder; unlike in the previous plane, however, the accompanying negative vorticity underneath is weak. Immediately behind the cylinder, a rather weak negative vorticity is displayed at the bed and upper layer. A boundary-flow positive vorticity is seen at the vicinity of the bed. In the remaining part of the scour hole, none of important activity can be observed.

- In the plane $\alpha = 90°$, a positive vorticity, but weak, is also observed on the brink of the cylinder. A positive and negative vorticities at the bottom corner of the cylinder is also detected, but with a much weaker strength than that in the other planes. In the remaining part, a weak negative vorticity is observed.

A similar observation, in the plane of symmetry upstream and downstream of the cylinder, was reported by *Kobayashi et al.*, (1997).

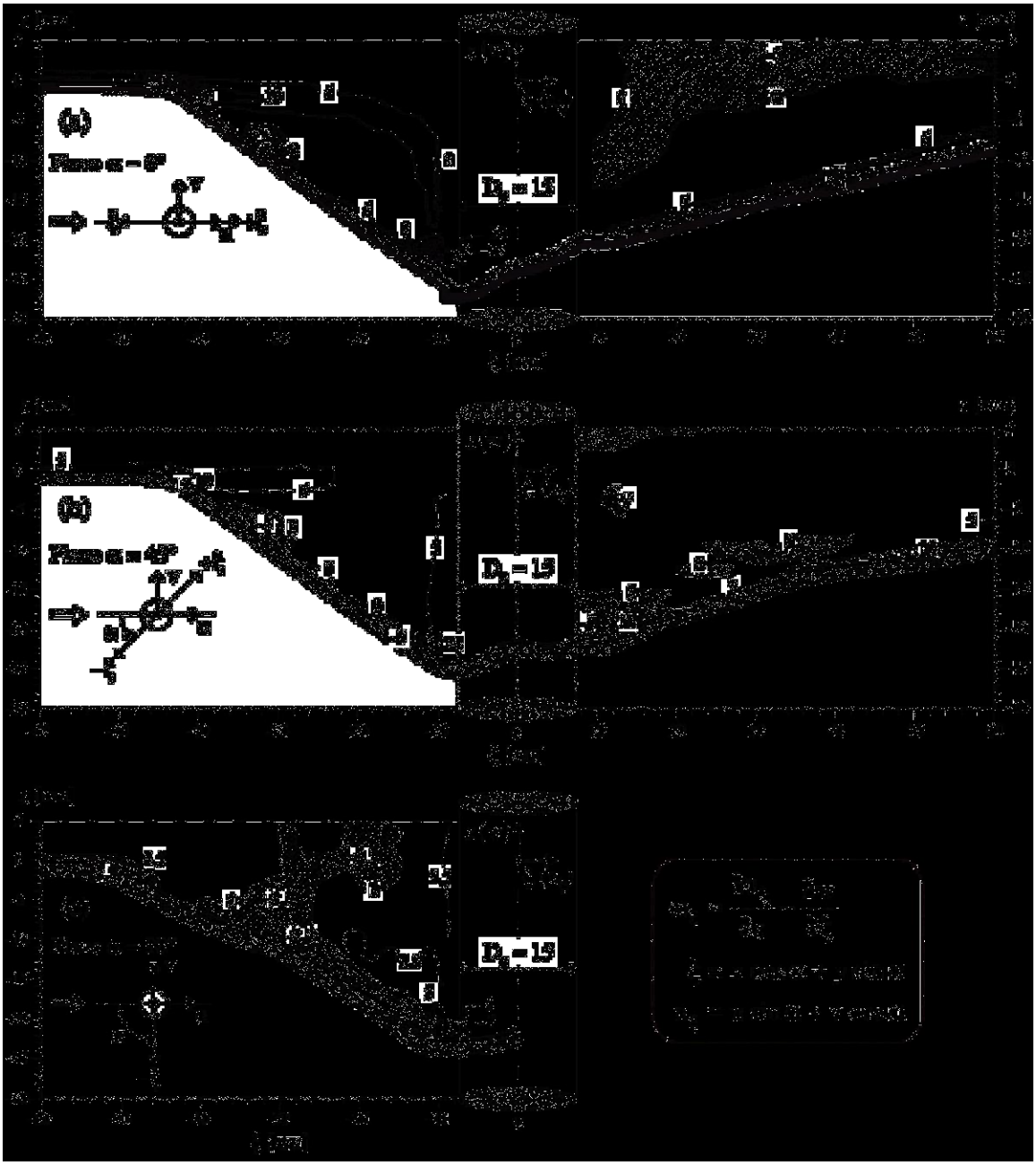

Fig. 3.8 Contours of the vorticity fields in vertical planes around the cylinder. Shaded area and dashed lines indicate negative vorticities.

3.3 Turbulence characteristics around the cylinder

3.3.1 Vertical distributions of the turbulence stresses

The results obtained from the turbulence measurements are shown in Fig. 3.9 for some selected profiles in the planes $\alpha = 0°$, 45°, 90°, 135°, and 180°. The shear velocity in the far-field approach flow, $u_{*,\infty} = 0.0265$ [m/s], is used to normalize the data. The following is to be observed:

- In the plane $\alpha = 0°$ and outside the scour hole, $z > 0$, the profiles of the turbulence intensities and the Reynolds stresses reasonably collapse, showing no significant change from the profiles in the far field approach flow. Inside the scour hole, $z \leq 0$, there is an increase of turbulence intensities and shear stresses approaching the cylinder. Near the scour bed, the longitudinal component of the Reynolds stress, $-\overline{u'w'}$, has negative values; this is in agreement with the reversed flow observed in that region. In the entire region, the longitudinal components of the turbulence intensities, $\sqrt{\overline{u'u'}}$, and of the Reynolds stresses, $-\overline{u'w'}$, are the dominant ones; this holds over the entire flow depth.

- In the plane $\alpha = 45°$, a similar observation as in the plane $\alpha = 0°$ can be made, with the exception that the transverse component of the turbulence intensities, $\sqrt{\overline{v'v'}}$, and of the Reynolds stresses, $-\overline{v'w'}$, have values close to the longitudinal ones.

- In the plane $\alpha = 90°$, the longitudinal turbulence intensities, $\sqrt{\overline{u'u'}}$, slightly decrease from the ones in the previous two planes, but the transverse components, $\sqrt{\overline{v'v'}}$, increase. On the other hand, the longitudinal Reynolds stresses, $-\overline{u'w'}$, show significant activities, notably inside the scour hole; distinguishable are the bulges of $-\overline{u'w'}$ beneath $z = 0$, moving downwards with decreasing values as they approach the cylinder.

- In the downstream planes, $\alpha = 135°$ and 180°, the turbulence is strong and rather isotropic, notably in the wake region behind the cylinder. It shows that the wake flow, being known to be 3D one, fluctuates about its mean value without directional preferences. The Reynolds stresses inside the scour hole in the plane $\alpha = 135°$ are quite strong, as much as twice or more of those in the upstream planes. The transverse stresses, $-\overline{v'w'}$, are also strong; their profiles display positive and negative values along the flow depth, indicating a transverse momentum exchange. Behind the cylinder in the plane $\alpha = 180°$, the Reynolds stresses are strong but demonstrate a chaotic picture. The flow itself is also chaotic and thus the interpretation of the measured data is rather difficult.

Unfortunately —to the best of our knowledge— no research is available for comparison. Studying a backward-facing step (*Etheridge and Kemp*, 1978, p. 555; and *Nakagawa and Nezu*, 1987, p. 70) showed rather similar trends.

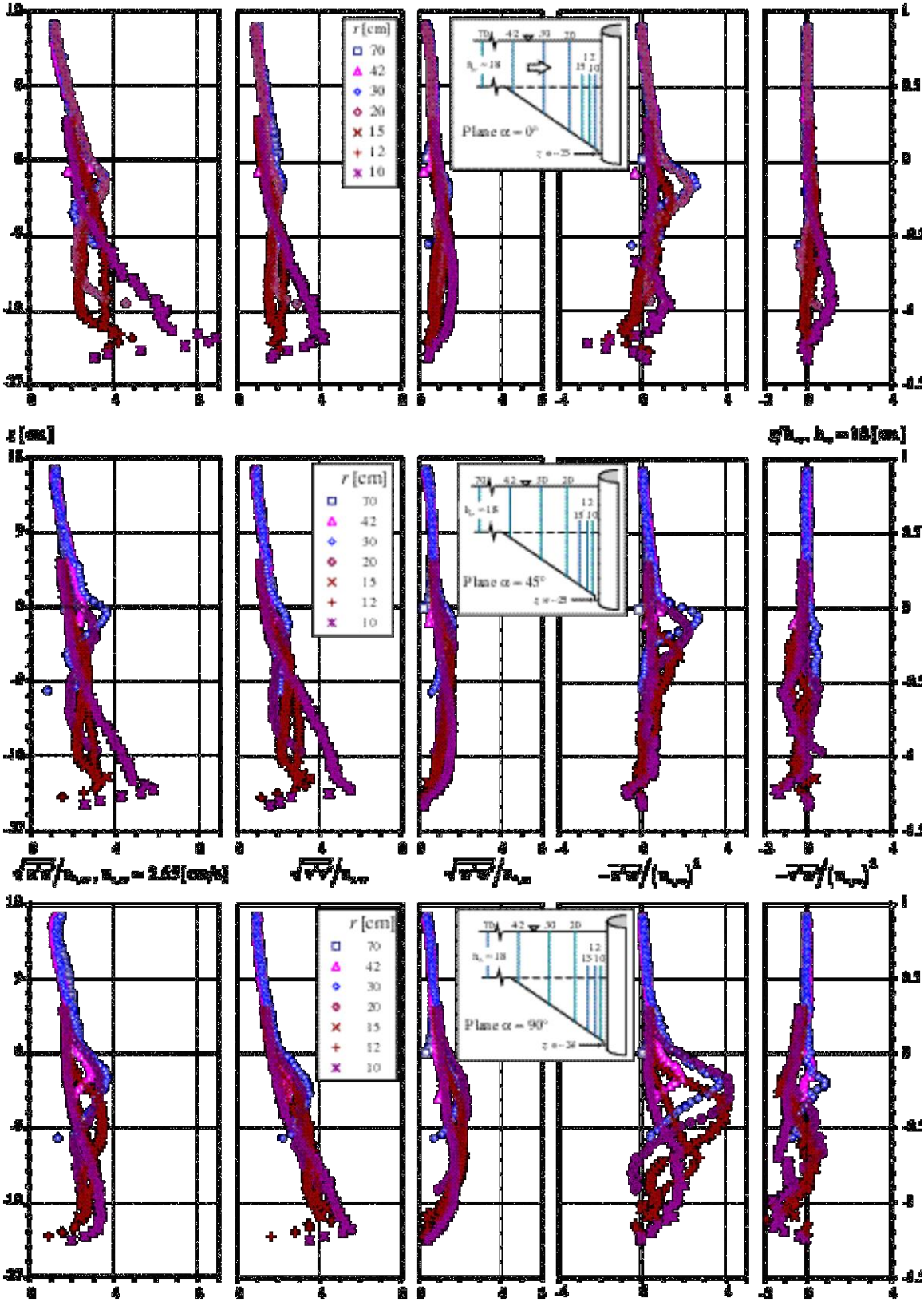

Fig. 3.9 Measured turbulence intensities and Reynolds stresses in radial planes around the cylinder.

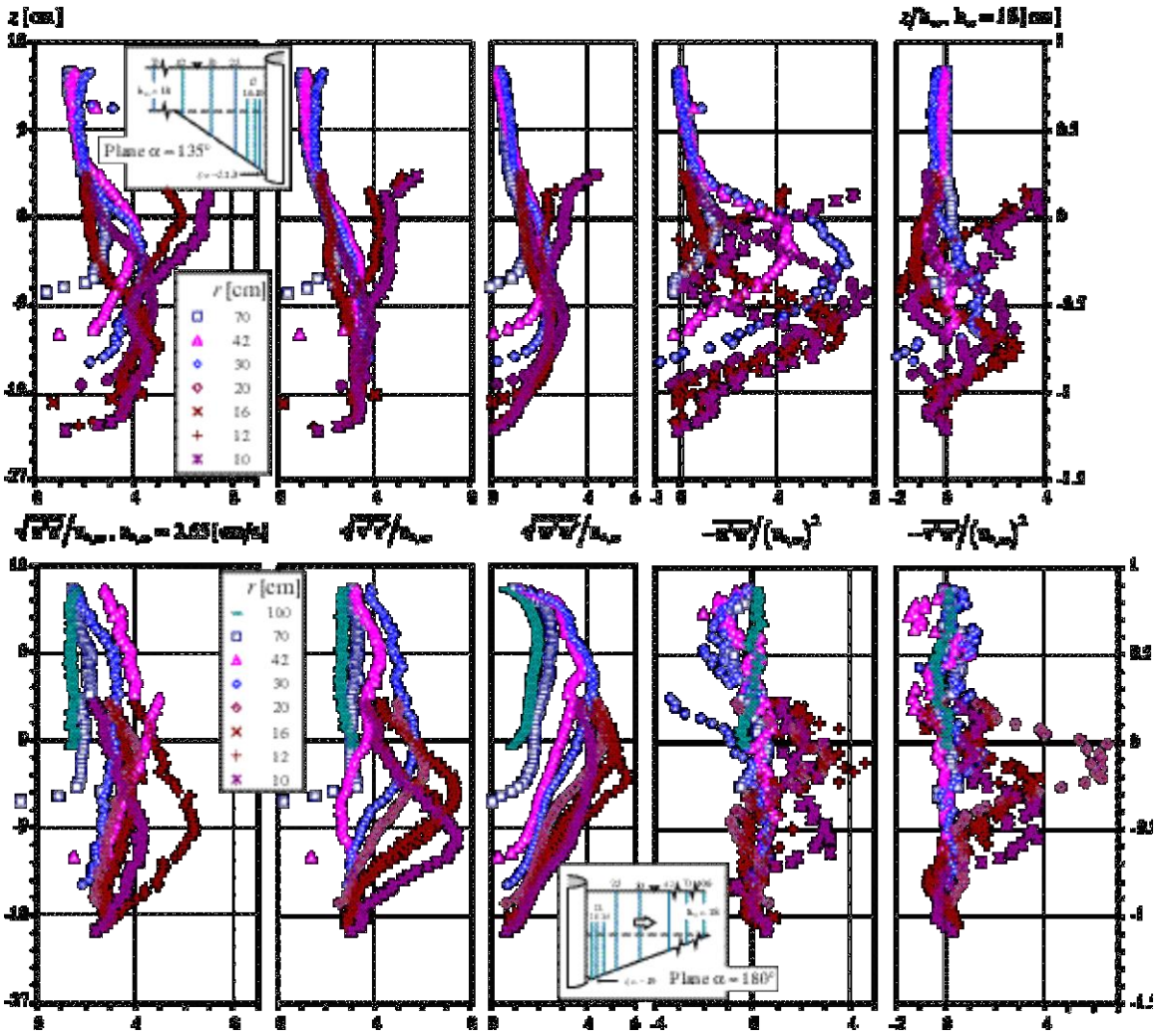

Fig. 3.9 Cont'd.

3.3.2 Turbulent kinetic energy

From the data of the turbulence intensities (see Fig. 3.9), the turbulent kinetic energy of the flow, k, defined as:

$$k = \tfrac{1}{2}\left(\overline{u'u'} + \overline{v'v'} + \overline{w'w'}\right) \tag{3.3}$$

can be computed and is presented in Fig. 3.10 and Fig. 3.11. In the first figure, the data values are normalized by using the shear velocity of the approach flow, $u_{*,\infty} = 0.0265$ [m/s]. In the second figure, the total kinetic energy, K + k, where K is the kinetic energy of the mean flow, defined as:

$$K = \tfrac{1}{2}\left(u^2 + v^2 + w^2\right) \tag{3.4}$$

is used to normalize the values of the turbulent kinetic energy.

The following is to be observed:

- In the plane $\alpha = 0°$ and approaching the cylinder, there is an increase in the turbulent kinetic energy over the entire scour hole. A distinguishable feature is the pronounced bulges immediately below the original bed level whose intensity and form enlarge approaching the cylinder (see Fig. 3.10a). The bulges, ranging between $k/u_{*,\infty}^2 \approx 7$ to 45, correspond to the isoline of 0.1(K+k) turbulent kinetic energy (see Fig. 3.11a), which delimitates the region of high turbulent energy inside the scour hole (as high as 90% of the total kinetic energy) from the one of low level turbulent outside the scour hole. The maximum value of the turbulent kinetic energy is found at the bottom corner of the cylinder where the strong reversed flow (see Fig. 3.2) and the vorticity peak (see Fig. 3.8) are observed.

- In the plane $\alpha = 45°$, the same as in the plane $\alpha = 0°$ is observed, but a slightly lower turbulent energy peak at the bottom corner of the cylinder.

- In the plane $\alpha = 90°$, the high turbulent kinetic energy is almost in the entire scour hole; the bulges seen in the preceding planes are here nearly extended (see Fig. 3.10c) with a maximum value of $k/u_{*,\infty}^2 \approx 40$. The kinetic energy inside the scour hole, as in the planes $\alpha = 0°$ and 45°, is largely due to the turbulence; it peaks at 90% of the total kinetic energy in the lower part of the scour hole at $r \leq 20$ [cm] (see Fig. 3.11c).

- In the plane $\alpha = 135°$, the trend seen in the plane $\alpha = 90°$ continues; moving away from the cylinder, the bulges in the kinetic energy profiles diminish.

- In the plane $\alpha = 180°$, there is a significant increase in the turbulent kinetic energy; this is observed in the entire flow depth. At the vicinity of the cylinder, a peak value of $k/u_{*,\infty}^2 \approx 45$ is measured until $r = 20$ [cm]. Leaving the cylinder and the scour hole, the turbulent kinetic energy gradually reduces (see Fig. 3.10e) and at $r = 100$ [cm] is becomes less than 10% of the total kinetic energy (see Fig. 3.11e). Again, it should be noted that the measured data must be interpreted with caution. In this wake region, the flow is chaotic, with a vortex shedding taking place; it is possible that the measurements do not have a sufficiently time resolution to resolve this shedding movement.

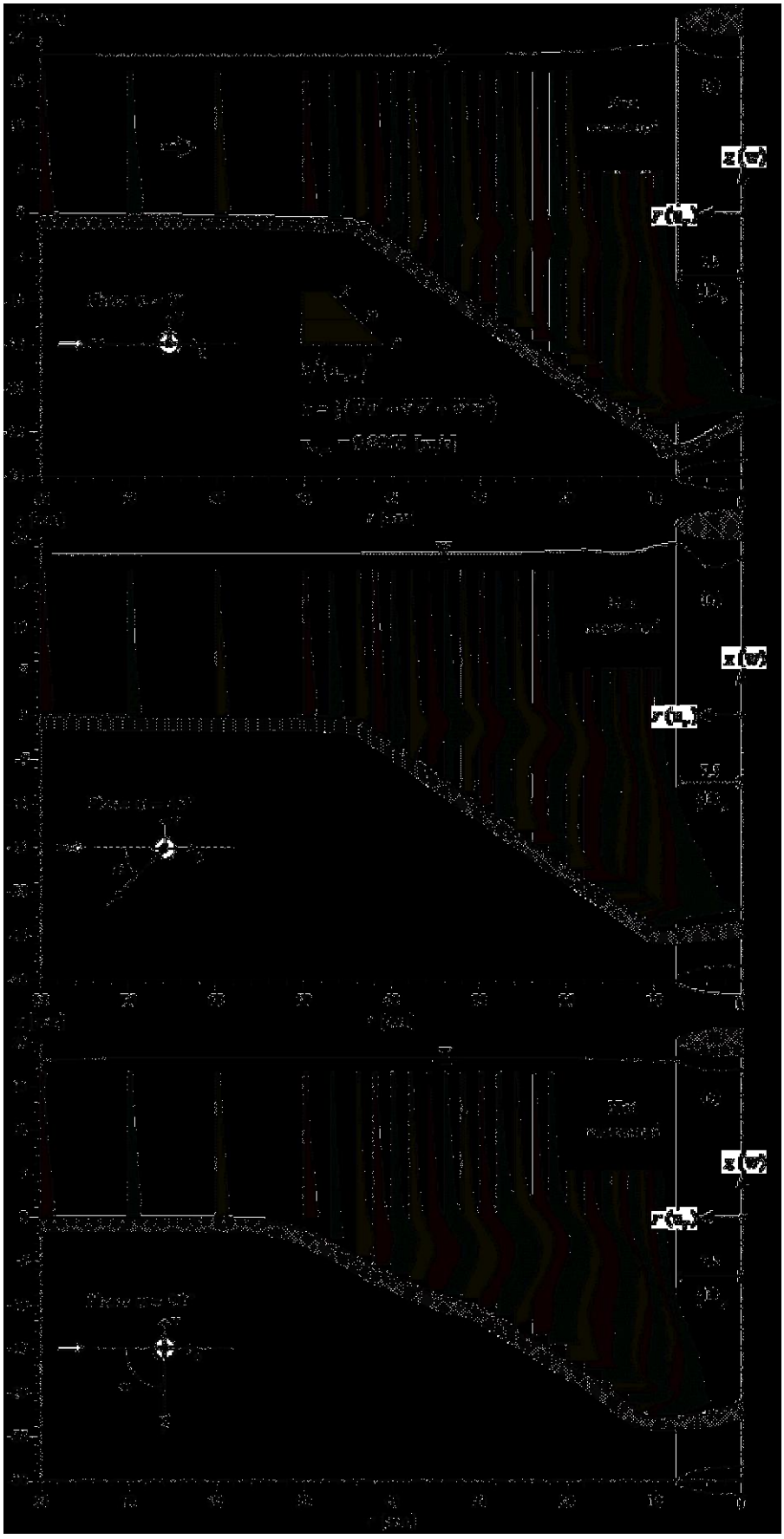

Fig. 3.10 Measured turbulent kinetic energy around the cylinder. The data are normalized by the shear velocity in the approach flow, $u_{*,\infty} = 0.0265$ [m/s].

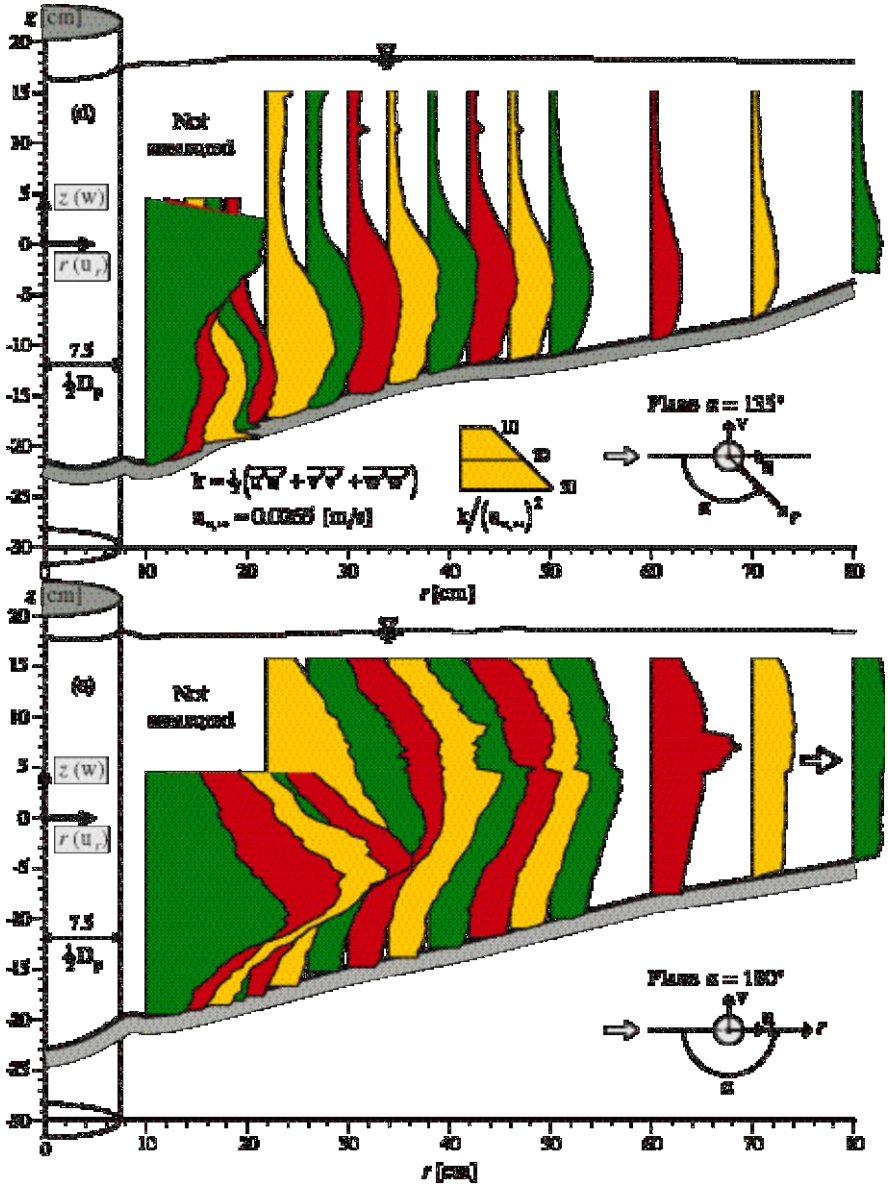

Fig. 3.10 Cont'd.

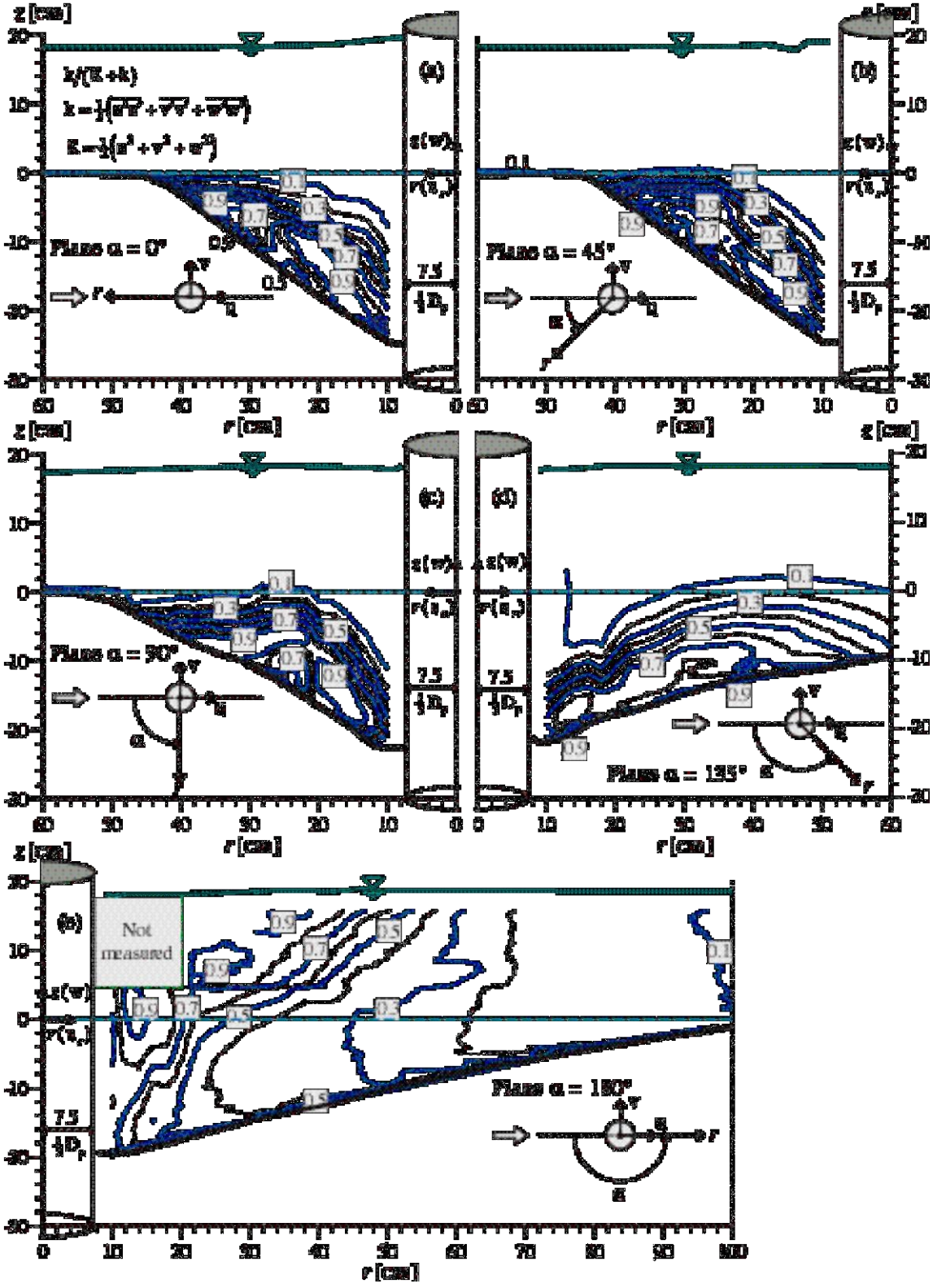

Fig. 3.11 Contour of the measured turbulence kinetic energy around the cylinder. The data are normalized by the total kinetic energy, $k/(K+k)$, where $k = \frac{1}{2}\left(\overline{u'u'} + \overline{v'v'} + \overline{w'w'}\right)$ and $K = \frac{1}{2}\left(u^2 + v^2 + w^2\right)$.

3.4 Bed shear-stresses along the plane of symmetry

Determination of the bed shear-stress, τ_o, from the experimental data is a rather difficult task. While a direct measurement technique would be most desirable, here we must content ourselves with the estimate values based on available data from the velocity and shear-stress distributions (see Fig. 3.1 and Fig. 3.9). Three alternative methods were used:

1. Based on the velocities, u and w, measured closest to the bed, $z \approx 4$ [mm], a velocity parallel to the bed —at a distance of δ_n— was calculated, V_t; the bed shear-stress was calculated as:

$$\tau_{o,1} = \rho\, \nu_t \left(\frac{\partial V_t}{\partial n}\right) \approx \rho\, \nu_t \left(\frac{V_t}{\delta n}\right) \tag{3.5}$$

   where $\nu_t = 1.3 \times 10^{-5}\ [m^2/s^2]$ was taken as the measured eddy-viscosity in the approach flow.

2. Based on the measured shear-stress distribution (see Fig. 3.9), a (rather subjective) extrapolation towards the bed was used to obtain the bed shear-stress, or:

$$\tau_{o,2} = -\rho \left(\overline{u'w'}\right)_{bed} \cos\Theta \tag{3.6}$$

3. Based on a relation for the velocity distribution (see *Graf and Altinakar*, 1998, pp. 73-74) the bed shear-stress was evaluated by:

$$\tau_{o,3} = \rho \left(u_{*,3}\right)^2 = \rho \left(U \sqrt{\frac{g}{C^2}} \right)^2 = \rho (0.07\, U)^2 \tag{3.7}$$

   where U is the local depth-averaged flow velocity and C is Chezy coefficient taken as $C = 44\ [m^{1/2}/s]$ (uniform sand bed with $d_{50} = 2.1$ [mm]).

A numerical simulation of the flow around the cylinder has also been performed (see Chapter 5), from which the bed shear-stresses can also be obtained; this is denoted as $\tau_{o,4}$. Its value was obtained with a similar equation as Eq. 3.5, in which the k-ε turbulence model-equation and the logarithmic law-of-the-wall were used to get the eddy viscosity, ν_t, and the velocity gradient, $\partial V_t / \partial n$, (see Chapter 4, Eq. 4.82). For clarity, the expression used to compute $\tau_{o,4}$ is rewritten below:

$$\tau_{o,4} = \rho\, c_\mu^{3/4}\, k^{1/2}\, \frac{\kappa V_t}{\ln\left(E\, \delta_n^+\right)} \tag{4.82}$$

where $c_\mu = 0.09$ is a k-ε model constant, k turbulent kinetic-energy, $\kappa = 0.4$ Karman constant, E roughness coefficient of the bed, $\delta_n^+ = u_* \delta_n / \nu$ dimensionless normal distance from the bed, and ν the kinematic viscosity of water. The sign convention of $\tau_{o,4}$ is the same as that of the velocity.

The bed shear-stress, τ_o, obtained by the three methods applied to the measured data is presented in Table 3.1 and Table 3.2, and is plotted in Fig. 3.12; shown also in the figure is the one obtained from the numerical simulation. Evaluation is only done for the plane of symmetry upstream and downstream of the cylinder. The following is to be remarked:

- In the approach region, $x \leq -45$ [cm], all three methods render rather similar results, being $0.6 \leq \tau_o$ [Pa] ≤ 1.0. The bed shear-stress in the approach region was earlier obtained as being $\tau_{o,\infty} = 0.70$ [Pa] or $u_{*,\infty} = 0.0265$ [m/s].

- In the scour hole upstream of the cylinder, $-45 \leq x$ [cm] ≤ -10, the agreement is less convincing. It appears that the data using the velocity measurements, Eq. 3.5, seem to be more reliable; evaluation of the measurement of the velocity, V_t, is more objective than the one of the shear-stress, $-\rho\left(\overline{u'w'}\right)$, at the bed. This is also evidenced by the numerical simulation, Eq 4.82, which depends on the velocity close to the bed. The global method, Eq. 3.7, would be simple, but applies essentially to uniform flow and does not take into account the flow reversal close to the bed; thus, the sign change is not respected. Note that the negative value indicates flow reversal at the bed.

- Behind the cylinder, $10 \leq x$ [cm] ≤ 80, the three methods render surprisingly similar results, being $0 \leq \tau_o$ [Pa] ≤ 0.5, thus almost constant over the entire length measured. The measured bed shear-stress is slightly larger than the one in the upstream part of the scour hole; this was also observed by *Melville and Raudkivi* (1977) and *Dey*, (1997). On leaving the scour hole, the shear stress has about the same (absolute) value as the one in the upstream part of the scour hole; there is a weak tendency of an increase as leaving the scour hole. This is also observed from the numerical simulation result.

- In both regions, upstream and downstream of the cylinder, the critical shear-stress, $\tau_{o,cr} = 1.36$ [Pa], as calculated from the Shields diagram (for uniform sand with $d_{50} = 2.1$ [mm]), $\tau^*_{cr} = 0.04$ [–], was not exceeded. This is in agreement with eye observations. Thus the experiment is well a clear-water scour run, where the capacity of transport in the approach flow and in the scour hole is zero.

The observation of the bed shear-stress variation as depicted in Fig. 3.12 reveals that the (high) bed shear-stress in the approach flow is gradually reduced on entering the scour hole, where it remains rather low on approaching the cylinder. Measurements by *Melville and Raudkivi* (1977) show a similar trend.

Table 3.1 Estimated bed shear-stresses based on the vertical distributions of the measured velocities and Reynolds stresses upstream of the cylinder.

x [cm]	U [m/s]	U/U_∞ [–]	$\tau_{o,1}$ [Pa]	$\tau_{o,1}/\tau_{o,cr}$ [–]	$\tau_{o,2}$ [Pa]	$\lvert\tau_{o,3}\rvert$ [Pa]	$u_{*,1}$ [m/s]	$u_{*,2}$ [m/s]	$u_{*,3}$ [m/s]
-10	0.091	0.201	-0.010	-0.007	-1.800	0.040	-0.003	-0.042	0.006
-11	0.095	0.212	-0.102	-0.075	-1.800	0.045	-0.010	-0.042	0.007
-12	0.114	0.253	-0.047	-0.035	-1.400	0.064	-0.007	-0.037	0.008
-13	0.121	0.268	-0.161	-0.118	-1.200	0.071	-0.013	-0.035	0.008
-14	0.125	0.278	-0.246	-0.181	-1.200	0.076	-0.016	-0.035	0.009
-15	0.139	0.309	-0.303	-0.223	-0.900	0.095	-0.017	-0.030	0.010
-16	0.143	0.318	-0.071	-0.052	-0.600	0.100	-0.008	-0.024	0.010
-18	0.156	0.346	-0.080	-0.059	-0.300	0.119	-0.009	-0.017	0.011
-20	0.268	0.596	-0.196	-0.144	0.300	0.353	-0.014	0.017	0.019
-22	0.281	0.625	-0.223	-0.164	0.300	0.388	-0.015	0.017	0.020
-24	0.297	0.659	-0.205	-0.151	0.400	0.432	-0.014	0.020	0.021
-26	0.312	0.693	-0.134	-0.098	0.300	0.476	-0.012	0.017	0.022
-28	0.324	0.720	-0.076	-0.056	0.400	0.514	-0.009	0.020	0.023
-30	0.343	0.763	-0.030	-0.022	0.700	0.577	-0.005	0.026	0.024
-32	0.352	0.782	-0.019	-0.014	0.300	0.607	-0.004	0.017	0.025
-34	0.360	0.801	-0.163	-0.120	1.000	0.636	-0.013	0.032	0.025
-36	0.387	0.861	-0.084	-0.062	0.900	0.735	-0.009	0.030	0.027
-38	0.404	0.897	-0.097	-0.071	0.700	0.798	-0.010	0.026	0.028
-40	0.429	0.952	-0.072	-0.053	0.600	0.900	-0.008	0.024	0.030
-42	0.449	0.997	-0.053	-0.039	0.600	0.986	-0.007	0.024	0.031
-44	0.467	1.037	0.246	0.181	0.600	1.068	0.016	0.024	0.033
-47	0.449	0.998	0.855	0.629	0.600	0.988	0.029	0.024	0.031
-50	0.466	1.035	0.718	0.528	0.600	1.063	0.027	0.024	0.033
-60	0.454	1.009	1.031	0.758	0.600	1.010	0.032	0.024	0.032
-70	0.451	1.002	0.866	0.637	0.700	0.997	0.029	0.026	0.032
-80	0.457	1.016	1.366	1.004	0.700	1.024	0.037	0.026	0.032

Notes:

U = local depth-averaged velocity

$U_\infty = 0.45$ [m/s] = approach velocity

$\tau_{o,1} = \rho \nu_t \, \partial V_t / \partial n \approx \rho \nu_t \, V_t / \delta n$

$\nu_t = 1.3 \times 10^{-5}$ [m²/s²] = measured eddy viscosity in the approach flow

V_t = velocity measured closest to the bed, $z \approx 4$ [mm], projected on a plane parallel to the bed

δ_n = normal distance between V_t and the bed

$\tau_{o,2} = -\rho \overline{u'w'}\big|_{bed} \cos\Theta$

$\lvert\tau_{o,3}\rvert = \rho\left(u_{*,3}\right)^2 = \rho\left(U\sqrt{g/C^2}\right)^2 = \rho\left(0.07\,U\right)^2$, with C = 44 [m$^{1/2}$/s] = Chezy coefficient

$\tau_{o,cr}$ = 1.36 [Pa] = critical shear-stress according to the Shields criterion for d_{50} = 2.1 [mm], or $\tau_{cr}^* = 0.04$.

Table 3.2 Estimated bed shear-stresses based on the vertical distributions of the measured velocities and Reynolds stresses downstream of the cylinder.

x [cm]	U [m/s]	U/U_∞ [–]	$\tau_{o,1}$ [Pa]	$\tau_{o,1}/\tau_{o,cr}$ [–]	$\tau_{o,2}$ [Pa]	$\lvert\tau_{o,3}\rvert$ [Pa]	$u_{*,1}$ [m/s]	$u_{*,2}$ [m/s]	$u_{*,3}$ [m/s]
10	0.014	0.030	0.200	0.147	0.189	0.001	0.014	0.014	0.001
12	0.043	0.096	0.179	0.131	0.300	0.009	0.013	0.017	0.003
14	0.076	0.168	0.098	0.072	0.584	0.028	0.010	0.024	0.005
16	0.091	0.202	0.138	0.102	0.616	0.040	0.012	0.025	0.006
18	0.108	0.239	0.181	0.133	0.487	0.057	0.013	0.022	0.008
22	0.152	0.337	0.214	0.157	0.453	0.113	0.015	0.021	0.011
26	0.099	0.220	0.263	0.193	0.243	0.048	0.016	0.016	0.007
30	0.103	0.229	0.372	0.274	0.026	0.052	0.019	0.005	0.007
34	0.125	0.279	0.542	0.399	0.193	0.077	0.023	0.014	0.009
38	0.139	0.309	0.376	0.277	0.099	0.095	0.019	0.010	0.010
42	0.165	0.366	0.204	0.150	0.212	0.133	0.014	0.015	0.012
46	0.191	0.425	0.258	0.190	0.312	0.179	0.016	0.018	0.013
50	0.207	0.459	0.428	0.315	-0.076	0.209	0.021	-0.009	0.014
60	0.243	0.540	0.481	0.353	0.086	0.289	0.022	0.009	0.017
70	0.279	0.620	0.426	0.313	-0.018	0.382	0.021	-0.004	0.020
80	0.290	0.644	0.397	0.292	0.000	0.412	0.020	0.000	0.020
90	0.307	0.682	0.584	0.429	0.022	0.462	0.024	0.005	0.021
100	0.336	0.747	0.646	0.475	-0.028	0.554	0.025	-0.005	0.024

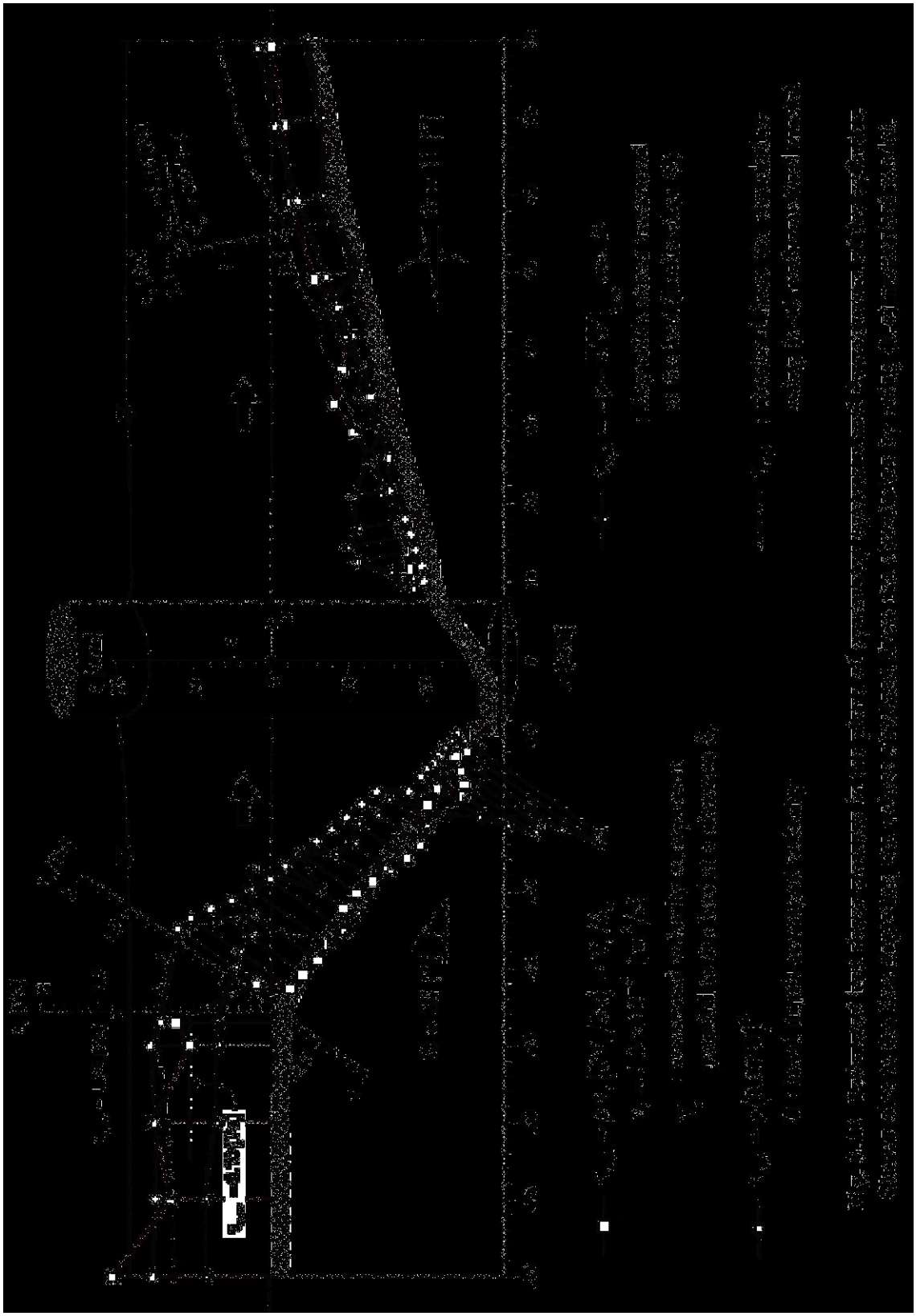

3.5 Summary and conclusions

The measured 3D instantaneous velocity profiles presented in the preceding chapter (see Chapter 2) were analyzed. The emphasize of the analyses is put on the (time-averaged) velocity fields, notably their spatial variation in vertical planes around the cylinder, in order to investigate the flow alteration due to the existence of the cylinder and the scour hole. The turbulence characteristics, such as the turbulence intensities, the turbulent kinetic energy, and the Reynolds stresses, were also analyzed. An attempt was also made to estimate the magnitude of the bed shear-stresses in the scour hole along the plane of symmetry.

A 3D flow establishes around the cylinder, being characterized principally by a clock-wise circulating flow inside the scour hole (see Fig. 3.2). This structure, known as a horseshoe vortex, was detected particularly in the plane of symmetry upstream of the cylinder. Moving around the cylinder towards downstream, it diminishes and becomes practically undetected on the side plane. Downstream of the cylinder, a flow reversal towards the surface was observed, being pronounced in the close vicinity of the cylinder. It gradually disappears as the flow moves away from the cylinder and returns back towards the uni-directional flow condition.

The velocity field outside the scour hole, i.e. in the upper layer above the original bed, is dominated by the longitudinal velocity component; only at the vicinity of the cylinder the transverse and, notably, the vertical velocity components are important (see Fig. 3.1). The flow direction of the approach flow passing the cylinder remains much the same. The effect of the cylinder in deflecting the approach flow is limited to regions close to the cylinder and in the scour hole.

The vertical velocity component, which primarily manifests itself as a downward velocity particularly along the cylinder face, was separately investigated. Its spatial variation around the cylinder was found to have a particular characteristic. Along the cylinder face its maximum values fall at 40% of the local flow depth (see Fig. 3.6) irrespective of the angular direction.

Presented in Fig. 3.13 are the measured flow pattern, showing the velocity components, (u_r,w), in different planes around the cylinder, whereas in Fig. 3.14 are the corresponding main velocity components, (u,w), in those planes. It can be clearly seen the uni-directional flow experiencing an alteration due to the cylinder and the scour hole, becoming a three-dimensional one. This alteration is notably observed in the region close to the cylinder and inside the scour hole. Outside the scour hole, the flow pattern is mainly dominated by the longitudinal velocity components.

The intensity of turbulence inside the scour hole is strong; an increasing turbulence was detected approaching the cylinder and moving around the cylinder towards downstream. In the wake region, where a separation evidenced by a flow reversal takes place, the turbulence attains its strongest intensity (see Fig. 3.9). The kinetic energy of the flow inside the scour hole, where a rotating flow is eminent, consists of high turbulent energy

(see Fig. 3.10 and Fig. 3.11), ranging from 10% to 90% of the total kinetic energy. The profiles of the turbulent kinetic energy are characterized by distinguishable bulges below the original bed level (see Fig. 3.10).

The longitudinal distribution of the bed shear-stresses along the plane of symmetry shows that the bed shear-stress is reduced upon entering the scour hole when compared to its value in the approach flow (see Fig. 3.12). The shear stress along the upstream scour bed has negative values corresponding to the flow reversal in that region. These observations are supported by the numerical simulation; this will be discussed in Chapter 5.

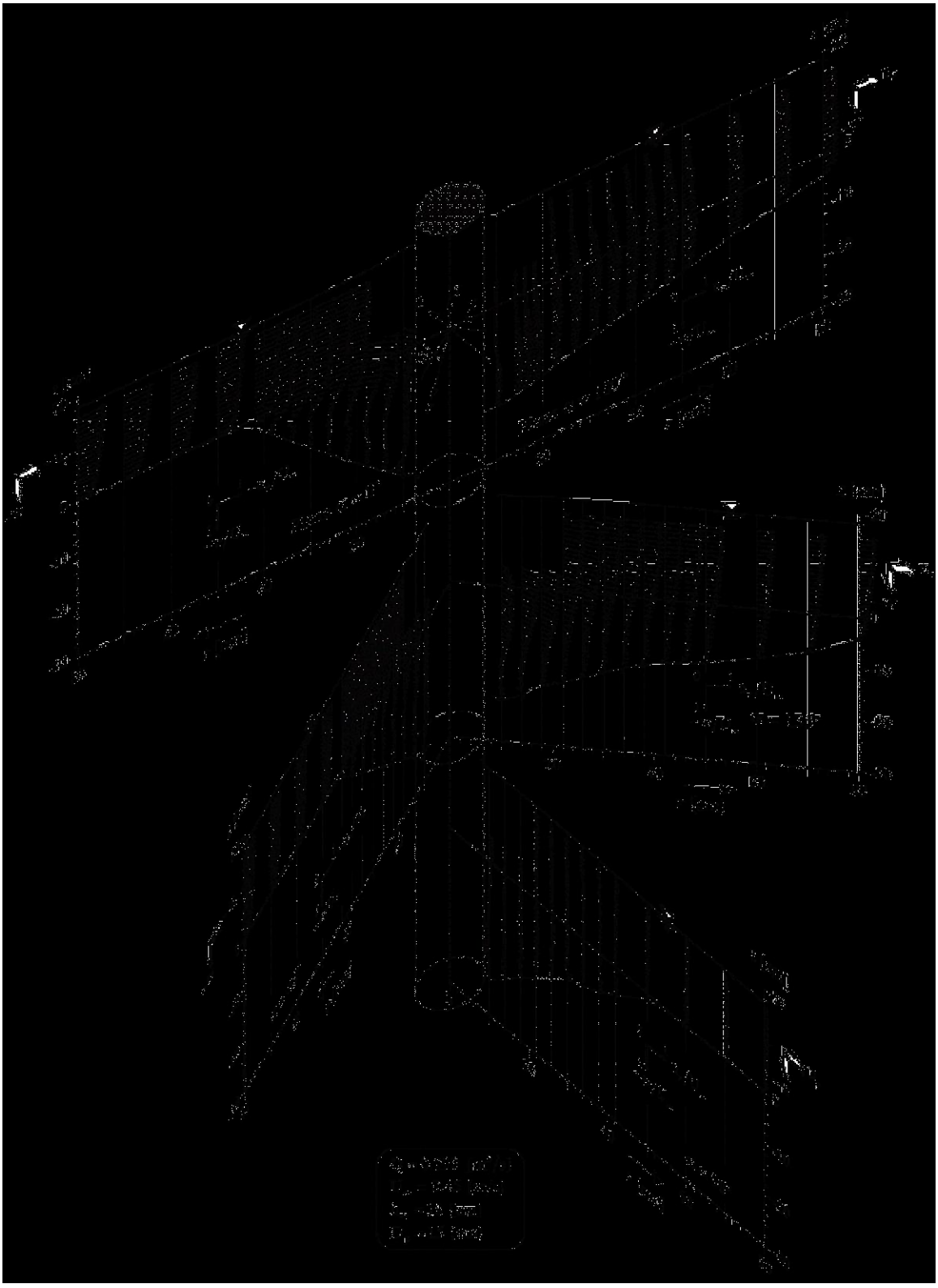

Fig. 3.13 Axonometric presentation of the flow pattern, showing the velocity components, (u_r,w), measured around the cylinder.

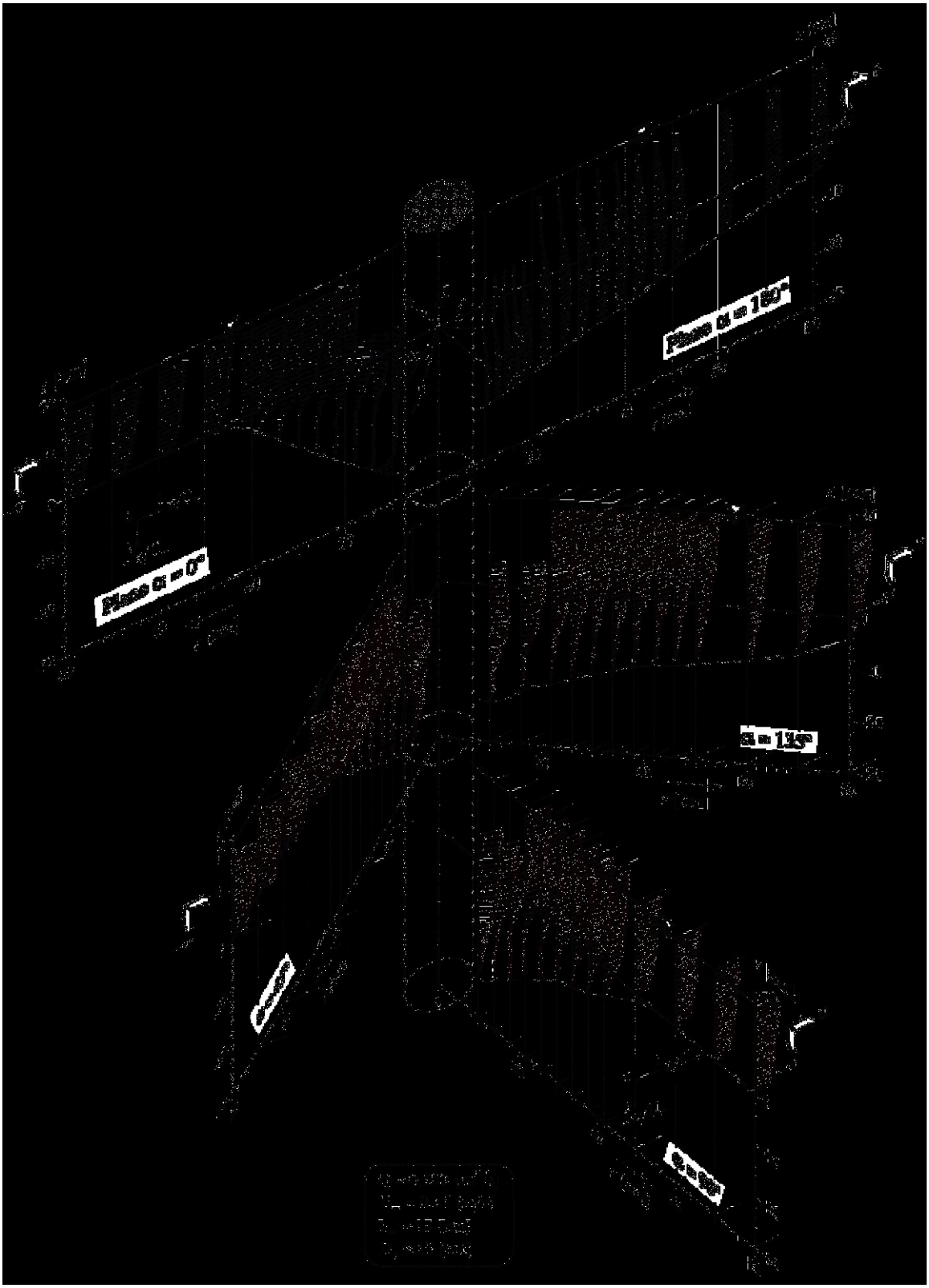

Fig. 3.14 Axonometric presentation of the flow pattern, showing the main velocity components, (u,w), measured around the cylinder.

References

Ahmed, F., and Rajaratnam, N. (1997). "The three-dimensional turbulent boundary layer flow around bridge piers." *IAHR, J. Hydr. Res.*, 35(2), 209-224.

Ahmed, F., and Rajaratnam, N. (1998). "Flow around bridge piers." *ASCE, J. Hydr. Engrg.*, 124(3), 288-300.

Dey, S. (1997). "Local scour at piers, part I: a review of developments of research." *IRTCES, Int. J. Sediment Res.*, 12(2), 23-44.

Dey, S., Bose, S. K., and Sastry, G. L. N. (1995). "Clear water scour at circular piers: a model." *ASCE, J. Hydr. Engrg.*, 121(12), 869-876.

Etheridge, D. W., and Kemp, P. H. (1978). "Measurements of turbulent flow downstream of a rearward-facing step." *J. Fluid Mech.*, 86(3), 545-566.

Graf, W. H., and Altinakar, M. S. (1998). *Fluvial Hydraulics*., John Wiley & Sons, Ltd., Chichester, England.

Graf, W. H., and Yulistiyanto, B. (1998). "Experiments on flow around a cylinder; the velocity and vorticity fields." *IAHR, J. Hydr. Res.*, 36(4), 637-653.

Kobayashi, T., Aibara, T., and Harada, H. (1997). "Vorticity distribution of horseshoe vortex on scoured bed." *Proc. 27th Congress of the IAHR*, San Francisco, California, Theme A, 202-207.

Melville, B. W., and Raudkivi, A. J. (1977). "Flow characteristics in local scour at bridge piers." *ASCE, J. Hydr. Engrg.*, 15(4), 373-380.

Nakagawa, H., and Nezu, I. (1987). "Experimental investigation on turbulent structure of backward-facing step flow in an open channel." *IAHR, J. Hydr. Res.*, 25(12), 67-88.

Yulistiyanto, B. (1997). *Flow around a cylinder installed in a fixed-bed open channel*., *Doctoral Dissertation*, No. 1631, EPFL, Lausanne, Switzerland.

Notations

C	$[m^{1/2}/s]$	Chezy coefficient.
c_μ	[–]	k-ε model constant, $c_\mu = 0.09$.
D_p	[m]	diameter of cylinder $D_p = 0.15$ [m].
d_{50}	[m]	mean diameter of sediment, $d_{50} = 2.1\times10^{-3}$ [m].
$\mathcal{E}$	[–]	bed roughness coefficient.
ε	$[m^2/s^3]$	kinetic energy dissipation.
g	$[m/s^2]$	gravitational acceleration, $g = 9.81$ $[m/s^2]$.
h, h_∞	[m]	flow depth, flow depth in the far-field approach flow.
K	$[m^2/s^2]$	mean-flow kinetic energy.
k	$[m^2/s^2]$	turbulent kinetic energy.
n	[m]	normal axis.
r	[m]	radial direction.

U, U_∞	[m/s]	sectional average velocity.
U_∞	[m/s]	average velocity in the approach flow, $U_\infty = 0.45$ [m/s].
u, v, w	[m/s]	Cartesian velocity components.
u', v', w'	[m/s]	Cartesian fluctuating velocity components.
u_r, u_α	[m/s]	cylindrical (radial and tangential) velocity components.
u_*	[m/s]	shear velocity.
$u_{*,\infty}$	[m/s]	shear velocity in the approach flow, $u_{*,\infty} = 0.45$ [m/s].
V, V_α, V_h	[m/s]	velocity, velocity projection on a plane α., velocity projection on a horizontal plane.
V_t	[m/s]	velocity component parallel to the bed at a distance δ_n.
x, y, z	[m]	Cartesian coordinate directions.
α	[°]	angular direction.
β	[°]	deviation angle of the v-velocity component with respect to the plane of symmetry.
δ_n	[m]	normal distance from the bed.
κ	[–]	Karman constant, $\kappa = 0.4$.
ν, ν_t	[m^2/s]	kinematic viscosity, turbulent eddy viscosity.
ω	[1/s]	vorticity.
Θ	[°]	slope of the inclined scour bed.
θ	[°]	angular direction.
ρ	[kg/m^3]	density of water.
τ, τ_o	[N/m^2]	shear stress, bed shear-stress.
ξ	[m]	rotated x-axis.

Chapter 4

4 Numerical Model Development

Abstract

Presented in this chapter is the development of a 3D numerical model intended to simulate flow around a cylinder. The model is based on the Reynolds-averaged Navier-Stokes and continuity equations for incompressible flow, closed with the k-ε turbulence model. The working equation of the model is obtained by discretizing the governing equations, written in a general convective-diffusive transport equation, using finite-volume techniques on a structured, collocated, boundary-fitted, hexahedral control-volume grid. The hybrid (*Spalding*, 1972) or power-law (*Patankar*, 1980) upwind-central difference scheme, combined with the deferred correction method (*Ferziger and Peric*, 1997), is employed in the discretisation of the governing equations. The solution of the working equation is achieved by an iterative method according to SIMPLE algorithm (*Patankar and Spalding*, 1972). Along solid boundaries, use is made of the wall function method, while along surface boundaries the pressure defect is used to define the surface position. On other boundaries, namely inlet, outlet, and symmetry boundaries, classical methods are used, such as zero gradients, zero stresses, or known functions.

Résumé

Ce chapitre présente un développement d'un modèle numérique pour simuler l'écoulement tridimensionnel autour d'un cylindre. Le modèle est basée sur la représentation en volumes finis des équations de Reynolds, de continuité et de k-ε. Les équations, sous forme d'une équation de transport, sont en suite formulées pour un maillage structuré dont les variables primitives sont définies au centre des volumes de contrôle. Les flux convectif et diffusif sont calculés par les méthodes *hybride* (*Spalding*, 1972) ou *loi de puissance* (*Patankar*, 1980) avec des corrections des termes non orthogonaux (*Ferziger and Peric*, 1997). Le modèle utilise la méthode itérative de SIMPLE pour résoudre les équations de travail ainsi obtenues. Les conditions aux bords le long d'une parois sont imposées par la loi logarithmique. La surface d'eau est déterminée à partir des pressions résiduelles dans les cellules de surface. En autres tipes des bords, par exemple à l'entré, à la sortie et aux plans de symétrie, des méthodes standards sont appliquées soit des gradients nuls, sans cisaillement ou des valeurs connues.

4.1 Governing equations

The flow model that is developed in this work is based on the approximate solution of the time-averaged equations of motion and continuity for incompressible flows by using finite-volume method. In the Cartesian coordinate system these equations read:

$$\frac{\partial u}{\partial t}+\frac{\partial uu}{\partial x}+\frac{\partial vu}{\partial y}+\frac{\partial wu}{\partial z}=-\frac{1}{\rho}\frac{\partial p}{\partial x}+\frac{1}{\rho}\frac{\partial \tau_{xx}}{\partial x}+\frac{1}{\rho}\frac{\partial \tau_{yx}}{\partial y}+\frac{1}{\rho}\frac{\partial \tau_{zx}}{\partial z}+g_x \tag{4.1}$$

$$\frac{\partial v}{\partial t}+\frac{\partial uv}{\partial x}+\frac{\partial vv}{\partial y}+\frac{\partial wv}{\partial z}=-\frac{1}{\rho}\frac{\partial p}{\partial y}+\frac{1}{\rho}\frac{\partial \tau_{xy}}{\partial x}+\frac{1}{\rho}\frac{\partial \tau_{yy}}{\partial y}+\frac{1}{\rho}\frac{\partial \tau_{zy}}{\partial z}+g_y \tag{4.2}$$

$$\frac{\partial w}{\partial t}+\frac{\partial uw}{\partial x}+\frac{\partial vw}{\partial y}+\frac{\partial ww}{\partial z}=-\frac{1}{\rho}\frac{\partial p}{\partial z}+\frac{1}{\rho}\frac{\partial \tau_{xz}}{\partial x}+\frac{1}{\rho}\frac{\partial \tau_{yz}}{\partial y}+\frac{1}{\rho}\frac{\partial \tau_{zz}}{\partial z}+g_z \tag{4.3}$$

$$\frac{\partial u}{\partial x}+\frac{\partial v}{\partial y}+\frac{\partial w}{\partial z}=0 \tag{4.4}$$

in which x, y, and z are Cartesian co-ordinates in the horizontal, transversal, and vertical, respectively; u, v, and w are the corresponding (time-averaged) velocity components, p is the (time-averaged) pressure, ρ is the mass density of water, g_x, g_y, g_z are the x, y , z components of the gravitational acceleration, and τ_{ij}'s are the j direction components of the shear stress acting on the surface normal to the i direction. These stresses are due to the molecular viscosity and turbulent fluctuation. For flows having sufficiently high Reynolds number, the viscous stresses are much smaller in comparison with those of the turbulence and thus can be neglected. Using Boussinesq's eddy viscosity concept, these stresses are proportional to the velocity gradients according to the following expressions (see *Rodi*, 1984, p. 10):

$$\begin{aligned}
\frac{\tau_{xx}}{\rho}&=\nu_t 2\frac{\partial u}{\partial x}-\tfrac{2}{3}k, & \frac{\tau_{xy}}{\rho}&=\frac{\tau_{yx}}{\rho}=\nu_t\left(\frac{\partial v}{\partial x}+\frac{\partial u}{\partial y}\right),\\
\frac{\tau_{yy}}{\rho}&=\nu_t 2\frac{\partial v}{\partial y}-\tfrac{2}{3}k, & \frac{\tau_{xz}}{\rho}&=\frac{\tau_{zx}}{\rho}=\nu_t\left(\frac{\partial w}{\partial x}+\frac{\partial u}{\partial z}\right),\\
\frac{\tau_{zz}}{\rho}&=\nu_t 2\frac{\partial w}{\partial z}-\tfrac{2}{3}k, & \frac{\tau_{yz}}{\rho}&=\frac{\tau_{zy}}{\rho}=\nu_t\left(\frac{\partial w}{\partial y}+\frac{\partial v}{\partial z}\right).
\end{aligned} \tag{4.5}$$

in which ν_t is the turbulent or eddy viscosity and k is the turbulent kinetic energy defined as $k=\frac{1}{2}\left(\overline{u'u'}+\overline{v'v'}+\overline{w'w'}\right)$ where superscripts mean the fluctuating components. Inserting the definitions in Eq. 4.5 into the momentum equations, Eqs. 4.1 to 4.3, one obtains:

$$\frac{\partial u}{\partial t}+\frac{\partial uu}{\partial x}+\frac{\partial vu}{\partial y}+\frac{\partial wu}{\partial z}=-\frac{1}{\rho}\frac{\partial p}{\partial x}-\frac{2}{3}\frac{\partial k}{\partial x}$$
$$+\frac{\partial}{\partial x}\nu_t 2\left(\frac{\partial u}{\partial x}\right)+\frac{\partial}{\partial y}\nu_t\left(\frac{\partial v}{\partial x}+\frac{\partial u}{\partial y}\right)+\frac{\partial}{\partial z}\nu_t\left(\frac{\partial w}{\partial x}+\frac{\partial u}{\partial z}\right)+g_x$$

$$\frac{\partial v}{\partial t}+\frac{\partial uv}{\partial x}+\frac{\partial vv}{\partial y}+\frac{\partial wv}{\partial z}=-\frac{1}{\rho}\frac{\partial p}{\partial y}-\frac{2}{3}\frac{\partial k}{\partial y}$$
$$+\frac{\partial}{\partial x}\nu_t\left(\frac{\partial v}{\partial x}+\frac{\partial u}{\partial y}\right)+\frac{\partial}{\partial y}\nu_t 2\left(\frac{\partial v}{\partial y}\right)+\frac{\partial}{\partial z}\nu_t\left(\frac{\partial w}{\partial y}+\frac{\partial v}{\partial z}\right)+g_y$$

$$\frac{\partial w}{\partial t}+\frac{\partial uw}{\partial x}+\frac{\partial vw}{\partial y}+\frac{\partial ww}{\partial z}=-\frac{1}{\rho}\frac{\partial}{\partial z}-\frac{2}{3}\frac{\partial k}{\partial z}$$
$$+\frac{\partial}{\partial x}\nu_t\left(\frac{\partial w}{\partial x}+\frac{\partial u}{\partial z}\right)+\frac{\partial}{\partial y}\nu_t\left(\frac{\partial w}{\partial y}+\frac{\partial v}{\partial z}\right)+\frac{\partial}{\partial z}\nu_t 2\left(\frac{\partial w}{\partial z}\right)+g_z$$

Separating the normal and cross second-derivatives and putting the former on the left-hand sides, one gets:

$$\frac{\partial u}{\partial t}+\frac{\partial uu}{\partial x}+\frac{\partial vu}{\partial y}+\frac{\partial wu}{\partial z}-\frac{\partial}{\partial x}\left(\nu_t\frac{\partial u}{\partial x}\right)-\frac{\partial}{\partial y}\left(\nu_t\frac{\partial u}{\partial y}\right)-\frac{\partial}{\partial z}\left(\nu_t\frac{\partial u}{\partial z}\right)=-\frac{1}{\rho}\frac{\partial p}{\partial x}$$
$$+\frac{\partial}{\partial x}\left(\nu_t\frac{\partial u}{\partial x}\right)+\frac{\partial}{\partial y}\left(\nu_t\frac{\partial v}{\partial x}\right)+\frac{\partial}{\partial z}\left(\nu_t\frac{\partial w}{\partial x}\right)+g_x \tag{4.6}$$

$$\frac{\partial u}{\partial t}+\frac{\partial uv}{\partial x}+\frac{\partial vv}{\partial y}+\frac{\partial wv}{\partial z}-\frac{\partial}{\partial x}\left(\nu_t\frac{\partial v}{\partial x}\right)-\frac{\partial}{\partial y}\left(\nu_t\frac{\partial v}{\partial y}\right)-\frac{\partial}{\partial z}\left(\nu_t\frac{\partial v}{\partial z}\right)=-\frac{1}{\rho}\frac{\partial p}{\partial y}$$
$$+\frac{\partial}{\partial x}\left(\nu_t\frac{\partial u}{\partial y}\right)+\frac{\partial}{\partial y}\left(\nu_t\frac{\partial v}{\partial y}\right)+\frac{\partial}{\partial z}\left(\nu_t\frac{\partial w}{\partial y}\right)+g_y \tag{4.7}$$

$$\frac{\partial w}{\partial t}+\frac{\partial uw}{\partial x}+\frac{\partial vw}{\partial y}+\frac{\partial ww}{\partial z}-\frac{\partial}{\partial x}\left(\nu_t\frac{\partial w}{\partial x}\right)-\frac{\partial}{\partial y}\left(\nu_t\frac{\partial w}{\partial y}\right)-\frac{\partial}{\partial z}\left(\nu_t\frac{\partial w}{\partial z}\right)=-\frac{1}{\rho}\frac{\partial p}{\partial z}$$
$$+\frac{\partial}{\partial x}\left(\nu_t\frac{\partial u}{\partial z}\right)+\frac{\partial}{\partial y}\left(\nu_t\frac{\partial v}{\partial z}\right)+\frac{\partial}{\partial z}\left(\nu_t\frac{\partial w}{\partial z}\right)+g_z \tag{4.8}$$

The second to fourth terms on the left-hand side of Eqs. 4.6 to 4.8 represent a convective transport and the next three terms represent a diffusive transport. The terms on the right-hand side are considered as sources and are treated as known quantities when solving the equations for the velocity components u, v, and w. The turbulent kinetic energy gradient, being small compared to the pressure gradient, is neglected.

From the k-ε turbulence model (*Launder and Spalding*, 1974; *Rodi*, 1984, p. 27), the turbulent viscosity, ν_t, is given by:

$$\nu_t = c_\mu \frac{k^2}{\varepsilon} \tag{4.9}$$

where ε is the dissipation of the turbulent kinetic energy. The field distributions of the turbulent kinetic energy and its dissipation are obtained from the following transport equations (*Launder and Spalding*, 1974; *Rodi*, 1984, p. 28):

$$\frac{\partial k}{\partial t} + \frac{\partial uk}{\partial x} + \frac{\partial vk}{\partial y} + \frac{\partial wk}{\partial z} - \frac{\partial}{\partial x}\left(\frac{\nu_t}{\sigma_k}\frac{\partial k}{\partial x}\right) - \frac{\partial}{\partial y}\left(\frac{\nu_t}{\sigma_k}\frac{\partial k}{\partial y}\right) - \frac{\partial}{\partial z}\left(\frac{\nu_t}{\sigma_k}\frac{\partial k}{\partial z}\right) = G - \varepsilon \tag{4.10}$$

$$\frac{\partial \varepsilon}{\partial t} + \frac{\partial u\varepsilon}{\partial x} + \frac{\partial v\varepsilon}{\partial y} + \frac{\partial w\varepsilon}{\partial z} - \frac{\partial}{\partial x}\left(\frac{\nu_t}{\sigma_\varepsilon}\frac{\partial \varepsilon}{\partial x}\right) - \frac{\partial}{\partial y}\left(\frac{\nu_t}{\sigma_\varepsilon}\frac{\partial \varepsilon}{\partial y}\right) - \frac{\partial}{\partial z}\left(\frac{\nu_t}{\sigma_\varepsilon}\frac{\partial \varepsilon}{\partial z}\right) = \frac{\varepsilon}{k}\left(c_1 G - c_2 \varepsilon\right) \tag{4.11}$$

in which G is the production of kinetic-energy given by:

$$\begin{aligned} G = \nu_t \Bigg\{ & 2\left(\frac{\partial u}{\partial x}\right)^2 + \left(\frac{\partial u}{\partial y} + \frac{\partial v}{\partial x}\right)\frac{\partial u}{\partial y} + \left(\frac{\partial u}{\partial z} + \frac{\partial w}{\partial x}\right)\frac{\partial u}{\partial z} + \left(\frac{\partial v}{\partial x} + \frac{\partial u}{\partial y}\right)\frac{\partial v}{\partial x} + 2\left(\frac{\partial v}{\partial y}\right)^2 \\ & + \left(\frac{\partial v}{\partial z} + \frac{\partial w}{\partial y}\right)\frac{\partial v}{\partial z} + \left(\frac{\partial w}{\partial x} + \frac{\partial u}{\partial z}\right)\frac{\partial w}{\partial x} + \left(\frac{\partial w}{\partial y} + \frac{\partial v}{\partial z}\right)\frac{\partial w}{\partial y} + 2\left(\frac{\partial w}{\partial z}\right)^2 \Bigg\} \end{aligned} \tag{4.12}$$

The model coefficients c_μ, c_1, c_2, σ_k, and σ_ε contained in the above transport equations are assumed to be constant and take the values given in Table 4.1 (*Launder and Spalding*, 1974; *Rodi*, 1984, p. 29).

Table 4.1 Values of coefficients in k-ε model.

c_μ	c_1	c_2	σ_k	σ_ε
0.09	1.44	1.92	1.0	1.3

It is more convenient to cast the continuity equation, Eq. 4.4, the momentum equations, Eqs. 4.6 to 4.8, and the transport equations of k and ε, Eqs. 4.10 and 4.11, into a general transport equation (*Versteeg and Malalasekera*, 1995, p. 25):

$$\frac{\partial \phi_\square}{\partial t} + \nabla\left(\phi_\square \vec{\mathbf{V}}\right) - \nabla\left(\Gamma_\square \vec{\nabla}\phi_\square\right) = R_\square \tag{4.13}$$

In the above equations, $\phi_\square$ is any dependent scalar variable, $\vec{\mathbf{V}}$ is the velocity vector, $\Gamma_\square$ is the diffusion coefficient, and $R_\square$ is a column matrix of scalar sources (see its definition in Table 4.2). Integrating this equation over a three-dimensional discrete control volume yields (*Versteeg and Malalasekera*, 1995, p. 25):

$$\frac{\partial}{\partial t}\iiint_\forall \phi_\square \, d\forall + \iiint_\forall \nabla\left(\phi_\square \vec{\mathbf{V}}\right) d\forall - \iiint_\forall \nabla\left(\Gamma_\square \vec{\nabla}\phi_\square\right) d\forall = \iiint_\forall R_\square \, d\forall \tag{4.14}$$

The volume integrals of the convective and diffusive terms, the second and third terms on the left-hand side, can be expressed as integral over the closed surface bounding the control volume by applying Gauss divergence theorem (*Versteeg and Malalasekera*, 1995, p. 26; *Hirsch*, 1988, p. 241):

$$\frac{\partial}{\partial t}\iiint_{\forall}\phi\,d\forall+\oiint_S\phi\,\vec{\mathbf{V}}\cdot d\vec{\mathbf{S}}-\oiint_S\Gamma\,\vec{\nabla}\phi\cdot d\vec{\mathbf{S}}=\iiint_{\forall}R\,d\forall \qquad (4.15)$$

where $\vec{\mathbf{S}}$ is the surface vector normal outward to the control volume $d\forall$.

Table 4.2 Terms in the general transport equation, Eq. 4.13.

$$\frac{\partial\phi}{\partial t}+\nabla\left(\phi\,\vec{\mathbf{V}}\right)-\nabla\left(\Gamma\,\vec{\nabla}\phi\right)=R \qquad (4.13)$$

	ϕ	Γ	R
1	u	ν_t	$-\frac{1}{\rho}\frac{\partial p}{\partial x}+\frac{\partial}{\partial x}\left(\nu_t\frac{\partial u}{\partial x}\right)+\frac{\partial}{\partial y}\left(\nu_t\frac{\partial v}{\partial x}\right)+\frac{\partial}{\partial z}\left(\nu_t\frac{\partial w}{\partial x}\right)+g_x$
2	v	ν_t	$-\frac{1}{\rho}\frac{\partial p}{\partial y}+\frac{\partial}{\partial x}\left(\nu_t\frac{\partial u}{\partial y}\right)+\frac{\partial}{\partial y}\left(\nu_t\frac{\partial v}{\partial y}\right)+\frac{\partial}{\partial z}\left(\nu_t\frac{\partial w}{\partial y}\right)+g_y$
3	w	ν_t	$-\frac{1}{\rho}\frac{\partial p}{\partial z}+\frac{\partial}{\partial x}\left(\nu_t\frac{\partial u}{\partial z}\right)+\frac{\partial}{\partial y}\left(\nu_t\frac{\partial v}{\partial z}\right)+\frac{\partial}{\partial z}\left(\nu_t\frac{\partial w}{\partial z}\right)+g_z$
4	1	0	0
5	k	ν_t/σ_k	G-ε
6	ε	ν_t/σ_ε	$c_1\frac{\varepsilon}{k}G-c_2\frac{\varepsilon}{k}\varepsilon$

4.2 Solution strategy: the iterative method

The integral form of the general transport equation, Eq. 4.15, is used to obtain the solution for u, v, w, k, and ε by substituting these variables to the scalar variable ϕ. The solution of the equation is sought at discrete time steps; calculations are performed at every discrete time steps and repeated until a steady-state solution is obtained. The time derivative term in Eq. 4.15 facilitates the application of the model to transient flow problems; in this case, the solution at each discrete time step must converge. When the problems concern steady case ones —as is the case in the present work— the time derivative serves as an iteration loop. In this case the solution at each time step is considered as an intermediate solution, and the end-solution (the steady-state one) is obtained when all variables ϕ's converge. Since the end-solution that is sought, it is not necessary to force the intermediate solution to converge at the same degree of convergence as that of the end-solution. The complete computational procedure is depicted in the flowchart shown in Fig. 4.1. The time loop, from the initial until the

steady-state solution is depicted as the n-iteration. Every variable in the governing equations, Eq. 4.15, is linked to each other since they appear in every equation. To obtain the solution of every variable that satisfies all equations at a time step, an iterative procedure is employed; this is called the m-iteration in Fig. 4.1. The basic idea of the procedure is to consecutively solve the equations for each variable in the order of the momentum, the continuity and the k-ε equations. The momentum equation is solved successively for the u, v, and w components. The order of the computation is not important. The solution of each variable is sought independently, for example when solving the *x*-momentum equation for u, the other variables appearing in that equation, the v, w, k and ε, are assumed as known. When all velocity components are obtained, the pressure is computed through the continuity equation, which in turn will modify the velocity. New solutions of the momentum equation are then necessary. When the velocity and pressure converge, the k-ε equations are solved based on the latest values of the velocity components. The k is solved first and the ε follows. When solving for ε, the latest value of k is used. The procedure is repeated until every variable satisfies all governing equations.

Eq. 4.15, however, cannot be used to obtain directly the pressure. The pressure appears in the momentum equations, but does not have any equation of its own. The fourth equation, the continuity, does not explicitly link the pressure to the velocity. The solution of the pressure is thus not straightforward; some kind of a 'trial-and-correction' procedure is employed. This is indicated as the □-iteration. Firstly, the pressure is estimated and supplied to the momentum equation to get the u, v, and w velocity components. Secondly, the continuity equation is imposed upon those velocities. If the velocities do not satisfy the continuity equation, the velocities and the pressure are then corrected. The corrected pressure is used as the new estimate and the procedure is repeated.

Upon the completion of the □-iteration, the computation continues to the k-ε model. Given the velocity obtained from the □-iteration, the k-ε equations are solved consecutively, and the eddy-viscosity is subsequently obtained. A check is carried out to all new variables ϕ's. If each ϕ satisfies all the governing equations, those variables are regarded as the values at the new time step, otherwise the computation goes back to the solution of the momentum equation (the m-iteration).

The surface boundary which determines the computational domain but its position is part of the solution, is handled at the n-iteration and kept constant during the m-iterations. Thus the positioning of the free surface is carried out explicitly. At the end of the m-iteration, the water surface is moved according to the pressure defect at the surface. This in turn will change the computational domain for the new time of the n-iteration.

The overall procedure thus involves three blocks of iteration. The first iteration block is to get solution of the velocity and pressure, i.e. solving the momentum equations and imposing the continuity. The second block solves the momentum, continuity, and k-ε equations within a time step. The last block is the time marching iteration to get the steady-state solution.

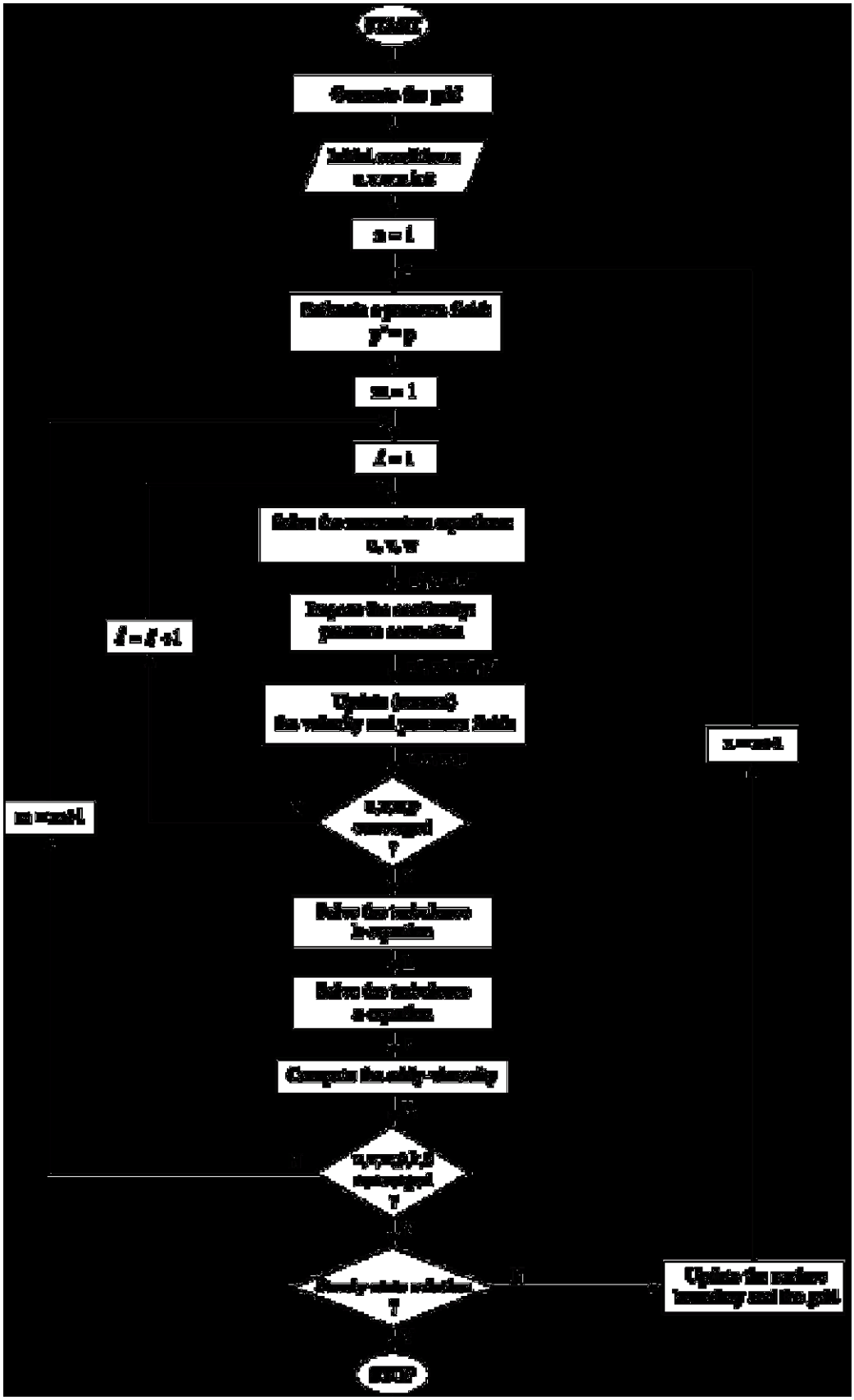

Fig. 4.1 Overall iterative procedure of the solution of Eq. 4.15.

4.3 Numerical method: the finite-volume approximation

4.3.1 Grid arrangement

The approximation to the solution of Eq. 4.15 is sought by finite-volume approach. The computational domain is discretized in a 3D grid having a finite number of control volumes (cells); the integration is then carried out in each cell. A non-orthogonal hexahedron cell is selected in the present model. A typical one is shown in Fig. 4.2. A *cell* is identified by its center, **P**, which makes up the *node* where the dependent variable is to be defined. A cell has six neighbors, named according to their respective compass directions, being the **E**ast, **W**est, **N**orth, **E**ast, **T**op, and **B**ottom. The cell faces are identified at the face center and named with lower-case letters, namely the **e**, **w**, **n**, **s**, **t**, and **b**. The Cartesian coordinate system is selected for describing both the geometrical and flow properties, being the *z* axis defines the bottom-to-top direction.

It is to be noted, however, that the grid in this model is selected such that the cell faces e, w, n, and s are parallel to the *z* axis. This choice is taken to facilitate the handling of the surface boundary. The discretisation of the governing equation, nevertheless, is carried out for general non-orthogonal cells.

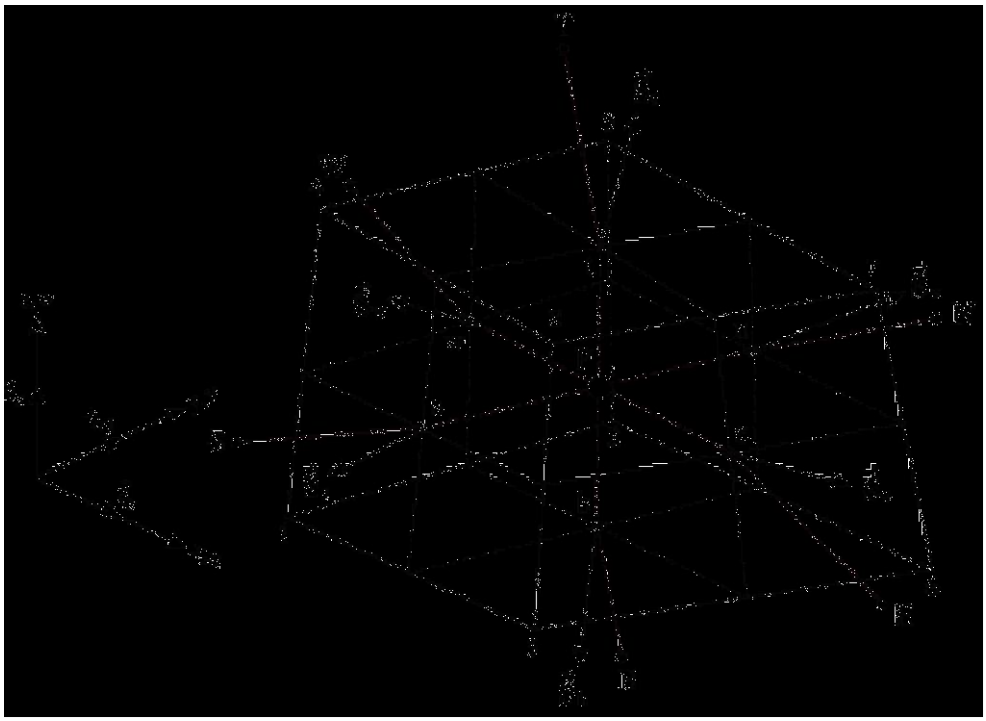

Fig. 4.2 Typical hexahedron control volume.

The dependent variables, ϕ (u,v,w,p,k,ε), are defined at the cell center P, thus constituting a *cell-centered non-staggered grid*. Non-staggered grid variable arrangements may yield a problem of pressure-velocity decoupling that creates a spurious oscillation in the solution. This problem does not exist with the use of staggered grid. However, staggered grids require separate control volumes for the velocity and other dependent variables that

increase the computer storage requirement. For flows with three-dimensional geometry, the storage space required for additional control volumes is enormous. In addition, the non-orthogonality of the cells gives another complexity since the velocity components are not related to the alignment of the cell face. This makes the non-staggered grid is more suitable for 3D problems. To avoid the problem of pressure-velocity decoupling, use is made of the interpolation method according to Rhie and Chow (*Rhie and Chow*, 1983). This method consists of determining the convective velocities on a non-staggered grid through the use of the discretized momentum equation, thus coupling the pressure field with the velocity field. The standard method for staggered grids, the SIMPLE (*Patankar and Spalding*, 1972), is then used to correct the pressure. The SIMPLE, an acronym for Semi-Implicit Method for Pressure-Linked, has been successfully employed for flow computations in two-dimensional problems (*Kobayashi and Pereira*, 1991; *Obi et al.*, 1989; *Ferziger and Peric*, 1997) as well as three-dimensional cases (*Olsen and Kjellesvig*, 1998; *Wu et al.*, 2000). The present model adopts a similar method.

4.3.2 Computation of the surface area and of the cell volume

Cell-face area

The surface vector of the cell faces can be evaluated from the vector products of the diagonals. As can be seen in Fig. 4.3, the area of the east face, quadrilateral 5678, is half of that of parallelogram ABCD built on the diagonals 57 and 68 (note the use of the clockwise convention, seen from the cell center, to index the corners). Hence the surface vector is (*Hirsch*, 1988, p. 247):

$$\vec{\mathbf{S}}_{5678} = \tfrac{1}{2}\vec{\mathbf{S}}_{\mathrm{ABCD}} = \tfrac{1}{2}\begin{bmatrix} \mathbf{e}_x & \mathbf{e}_y & \mathbf{e}_z \\ \Delta x_{57} & \Delta y_{57} & \Delta z_{57} \\ \Delta x_{68} & \Delta y_{68} & \Delta z_{68} \end{bmatrix} = \tfrac{1}{2}\begin{bmatrix} \mathbf{e}_x & \mathbf{e}_y & \mathbf{e}_z \\ (x_7 - x_5) & (y_7 - y_5) & (z_7 - z_5) \\ (x_8 - x_6) & (y_8 - y_6) & (z_8 - z_6) \end{bmatrix} \tag{4.16}$$

When the cell face is not coplanar, the above expression gives the projection area of two triangles sharing a common side 57 or 68. The unit vector normal to a cell face is computed as follows:

$$\mathbf{e}_n = \vec{\mathbf{S}} / \left\| \vec{\mathbf{S}} \right\| \tag{4.17}$$

The normal distance from point P to the east face can then be defined as $\delta_n = \vec{\mathbf{L}}_{\mathrm{Pe}} \cdot (\mathbf{e}_n)_{\mathrm{e}}$, where $\vec{\mathbf{L}}_{\mathrm{Pe}}$ is the vector originating from P to face center e (note that $\vec{\mathbf{L}}_{\mathrm{eP}} = -\vec{\mathbf{L}}_{\mathrm{Pe}}$).

Cell volume

The cell volume is obtained by dividing the hexahedron into six tetrahedrons sharing one common diagonal 17 and one crest 1. Hence with $\vec{\mathbf{L}}_{17} = \vec{\mathbf{L}}_7 - \vec{\mathbf{L}}_1$, where $\vec{\mathbf{L}}_1$ and $\vec{\mathbf{L}}_7$ are the position vectors of 1 and 7, the cell volume is thus:

$$\begin{aligned}\forall_{12345678} &= \forall_{1857} + \forall_{1567} + \forall_{1627} + \forall_{1237} + \forall_{1347} + \forall_{1487} \\ &= \tfrac{1}{6}\left\{\vec{L}_{17}\cdot\left[\left(\vec{L}_{18}\times\vec{L}_{15}\right)+\left(\vec{L}_{15}\times\vec{L}_{16}\right)+\left(\vec{L}_{16}\times\vec{L}_{12}\right)+\right.\right. \\ &\qquad \left.\left.\left(\vec{L}_{12}\times\vec{L}_{13}\right)+\left(\vec{L}_{13}\times\vec{L}_{14}\right)+\left(\vec{L}_{14}\times\vec{L}_{18}\right)\right]\right\}\end{aligned} \tag{4.18}$$

in which $\vec{L}_{mn} = \Delta x_{mn}\mathbf{e}_x + \Delta y_{mn}\mathbf{e}_y + \Delta z_{mn}\mathbf{e}_z = (x_n - x_m)\mathbf{e}_x + (y_n - y_m)\mathbf{e}_y + (z_n - z_m)\mathbf{e}_z$

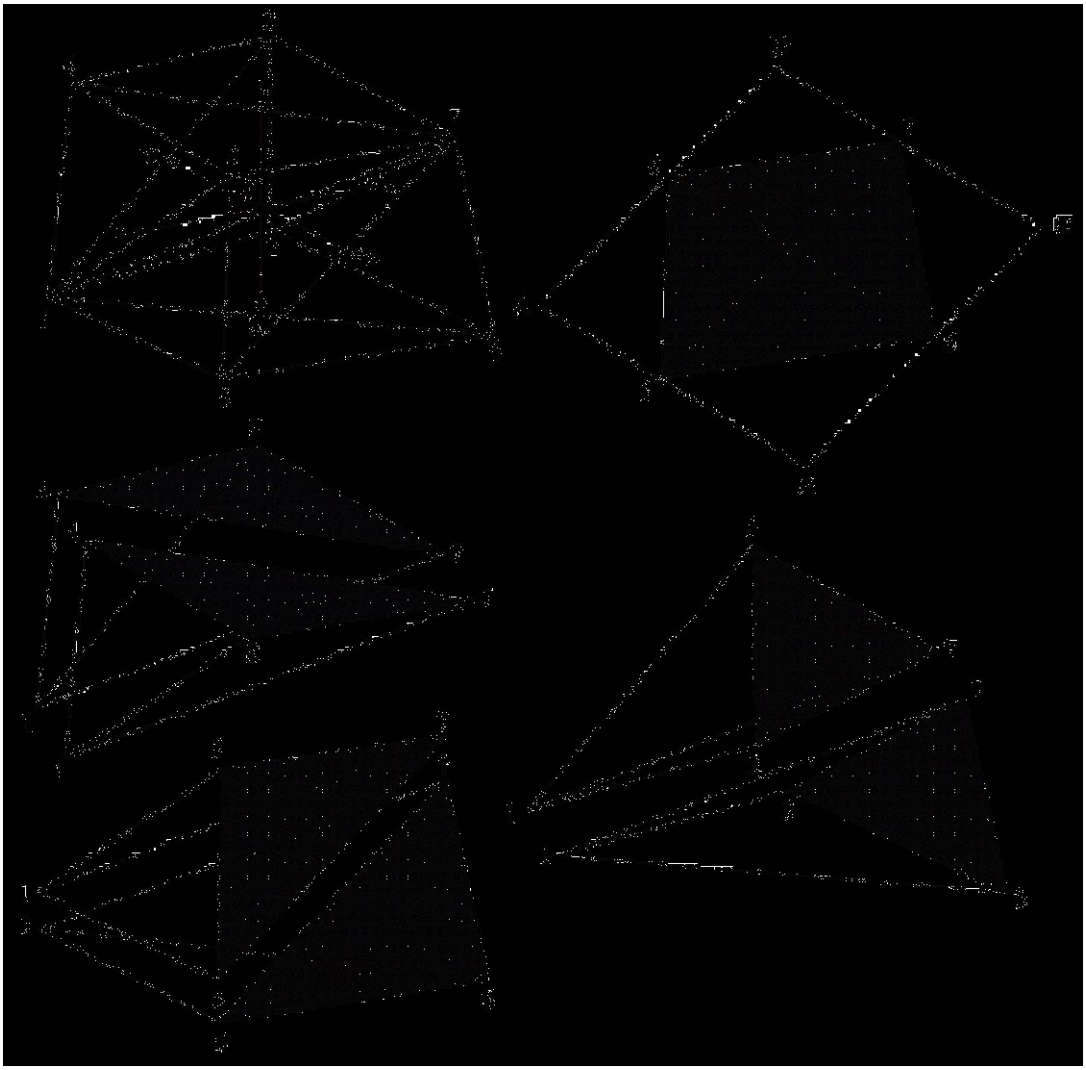

Fig. 4.3 Evaluation of the surface vector and cell volume.

4.3.3 Cell-face interpolation and gradient computation

Cell-face interpolation

Non-staggered grids define all computed variables at the cell centers. When values at the cell face are required, linear interpolation applies. Writing for the east face, the linear interpolation takes the following form:

$$\overline{(\phi)}_e = (1-\beta_e)\phi_P + \beta_e\,\phi_E \tag{4.19}$$

with the interpolation factor β_e defined as: $\beta_e = L_{Pe}/L_{PE}$.

This expression is extensively used in the model, except in two cases, namely (a) when evaluating convective terms by using upwind differences (Sect. 4.3.5), and (b) when computing interpolated coefficients and starred velocities in the pressure-correction equation (Sect. 4.4).

Gradients

The Gauss theorem provides the gradient at the cell center. The gradients along the *x*, *y*, and *z* directions read (*Hirsch*, 1988, p. 253):

$$\begin{aligned}
\left(\frac{\partial\phi}{\partial x}\right)_P &\approx \frac{1}{\forall}\iiint_{\forall}\vec{\nabla}(\phi\,\mathbf{e}_x)\,d\forall = \frac{1}{\forall}\oiint_S \phi\,\mathbf{e}_x\cdot d\vec{\mathbf{S}} \approx \frac{1}{\forall_P}\sum_{cf=ewnstb}(\phi\,S_x)_{cf}\\
\left(\frac{\partial\phi}{\partial y}\right)_P &\approx \frac{1}{\forall}\iiint_{\forall}\vec{\nabla}(\phi\,\mathbf{e}_y)\,d\forall = \frac{1}{\forall}\oiint_S \phi\,\mathbf{e}_y\cdot d\vec{\mathbf{S}} \approx \frac{1}{\forall_P}\sum_{cf=ewnstb}(\phi\,S_y)_{cf}\\
\left(\frac{\partial\phi}{\partial z}\right)_P &\approx \frac{1}{\forall}\iiint_{\forall}\vec{\nabla}(\phi\,\mathbf{e}_z)\,d\forall = \frac{1}{\forall}\oiint_S \phi\,\mathbf{e}_z\cdot d\vec{\mathbf{S}} \approx \frac{1}{\forall_P}\sum_{cf=ewnstb}(\phi\,S_z)_{cf}
\end{aligned} \tag{4.20}$$

The summation extends over the six cell faces, cf: the east, west, north, south, top, and bottom. The dependent variable at the cell face, ϕ_{cf}, is obtained by linear interpolation of the variables at the two intermediate neighboring cell centers (see Eq. 4.19). The same linear interpolation is applied when gradients are needed at the cell face. Using an overbar symbol to denote linear interpolated values, the gradients at the east face read:

$$\begin{aligned}
\overline{\left(\frac{\partial\phi}{\partial x}\right)}_e &= (1-\beta_e)\left(\frac{\partial\phi}{\partial x}\right)_P + \beta_e\left(\frac{\partial\phi}{\partial x}\right)_E\\
\overline{\left(\frac{\partial\phi}{\partial y}\right)}_e &= (1-\beta_e)\left(\frac{\partial\phi}{\partial y}\right)_P + \beta_e\left(\frac{\partial\phi}{\partial y}\right)_E\\
\overline{\left(\frac{\partial\phi}{\partial z}\right)}_e &= (1-\beta_e)\left(\frac{\partial\phi}{\partial z}\right)_P + \beta_e\left(\frac{\partial\phi}{\partial z}\right)_E
\end{aligned} \tag{4.21}$$

4.3.4 Discretisation of the time derivative terms

The (pseudo-) time derivative term serves as a global iteration that embodies the iterative solution procedure as described in Sect. 4.2. The time iteration can be considered as an iteration level marking the progress of the surface computation since the surface boundary is updated at the end of a time step. The solution of Eq.4.15 at a given time step (n-iteration) designates an intermediate solution. The final solution will be achieved when

the iteration converges towards the steady-state solution. For an intermediate solution, a simple first-order finite-difference scheme can be appropriately used to evaluate the time derivative of Eq. 4.15:

$$\frac{\partial}{\partial t}\iiint_{\forall}\phi\,d\forall \approx \frac{\phi^{n+1}-\phi^{n}}{\Delta t}\,\forall^{n} \tag{4.22}$$

The cell volume $\forall$ is explicitly defined at time level n ($\forall^{n}$), since the new geometry of the computational domain is not yet known *a priori*. This applies also to all geometrical parameters such as surface area (S^{n}) and spatial coordinate and distance ($x^{n}, y^{n}, z^{n}, L^{n}$).

In solving Eq. 4.15 for ϕ^{n+1}, iterations have to be carried out to handle the non-linear terms. As shown in Fig. 4.1, there are two iteration loops, the □- and m-iterations, in arriving to ϕ^{n+1} from known values ϕ^{n}. When these iterations converge, that is □ = ∞ and m = ∞, we have $\phi^{n+1}_{\square} = \phi^{n,\square\approx\infty,m\approx\infty}$. Eq. 4.22 thus can be approximated as:

$$\frac{\partial}{\partial t_{\square}}\iiint_{\forall}\phi\,d\forall \approx \frac{\phi^{n+1}-\phi^{n}}{\Delta t}\,\forall^{n} = \frac{\forall^{n,\square+1}}{\Delta t}\left(\phi^{n,\square+1}-\phi^{n,\square+1}\right) \tag{4.23}$$

The variable index □ is used to refer either □- or m-iteration. With this approach, the transport equation, Eq. 4.15, can be rewritten as:

$$\underbrace{\frac{\forall^{n,\square+1}}{\Delta t}\left(\phi^{n,\square+1}-\phi^{n,\square+1}\right)}_{\text{time derivation}} + \underbrace{\left[\oint_{S}\phi\,\vec{V}\cdot d\vec{S}\right]^{n\to n+1}}_{\text{convection}} - \underbrace{\left[\oint_{S}\Gamma\,\vec{\nabla}\phi\cdot d\vec{S}\right]^{n\to n+1}}_{\text{diffusion}} = \underbrace{\left[\iiint_{\forall} R\,d\forall\right]^{n\to n+1}}_{\text{source}} \tag{4.24}$$

The pseudo-time index $n \to n+1$ is introduced to indicate the progress of the iterations n, m, and □, used to evaluate the terms in bracket. Since the geometrical parameters are all evaluated at time level n, the convection-diffusion and the source terms contain explicit terms. The scheme is thus explicit. The pseudo-time step, Δt, is related to the under-relaxation factor used in the iterative procedure of the pressure computation; this will be discussed later in Sect. 4.4.3.

4.3.5 Discretisation of the convective terms

The discrete form of the convective terms in Eq. 4.24 for cell P reads:

$$\left(F^{C}\right)_{P}^{n\to n+1} = \left[\oint_{S}\phi^{\square+1}\left(\vec{V}\right)^{n}\cdot\left(d\vec{S}\right)^{n}\right]_{P} \approx \sum_{cf=ewnstb}\left[\phi^{\square+1}\left(\vec{V}\right)^{n}\cdot\left(\vec{S}\right)^{n}\right]_{cf} \tag{4.25}$$

The usual convention of the summation index applies, that is the summation runs over the six cell faces: the east, west, north, south, top, and bottom. The evaluation of the

convective transport through the east face is elaborated in the following paragraphs and a similar approach applies to the other faces.

$$\left(F_e^C\right)^{n\to n+1} = \left(\phi\,\vec{\mathbf{V}}\cdot\vec{\mathbf{S}}\right)_e^{n\to n+1} = \left(\vec{\mathbf{V}}\cdot\vec{\mathbf{S}}\right)_e^{n\to n+1}\phi_e^{n\to n+1}$$
$$= \left(u_e^{n,i}S_{e,x}^n + v_e^{n,i}S_{e,y}^n + w_e^{n,i}S_{e,z}^n\right)\phi_e^{n,i+1} = q_e^{i}\,\phi_e^{i+1} \tag{4.26}$$

In the above equation, q_e is the discharge (the mass flux per unit mass) *normal* to the east face. For simplicity, the time index 'n' is omitted and the notation q_e^i stands for the discharge obtained from $u_e^{n,i}$ and S_e^n. A linearisation has been applied to the convective term in Eq. 4.26 by setting ϕ as the only unknown while taking the discharge, q_e, explicitly from the previous iteration.

The unknown variable at the east face, ϕ_e, is estimated by using upwind scheme, that is by taking its value at the upstream control volume which depends on the flow direction (*Versteeg and Malalasekera*, 1995, p. 115):

$$\phi_e^{i+1} = \phi_P^{i+1} \text{ if } q_e^i \geq 0, \quad \phi_e^{i+1} = \phi_E^{i+1} \text{ if } q_e^i < 0 \tag{4.27}$$

The convective flux across the east face, Eq. 4.26, is then:

$$\left(F_e^C\right)^{n\to n+1} = \max\left[q_e^i, 0\right]\phi_P^{i+1} - \max\left[-q_e^i, 0\right]\phi_E^{i+1} \tag{4.28}$$

Note that the discharge, q_e, is a scalar product of the velocity and the surface vector and it has a positive sign when leaving the cell. Thus the discharge across the west cell face of cell P is equal to the opposite value of that across the east face of cell W. The same is true for the other cell faces. The discharge across the north or top faces of cell P is equal to the opposite value of that across the south or bottom face of cells N or T, respectively. This property has to be kept in the calculation of the convective flux in order to maintain the flux consistency. The convective flux leaving the cell P across the east face is equal to that entering cell W; otherwise a discrepancy occurs between neighboring cells. The convective flux across the west face thus reads:

$$\left(F_w^C\right)^{n\to n+1} = \max\left[q_w^i, 0\right]\phi_P^{i+1} - \max\left[-q_w^i, 0\right]\phi_W^{i+1} \tag{4.28a}$$

4.3.6 Discretisation of the diffusive terms

The discrete form of the diffusive terms reads in Eq. 4.24 for cell P:

$$\left(F^D\right)^{n\to n+1} = \oiint_S\left[\Gamma\,\vec{\nabla}\phi\cdot d\vec{\mathbf{S}}\right]^{\to n+1} \approx \sum_{cf=ewnstb}\left(\Gamma\,\vec{\nabla}\phi\cdot\vec{\mathbf{S}}\right)_{cf}^{n\to n+1} \tag{4.29}$$

in which the summation extends over the six cell faces and the non-linear terms are linearized as in the evaluation of the convection term. The diffusion across the east face is elaborated and a similar approach applies for the other faces.

In evaluating the diffusive term across the east face, it is convenient to use a *local coordinate system* attached to the east face as shown in Fig. 4.4. Across the east face, Eq. 4.29 reads:

$$\left(F^D\right)_e^{n\to n+1} = \left(\Gamma\,\vec{\nabla}\phi\cdot\vec{S}\right)_e^{n\to n+1} = \Gamma_e^{n,\,n+1}\left(\frac{\partial\phi}{\partial n}\right)_e^{n,\,n+1}\left(\vec{e}_n\cdot\vec{S}\right)_e^{n} \tag{4.30}$$

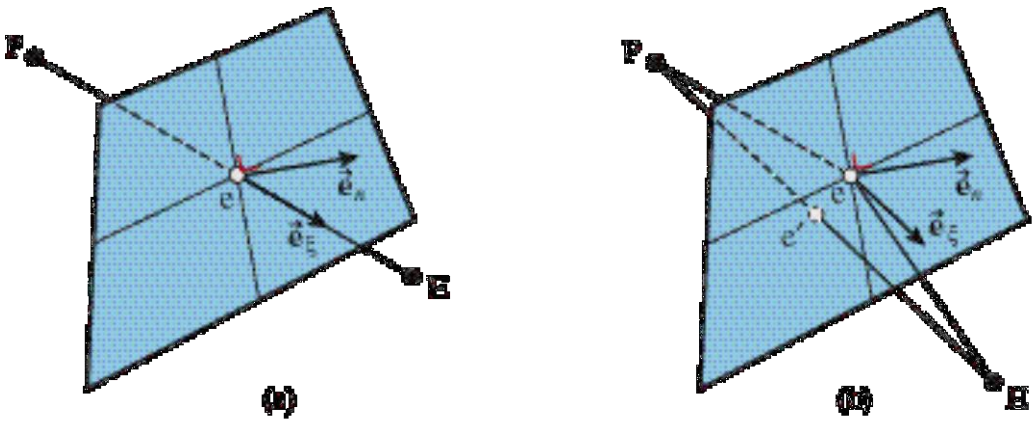

Fig. 4.4 Evaluation of the diffusion terms across the east face

The evaluation of the normal gradient presents some difficulties for its *y* and *z* components. Besides the variable at the neighbor cell E, additional ones at NE, SE, S, and N might have to be taken into consideration. This would increase the number of unknowns. To overcome this problem, the so called *deferred-correction approach* (*Ferziger and Peric*, 1997) is selected in the present model, where only the immediate neighbor cell needs to be considered. In this approach the normal gradient term is evaluated implicitly by a simple approximation and a correction is added. The correction is taken as the difference between the correct and approximate gradients; both are explicitly obtained from the previous iteration. This correction is put in the source terms at the right-hand side. The diffusion term evaluated with this approach reads (*Ferziger and Peric*, 1997, pp. 218-222):

$$\left(F^D\right)_e^{n\to n+1} = \Gamma_e S_e\left(\frac{\partial\phi}{\partial\xi}\right)_e^{n+1} + \Gamma_e S_e\left[\overline{\left(\frac{\partial\phi}{\partial n}\right)}_e^{n} - \overline{\left(\frac{\partial\phi}{\partial\xi}\right)}_e^{n}\right] \tag{4.31}$$

correction, explicit

In the above expression, the time index n is omitted for simplicity and a term without any index refers to the initial solution of the time step $n\to n+1$ (for example S_e is constant

during a time step, $S_e = S_e^{n,\tau=1}$). In the local coordinate, ξ is the direction of a straight line joining P and E (see Fig. 4.4). An approximation is used to evaluate the gradient in the implicit term of Eq. 4.31 where a central difference is used (*Ferziger and Peric*, 1997; p. 224).

$$\left(\frac{\partial\phi}{\partial\xi}\right)_e^{\tau+1} = \frac{\phi_E^{\tau+1} - \phi_P^{\tau+1}}{L_{PE}} \qquad \text{with} \quad L_{PE} = \left\|\vec{\mathbf{L}}_{PE}\right\| \tag{4.32}$$

Substituting this relation to the implicit gradient, the diffusive flux reads:

$$\left(F^D\right)_e^{n\to n+1} = \left(\frac{\Gamma_e S_e}{L_{PE}}\right)\phi_E^{\tau+1} - \left(\frac{\Gamma_e S_e}{L_{PE}}\right)\phi_P^{\tau+1} + \Gamma_e S_e \underbrace{\left[\overline{\left(\frac{\partial\phi}{\partial n}\right)}_e^{\tau} - \overline{\left(\frac{\partial\phi}{\partial\xi}\right)}_e^{\tau}\right]}_{\text{correction, explicit}} \tag{4.33}$$

and for the west face, it reads:

$$\left(F^D\right)_w^{n\to n+1} = \left(\frac{\Gamma_w S_w}{L_{PW}}\right)\phi_W^{\tau+1} - \left(\frac{\Gamma_w S_w}{L_{PW}}\right)\phi_P^{\tau+1} + \Gamma_w S_w \underbrace{\left[\overline{\left(\frac{\partial\phi}{\partial n}\right)}_w^{\tau} - \overline{\left(\frac{\partial\phi}{\partial\xi}\right)}_w^{\tau}\right]}_{\text{correction, explicit}} \tag{4.33a}$$

The explicit parts can be easily obtained since the Cartesian components of the gradient are known from the previous computation.

$$\begin{aligned}
\overline{\left(\frac{\partial\phi}{\partial n}\right)}_e^{\tau} &= \overline{\left(\frac{\partial\phi}{\partial x}\right)}_e^{\tau}\frac{S_{e,x}}{S_e} + \overline{\left(\frac{\partial\phi}{\partial y}\right)}_e^{\tau}\frac{S_{e,y}}{S_e} + \overline{\left(\frac{\partial\phi}{\partial z}\right)}_e^{\tau}\frac{S_{e,z}}{S_e} \\
\overline{\left(\frac{\partial\phi}{\partial\xi}\right)}_e^{\tau} &= \overline{\left(\frac{\partial\phi}{\partial x}\right)}_e^{\tau}\frac{\Delta x_{PE}}{L_{PE}} + \overline{\left(\frac{\partial\phi}{\partial y}\right)}_e^{\tau}\frac{\Delta y_{PE}}{L_{PE}} + \overline{\left(\frac{\partial\phi}{\partial z}\right)}_e^{\tau}\frac{\Delta z_{PE}}{L_{PE}}
\end{aligned} \tag{4.34}$$

Applying Eq. 4.31 to the six cell faces gives 7 unknowns to the diffusion transport term for each computational cell P. Errors due to the use of a simple central difference to obtain diffusion across a cell face, Eq. 4.32, are minimized by the correction given in the explicit part of Eq. 4.31. It shall be nevertheless noted that the error will be magnified when the ξ direction of the cell face is far from its *n*-direction or when the east face center does not coincide with the ξ line (see Fig. 4.4b).

4.3.7 Convective-diffusive terms: hybrid and power-law schemes

The convective upwind scheme, Eq. 4.27, is simple and easy to implement; it accounts for the flow direction. The scheme, however, is first order accurate and produces considerable error when diffusive transport is important. To avoid that problem, the so-called *hybrid scheme* (*Spalding*, 1972) and *power-law scheme* (*Patankar*, 1980) give

formulae which combine the convective and diffusive transports in a special way. Depending on the grid Peclet number Pe, being the ratio of the convective and diffusive conductance, $Pe = q\,L/\Gamma S$ where L is the nodal distance, either the upwind-scheme convection, central-difference diffusion, or combination of the two, is considered to transport any scalar quantity ϕ across a cell face.

The *hybrid scheme* (*Spalding*, 1972) uses the upwind scheme for large Peclet numbers ($|Pe| \geq 2$) and central difference for small Peclet numbers ($|Pe| < 2$). According to this scheme, the total flux across the east face, $F_e = F_e^C - F_e^D$, is defined as follows:

- for $Pe_e = q_e L_{PE}/\Gamma_e S_e < -2$, only the convective transport is taken into account:

$$F_e^{n\to n+1} = q_e\,\phi_E^{n+1} \tag{4.35}$$

- for $-2 \leq Pe_e = q_e L_{PE}/\Gamma_e S_e < 0$, a part of the diffusive transport is also taken into consideration:

$$F_e^{n\to n+1} = q_e\,\phi_E^{n+1} - (1 + 0.5Pe_e)\left\{\frac{\Gamma_e\,S_e}{L_{PE}}\left(\phi_E^{n+1} - \phi_P^{n+1}\right) + \Gamma_e\,S_e\left[\overline{\left(\frac{\partial\phi}{\partial n}\right)}_e^{\,n} - \overline{\left(\frac{\partial\phi}{\partial\xi}\right)}_e^{\,n}\right]\right\} \tag{4.36}$$

- for $0 \leq Pe_e = q_e L_{PE}/\Gamma_e S_e < 2$, a part of the diffusive transport is also taken into consideration:

$$F_e^{n\to n+1} = q_e\,\phi_P^{n+1} - (1 - 0.5Pe_e)\left\{\frac{\Gamma_e\,S_e}{L_{PE}}\left(\phi_E^{n+1} - \phi_P^{n+1}\right) + \Gamma_e\,S_e\left[\overline{\left(\frac{\partial\phi}{\partial n}\right)}_e^{\,n} - \overline{\left(\frac{\partial\phi}{\partial\xi}\right)}_e^{\,n}\right]\right\} \tag{4.37}$$

- for $Pe_e = q_e L_{PE}/\Gamma_e S_e > 2$, only the convective transport is taken into account:

$$F_e^{n\to n+1} = q_e\,\phi_P^{n+1} \tag{4.38}$$

The *power-law scheme* (*Patankar*, 1980, p. 90-91) sets the limiting value of Pe where the diffusion no longer affects the transport at Pe = 10, instead of Pe = 2 used in the hybrid scheme.

- for $Pe_e = q_e L_{PE}/\Gamma_e S_e < -10$:

$$F_e^{n\to n+1} = q_e\,\phi_E^{n+1} \tag{4.39}$$

- for $-10 \leq Pe_e = q_e L_{PE}/\Gamma_e S_e < 0$:

$$F_e^{n\to n+1} = q_e\,\phi_E^{n+1} - (1 + 0.1Pe_e)^5\left\{\frac{\Gamma_e\,S_e}{L_{PE}}\left(\phi_E^{n+1} - \phi_P^{n+1}\right) + \Gamma_e\,S_e\left[\overline{\left(\frac{\partial\phi}{\partial n}\right)}_e^{\,n} - \overline{\left(\frac{\partial\phi}{\partial\xi}\right)}_e^{\,n}\right]\right\} \tag{4.40}$$

- for $0 \le Pe_e = q_e L_{PE}/\Gamma_e S_e < 10$:

$$F_e^{n\to n+1} = q_e \phi_P^{n+1} - (1 - 0.1|Pe_e|)^5 \left\{ \frac{\Gamma_e S_e}{L_{PE}} \left(\phi_E^{n+1} - \phi_P^{n+1} \right) + \Gamma_e S_e \left[\overline{\left(\frac{\partial \phi}{\partial n} \right)}_e - \overline{\left(\frac{\partial \phi}{\partial \xi} \right)}_e \right] \right\} \quad (4.41)$$

- for $Pe_e = q_e L_{PE}/\Gamma_e S_e > 10$:

$$F_e^{n\to n+1} = q_e \phi_P^{n+1} \quad (4.42)$$

Equations 4.35 to 4.42 can be combined into a compact form as follows (*Patankar*, 1980, pp. 94-95):

$$F_e^{n\to n+1} = \max[q_e, 0]\phi_P^{n+1} - \max[-q_e, 0]\phi_E^{n+1} - f_e^D \left\{ \frac{\Gamma_e S_e}{L_{PE}} \left(\phi_E^{n+1} - \phi_P^{n+1} \right) + \Gamma_e S_e \left[\overline{\left(\frac{\partial \phi}{\partial n} \right)}_e - \overline{\left(\frac{\partial \phi}{\partial \xi} \right)}_e \right] \right\} \quad (4.43)$$

where f^D is a factor that depends on the absolute value of grid Peclet number; it has a different form for the hybrid and power-law schemes as shown in Table 4.3.

Table 4.3 Hybrid and power-law scheme diffusion factors.

Scheme	$f^D = f(\|Pe\|) = f(\|qL/\Gamma S\|)$
Hybrid	$\max[(1 - 0.5\|Pe\|), 0]$
Power-law	$\max[(1 - 0.1\|Pe\|)^5, 0]$

Arranging the terms in Eq. 4.43, one has:

$$F_e^{n\to n+1} = \underbrace{\left\{ \max[q_e, 0] + f_e^D \frac{\Gamma_e S_e}{L_{PE}} \right\} \phi_P^{n+1} + \left\{ -\max[-q_e, 0] - f_e^D \frac{\Gamma_e S_e}{L_{PE}} \right\} \phi_E^{n+1}}_{\text{implicit}} - \underbrace{f_e^D \left\{ \Gamma_e S_e \left[\overline{\left(\frac{\partial \phi}{\partial n} \right)}_e - \overline{\left(\frac{\partial \phi}{\partial \xi} \right)}_e \right] \right\}}_{\text{explicit}} \quad (4.43a)$$

and for the west face, the convective-diffusive flux reads:

$$F_w^{n\to n+1} = \underbrace{\left\{ \max\left[q_w^{\square},0\right] + f_w^D \frac{\Gamma_w^{\square} S_w}{L_{PW}} \right\} \phi_P^{\square+1} + \left\{ -\max\left[-q_w^{\square},0\right] - f_w^D \frac{\Gamma_w^{\square} S_w}{L_{PW}} \right\} \phi_W^{\square+1}}_{\text{implicit}}$$

$$\underbrace{-f_w^D \left\{ \Gamma_w^{\square} S_w \left[\overline{\left(\frac{\partial\phi}{\partial n}\right)}_w^{\square} - \overline{\left(\frac{\partial\phi}{\partial\xi}\right)}_w^{\square} \right] \right\}}_{\text{explicit}} \qquad (4.43b)$$

Shorter notations is used to write the expression of the convective-diffusive flux, for example Eq. 4.43a maybe rewritten as $F_e^{n\to n+1} = \left(a_P^C + a_P^D\right)\phi_P^{\square+1} + \left(a_E^C + a_E^D\right)\phi_E^{\square+1} + b_E^D$, in such a way that by summing up the convective-diffusive fluxes across the six faces of cell P, one obtains:

$$F^{n\to n+1} = \left(a_E^C + a_E^D\right)\phi_E^{\square+1} + \left(a_W^C + a_W^D\right)\phi_W^{\square+1} + \left(a_N^C + a_N^D\right)\phi_N^{\square+1} + \left(a_S^C + a_S^D\right)\phi_S^{\square+1} + \left(a_T^C + a_T^D\right)\phi_T^{\square+1} + \left(a_B^C + a_B^D\right)\phi_B^{\square+1} + \left(a_P^C + a_P^D\right)\phi_P^{\square+1} + b^D \qquad (4.44)$$

where the coefficients indicate contribution of convective-diffusive terms from neighboring cells as presented in Table 4.4. The diffusive-correction terms, being evaluated explicitly, are known from the previous iteration and are included in the independent coefficient b^D.

Table 4.4 Coefficients of the discretized convective-diffusive equations.

Convective terms	Diffusive terms
$a_E^C = -\max\left[-q_e^{\square},0\right]$	$a_E^D = -f^D \Gamma_e^{\square} S_e / L_{PE}$
$a_W^C = -\max\left[-q_w^{\square},0\right]$	$a_W^D = -f^D \Gamma_w^{\square} S_w / L_{PW}$
$a_N^C = -\max\left[-q_n^{\square},0\right]$	$a_N^D = -f^D \Gamma_n^{\square} S_n / L_{PN}$
$a_S^C = -\max\left[-q_s^{\square},0\right]$	$a_S^D = -f^D \Gamma_s^{\square} S_s / L_{PS}$
$a_T^C = -\max\left[-q_t^{\square},0\right]$	$a_T^D = -f^D \Gamma_t^{\square} S_t / L_{PT}$
$a_B^C = -\max\left[-q_b^{\square},0\right]$	$a_B^D = -f^D \Gamma_b^{\square} S_b / L_{PB}$
$a_P^C = \sum_{nb=EWNSTB} -a_{nb}^C + \sum_{cf=ewnstb} q_{cf}^{\square}$	$a_P^D = \sum_{nb=EWNSTB} -a_{nb}^D$
—	$b^D = \sum_{cf=ewnstb} -\left(f^D \Gamma^{\square} S\right)_{cf} \left[\overline{\left(\frac{\partial\phi}{\partial n}\right)}_{cf}^{\square} - \overline{\left(\frac{\partial\phi}{\partial\xi}\right)}_{cf}^{\square} \right]$

4.3.8 Source terms

The source terms may consist of scalar quantities, first derivatives, or second derivatives of a scalar quantity. The source, in addition, may also include the time integration term, the diffusion correction, and known variables from the boundary conditions. Sometimes a term initially considered as a source takes advantage to be expressed as a function of the unknown variable at the cell center, such as cells next to a boundary. In that case, the term is linearized which gives (*Versteeg and Malalasekera*, 1995, p. 87):

$$\iiint_{\forall} R \, d\forall \approx \bar{R} \, \forall_P = b + b_P \, \phi_P^{n+1} \tag{4.45}$$

in which b includes all known quantities (either constants, prescribed, or known from previous iteration) and b_P is the coefficient of the unknown variable at P.

Scalar source terms

The source term containing scalar quantities, b^S, comes from the gravity accelerations, g_x, g_y, g_z, or the turbulent energy production and dissipation, G and ε. The scalar source at P represents the average value of those quantities in the cell being considered. It is known and thus is considered as a constant. Therefore, the source terms containing scalar quantities can be easily evaluated according to the following expression:

$$b_{\phi}^{S} = \iiint_{\forall} \phi^{n} \, d\forall = \phi_P^{n} \forall_P \tag{4.46}$$

In applying the above relation to the source terms of the k equation coming from the turbulent energy production, G, some approximations are needed. Writing Eq. 4.46 for G, we have:

$$\iiint_{\forall} G \, d\forall = G_P \, \forall_P$$

Since the G term contains non-linear gradient terms (see Eq. 4.12), the above relation implies that these terms are evaluated individually (that is by using Eq. 4.20). This means that the integral of these terms are computed in the following fashion (an example is given here for the $(\partial u/\partial x)^2$ term):

$$\iiint_{\forall} \left(\frac{\partial u}{\partial x}\right)^2 d\forall = \left(\frac{\partial u}{\partial x}\right)_P^2 \forall_P = \left(\frac{1}{\forall_P} \iiint_{\forall} \frac{\partial u}{\partial x} d\forall\right)^2 \forall_P$$

This approximation, of course, will be inaccurate when the velocity gradient is important. Nevertheless, this method is selected for its easiness to implement.

In the ε equation, the source term is linearized for the term containing ε^2 in the following form:

$$b = c_1 \left(\frac{\varepsilon G}{k}\right)_P \forall_P - c_2 \left(\frac{\varepsilon}{k}\right)_P \forall_P \varepsilon_P^{+1} \qquad (4.47)$$

b^S b_P^S

the last term of which will join the coefficient a_P.

First derivative source terms

The source term containing first derivatives, b^{1D}, is found in the pressure gradient of the momentum equation and in the velocity gradient of the energy production for the k-ε equations. Following the method described in Sect. 4.3.3, the source terms containing first derivatives in the *x*-, *y*-, and *z*-directions are evaluated as follows (the terms within brackets are generally predominant):

$$\left(b^{1D}\right)_x = \iiint_\forall \left(\frac{\partial \phi}{\partial x}\right) d\forall = \iiint_\forall \vec{\nabla}(\phi \vec{e}_x)\, d\forall \approx \oiint_S \phi \vec{e}_x \cdot d\vec{S} = \sum_{cf=ewnstb} \left(\phi S_x\right)_{cf} \qquad (4.48a)$$

$$= \left(\phi_e S_{e,x} + \phi_w S_{w,x}\right) + \phi_n S_{w,x} + \phi_s S_{s,x} + \phi_t S_{t,x} + \phi_b S_{b,x}$$

$$\left(b^{1D}\right)_y = \iiint_\forall \left(\frac{\partial \phi}{\partial y}\right) d\forall = \iiint_\forall \vec{\nabla}(\phi \vec{e}_y)\, d\forall \approx \oiint_S \phi \vec{e}_y \cdot d\vec{S} = \sum_{cf=ewnstb} \left(\phi S_y\right)_{cf} \qquad (4.48b)$$

$$= \left(\phi_n S_{n,y} + \phi_s S_{s,y}\right) + \phi_t S_{t,y} + \phi_b S_{b,y} + \phi_e S_{e,y} + \phi_w S_{w,y}$$

$$\left(b^{1D}\right)_z = \iiint_\forall \left(\frac{\partial \phi}{\partial z}\right) d\forall = \iiint_\forall \vec{\nabla}(\phi \vec{e}_z)\, d\forall \approx \oiint_S \phi \vec{e}_z \cdot d\vec{S} = \sum_{cf=ewnstb} \left(\phi S_z\right)_{cf} \qquad (4.48c)$$

$$= \left(\phi_t S_{t,z} + \phi_b S_{b,z}\right) + \phi_e S_{e,z} + \phi_w S_{w,z} + \phi_n S_{w,z} + \phi_s S_{s,z}$$

Second derivative source terms

The source term containing second derivatives, b^{2D}, is found in the momentum equation. These are due to the non-orthogonal terms of the stresses (see Eqs. 4.6 to 4.8) and the explicit parts of the diffusion terms (see Eq. 4.43). An example is given below for the evaluation of the source terms containing second derivatives in the u-momentum equation.

$$
\begin{aligned}
\left(b^{2D}\right)_x &= \iiint_{\forall} \frac{\partial}{\partial x}\left(\nu_t \frac{\partial u}{\partial x}\right) d\forall = \iiint_{\forall} \vec{\nabla}\left[\left(\nu_t \frac{\partial u}{\partial x}\right) \mathbf{e}_x\right] d\forall \\
&= \oiint_S \left(\nu_t \frac{\partial u}{\partial x}\right) \mathbf{e}_x \cdot d\vec{\mathbf{S}} \approx \sum_{cf}\left[\left(\nu_t \frac{\partial u}{\partial x}\right) S_x\right]_{cf} \\
&= \overline{(\nu_t)}_e \overline{\left(\frac{\partial u}{\partial x}\right)}_e S_{e,x} + \overline{(\nu_t)}_w \overline{\left(\frac{\partial u}{\partial x}\right)}_w S_{w,x} + \overline{(\nu_t)}_n \overline{\left(\frac{\partial u}{\partial x}\right)}_n S_{n,x} + \\
&\quad \overline{(\nu_t)}_s \overline{\left(\frac{\partial u}{\partial x}\right)}_s S_{s,x} + \overline{(\nu_t)}_t \overline{\left(\frac{\partial u}{\partial x}\right)}_t S_{t,x} + \overline{(\nu_t)}_b \overline{\left(\frac{\partial u}{\partial x}\right)}_b S_{b,x}
\end{aligned}
\tag{4.49a}
$$

$$
\begin{aligned}
\left(b^{2D}\right)_y &= \iiint_{\forall} \frac{\partial}{\partial y}\left(\nu_t \frac{\partial v}{\partial x}\right) d\forall = \iiint_{\forall} \vec{\nabla}\left[\left(\nu_t \frac{\partial v}{\partial x}\right) \mathbf{e}_y\right] d\forall \\
&= \oiint_S \left(\nu_t \frac{\partial v}{\partial x}\right) \mathbf{e}_y \cdot d\vec{\mathbf{S}} \approx \sum_{cf}\left[\left(\nu_t \frac{\partial v}{\partial x}\right) S_y\right]_{cf} \\
&= \overline{(\nu_t)}_n \overline{\left(\frac{\partial v}{\partial x}\right)}_n S_{n,y} + \overline{(\nu_t)}_s \overline{\left(\frac{\partial v}{\partial x}\right)}_s S_{s,y} + \overline{(\nu_t)}_t \overline{\left(\frac{\partial v}{\partial x}\right)}_t S_{t,y} + \\
&\quad \overline{(\nu_t)}_b \overline{\left(\frac{\partial v}{\partial x}\right)}_b S_{b,y} + \overline{(\nu_t)}_e \overline{\left(\frac{\partial v}{\partial x}\right)}_e S_{e,y} + \overline{(\nu_t)}_s \overline{\left(\frac{\partial v}{\partial x}\right)}_w S_{w,y}
\end{aligned}
\tag{4.49b}
$$

$$
\begin{aligned}
\left(b^{2D}\right)_z &= \iiint_{\forall} \frac{\partial}{\partial z}\left(\nu_t \frac{\partial w}{\partial x}\right) d\forall = \iiint_{\forall} \vec{\nabla}\left[\left(\nu_t \frac{\partial w}{\partial x}\right) \mathbf{e}_z\right] d\forall \\
&= \oiint_S \left(\nu_t \frac{\partial w}{\partial x}\right) \mathbf{e}_z \cdot d\vec{\mathbf{S}} \approx \sum_{cf}\left[\left(\nu_t \frac{\partial w}{\partial x}\right) S_z\right]_{cf} \\
&= \overline{(\nu_t)}_t \overline{\left(\frac{\partial w}{\partial x}\right)}_t S_{t,z} + \overline{(\nu_t)}_b \overline{\left(\frac{\partial w}{\partial x}\right)}_b S_{b,z} + \overline{(\nu_t)}_e \overline{\left(\frac{\partial w}{\partial x}\right)}_e S_{e,z} + \\
&\quad \overline{(\nu_t)}_w \overline{\left(\frac{\partial w}{\partial x}\right)}_w S_{w,z} + \overline{(\nu_t)}_n \overline{\left(\frac{\partial w}{\partial x}\right)}_n S_{n,z} + \overline{(\nu_t)}_s \overline{\left(\frac{\partial w}{\partial x}\right)}_s S_{s,z}
\end{aligned}
\tag{4.49c}
$$

The last four terms on the right-hand side are due to the grid non-orthogonality; they vanish for orthogonal cells. The cell face values of the velocity gradients are obtained by linear interpolation (see Sect. 4.3.3 and Eq. 4.21).

4.3.9 Assembly of the coefficients

After evaluating all terms of the convection, diffusion, and sources over the entire computational domain and rearranging the coefficients, the discretized transport equation

produces a series of algebraic equations. For the unknown variable ϕ at the cell center P, $\phi_P(x,y,z,t)$, and at the neighboring cell centers nb, $\phi_{nb}(x,y,z,t)$, the equation reads:

$$a_P \phi_P^{\square+1} + \sum_{nb} a_{nb} \phi_{nb}^{\square+1} = b \qquad (4.50)$$

The coefficients a_{nb}, a_P, and b in the above equation are listed below:

- coefficients a_{nb} consist of the convective and diffusive terms (see Table 4.4):

$$a_E = a_E^C + a_E^D = -\max\left[-q_e^{\square}, 0\right] - f_e^D \left(\frac{\Gamma S}{L_{PE}}\right)_e^{\square},$$

$$a_W = a_W^C + a_W^D = -\max\left[-q_w^{\square}, 0\right] - f_w^D \left(\frac{\Gamma S}{L_{PW}}\right)_w^{\square},$$

$$a_N = a_N^C + a_N^D = -\max\left[-q_n^{\square}, 0\right] - f_n^D \left(\frac{\Gamma S}{L_{PN}}\right)_n^{\square},$$

$$a_S = a_S^C + a_S^D = -\max\left[-q_s^{\square}, 0\right] - f_s^D \left(\frac{\Gamma S}{L_{PS}}\right)_s^{\square},$$

$$a_T = a_T^C + a_T^D = -\max\left[-q_t^{\square}, 0\right] - f_t^D \left(\frac{\Gamma S}{L_{PT}}\right)_t^{\square}, \quad \text{and}$$

$$a_B = a_B^C + a_B^D = -\max\left[-q_b^{\square}, 0\right] - f_b^D \left(\frac{\Gamma S}{L_{PB}}\right)_b^{\square}.$$

- coefficient a_P is formed from various terms, namely the pseudo-temporal integration, convective-diffusive terms (Table 4.4), and terms coming from the source linearisation (see Eq. 4.47):

$$a_P = a_P^T + a_P^C + a_P^D - b_P$$
$$= \frac{\forall_P}{\Delta t} + \left(\sum_{nb} -a_{nb}^C + \sum_{cf} q_{cf}\right) + \left(\sum_{nb} -a_{nb}^D\right) - b_P$$

- source terms, b:

$$b = b^S + \left(b^{1D}\right)_x + \left(b^{1D}\right)_y + \left(b^{1D}\right)_z + \left(b^{2D}\right)_x + \left(b^{2D}\right)_y + \left(b^{2D}\right)_z + b^T - b^D$$

b^S — scalar sources: Eq. 4.46 or 4.47,
b^{1D} — first derivative sources: Eqs. 4.48,
b^{2D} — second derivative sources: Eqs. 4.49,

$b^T = \dfrac{\forall_P}{\Delta t}\phi_P^n$ — pseudo-time derivative source: Eq. 4.22, and

$b^D = \sum_{cf} -\left(f^D \Gamma S\right)_{cf} \left[\overline{\left(\dfrac{\partial \phi}{\partial n}\right)}_{cf} - \overline{\left(\dfrac{\partial \phi}{\partial \xi}\right)}_{cf} \right]$ — diffusive correction terms: Eq. 4.43.

Note that for the boundary cells, the coefficients may change from the above definitions. This will be described in Sect. 4.5.

Under-relaxation factor

The solution of Eq. 4.50 for any dependent variable ϕ through out the computational domain is achieved by iterative procedure, marching from known values at the iteration level $\square$ to new values at the iteration $\square+1$. During the process, oscillation may occur. In order to avoid such a problem, an under-relaxation factor is applied to updating the solution from iteration $\square$ to $\square+1$. Suppose that the solution at a particular iteration level is $\tilde{\phi}_P$, thus:

$$a_P \tilde{\phi}_P + \sum_{nb} a_{nb} \phi_{nb}^{\square+1} = b \qquad (4.50a)$$

Now, instead of taking that solution for the value of $\phi_P^{\square+1}$, one may take also into the consideration its value at the previous iteration level, $\phi_P^{\square}$, arguing that $\phi_P^{\square+1}$ should not too much different from $\phi_P^{\square}$. The under-relaxation factor, ϖ, is then applied according to the following form:

$$\phi_P^{\square+1} = \varpi \tilde{\phi}_P + (1-\varpi)\phi_P^{\square}, \qquad \text{or} \qquad \tilde{\phi}_P = \frac{1}{\varpi}\phi_P^{\square+1} - \frac{1-\varpi}{\varpi}\phi_P^{\square} \qquad (4.51)$$

Substituting this relation to the term $\tilde{\phi}_P$ in Eq. 4.50a, one finds:

$$a_P\left(\frac{1}{\varpi}\phi_P^{\square+1} - \frac{1-\varpi}{\varpi}\phi_P^{\square}\right) + \sum_{nb} a_{nb}\phi_{nb}^{\square+1} = b$$

which, after some arrangements of the terms, yields:

$$\tilde{a}_P \phi_P^{\square+1} + \sum_{nb} a_{nb}\phi_{nb}^{\square+1} = \tilde{b} \qquad (4.52)$$

where the coefficients are now:

$$\tilde{a}_P = \frac{a_P}{\varpi} \quad \text{and} \quad \tilde{b} = b + (1-\varpi)\frac{a_P}{\varpi}\phi_P^{\square} = b + (1-\varpi)\tilde{a}_P\phi_P^{\square}$$

4.4 Pressure-velocity coupling

4.4.1 SIMPLE algorithm

When solving the momentum equation for velocity, the pressure is unknown and an estimated value, p^*, is firstly used instead. In general, the velocity that is obtained does not satisfy the continuity equation. A correction to the estimated pressure is added and a new solution is sought for the new velocity. This procedure is repeated until it gives pressure and velocity fields satisfying not only the momentum equation but also the continuity equation. An iterative solution procedure known as SIMPLE (**S**emi-**I**mplicit **M**ethod for **P**ressure-**L**inked **E**quation) method (*Patankar and Spalding*, 1972) is widely used for this velocity-pressure computation. The method requires velocity and discharge at cell faces, which are not immediately available with the use of non-staggered grids in the present model. The interpolation technique of Rhie-and-Chow (*Rhie and Chow*, 1983) solves this problem. The technique gives interpolated velocity at cell faces from the nodal values. The standard SIMPLE algorithm is then used to perform the pressure correction. This section gives some details of the procedure, which follows the derivation given by Patankar (*Patankar and Spalding*, 1972; *Versteeg and Malalasekera*, 1995; *Ferziger and Peric*, 1997).

In the iteration $\square \rightarrow \square+1$, the discretized momentum equation, Eq. 4.52 with ϕ = u, v, w, can be rewritten as:

$$\tilde{a}_P u_{i,P}^{\square+1} + \sum_{nb} a_{nb} u_{i,nb}^{\square+1} = \tilde{b} - \frac{1}{\rho} \forall_P \left(\frac{\partial p^{\square+1}}{\partial x_i} \right)_P \qquad (4.53)$$

where the symbols u_i and x_i are used to denote the Cartesian components of the velocity and direction, $u_i = u, v, w$ and $x_i = x, y, z$, respectively. Note that the pressure gradient in the above expression has intentionally been extracted from the source term, $\tilde{b}$, for a reason that will be evidenced later ($\tilde{b}$ in Eq. 4.53 is thus not exactly the same as that in Eq. 4.52).

The coefficients $\tilde{a}_P, a_{nb}$, and the source terms, $\tilde{b}$, are functions of the known variables either at the precedent iteration, $\square$, or time step, n. For practical solutions of Eq. 4.53, since there are only 3 equations for 4 unknowns, the pressure p is temporarily fixed at its initial value. The following system of equations is solved in the first stage:

$$\tilde{a}_P u_{i,P}^* + \sum_{nb} a_{nb} u_{i,nb}^* = \tilde{b} - \frac{\forall_P}{\rho} \left(\frac{\partial p^*}{\partial x_i} \right)_P \qquad (4.54a)$$

$$p^* = p^{\square} \qquad (4.54b)$$

The estimated pressure, p^*, and the velocities obtained from this pressure, u^*, v^*, w^*, are of course to be corrected:

$$u_i^{\square+1} = u_i^* + u_i^c \tag{4.55a}$$

$$p^{\square+1} = p^* + p^c \tag{4.55b}$$

where the corrections, u_i^c and p^c, will result from the momentum equations combined with the continuity equation. The corrections are such that the velocity will satisfy the continuity and momentum equations when the iteration converges. It can therefore be said that Eqs. 4.54a,b become Eq. 4.53 when $\square \to \infty$. In that case, having a sufficiently large number of $\square$-iterations, we have $\left(u_i^*\right)^{\square\to\infty} = u_i^{\square+1}$; and this is so for the coefficients and source terms. We can therefore obtain the relation between the pressure and velocity corrections by subtraction of Eqs. 4.54a,b from Eq. 4.53:

$$\tilde{a}_P\, u_{i,P}^c + \sum_{nb} a_{nb} u_{i,nb}^c = -\frac{\forall_P}{\rho}\left(\frac{\partial p^c}{\partial x_i}\right)_P \tag{4.56}$$

Eq. 4.56 is a relation in which the corrections tend towards zero. A simplifying approximation can then be introduced by neglecting *à priori* the correction terms of the neighboring cells (*Patankar and Spalding*, 1972). The velocity correction thus reduces to:

$$u_{i,P}^c = -\frac{1}{\rho}\frac{\forall_P}{\tilde{a}_P}\left(\frac{\partial p^c}{\partial x_i}\right)_P \tag{4.57}$$

Since the coefficient $\tilde{a}_P^{\square}$ is derived in such a way that it is the same for all velocity components, i.e. $\tilde{a}_P^u = \tilde{a}_P^v = \tilde{a}_P^w = \tilde{a}_P$, the above relation is valid for *any velocity component at any point* and thus also for the normal velocity component at a cell face. Writing for the east face, one has:

$$u_{n,e}^c = -\frac{1}{\rho}\left(\frac{\forall}{\tilde{a}}\right)_e\left(\frac{\partial p^c}{\partial n}\right)_e \tag{4.58}$$

The coefficient at the cell face, $\left(\forall/\tilde{a}\right)_e^{\square}$, is defined as the average value of those of the neighboring cell centers P and E:

$$\left(\frac{\forall}{\tilde{a}}\right)_e = \frac{1}{2}\left[\left(\frac{\forall}{\tilde{a}_P}\right)_P + \left(\frac{\forall}{\tilde{a}_P}\right)_E\right] \tag{4.59}$$

Note that $\left(\tilde{a}_P\right)_E$ represents the coefficient $\tilde{a}_P$ of Eq. 4.52 written for the cell E, that is not the coefficient a_E of Eq. 4.52 written for the cell P. Note also that the interpolation in Eq. 4.59 does not match the linear interpolation in Eq. 4.19 since this latter is not relevant for the volumes. Indeed the volume related to a cell for the east face is composed of the half volume of cell P and the half volume of cell E. Using the deferred-correction method as in the discretisation of the diffusive terms (see Sect. 4.3.6, Eq. 4.31) to compute the normal pressure gradient yields:

$$u^{c}_{n,e} = \underbrace{-\frac{1}{\rho}\left(\frac{\forall}{\tilde{a}}\right)_e\left[\frac{p^{c}_{E}-p^{c}_{P}}{L_{PE}}\right]}_{u^{impl}_{n,e}:\ implicit} \underbrace{-\frac{1}{\rho}\left(\frac{\forall}{\tilde{a}}\right)_e\left[\left(\overline{\frac{\partial p^{c}}{\partial n}}\right)_e - \left(\overline{\frac{\partial p^{c}}{\partial \xi}}\right)_e\right]^{old}}_{u^{no}_{n,e}:\ explicit} \tag{4.60}$$

in which the terms in the second square bracket are due to non-orthogonality of the cell and are evaluated explicitly. From the starred-velocity and the velocity correction, the normal velocity component can be computed:

$$u_{n,e} = u^{*}_{n,e} + u^{c}_{n,e} = u^{*}_{n,e} + u^{impl}_{n,e} + u^{no}_{n,e} \tag{4.61}$$

Here the velocity correction due to the cell non-orthogonality is written separately. Whilst the velocity correction is obtainable from Eq. 4.60, the starred-velocity unfortunately is not directly available at the cell face. Interpolating the starred velocity at the neighboring cell centers to get the cell face value would result in the decoupling of the velocity from the pressure that causes an oscillation of the solution. A remedy to this problem is to use the so-called Rhie-and-Chow interpolation technique (*Rhie and Chow*, 1983) which replaces the interpolated pressure gradient at a cell face with the one computed from the pressure at the immediate neighboring cell centers. As can be seen in the relation below, writing the equivalent of Eq. 4.54a at the east face by simply interpolating these starred velocities would result in velocities that have no direct relation with the pressure difference between P and E:

$$\overline{\left(u^{*}_{n}\right)}_e = \overline{\left(\frac{\tilde{b}-\sum a_{nb}u^{*}_{n,nb}}{\tilde{a}_P}\right)}_e - \frac{1}{\rho}\overline{\left(\frac{\forall}{\tilde{a}}\right)}_e\overline{\left(\frac{\partial p^{*}}{\partial n}\right)}_e \tag{4.62}$$

In order to relate the velocity at the east face back to the pressure difference between P and E, a correction is given to this interpolated velocity:

$$u^{*}_{n,e} = \left[\overline{\left(\frac{\tilde{b}-\sum a_{nb}u^{*}_{n,nb}}{\tilde{a}_P}\right)}_e - \frac{1}{\rho}\overline{\left(\frac{\forall}{\tilde{a}}\right)}_e\overline{\left(\frac{\partial p^{*}}{\partial n}\right)}_e\right] + \frac{1}{\rho}\overline{\left(\frac{\forall}{\tilde{a}}\right)}_e\left[\overline{\left(\frac{\partial p^{*}}{\partial n}\right)}_e - \frac{p^{*}_{E}-p^{*}_{P}}{L_{PE}}\right] \tag{4.63}$$

This expression can be seen as the velocities at the cell centers P and E interpolated to the east face and corrected by a factor due to the interpolation:

$$u^{*}_{n,e} = \overline{\left(u^{*}_{n}\right)}_e + u^{RC}_{n,e} \tag{4.64}$$

where the overbar term is obtained from linear interpolation of the velocities in cell centers P and E. Using this expression to substitute the starred velocity in Eq. 4.61 gives:

$$u_{n,e} = \overline{\left(u^{*}_{n}\right)}_e + u^{RC}_{n,e} + u^{impl}_{n,e} + u^{no}_{n,e} \tag{4.65}$$

Next, we need to define the equation of the pressure correction, which is carried out by using the continuity equation. The discretized continuity equation can be obtained by writing the governing equation, Eq. 4.15, with $\phi = 1$, $\Gamma = 0$, and $R = 0$ that gives:

$$\oint\!\!\oint_S \vec{\mathbf{v}} \cdot d\mathbf{S} \approx \sum_{cf=ewnstb} \left(\vec{\mathbf{v}} \cdot d\mathbf{S}\right)_{cf} = \sum_{cf=ewnstb} q_{cf} = \sum_{cf=ewnstb} \left(u_{n,cf}\, S_{cf}\right) = 0 \tag{4.66}$$

Using Eq. 4.65 with the development of the implicit term in Eq. 4.60, and inserting the result to the above continuity equation, one gets the pressure correction equation of the form:

$$\begin{aligned} &-\frac{1}{\rho}\left(\frac{\forall}{\tilde{a}}\right)_e \frac{S_e}{L_{PE}}\left(p_E^c - p_P^c\right) - \frac{1}{\rho}\left(\frac{\forall}{\tilde{a}}\right)_w \frac{S_w}{L_{PW}}\left(p_W^c - p_P^c\right) - \frac{1}{\rho}\left(\frac{\forall}{\tilde{a}}\right)_n \frac{S_n}{L_{PN}}\left(p_N^c - p_P^c\right) \\ &-\frac{1}{\rho}\left(\frac{\forall}{\tilde{a}}\right)_s \frac{S_s}{L_{PS}}\left(p_S^c - p_P^c\right) - \frac{1}{\rho}\left(\frac{\forall}{\tilde{a}}\right)_t \frac{S_t}{L_{PT}}\left(p_T^c - p_P^c\right) - \frac{1}{\rho}\overline{\left(\frac{\forall}{\tilde{a}}\right)}_b \frac{S_b}{L_{PB}}\left(p_B^c - p_P^c\right) \\ &+ \sum_{cf=ewnstb}\left[\overline{\left(q^*\right)}_{cf} + q_{cf}^{RC} + q_{cf}^{no}\right] = 0 \end{aligned} \tag{4.67}$$

where:

$$\overline{\left(q^*\right)}_{cf} = \overline{\left(u_{cf}^*\right)} S_{cf,x} + \overline{\left(v_{cf}^*\right)} S_{cf,y} + \overline{\left(w_{cf}^*\right)} S_{cf,z} \quad \text{interpolated discharge}$$

$$q_{cf}^{RC} = \frac{1}{\rho}\left(\frac{\forall}{\tilde{a}}\right)_{cf}\left[\overline{\left(\frac{\partial p^*}{\partial n}\right)}_{cf} - \frac{p_{nb}^* - p_P^*}{L_{nbP}}\right] S_{cf} \quad \text{correction due to cell - face interpolation}$$

$$q_{cf}^{no} = -\frac{1}{\rho}\left(\frac{\forall}{\tilde{a}}\right)_{cf}\left[\overline{\left(\frac{\partial p^c}{\partial n}\right)}_{cf} - \overline{\left(\frac{\partial p^c}{\partial \xi}\right)}_{cf}\right]^{old} S_{cf} \quad \text{correction due to non - orthogonal terms}$$

After arranging the terms, one has:

$$a_P^p\, p_P^c + \sum_{nb}\left(a_{nb}^p\, p_{nb}^c\right) = b^p \tag{4.68}$$

where:

$$a_E^p = -\frac{1}{\rho}\left(\frac{\forall}{\tilde{a}}\right)_e \frac{S_e}{L_{PE}}, \qquad a_W^p = -\frac{1}{\rho}\overline{\left(\frac{\forall}{\tilde{a}}\right)}_w \frac{S_w}{L_{PW}}, \qquad a_N^p = -\frac{1}{\rho}\left(\frac{\forall}{\tilde{a}}\right)_n \frac{S_n}{L_{PN}},$$

$$a_S^p = -\frac{1}{\rho}\overline{\left(\frac{\forall}{\tilde{a}}\right)}_s \frac{S_s}{L_{PS}}, \qquad a_T^p = -\frac{1}{\rho}\left(\frac{\forall}{\tilde{a}}\right)_t \frac{S_t}{L_{PT}}, \qquad a_B^p = -\frac{1}{\rho}\left(\frac{\forall}{\tilde{a}}\right)_w \frac{S_b}{L_{PB}},$$

$$a_P^p = -\sum_{nb} a_{nb}^p, \qquad b^p = -\sum_{cf}\left[\overline{\left(q^*\right)}_{cf} + q_{cf}^{RC} + q_{cf}^{no}\right]$$

The pressure gradients encountered in the source terms are computed according to the following relations:

$$\begin{aligned}
\overline{\left(\frac{\partial \mathrm{p}^*}{\partial n}\right)}_{\mathrm{e}} &= \overline{\left(\frac{\partial \mathrm{p}^*}{\partial x}\right)}_{\mathrm{e}}\left(\frac{\mathrm{S}_{\mathrm{e},x}}{\mathrm{S}_{\mathrm{e}}}\right) + \overline{\left(\frac{\partial \mathrm{p}^*}{\partial y}\right)}_{\mathrm{e}}\left(\frac{\mathrm{S}_{\mathrm{e},y}}{\mathrm{S}_{\mathrm{e}}}\right) + \overline{\left(\frac{\partial \mathrm{p}^*}{\partial z}\right)}_{\mathrm{e}}\left(\frac{\mathrm{S}_{\mathrm{e},z}}{\mathrm{S}_{\mathrm{e}}}\right) \\
\overline{\left(\frac{\partial \mathrm{p}^{\mathrm{c}}}{\partial n}\right)}_{\mathrm{e}} &= \overline{\left(\frac{\partial \mathrm{p}^{\mathrm{c}}}{\partial x}\right)}_{\mathrm{e}}\left(\frac{\mathrm{S}_{\mathrm{e},x}}{\mathrm{S}_{\mathrm{e}}}\right) + \overline{\left(\frac{\partial \mathrm{p}^{\mathrm{c}}}{\partial y}\right)}_{\mathrm{e}}\left(\frac{\mathrm{S}_{\mathrm{e},y}}{\mathrm{S}_{\mathrm{e}}}\right) + \overline{\left(\frac{\partial \mathrm{p}^{\mathrm{c}}}{\partial z}\right)}_{\mathrm{e}}\left(\frac{\mathrm{S}_{\mathrm{e},z}}{\mathrm{S}_{\mathrm{e}}}\right) \\
\overline{\left(\frac{\partial \mathrm{p}^{\mathrm{c}}}{\partial \xi}\right)}_{\mathrm{e}} &= \overline{\left(\frac{\partial \mathrm{p}^{\mathrm{c}}}{\partial x}\right)}_{\mathrm{e}}\left(\frac{\Delta x_{\mathrm{PE}}}{\mathrm{L}_{\mathrm{PE}}}\right) + \overline{\left(\frac{\partial \mathrm{p}^{\mathrm{c}}}{\partial y}\right)}_{\mathrm{e}}\left(\frac{\Delta y_{\mathrm{PE}}}{\mathrm{L}_{\mathrm{PE}}}\right) + \overline{\left(\frac{\partial \mathrm{p}^{\mathrm{c}}}{\partial z}\right)}_{\mathrm{e}}\left(\frac{\Delta z_{\mathrm{PE}}}{\mathrm{L}_{\mathrm{PE}}}\right)
\end{aligned} \tag{4.69}$$

in which the interpolation of the pressure gradients along the Cartesian coordinates is done using Eq. 4.21.

4.4.2 Pressure correction procedure

The source term, b^{p}, has pressure correction terms contained in the discharge due to non-orthogonality of the cells, $\mathrm{q}_{\mathrm{e}}^{\mathrm{no}}$. These terms are evaluated explicitly by a double-step pressure correction procedure as follows:

- Solve Eq. 4.68 for p^{c} by neglecting the non-orthogonal terms, $\mathrm{q}_{\mathrm{cf}}^{\mathrm{no}} = 0$, and correct the velocities and pressure according to Eqs. 4.55a,b.
- Solve again Eq.4.4 with the non-orthogonal terms now available from the first step and correct once again the velocities and pressure.

4.4.3 Under-relaxation factor and time step

To avoid instability of the computation, it is a common practice to put an under-relaxation factor to the pressure correction, $0 \le \varpi^{\mathrm{p}} \le 1$, in updating the pressure:

$$\mathrm{p} = \mathrm{p}^* + \varpi^{\mathrm{p}}\,\mathrm{p}^{\mathrm{c}} \tag{4.70}$$

As mentioned in Sect. 4.2, the time step plays also as an under-relaxation factor for steady flow cases. This type of application, that is using the transient equations to solve steady flows, is generally known as a pseudo-transient computation. In order to achieve the effects of under-relaxed iterative steady-state computations from a given initial field by means of a pseudo-transient computation starting from the same initial field, the time-step size is taken such that (*Fletcher*, 1997, p. 365):

$$\varpi^{\mathrm{p}} = \frac{1}{1 + \mathrm{E}_{\Delta \mathrm{t}}} \quad \text{with} \quad \mathrm{E}_{\Delta \mathrm{t}} = \frac{\tilde{\mathrm{a}}_{\mathrm{P}}}{\forall_{\mathrm{P}}}\,\Delta \mathrm{t} \tag{4.71}$$

4.5 Boundary conditions

4.5.1 Boundary placement

The boundary conditions that can be considered in the model are inflow, outflow, wall, (water) surface, and symmetry boundaries. The spatial discretisation of the computational domain is done in such a way that the boundaries coincide with the cell face (see Fig. 4.5). The cell neighboring the boundary has special characteristics that modify the definition of cell set forth in Sect. 4.3.1; it has more than one node and less than six neighbors. Three types of cell and node are introduced (see Fig. 4.5):

- *Interior cell* (the white cell) is a computational cell where the dependent variable, ϕ, is unknown and is to be computed at the *interior node* (the solid circle); an interior cell has only one node, the interior node.
- *Boundary cell* (the gray cell) is a boundary neighboring cell whose one or more of its faces coincide with a boundary. A boundary cell has one *interior node* (the solid circle) at the center of the cell and one *boundary node* (the gray circle) at the center of each face that coincides with the boundary. The known boundary values of all variables ϕ are to be defined at the boundary node, either given or extrapolated from the interior nodes.
- *Dummy cell* (hatched cell) and *dummy node* (white node) are used to denote the domain which is excluded from the computation, for example blocked-regions, cylinders, and corners. These dummy cells and nodes are necessary in order to maintain a continuous ordering of the cell and node indexes.

Except of some special cases for the k and ε equations, the effect of the boundaries to the computation for the interior node of a boundary cell is additive. In the discretized equation of u, v, w, and p^c, the contribution of each boundary node is added to the source term, b, of the interior node of the boundary cell, and the coefficient related to this boundary node is eventually set to zero. The k and ε for the interior nodes of boundary cells having wall or free-surface boundaries, however, are defined by a given expression. In the following sections are presented the method of computation for the boundary cells.

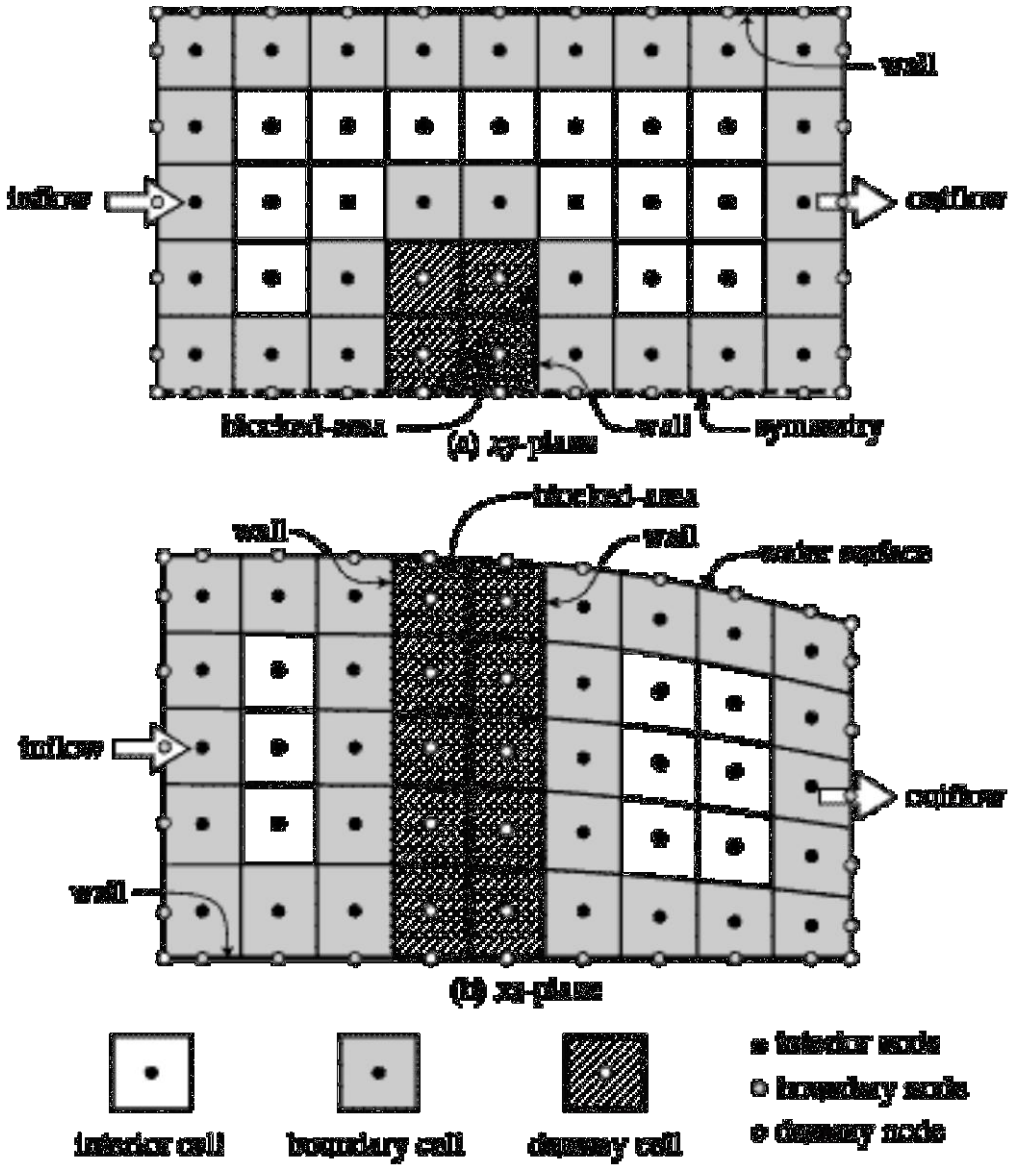

Fig. 4.5 Boundary conditions implemented in the model.

4.5.2 Inflow boundary

Suppose that the inflow boundary lies at the west face, w, of the boundary cell P (see Fig. 4.6). The inflow boundary values across the face w are imposed as the boundary condition, whose values are defined at the boundary node W located at the same place as w (see Sect. 4.5.1):

$$\phi_W = \phi_{in} \tag{4.72}$$

The pressure is assumed to vary linearly between W, P and E:

$$\frac{p_W - p_P}{L_{PW}} = \frac{p_E - p_P}{L_{PE}} \quad \Rightarrow \quad p_W = (1+\beta_e)p_P - \beta_e\, p_E \tag{4.73}$$

The above relation holds as well for p^* and p^c values.

The boundary node denoted by W (instead of w) upon which the inflow boundary values are defined allows the discretized equations formerly established for interior nodes to be applied to the boundary node W without the need to change the notation.

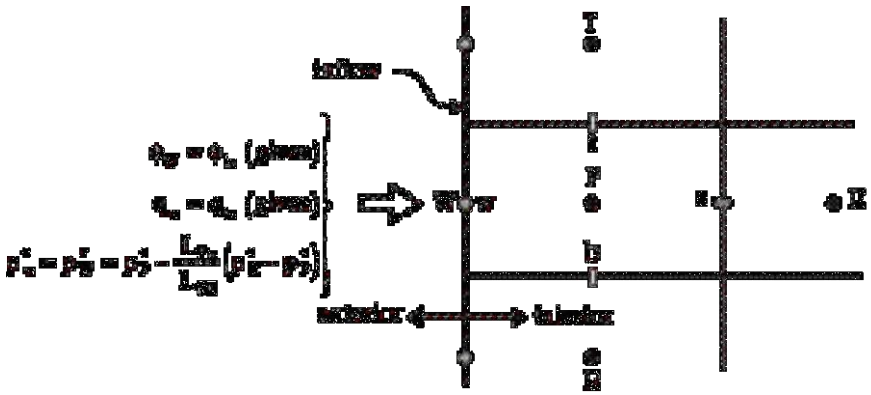

Fig. 4.6 Inflow boundary.

Momentum and k-ε equations

In forming the coefficients in Eq. 4.52, the following steps apply:

- all variables at the inlet are given: $\phi_W = \phi_{in}$
- evaluate the convective-diffusive terms as for normal interior cells: $a_W^C, a_W^D, \left(a_P^C\right)_W, \left(a_P^D\right)_W, \left(b^D\right)_W, \left(b^{lD}\right)_W, \left(b^{2D}\right)_W$
- bring the contribution of node W to the source term: $b \leftarrow b - \left(b^D\right)_W - \left(a_W^C + a_W^D\right)\phi_W$
- set the coefficient at node W to zero: $a_W = 0$

Pressure and velocity corrections

The contribution of the discharge across the west face, q_w, to the continuity equation, Eq. 4.66, is replaced by the imposed discharge, q_{in}. In forming the coefficients in Eq. 4.68, the following steps apply:

- set the coefficient at node W to zero: $a_W^p = 0$
- set the contribution of the inflowing discharge to the source term: $\left(b^p\right)_w = -q_{in}$

For the velocity correction, Eq. 4.57, the pressure correction gradient, $\partial p^c / \partial x_i$, is computed by the finite-volume technique, Eq. 4.20, which requires the value of $\left(p^c\right)_w = \left(p^c\right)_W$. This latter is obtained by Eq. 4.73.

4.5.3 Outflow boundary

Suppose that the outflow lies at the east face of the boundary cell P (see Fig. 4.7). Across the outflow face, the convective flux is computed according to the upwinding principle of Eq. 4.28:

$$\left(F^C\right)_e = q_e \phi_P^{\square+1} = q_{out}^{\square} \phi_P^{\square+1}$$

while the diffusion flux is set to zero:

$$\left(F^D\right)_e = 0$$

leading to a simplified form of Eq. 4.43:

$$F_e = q_{out}^{\square} \phi_P^{\square+1}$$

where $q_{out}^{\square}$ is either imposed or computed from the upwinding of P value at the former iteration step:

$$q_{out}^{\square} = \vec{V}_{out}^{\square} \cdot \vec{S}_e = \vec{V}_P^{\square} \cdot \vec{S}_e$$

The same upwinding process finds the other variables at the boundary node E.

$$\phi_E = \phi_e = \phi_P$$

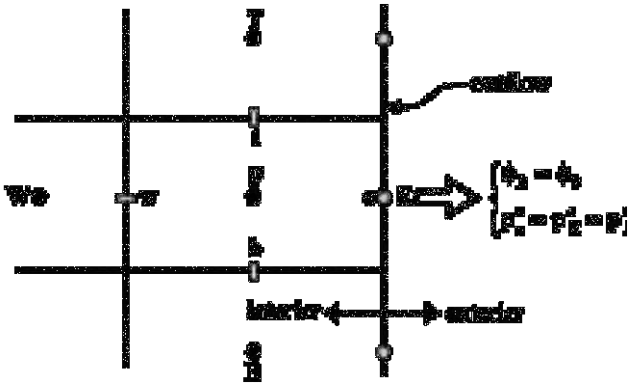

Fig. 4.7 Outflow boundary.

Momentum and k-ε equations

- set all coefficients related to node E in Eq. 4.52 to zero:
  $a_E^C = a_E^D = \left(a_P^C\right)_E = \left(a_P^D\right)_E = \left(b^D\right)_E = \left(b^{1D}\right)_E = \left(b^{2D}\right)_E = 0$

- extrapolate all variables at P to E: $\phi_E = \phi_P$
- the outflowing discharge results: $q_{out} = \vec{V}_e \cdot \vec{S}_e = \vec{V}_P \cdot \vec{S}_e$

Pressure and velocity corrections

The contribution of the discharge across the east face, q_e, to the continuity equation, Eq. 4.66, is replaced by the outflowing discharge, q_{out}. In forming the coefficients in Eq. 4.68, the following steps are done:

- set the coefficient at node E to zero: $a_E^p = 0$
- set the contribution of the inflowing discharge to the source term: $\left(b^p\right)_e = -q_{out}$

For the velocity correction, Eq. 4.57, the pressure correction gradient, $\partial p^c / \partial x_i$, is computed by the finite-volume technique, Eq. 4.20, which requires the value of $\left(p^c\right)_e = \left(p^c\right)_E$; this latter is obtained by the upwinding: $\left(p^c\right)_E = \left(p^c\right)_P$.

4.5.4 Wall boundary

Wall function approach

The wall function approach (*Launder and Spalding*, 1974) is applied to the cell whose face is a rigid wall. Major assumptions used in this approach merit to be put forward before presenting the derivation of the wall function; they are: (1) the no-slip flow condition prevails at the wall with the universal logarithmic velocity distribution normal to the wall, (2) the production of the turbulent kinetic energy is merely due to the (turbulent) shear stress, thus neglecting the effect of the normal stress, and (3) a local energy balance exists, i.e. the dissipation of the turbulent kinetic energy is equal to the production. Given in the following paragraphs are the derivations of the wall function in which those assumptions are further highlighted.

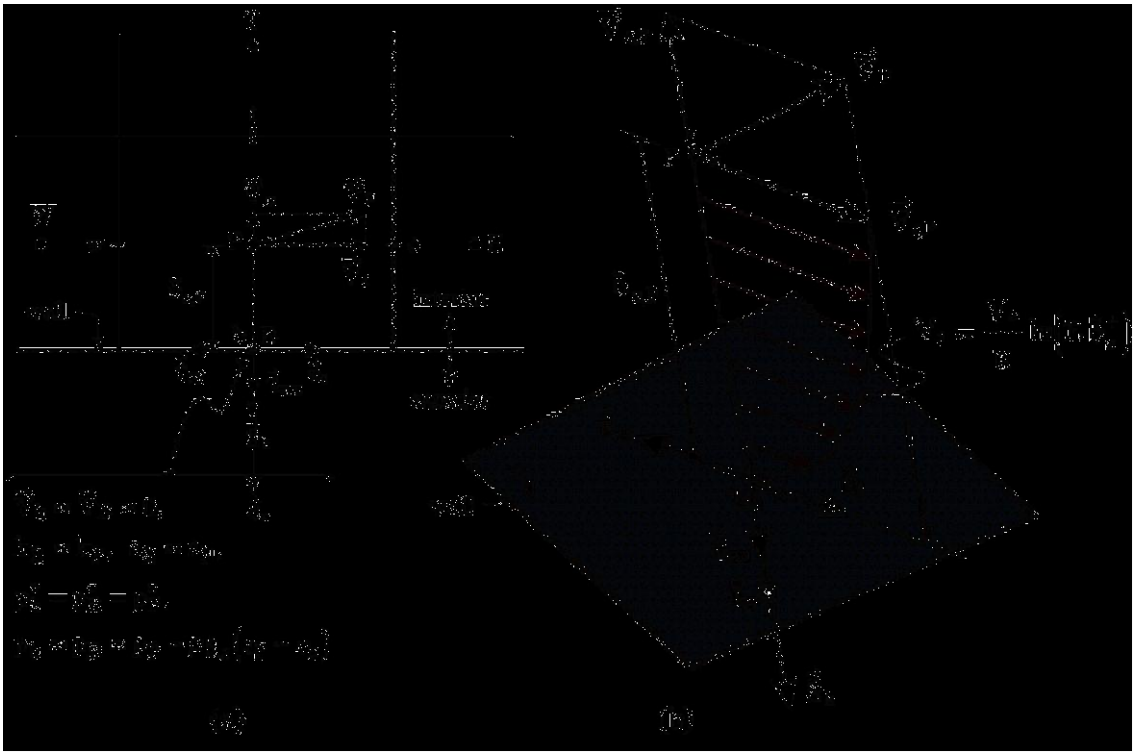

Fig. 4.8 Wall boundary.

(1) In wall boundaries, the center of the cells is located sufficiently close to the wall but outside the viscous sub-layer (see Fig. 4.8a); the universal logarithmic velocity distribution then prevails in the region $\overline{Pb}$ (see Fig. 4.8b):

$$V_t = \frac{V_*}{\kappa} \ln\left(E\ \delta_n^+\right) \quad \text{or} \quad V_* = \frac{\kappa\, V_t}{\ln\left(E\ \delta_n^+\right)}, \qquad \text{with} \quad V_t = \left\| \vec{\mathbf{V}}_t \right\| \quad \text{and} \quad \delta_n^+ = \frac{V_* \delta_n}{\nu} \tag{4.74}$$

in which V_* is the shear velocity, V_t is the velocity component parallel to the wall, κ is the Karman universal constant, δ_n is the normal distance from the wall, ν is the molecular viscosity of water, and E is the wall roughness coefficient. The coefficient E in the above relation accounts for all flow regimes, either hydraulically smooth, rough, or transition. Note the directions of stresses on the wall face b; the shear stress, $\boldsymbol{\tau}_{nt}$, is to the opposite direction of $\mathbf{e}_t$, whereas the normal stress, $\boldsymbol{\tau}_{nn}$, is according to $\mathbf{e}_n$. These directions are consistent with the convention that shear forces are in the direction of positive increases of velocity (positive velocity gradients). In the direction of $\mathbf{e}_n$ of the (local) wall coordinate, ($\mathbf{e}_t, \mathbf{e}_n$), the velocity gradient $\partial V_t / \partial n$ is negative, whereas $\partial V_n / \partial n$ is positive.

(2) The equation of the turbulent kinetic-energy production, Eq. 4.12, written in the wall coordinate system, ($\mathbf{e}_t, \mathbf{e}_n$), shown in Fig. 4.8b, is:

$$G = \nu_t \left[2\left(\frac{\partial V_t}{\partial t}\right)^2 + \left(\frac{\partial V_n}{\partial t} + \frac{\partial V_t}{\partial n}\right)^2 + 2\left(\frac{\partial V_n}{\partial n}\right)^2 \right] \tag{4.12a}$$

Since the velocity is zero everywhere along the wall, $V_t = 0$ (no-slip condition) and $V_n = 0$ (no-flow across the wall), all velocity gradients along the wall (the tangential components) disappear. The above expression thus reduces into:

$$G = \nu_t \left(\frac{\partial V_t}{\partial n}\right)^2 + \nu_t 2\left(\frac{\partial V_n}{\partial n}\right)^2 \tag{4.75a}$$

The first and the second terms depict the turbulent kinetic-energy production due to the shear and normal stresses, respectively. In the wall function, the second term is neglected, which implies that the normal velocity component cannot develop in the wall region. This yields the following:

$$G = \nu_t \left(\frac{\partial V_t}{\partial n}\right)^2 \tag{4.75b}$$

The validity of the above equation is strictly limited at the wall b, but is generally extended to the cell center P where it constitutes an approximation. The omission of the normal velocity gradient in Eq. 4.75a and the extension of Eq. 4.75b to the cell center are, of course, a rather rude approximation, notably in the case of flow around a cylinder. Measurement data in front of the cylinder (see Chapters 2 and 3) show that the radial velocity (the normal component) and the downward velocity (the tangential component) have the same order of magnitude. The normal velocity gradient, therefore, should be accounted for in the turbulent kinetic-energy production. However, the present model adopts Eq. 4.75b since it leads to a numerical simplification.

(3) The third assumption in the wall function is the existence of a local balance between the turbulent kinetic-energy dissipation and its production, $\varepsilon = G$ (see *Launder and Spalding*, 1974; *Versteeg and Malalasekera*, 1995, p. 73). This yields:

$$\varepsilon_P = G_P = \left[\nu_t \left(\frac{\partial V_t}{\partial n}\right)^2 \right]_P \tag{4.76}$$

The eddy viscosity can be found from the Boussinesq concept, Eq. 4.5, and the definition of the friction velocity, $\tau_{nt,b} = \rho V_*^2$. Considering that the variation of the shear stress is negligible in the wall region, $\tau_{nt,b} = \tau_{nt,P}$, and that the velocity gradient along the wall is negligible, $(\partial V_n/\partial t)_P \approx 0$, one may write:

$$V_*^2 = \frac{\tau_{nt,b}}{\rho} = \frac{\tau_{nt,P}}{\rho} = \left[\nu_t \left(\frac{\partial V_t}{\partial n} + \frac{\partial V_n}{\partial t} \right) \right]_P = \left(\nu_t \frac{\partial V_t}{\partial n} \right)_P \tag{4.77}$$

The velocity gradient is obtainable from the logarithmic velocity distribution, Eq. 4.74:

$$\left(\frac{\partial V_t}{\partial n}\right)_P = \frac{V_*}{\kappa\, \delta_{n,P}} \tag{4.78}$$

Inserting this relation into Eq. 4.77, one obtains:

$$\nu_{t,P} = V_*\, \kappa\, \delta_{n,P} \tag{4.79}$$

Substituting Eqs. 4.78 and 4.79 into the right-hand-side of Eq. 4.76 yields:

$$\varepsilon_P = G_P = V_*\, \kappa\, \delta_{n,P} \left(\frac{V_*}{\kappa\, \delta_{n,P}}\right)^2 = \frac{V_*^{\,3}}{\kappa\, \delta_{n,P}} \tag{4.80}$$

Combining Eqs. 4.79 and 4.80 to the definition of the eddy viscosity in the k-ε model, Eq. 4.9, one gets:

$$\nu_{t,P} = c_\mu \frac{k_P^{\,2}}{\varepsilon_P}$$

$$V_*\, \kappa\, \delta_n = c_\mu \left(\frac{k_P^{\,2}\, \kappa\, \delta_n}{V_*^{\,3}}\right)$$

$$V_* = c_\mu^{\,1/4}\, k_P^{\,1/2} \tag{4.81}$$

There are now two expressions of the friction velocity, i.e. Eqs. 4.74 and 4.81. Both relations are used to evaluate the shear stress at the wall:

$$\vec{\tau}_{nt,b} = -\rho\, V_* V_* = -\rho c_\mu^{\,1/4} k_P^{\,1/2} \frac{\kappa \vec{V}_{t,P}}{\ln\left(E\, \delta_{n,P}^+\right)} \vec{e}_t \tag{4.82}$$

The negative sign is required since $\vec{\tau}_{nt}$ is acting to the opposite direction of $\vec{e}_t$ (see Fig. 4.8). This relation is the one necessary to evaluate the contribution of the wall boundary to the flow momentum equation; its implementation will be further presented later.

Wall function: the final equations

The link between the wall function and the k equation is achieved through the turbulent kinetic-energy production, Eq. 4.76, the velocity gradient, Eq. 4.78, and the shear velocity, Eq. 4.81. Combining these equations, one gets:

$$G_P = \left[\nu_t \left(\frac{\partial V_t}{\partial n}\right)^2\right]_P = \frac{\tau_{nt,P}}{\rho} \left(\frac{\partial V_t}{\partial n}\right)_P = \frac{\tau_{nt,b}}{\rho} \left(\frac{V_*}{\kappa\, \delta_{n,P}}\right) = \frac{\tau_{nt,b}}{\rho} \frac{c_\mu^{\,1/4}\, k_P^{\,1/2}}{\kappa\, \delta_{n,P}} \tag{4.83}$$

with $\tau_{nt,\mathrm{b}} = \left\| \vec{\boldsymbol{\tau}}_{nt,\mathrm{b}} \right\|$.

This equation is used to define the energy production in the source term of the k equation (see Table 4.2) for cells neighboring the wall.

For the ε equation, the energy dissipation is obtained from Eqs. 4.80 and 4.81:

$$\varepsilon_{\mathrm{P}} = \frac{c_{\mu}^{3/4}\, k_{\mathrm{P}}^{3/2}}{\kappa\, \delta_{n,\mathrm{P}}} \tag{4.84}$$

Before detailing the implementation of the wall function to the discretized momentum and k-ε transport equations, two variables need to be defined, namely the wall roughness coefficient, E, and the parallel velocity components, $\vec{\mathbf{V}}_t$.

Wall roughness coefficient. The wall roughness coefficient, E, in the logarithmic velocity profile is adjusted according to the equivalent (standard) roughness, k_s, whether it is hydraulically smooth, rough, or transition between smooth and rough. The following relation is used to define the roughness coefficient (*Wu et al.*, 2000):

$$E = \exp\left[\kappa(B - \Delta B)\right] \tag{4.85}$$

where B is an additive constant and ΔB is a roughness function determined according to the standard roughness, k_s, as follows (*Cebeci and Bradshaw*, 1977):

$$\Delta B = \begin{cases} 0 & \text{for} \quad k_s^+ < 2.25 \\ \left[B - 8.5 + \dfrac{1}{\kappa} \ln k_s^+ \right] \sin\left[0.4258 \left(\ln k_s^+ - 0.811 \right) \right] & \text{for} \quad 2.25 \le k_s^+ < 90 \\ B - 8.5 + \dfrac{1}{\kappa} \ln k_s^+ & \text{for} \quad k_s^+ \ge 90 \end{cases} \tag{4.86}$$

with $B = 5.2$, $\kappa = 0.4$, and $k_s^+ = V_* k_s / \nu$ being the roughness Reynolds number.

Tangential velocity component. The velocity at the cell center P needs to be decomposed into its normal and tangential components with respect to the wall (see Fig. 4.8b). The unit vector normal to the wall, $\vec{\mathbf{e}}_n$, has an outward direction (see Eq. 4.17), while the unit vector tangential to the wall, $\vec{\mathbf{e}}_t$, has the direction of the projection of $\vec{\mathbf{V}}_{\mathrm{P}}$ on the wall. Both unit vectors are perpendicular in such a way that any vector (for example $\vec{\mathbf{V}}_{\mathrm{P}}$) can be decomposed along them in the plane ($\vec{\mathbf{e}}_t$, $\vec{\mathbf{e}}_n$) which also contains $\vec{\mathbf{V}}_{\mathrm{P}}$. For determining $\vec{\mathbf{e}}_t$, it is necessary to find the projection $\vec{\mathbf{V}}_{t,\mathrm{P}}$, which can be obtained from:

$$\vec{\mathbf{V}}_{t,\mathrm{P}} = \vec{\mathbf{V}}_{\mathrm{P}} - \vec{\mathbf{V}}_{n,\mathrm{P}} = \vec{\mathbf{V}}_{\mathrm{P}} - \left(\vec{\mathbf{V}}_{\mathrm{P}} \cdot \vec{\mathbf{e}}_n \right) \vec{\mathbf{e}}_n \tag{4.87}$$

Knowing $\vec{\mathbf{V}}_{t,\mathrm{P}}$ the unit vector $\mathbf{e}_t$ can be easily computed:

$$\mathbf{e}_t = \left(\vec{\mathbf{V}}_t / \left\|\vec{\mathbf{V}}_t\right\|\right)_{\mathrm{P}} \tag{4.88}$$

Implementation of the wall function

Wall function for the momentum equation. Since there is no discharge across the wall, the convective flux does not exist across the wall face; the only flux is due to the diffusion. In the discretized momentum equation, Eq. 4.52, the diffusion term is not evaluated by Eq. 4.33, but by evaluating this term as a normal force (per unit mass) acting on the wall. Similarly the wall shear-stress, Eq. 4.82, is also transformed as a shear force. Both forces are considered as a source term and are evaluated at iteration k, which then linearized such that the velocities at the cell center P become unknown variables.

The force due to the normal stress acting on the wall (see Fig. 4.8) can be computed as:

$$\left(\frac{\vec{\mathbf{F}}_n}{\rho}\right)_{\mathrm{b}}^{k} = \left(\frac{\boldsymbol{\tau}_{nn}}{\rho}\right)_{\mathrm{b}}^{k} \mathrm{S_b} = \left(-\nu_{\mathrm{t}}\, 2\, \frac{\partial \mathrm{V}_n}{\partial n}\, \mathbf{e}_n\right)_{\mathrm{b}}^{k} \mathrm{S_b} \approx \left(-\nu_{\mathrm{t}}\, 2\, \frac{\partial \mathrm{V}_n}{\partial n}\, \mathbf{e}_n\right)_{\mathrm{P}}^{k} \mathrm{S_b} = \left(-\nu_{\mathrm{t}}\, 2\, \frac{\mathrm{V}_n}{\delta_n}\, \mathbf{e}_n\right)_{\mathrm{P}}^{k} \mathrm{S_b} \tag{4.89}$$

The negative sign is necessary since the normal stress, $\boldsymbol{\tau}_{nn}$, is in the negative direction of $\vec{\mathbf{V}}_n$ (see Fig. 4.8). All terms are evaluated explicitly, that is the velocity is from the k^{th} iteration, the kinetic energy is from the m^{th} iteration, and the geometry is from the n^{th} time iteration.

The force due to the shear stress acting on the wall is obtained from Eq. 4.82, but its form is modified to allow easy computation of the turbulent viscosity later on.

$$\left(\frac{\vec{\mathbf{F}}_t}{\rho}\right)_{\mathrm{b}}^{k} = \left(\frac{\boldsymbol{\tau}_{nt}}{\rho}\right)_{\mathrm{b}}^{k} \mathrm{S_b} = -\underbrace{\left[\frac{\mathrm{c}_\mu^{1/4}\left(\mathrm{k}^{m}\right)^{1/2}\kappa\,\delta_n}{\ln\left(\mathrm{E}\,\delta_n^{+}\right)}\right]_{\mathrm{P}}}_{(1)} \underbrace{\left(\frac{\mathrm{V}_t}{\delta_n}\,\mathbf{e}_t\right)_{\mathrm{P}}^{k}}_{(2)} \mathrm{S_b}$$

The terms grouped in the first bracket on the right-hand side of the above expression have together the dimension of a viscosity, thus can be considered as the *wall turbulent-viscosity*, $\nu_{\mathrm{t,wall}}$:

$$\left(\frac{\vec{\mathbf{F}}_t}{\rho}\right)_{\mathrm{b}}^{k} = -\,\nu_{\mathrm{t,wall}} \left(\frac{\vec{\mathbf{V}}_t}{\delta_n}\right)_{\mathrm{P}}^{k} \mathrm{S_b}, \quad \text{with} \quad \nu_{\mathrm{t,wall}} = \left[\frac{\mathrm{c}_\mu^{1/4}\left(\mathrm{k}^{m}\right)^{1/2}\kappa\,\delta_n}{\ln\left(\mathrm{E}\,\delta_n^{+}\right)}\right]_{\mathrm{P}} \tag{4.90}$$

Both forces are added to the source term of the boundary cell P, as the contribution from the wall boundary node B. The other coefficients related to the contribution from the

boundary node B are then assigned to zero. The following steps are used in evaluating the coefficients in Eq. 4.52:

- set all coefficients related to the contribution of the boundary node B to zero: $a_B^C = a_B^D = 0,\ \left(a_P^C\right)_B = \left(a_P^D\right)_B = \left(b^D\right)_B = 0,$ and $\left(b^{2D}\right)_B = 0$
- compute $\mathbf{e}_t$ using Eqs. 4.87 and 4.88
- compute the forces due to the normal and shear stresses as source terms and linearise the source:

  <u>*x*-momentum</u>:

$$\left(b + b_P\ u_P^{+1}\right)_B = \left(\frac{F_{n,x}}{\rho} + \frac{F_{t,x}}{\rho}\right)_b$$

$$= -\left[\nu_t\left(u e_{n,x} + 2v e_{n,y} + 2w e_{n,z}\right)e_{n,x} + \nu_{t,\text{wall}}\left(v e_{t,y} + w e_{t,z}\right)e_{t,x}\right]_P \frac{S_b}{\delta_{n,P}} \qquad (4.91a)$$

$$\left(b\right)_B$$

$$- \left[\nu_t\left(e_{n,x}\ e_{n,x}\right) + \nu_{t,\text{wall}}\left(e_{t,x}\ e_{t,x}\right)\right]_P \frac{S_b}{\delta_{n,P}}\ u_P^{+1}$$

$$\left(b_P\right)_B$$

  <u>*y*-momentum</u>:

$$\left(b + b_P\ u_P^{+1}\right)_B = \left(\frac{F_{n,y}}{\rho} + \frac{F_{t,y}}{\rho}\right)_b$$

$$= -\left[\nu_t\left(2u e_{n,x} + v e_{n,y} + 2w e_{n,z}\right)e_{n,y} + \nu_{t,\text{wall}}\left(u e_{t,x} + w e_{t,z}\right)e_{t,y}\right]_P \frac{S_b}{\delta_{n,P}} \qquad (4.91b)$$

$$\left(b\right)_B$$

$$- \left[\nu_t\left(e_{n,y}\ e_{n,y}\right) + \nu_{t,\text{wall}}\left(e_{t,y}\ e_{t,y}\right)\right]_P \frac{S_b}{\delta_{n,P}}\ v_P^{+1}$$

$$\left(b_P\right)_B$$

<u>*z*-momentum</u>:

$$\left(b + b_P\ u_P^{m+1}\right)_B = \left(\frac{F_{n,z}}{\rho} + \frac{F_{t,z}}{\rho}\right)_b$$

$$= -\left[\nu_t \left(2\,ue_{n,x} + 2\,ve_{n,y} + we_{n,z}\right)e_{n,z} + \nu_{t,wall}\left(ue_{t,x} + ve_{t,y}\right)e_{t,z}\right]_P \frac{S_b}{\delta_{n,P}} \qquad (4.91c)$$

$$\underbrace{\qquad\qquad\qquad\qquad\qquad\qquad\qquad\qquad\qquad\qquad\qquad\qquad}_{(b)_B}$$

$$- \underbrace{\left[\nu_t \left(e_{n,z}\ e_{n,z}\right) + \nu_{t,wall}\left(e_{t,z}\ e_{t,z}\right)\right]_P \frac{S_b}{\delta_{n,P}}}_{(b_P)_B}\ w_P^{m+1}$$

Wall function for the k equation. The wall function is used to evaluate the source term of the k equation, $G - \varepsilon$. The turbulent kinetic-energy production, G, for cells neighboring the wall is not evaluated by Eq. 4.12, but is directly obtained from Eq. 4.83. Since the velocity has been known when solving the k equation, this information can be used in calculating the wall shear-stress term in the G equation, Eq. 4.83. The turbulent kinetic-energy dissipation, ε, is evaluated by Eq. 4.84; this contains a non-linear term in k which is then linearized. The following steps apply:

- set all coefficients related to the contribution from the boundary node B to zero: $a_B^C = a_B^D = 0,\ \left(a_P^C\right)_B = \left(a_P^D\right)_B = \left(b^D\right)_B = 0$
- compute the source, that is the energy production and dissipation, and linearise the source:

$$b + b_P\ k_P^{m+1} = \left(G_P - \varepsilon_P\right)\forall_P$$

$$= \underbrace{\left(\frac{\tau_{nt}}{\rho}\right)_b^m \frac{c_\mu^{1/4}\left(k_P^m\right)^{1/2}}{\kappa\,\delta_{n,P}}\forall_P}_{b} - \underbrace{\frac{c_\mu^{3/4}\left(k_P^m\right)^{1/2}}{\kappa\,\delta_{n,P}}\forall_P}_{b_P}\ k_P^{m+1} \qquad (4.92)$$

where the magnitude of the shear stress is evaluated with the velocity already computed from the momentum equations (see Eq. 4.82):

$$\left(\frac{\tau_{nt}}{\rho}\right)_b^m = \frac{1}{\rho}\left\|\boldsymbol{\tau}_{nt,b}\right\| = \left[\frac{c_\mu^{1/4}\left(k^m\right)^{1/2}}{\ln\left(E\,\delta_n^+\right)}\right]_P \left\|\vec{\mathbf{V}}_{t,P}^{m+1}\right\| = \left(\frac{\nu_{t,wall}}{\delta_n}\right)_P^m \left\|\vec{\mathbf{V}}_P^{m+1}\cdot\mathbf{e}_t\right\|$$

$$= \left(\frac{\nu_{t,wall}}{\delta_n}\right)_P^m \left|\left(u_P^{m+1}\,e_{t,x} + v_P^{m+1}\,e_{t,y} + w_P^{m+1}\,e_{t,z}\right)\right|$$

Note that k_P^{m+1} is unknown for this computation step, while u_P^{m+1}, v_P^{m+1}, and w_P^{m+1} are already fixed.

Wall function for the ε equation. The turbulent kinetic-energy dissipation for cells neighboring the wall is defined by Eq. 4.84. This can be easily implemented as follows:

- set all coefficients related to the neighboring cells to zero:
  $a_E = a_W = a_N = a_S = a_T = a_B = 0$
- set the coefficient at cell P to unity: aP = 1
- set the source terms by (see Eq. 4.84):

$$b = \varepsilon_P^{m+1} = \frac{c_\mu^{3/4} \left(k_P^{m+1}\right)^{3/2}}{\kappa \, \delta_{n,P}} \tag{4.93}$$

  where k_P^{m+1} is already computed in the previous step

Wall function and pressure correction. Since the discharge across the wall is zero, the coefficient of the boundary node B in Eq. 4.68 is set to zero: $a_B^p = 0$. The pressure correction at the boundary node is obtained by direct extrapolation from the cell center P: $p_B^c = p_P^c$.

4.5.5 Symmetry boundary

At the symmetry plane, for example at the east face (see Fig. 4.9), the convective transport across the plane and the shear stress along the plane are zero. These properties make the velocity at E be easily obtained from the projection of the velocity at P to the plane. For the scalar variables, k and ε, an approximation is used by extrapolating the values at P to the boundary E. The following expressions thus apply at symmetry boundaries:

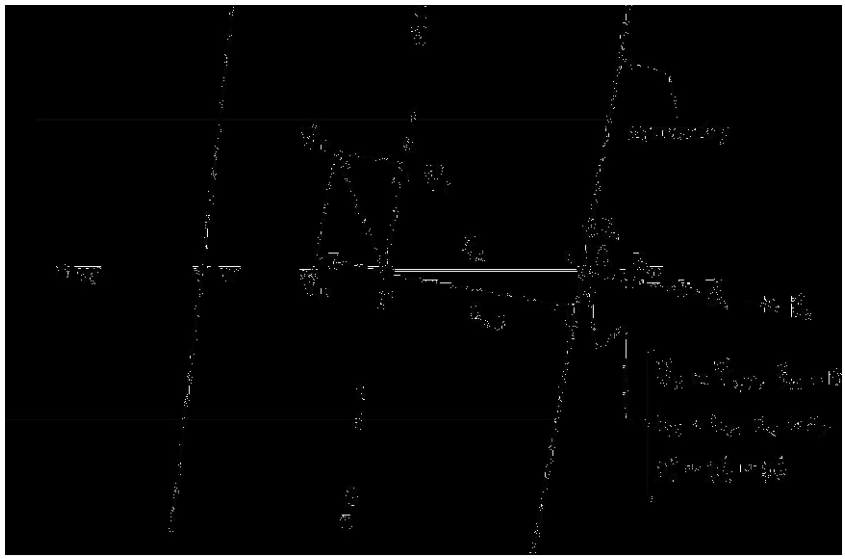

Fig. 4.9 Symmetry boundary.

$$\left.\begin{array}{l}\left(F^C\right)_e = 0 \quad \text{for all } \phi \\ \tau_{nt,e} = 0\end{array}\right\} \Rightarrow \vec{\mathbf{V}}_E = \vec{\mathbf{V}}_{t,P}$$

$$\phi_E = \phi_P \quad \text{for } \phi = k \text{ and } \varepsilon$$

The diffusive term in the momentum equations, which is due to the normal stress, is evaluated with the same method as that for the wall function approach. This term is considered as a force per unit mass acting on the plane.

Momentum equations

- set all coefficients related to the boundary node E in Eq. 4.52 to zero:
  $a_E^C = a_E^D = \left(a_P^C\right)_E = \left(a_P^D\right)_E = \left(b^D\right)_E = \left(b^{1D}\right)_E = \left(b^{2D}\right)_E = 0$
- compute $\vec{e}_t$ using Eqs. 4.87 and 4.88; its components are $e_{t,x}, e_{t,y}, e_{t,z}$.
- compute the forces due to the normal stress as source terms:

x-momentum:

$$\left(b + b_P\, u_P^{\square+1}\right)_E = \left(\frac{F_{n,x}}{\rho}\right)_e$$

$$= -\underbrace{\left[\nu_t\left(u e_{n,x} + 2v e_{n,y} + 2w e_{n,z}\right)e_{n,x}\right]_P \frac{S_e}{\delta_n}}_{(b)_E} - \underbrace{\left[\nu_t\left(e_{n,x}\, e_{n,x}\right)\right]_P \frac{S_e}{\delta_{n,P}}}_{(b_P)_E} u_P^{\square+1} \qquad (4.94a)$$

□□

y-momentum:

$$\left(b + b_P\, u_P^{\square+1}\right)_E = \left(\frac{F_{n,y}}{\rho}\right)_e$$

$$= -\underbrace{\left[\nu_t\left(2u e_{n,x} + v e_{n,y} + 2w e_{n,z}\right)e_{n,y}\right]_P \frac{S_e}{\delta_n}}_{(b)_E} - \underbrace{\left[\nu_t\left(e_{n,y}\, e_{n,y}\right)\right]_P \frac{S_e}{\delta_{n,P}}}_{(b_P)_E} v_P^{\square+1} \qquad (4.94b)$$

□□

z-momentum:

$$\left(b + b_P\, u_P^{\square+1}\right)_E = \left(\frac{F_{n,z}}{\rho}\right)_e$$

$$= -\underbrace{\left[\nu_t\left(2u e_{n,x} + 2v e_{n,y} + w e_{n,z}\right)e_{n,z}\right]_P \frac{S_e}{\delta_n}}_{(b)_E} - \underbrace{\left[\nu_t\left(e_{n,z}\, e_{n,z}\right)\right]_P \frac{S_e}{\delta_{n,P}}}_{(b_P)_E} w_P^{\square+1} \qquad (4.94c)$$

□□

k and ε equations

- set all coefficients related to the boundary node E in Eq. 4.52 to zero:
  $a_E^C = a_E^D = \left(a_P^C\right)_E = \left(a_P^D\right)_E = \left(b^D\right)_E = \left(b^{1D}\right)_E = \left(b^{2D}\right)_E = 0$
- extrapolate k and ε at P to E: $k_E = k_P$ and $\varepsilon_E = \varepsilon_P$

Pressure and velocity corrections

Since the discharge across the boundary is zero, the coefficients related to the contribution from the boundary node E in the discretized pressure correction equation, Eq. 4.68, are set to zero: $a_E^p = 0$ and $\left(b^p\right)_e = 0$.

The pressure correction gradient, $\partial p^c / \partial x_i$, needed for the velocity correction, Eq. 4.57, is computed by the finite-volume technique, Eq. 4.20, which requires the value of $\left(p^c\right)_e = \left(p^c\right)_E$. This latter is obtained by: $\left(p^c\right)_E = \left(p^c\right)_P$. The velocity at E has to be corrected such that it is parallel to the symmetry plane, since the flux across the boundary is zero. This is similar to assuming that the velocity at E is the same as the projection of the velocity vector at P on a plane parallel to the symmetry boundary: $\vec{\mathbf{V}}_E = \vec{\mathbf{V}}_{t,P}$.

4.5.6 Surface boundary

At the (water) surface (see Fig. 4.10) the velocity is parallel to the boundary, the discharge across the (water) surface is zero, and thus there is no convective transport across this boundary. The shear stress along the surface, in addition, is neglected. This allows the specification of the velocity along the surface boundary the same as the projection of the velocity at the cell center. The water surface does not create turbulence; therefore, the kinetic energy along the surface boundary is set to zero. The energy dissipation, ε, at cell center is obtained in a similar manner as that at the wall boundary; a correction may be given to reduce the computed value as has been reported in some previous works (*Krishnappan and Lau*, 1986).

For the pressure, a hydrostatic distribution is assumed between the surface and the cell center. The pressure at the surface is supposed to be atmospheric; if it is not the case, the surface is moved according to the pressure defect, relative to a reference pressure, which is prescribed at a particular cell. This reference cell is normally defined at the top-most cell of the outflow boundary. This is similar to prescribe a constant flow-depth condition at the outflow. The surface correction is done at the end of each time step. An under-relaxation factor and a limitation may be imposed to avoid excessive change of the computational domain. The procedures to handle surface boundary are described in the following paragraphs.

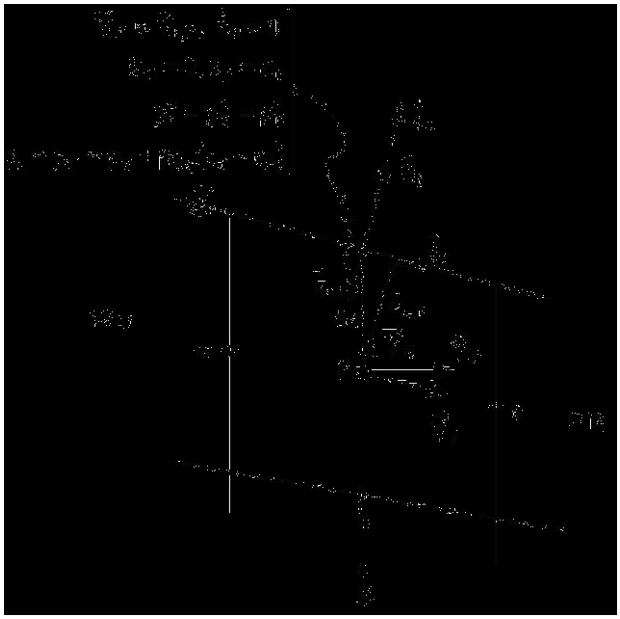

Fig. 4.10 Surface boundary.

Momentum equations

- set all coefficient related to the boundary node T in Eq. 4.52 to zero:
  $a_T^C = a_T^D = \left(a_P^C\right)_\Gamma = \left(a^D\right)_\Gamma = \left(b^D\right)_\Gamma = \left(b^{2D}\right)_\Gamma = 0$
- compute $\mathbf{e}_{\ell}$ using Eqs. 4.87 and 4.88
- compute the forces due to the normal stress as source terms:

<u>*x*-momentum</u>:

$$\left(b + b_P\, u_P^{\square+1}\right)_T = \left(\frac{F_{n,x}}{\rho}\right)_t$$

$$= \underbrace{-\left[\nu_t\left(u e_{n,x} + 2v e_{n,y} + 2w e_{n,z}\right)e_{n,x}\right]_P \frac{S_t}{\delta_n}}_{(b)_T} \underbrace{-\left[\nu_t\left(e_{n,x}\, e_{n,x}\right)\right]_P \frac{S_t}{\delta_{n,P}}}_{(b_P)_T} u_P^{\square+1} \qquad (4.95a)$$

<u>*y*-momentum</u>:

$$\left(b + b_P\, u_P^{\square+1}\right)_T = \left(\frac{F_{n,y}}{\rho}\right)_t$$

$$= \underbrace{-\left[\nu_t\left(2u e_{n,x} + v e_{n,y} + 2w e_{n,z}\right)e_{n,y}\right]_P \frac{S_t}{\delta_n}}_{(b)_T} \underbrace{-\left[\nu_t\left(e_{n,y}\, e_{n,y}\right)\right]_P \frac{S_t}{\delta_{n,P}}}_{(b_P)_T} v_P^{\square+1} \qquad (4.95b)$$

z-momentum:

$$\left(b + b_P\ u_P^{+1}\right)_T = \left(\frac{F_{n,z}}{\rho}\right)_t$$

$$= \underbrace{-\left[\nu_t\left(2\,ue_{n,x} + 2\,ve_{n,y} + we_{n,z}\right)e_{n,z}\right]\frac{S_t}{\delta_n}}_{(b)_T} \underbrace{- \left[\nu_t\left(e_{n,z}\ e_{n,z}\right)\right]\frac{S_t}{\delta_{n,P}}}_{(b_P)_T}\ w_P^{+1} \qquad (4.95c)$$

k equation

- set all coefficient related to the boundary node T in Eq. 4.52 to zero:
  $a_T^C = a_T^D = \left(a_P^C\right)_T = \left(a^D\right)_T = \left(b^D\right)_T = \left(b^{2D}\right)_T = 0$
- set the surface kinetic energy at T to zero: $k_T = 0$

ε equation

- set all coefficients related to all neighboring cells to zero:
  $a_E = a_W = a_N = a_S = a_T = a_B = 0$
- set the coefficient at cell P to unity: $a_P = 1$
- set the source terms by (see Eq. 4.84 and also *Krishnappan and Lau*, 1986):
  $$\varepsilon_P^{m+1} = c_f \frac{c_\mu^{3/4}\left(k_P^{m+1}\right)^{3/2}}{\kappa\,\delta_{n,P}} \qquad (4.96)$$
  where c_f is an empirical constant, which is set to 0.164

Pressure and velocity corrections

- set the coefficient at T in Eq. 4.68 to zero: $a_T^p = 0$
- extrapolate the pressure correction at P to T: $p_T^c = p_P^c$
- correct the pressure and the velocity
- extrapolate the velocity at P to T and correct this velocity: $\vec{\mathbf{V}}_T = \vec{\mathbf{V}}_{t,P}$

Surface correction

- extrapolate the pressure at P to T by assuming a hydrostatic distribution:
  $p_T = p_P + \rho g_z \Delta z_{PT}$ (see Fig. 4.11a), with g_z the *z*-component of $\vec{\mathbf{g}}$ (generally negative)
- compute the surface correction based on the pressure-defect relative to the reference pressure: $\Delta h^{(p)} = \left(p_T - p_{ref}\right)/\left(\rho|g_z|\right)$

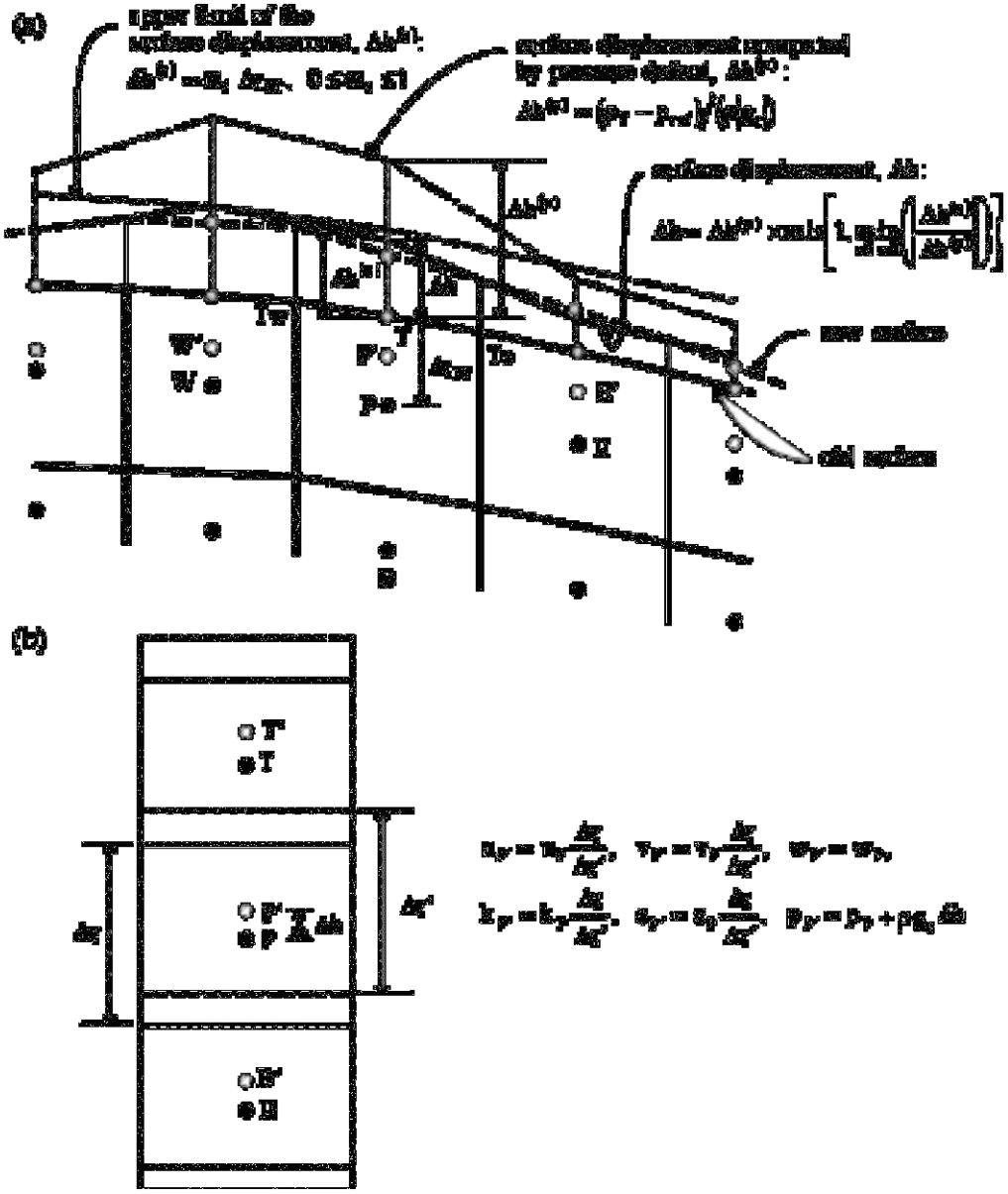

Fig. 4.11 Surface correction: (a) displacement of the vertices of the surface boundary cells, (b) modification of the variables at the new cell centers.

- compute the upper limit of the surface correction based on the cell thickness:
  $\Delta h^{(z)} = \varpi_1 \Delta z_{PT}$, $0 \le \varpi_1 \le 1$
- compute the displacement of the boundary node T by:
  $$\Delta h = \Delta h^{(p)} \times \min\left[1, \min_{\text{all cells}}\left(\left|\frac{\Delta h^{(z)}}{\Delta h^{(p)}}\right|\right)\right]$$
- since a cell is defined by its vertices, □ h at T needs to be distributed over the vertices, Te, Tw, Tn, Ts (see Fig. 4.11a); linear interpolation is used
- move the cell vertices of the free-surface boundary cells according to the new coordinates of Te, Tw, Tn, Ts

- reconstruct the mesh, maintain the number of cells in the vertical and their relative positions to the local depth
- use linear interpolation to get variables at the new cell centers (see Fig. 4.11b) in order to maintain the continuity:

$$u_{P'} = u_P \frac{\Delta z}{\Delta z'}, \quad v_{P'} = v_P \frac{\Delta z}{\Delta z'}, \quad w_{P'} = w_P,$$

$$k_{P'} = k_P \frac{\Delta z}{\Delta z'}, \quad \varepsilon_{P'} = \varepsilon_P \frac{\Delta z}{\Delta z'}, \quad p_{P'} = p_P + \rho g_z \Delta h$$

- continue the computation to the next time level

4.6 Solution procedures

4.6.1 Spatial discretisation

Applying the discretized governing equations, Eqs. 4.52 and 4.68 requires spatial discretisation of the computational domain. The domain is divided into Ni–2, Nj–2, and Nk–2 cells in the *x*-, *y*-, *z*-directions, respectively, from which there are Ni, Nj, and Nk nodes (interior, boundary, and dummy nodes) in the corresponding directions. A typical spatial discretisation is shown in Fig. 4.12. The cell and node are denoted by a single index; the cells are indexed by ijk = 2,3,…,Nijkm, going along the *y*-direction (j = 2,3,…,Nj–1), the *x*-direction (i = 2,3,…,Ni–1), and the *z*-direction (k = 2,3,…,Nk–1), while the nodes are indexed by ijk = 1,2,…,Nijk. With this indexing, the single-index ijk for a cell and for its six-neighbors can be easily obtained from their position in the (*x*,*y*,*z*) space (see Table 4.5).

Writing Eq. 4.52 or 4.68 for all cells, ijk = 2,3,…,Nijkm, produces a series of algebraic linear equations which can be presented in a matrix form as follows:

$$\mathbf{A}\,\mathbf{\Phi} = \mathbf{B} \tag{4.97}$$

The matrix **A** contains the coefficients of the equations, a_{nb} and a_P, **Φ** is a column matrix of the dependent variable, and **B** is a column matrix of the source terms. The matrix **A** has diagonal blocks which are themselves tridiagonal, and sub- and super-diagonal blocks in which each block has two diagonals, thus it has only 7 non-zero diagonals while the other elements are zero. It is then not necessary to store all elements of the matrix A; only those seven diagonals need to be stored. To facilitate the storage, each non-zero diagonal is stored in a separate column matrix, i.e. $\mathbf{A}_{nb}$, nb = EWNSTB, and $\mathbf{A}_P$. Fig. 4.13 shows the form of the matrix **A**.

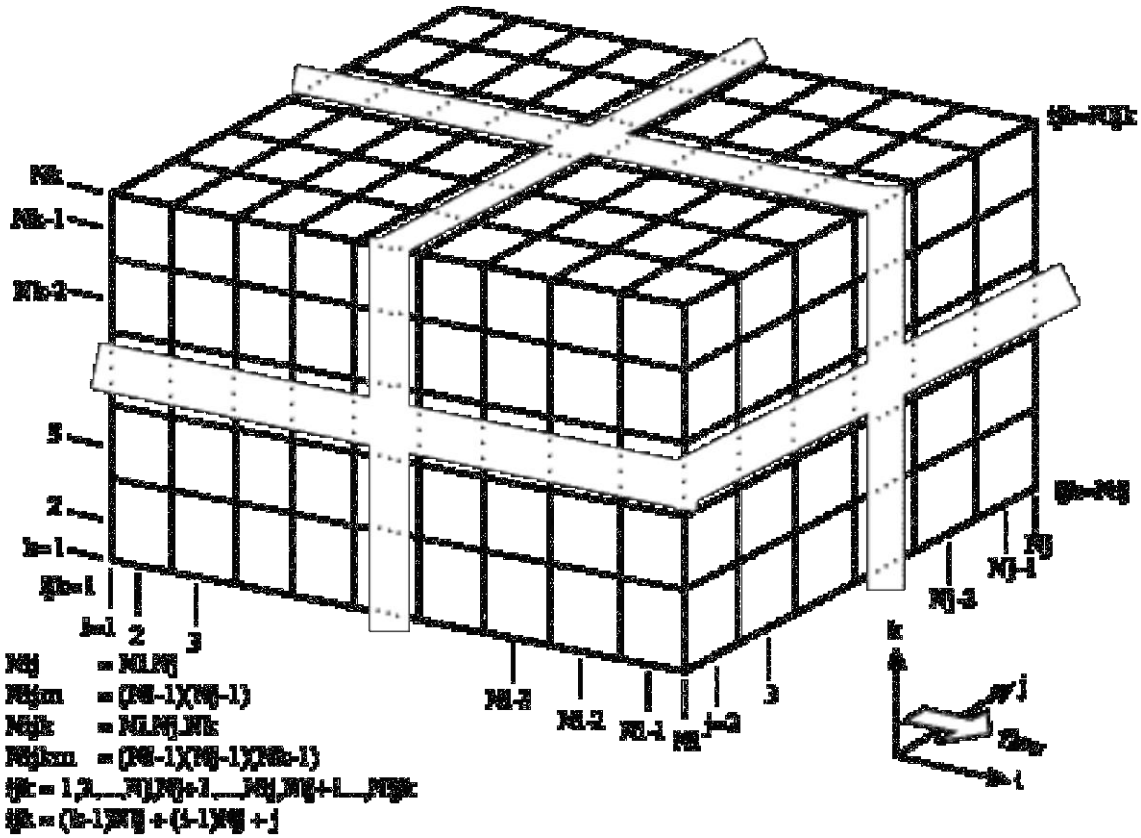

Fig. 4.12 Typical spatial discretisation of the computational domain.

Table 4.5 Triple and single indexing of computational cells.

Direction	Nodal index	Cell index
x–direction	i = 1, 2, ..., Ni	i = 2, 3, ..., Ni–1
y–direction	j = 1, 2, ..., Nj	j = 2, 3, ..., Nj–1
z–direction	k = 1, 2, ..., Nk	k = 2, 3, ..., Nk–1
Cells in the *xy*–plane	ij = 1, 2, ..., Nij (Nij = Ni × Nj)	ij = 2, 3, ..., Nijm [Nijm = (Ni–1) × (Nj–1)]
Cells in the domain	ijk = 1, 2, ..., Nijk (Nijk = Nij × Nk)	ijk = 2, 3, ..., Nijkm [Nijkm = Nijm × (Nk–1)]
Cell	Triple-index	Single-index
P	i,j,k	ijk = (k–1) Nij + (i-1) Nj + j
E	i+1,j,k	ijk + Nj
W	i–1,j,k	ijk – Nij
N	i,j+1,k	ijk + 1
S	i,j–1,k	ijk – 1
T	i,j,k+1	ijk + Nij
B	i,j,k–1	ijk – Nij

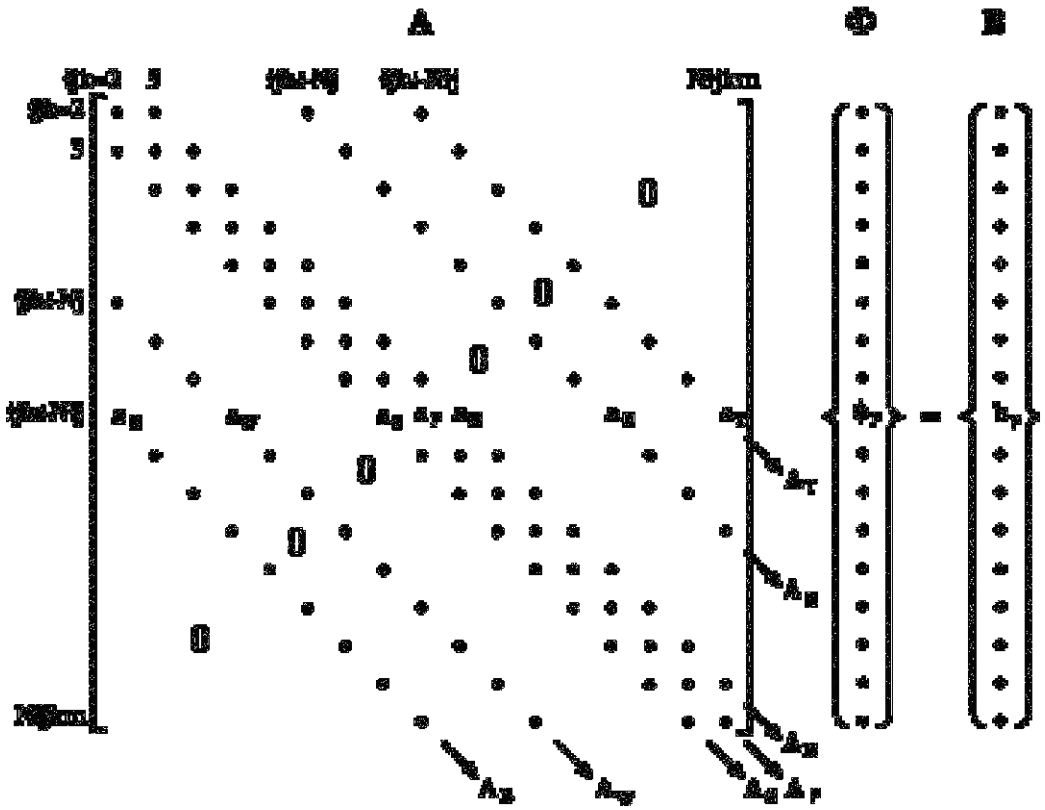

Fig. 4.13 The structure of the matrix coefficient **A**; all elements not shown are zero.

4.6.2 Matrix solvers

The solution of Eq. 4.97 is achieved by iteration techniques. Two matrix-solver routines are available in this model, i.e. the SIPSOL, for the **S**trongly-**I**mplicit **P**rocedure method (*Stone*, 1968), and the CGSTAB, for the **C**onjugate **G**radient **S**tabilized method of Van den Vorst (see *Ferziger and Peric*, 1997, pp. 105-106). For the first solver, the SIPSOL, the solution procedure follows the one proposed by Jesshope (*Jesshope*, 1979) with some modification to suit for the 7-point computational-cells of the three-dimensional cases. The CGSTAB routine is taken from the reference (*Ferziger and Peric*, 1997, pp. 105-106) without any major modification. Without going into detail, the iterative procedure of the routines can be summarized as follows:

- given an initial solution, define a residue, that is the difference between the left- and right-hand side of Eq. 4.97,
- calculate an increment based on the initial solution and residue,
- update the solution by adding the increment to the initial solution,
- repeat the procedure until convergence.

The iterative procedure to get the solution of Eq. 4.97 is commonly denoted as *inner-iteration*. This is to be distinguished from the *outer-iteration*, that is the one necessary to seek the solution satisfying the momentum and continuity equations (the □-iteration) or all the governing equations, the momentum, continuity, and k-ε equations (the m-

iteration). The inner-iteration seeks the solution for each dependent variable, ϕ, across the computational domain for given coefficient and source terms, **A** and **B**, which are constants. The solution for every dependent variable, ϕ (ϕ = u,v,w,p,k,ε), is sought one after another. In the outer-iteration, solution is obtained for every dependent variable that all together satisfies the governing equations. In each outer-iteration, the coefficient and source terms are adjusted, where as in the inner-iteration, they are kept constant.

When performing the inner-iteration, it is important to decide when to quit the solver. Since the solution of Eq. 4.97 for a particular variable, u for example, at a particular iteration level, □, does not necessarily satisfy all governing equations for u,v,w,p,k,ε, it is inefficient to carry out a rigorous iteration at this stage. A restricted number of iterations and a moderate convergence criterion will do. A single or at most a two inner-iteration is generally sufficient to solve the momentum equation for u, v, and w since their equations are of convection types. The pressure correction however requires a number of sweeps over the entire domain to have a solution error within a sufficiently small allowable limit. The convergence of the k and ε equations, being of convection-diffusion types, may also be slow. This is due to the need of a small relaxation factor in the iteration process to avoid oscillations. The residue of the solution of Eq. 4.97 is used as the basis to detect the solution error; it is defined as:

$$\Re_\phi = \sum_{\text{all cells}} \left| b - a_P \phi_P - \sum a_{nb} \phi_{nb} \right| \tag{4.98}$$

The calculation in the inner-iteration is stopped when either one of the following criteria is satisfied:

$$\Re_\phi^{mi} \le \lambda_1 \tag{4.99a}$$

$$\Re_\phi^{mi} / \Re_\phi^{mi=1} \le \lambda_2 \tag{4.99b}$$

$$mi > NIT_\phi \tag{4.99c}$$

in which $\Re_\phi^{mi}$ is the sum of absolute residues over all cells after mi^{th} iterations for any variable ϕ; λ_1 and λ_2 are prescribed convergence criteria; and NIT is the maximum number of inner-iterations. Table 4.6 gives the default values of these criteria for each variable ϕ.

Table 4.6 Criteria to stop the inner iteration

ϕ	λ_1	λ_2	NIT
u,v,w	10^{-6} [m^4/s^2]	10^{-3}	2
p	10^{-5} [m^3/s]	10^{-2}	20
k	10^{-6} [m^5/s^3]	10^{-3}	5
ε	10^{-6} [m^5/s^4]	10^{-3}	5

The calculation sequence is presented in the calculation diagram depicted in Fig. 4.14, and is summarized as follows:

a) Initialize all dependent variable: $\phi = \phi^o$ (u,v,w,p,k,ε are given).

b) Define the geometrical properties, discretise the spatial domain.

c) Compute initial discharges, q_{cf}, and eddy viscosity, ν_t.

d) Assign estimated pressures p^*,.

e) Construct coefficients of the discretized momentum equations.

f) Solve the momentum equations for u^*, v^*, and w^*, consecutively.

g) Construct coefficients of the discretized pressure correction equation.

h) Solve the pressure-correction equation for p^c and subsequently update the pressure, p, and velocities at the cell centers, u, v, and w.

i) Compute the new discharge across cell faces, q_{cf}.

j) Return to step ‘d’ if the velocity components and pressure do not satisfy the momentum and continuity equations.

k) Construct coefficients of the discretized k transport equation and solve for k; do the same procedure to get ε.

l) Compute the eddy viscosity, ν_t, from the new k and ε

m) Update the water surface if the solution has converged, otherwise assign the new u, v, w, p, k, and ε as the new ‘old’ values and return to step ‘d’.

n) Stop the iteration if the steady-state solution has been reached, otherwise proceed to the next time step, return to step ‘d’.

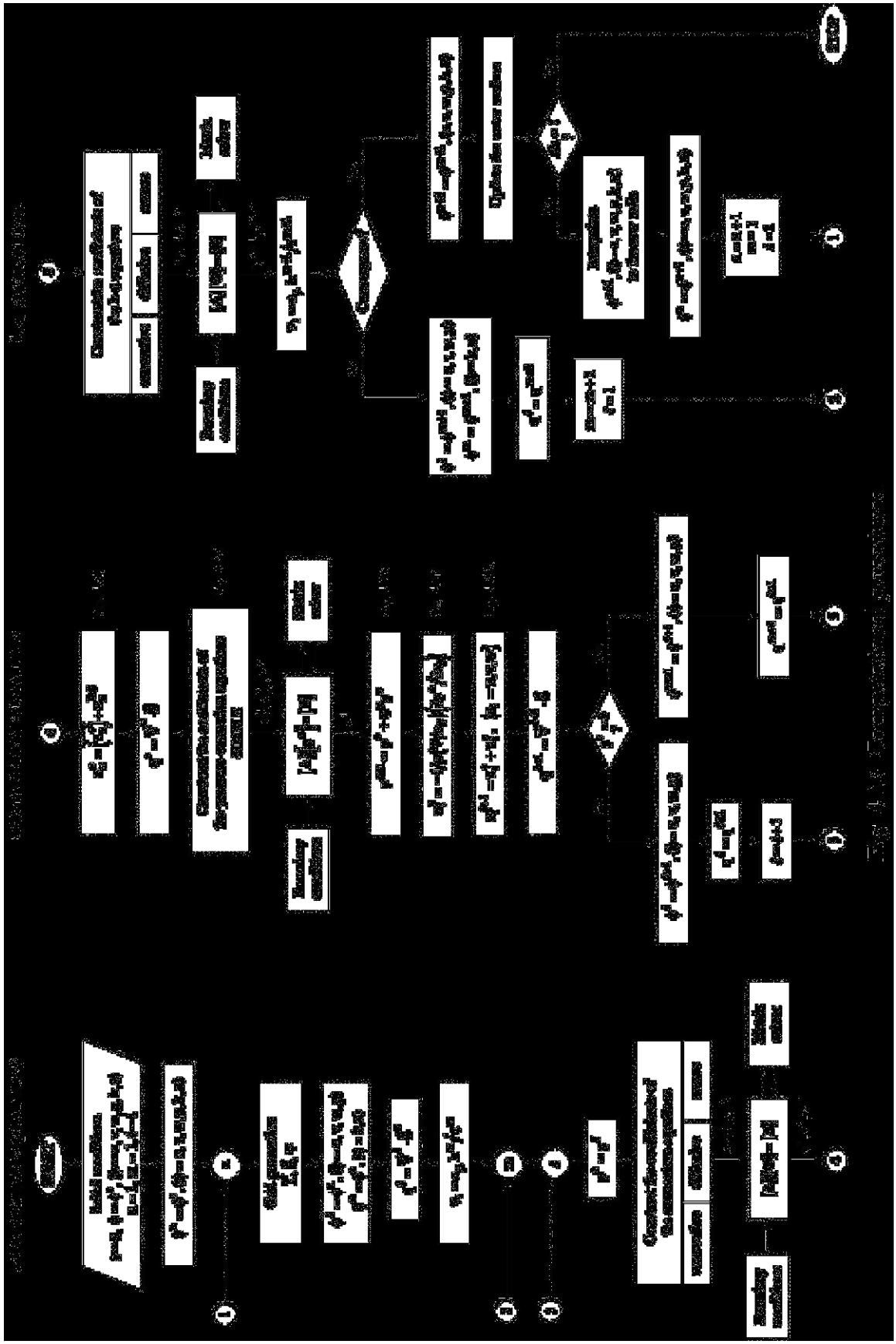

4.7 Summary

Development of a three-dimensional numerical flow model has been presented. The model is based on the approximate solution of the Reynolds averaged Navier-Stokes equations, the continuity equations, and the k-ε turbulence closure model. These equations are expressed in a general convective-diffusive transport equation on a Cartesian coordinate system. The working equation of the model is obtained by discretizing this transport equation by using finite volume techniques on a structured, collocated, boundary-fitted, hexahedral control-volume grid. The hybrid (*Spalding*, 1972) or power-law (*Patankar*, 1980) upwind-central difference scheme, combined with the deferred correction method (*Ferziger and Peric*, 1997), is employed in the discretisation of the governing equations. The solution of the working equation is achieved by an iterative method according to SIMPLE algorithm (*Patankar and Spalding*, 1972). Along solid boundaries, use is made of the wall function method, while along surface boundaries the pressure defect is used to define the surface position. On other boundaries, namely inlet, outlet, and symmetry boundaries, classical methods are used, such as zero gradients, zero stresses, or known functions.

The model is applicable for steady state flow cases, but not for transient ones. The time step is used as an iteration step to mark, notably, the change of the computational domain due to the moving surface boundary.

References

Cebeci, T., and Bradshaw, P. (1977). *Momentum Transfer in Boundary Layers*., Hemisphere Publ. Co., Washington, USA.

Ferziger, J. H., and Peric, M. (1997). *Computational Methods for Fluid Dynamics*., Springer-Verlag, Berlin, Germany.

Fletcher, C. A. J. (1997). *Computational Techniques for Fluid Dynamics, Vol. 1*., Springer, Berlin, Germany.

Hirsch, C. (1988). *Numerical Computation of Internal and External Flows, Vol. 1: Fundamentals of Numerical Discretization*., John Wiley & Sons, Chichester, England.

Jesshope, C. R. (1979). "SIPSOL – A suite of subprograms for the solution of the linear equations arising from elliptical partial differential equations." *Computer Physics Communications*, 17383-391.

Kobayashi, M. H., and Pereira, J. C. F. (1991). "Numerical comparison of momentum interpolation methods and pressure-velocity algorithms using non-staggered grids." *Communications in Applied Numerical Methods*, 7173-186.

Krishnappan, B. G., and Lau, Y. L. (1986). "Turbulence modeling of flood plain flows." *ASCE, J. Hydr. Engrg.*, 112(4), 251-266.

Launder, B. E., and Spalding, D. B. (1974). "The numerical computation of turbulent flows." *Computer Methods in Applied Mechanics and Engineering*, 3269-289.

Obi, S., Peric, M., and Scheuerer, G. (1989). "A finite-volume calculation procedure for turbulent flows with second-order closure and collocated variable arrangement." *Seventh Symposium on Turbulent Shear Flows*, Stanford University, California, 2, 17.4.1-17.4.6.

Olsen, N. R. B., and Kjellesvig, H. M. (1998). "Three-dimensional numerical flow modeling for estimation of spillway capacity." *IAHR, J. of Hydr. Res.*, 36(5), 775-784.

Patankar, S. V. (1980). *Numerical Heat Transfer and Fluid Flow.*, Hemisphere Publishing Corp., New York, USA.

Patankar, S. V., and Spalding, D. B. (1972). "A calculation procedure for heat, mass and momentum transfer in three-dimensional parabolic flows." *Int. J. Heat Mass Transfer*, 151787-1806.

Rhie, C. M., and Chow, W. L. (1983). "Numerical study of the turbulent flow past an airfoil with trailing edge separation." *AIAA Journal*, 21(11), 1525-1532.

Rodi, W. (1984). *Turbulence models and their application in hydraulics: A state of the art review.*, IAHR Monograph, Delft, NL.

Spalding, D. B. (1972). "A novel finite difference formulation for differential expressions involving both first and second derivatives." *Int. Journal for Numerical Methods in Engineering*, 4551-559.

Stone, H. L. (1968). "Iterative solution of implicit approximation of multidimensional partial differential equations." *SIAM J. on Numerical Analysis*, 5530-558.

Versteeg, H. K., and Malalasekera, W. (1995). *An Introduction to Computational Fluid Dynamics: The Finite Volume Method.*, Longman Group, Essex, England.

Wu, W., Rodi, W., and Wenka, T. (2000). "3D Numerical modeling of flow and sediment transport in open channels." *ASCE, J. Hydr. Engrg.*, 126(1), 4-15.

Notations

Capital letters

$\mathbf{A}$	$[m^3/s]$	coefficient matrix of the momentum and k-ε equations.
$\mathbf{A}^p$	$[m^3/s/Pa]$	coefficient matrix of the pressure-correction equation.
$\mathbf{B}$		vector matrix of the source terms:
	$[m^4/s^2]$	for the momentum equation,
	$[m^5/s^3]$	for the k-equation,
	$[m^5/s^4]$	for the ε-equation.
$\mathbf{B}^p$	$[m^3/s]$	vector matrix of the source terms for the pressure-correction equation.

$\mathcal{B}$, $\Delta\mathcal{B}$	[–]	constant and wall roughness function.
$\mathcal{E}$	[–]	wall roughness coefficient.
$E_{\Delta t}$	[–]	time step factor.
F, F^C, F^D		total, convective, and diffusive transports:
	[m^4/s^2]	of the momentum flux,
	[m^5/s^3]	of the turbulent kinetic-energy flux,
	[m^5/s^4]	of the dissipation of kinetic-energy flux.
G	[m^2/s^3]	turbulence kinetic-energy production.
$\vec{\mathbf{L}}$	[m]	length vector.
NIT	[–]	number of inner iterations.
P	[–]	cell center.
Pe	[–]	grid Peclet number, the ratio between the convective and diffusive conductance.
Q	[m^3/s]	discharge across sectional area of channels.
R		source terms:
	[m/s^2]	of the momentum equation,
	[m^2/s^3]	of the k-equation,
	[m^2/s^4]	of the ε-equation.
Re	[–]	Reynolds number.
$\vec{\mathbf{S}}$	[m^2]	cell-face surface vector.
$\vec{\mathbf{V}}$	[m/s]	velocity vector.
$\vec{\mathbf{V}}_n$	[m/s]	normal velocity vector.
$\vec{\mathbf{V}}_t$	[m/s]	parallel (tangential) velocity vector.
$\vec{\mathbf{V}}_*$	[m/s]	friction velocity vector.
$\forall$	[m^3]	cell volume.
Lower case letters		
a_P, a_{nb}	[m^3/s]	matrix coefficients of the momentum and k-ε equations.
a_P^C, a_{nb}^C	[m^3/s]	matrix coefficients of the momentum and k-ε equations due to the convective transport.
a_P^D, a_{nb}^D	[m^3/s]	matrix coefficients of the momentum and k-ε equations due to the diffusive transport.
a_P^p, a_{nb}^p	[$m^3/s/Pa$]	matrix coefficients of the pressure-correction equations.
$\tilde{a}_P$	[m^3/s]	under-relaxed matrix coefficient.
$b, \tilde{b}$		source term and under-relaxed source term:
	[m^4/s^2]	of the momentum equation,
	[m^5/s^3]	of the k-equation,
	[m^5/s^4]	of the ε-equation.
b^D	[m^4/s^2]	source term due to the diffusive-correction.
b_P	[m^3/s]	source term coefficient due to the source linearisation.
b^p	[m^3/s]	source term coefficient of the pressure-correction equation.
c_1, c_2, c_μ	[–]	constants of the k-ε equation.
$\vec{\mathbf{e}}$	[m]	directional unit vector.
f^D	[–]	coefficient of the hybrid and power-law convective-diffusive schemes, a function of the grid Peclet number.

g_x, g_y, g_z	[m/s^2]	Cartesian components of the gravitational acceleration.
k	[m^2/s^2]	turbulent kinetic energy.
k_s	[m]	wall roughness height.
k_s^+	[–]	Reynolds number based on the friction velocity and wall roughness.
n	[m]	normal direction.
p, p^*, p^c	[Pa]	pressure, estimated pressure, and pressure correction.
q	[m^3/s]	discharge.
q^*	[m^3/s]	estimated discharge obtained from (u^*, v^*, w^*).
q^c, q^{RC}, q^{no}	[m^3/s]	discharge corrections due to the velocity-correction, cell-face interpolation, and non-orthogonal terms.
t, Δt	[s]	pseudo-time and pseudo-time step.
u,v,w	[m/s]	Cartesian velocity components.
u^*, v^*, w^*	[m/s]	Cartesian velocity components obtained with estimated pressures.
u', v', w'	[m/s]	fluctuating parts of Cartesian velocity components.
u_*, v_*, w_*	[m/s]	Cartesian friction-velocity components.
u_n^*	[m/s]	velocity obtained with estimated pressure.
u_n^c	[m/s]	pressure corrections.
$u_n^{impl}, u_n^{RC}, u_n^{no}$	[m/s]	pressure correction components: implicit, Rhie-and-Chow, non-orthogonal.
x, y, z	[m]	Cartesian coordinate components.
Greek characters		
Γ	[m2/s]	diffusion coefficient.
β	[–]	linear interpolation factor.
Δh	[m]	surface displacement.
$\Delta h^{(p)}$	[m]	surface displacement due to the pressure.
$\Delta h^{(z)}$	[m]	surface displacement limitation according to the cell size.
δ_n	[m]	normal distance.
δ_n^+	[–]	dimensionless normal-distance.
ε	[m^2/s^3]	dissipation of the turbulent kinetic energy.
ϕ		flow variable, the dimensional unit depends on the variable of which it represents.
$\mathbf{\Phi}$		matrix of the flow variables.
κ	[–]	Karman constant.
λ_1		convergence criterion: allowable maximum residue of the solution:
	[m^4/s^2]	of the momentum equation,
	[m^4/s^2]	of the k-equation,
	[m^4/s^2]	of the ε-equation,
	[m^3/s]	of the pressure-correction equation.
λ_2	[–]	convergence criterion: allowable relative maximum-residue of the solution.
ν, ν_t	[m^2/s]	kinematic viscosity and turbulent eddy viscosity.
$\nu_{t,wall}$	[m^2/s]	wall eddy-viscosity.
ρ	[kg/m^3]	density of water.

$\varpi, \varpi_1, \varpi^p$	[–]	under-relaxation factors.
$\sigma_k, \sigma_\varepsilon$	[–]	constants of the k-ε model.
τ	[N/m^2]	Reynolds stress.
ξ, η, ζ	[m]	local coordinate directions.
Other characters		
$\Re_\phi$		total residue:
	[m^4/s^2]	of the momentum equation,
	[m^4/s^2]	of the k-equation,
	[m^4/s^2]	of the ε-equation,
	[m^3/s]	of the pressure-correction equation.
$\nabla, \vec{\nabla}$	[1/s]	divergent and gradient nabla operators.
Superscripts		
c		corrected value.
□+1		iteration level indices.
m, m+1		iteration level indices.
n, n+1		time level indices.
*		estimated value.
Subscripts		
P		cell center.
i, j, k		Cartesian component indices.
cf = e,w,n,s,t,b		cell faces: the east, west, north, south, top, and bottom.
□		dependent variable index.
n, *t*		normal and tangential direction component indices.
nb = E,W,N,S,T,B		neighboring cells: the East, West, North, South, Top, and Bottom.

Chapter 5

5 Numerical Simulation

Abstract

The numerical model presented in the preceding chapter is here applied to simulate the flow around a cylinder. Before the simulation, a series of calibration and test runs were performed, in which the measured data in the uniform approach flow were used. A calibration run was performed to find the model value of the equivalent roughness of the bed. The test run was intended as a verification of the model basic performance, notably against different criteria of pressure convergence *vis à vis* surface boundary computation. Two cases of flow around a cylinder, namely the flat channel bed of the previous study (*Yulistiyanto*, 1997) and the scoured channel bed of the present work (see Chapters 2 and 3), were subsequently simulated. The validation of the model has been evidenced by the good comparison between the model results and the measured data for both cases. This was shown notably by the velocity comparison, which was done in several forms such as velocity profiles, velocity vectors, and vorticities. For the scoured channel-bed case, an attempt was also made to evaluate the computed turbulent kinetic energy. Except in the downstream of the cylinder, the computed values compare favorably with the measured ones. A good comparison of the computed and measured water surface profiles was achieved, with the exception in regions of strong pressure gradient. An improvement of the surface boundary treatment, i.e. by enforcing kinematic condition, is proposed at the end of the chapter.

Résumé

Un modèle mathématique tridimensionnel de l'écoulement en surface libre a été présenté dans le chapitre précédent (voir Chapitre 4). Ce modèle a été testé pour un écoulement uniforme. Il a été ensuite appliqué pour simuler deux cas d'écoulements autour d'un cylindre soit dans un canal à fond plat et dans une fosse d'érosion (affouillement) supposée rigide. Les résultats des calculs ont pu être comparés avec les mesures. Le modèle est satisfaisant, les calculs correspondent aux mesures. Le modèle produit un champ de vitesses autour du cylindre qui concorde avec les mesures. Le profil de la surface est moins satisfaisant, le modèle ayant sous-estimé la profondeur de l'eau dans le plan normal de l'écoulement. Une proposition d'amélioration de calcul de la surface libre est abordée à la fin du chapitre.

5.1 Introduction

The numerical model presented in the preceding chapter (Chapter 4) shall be used to simulate flow around a cylinder. Two cases of flow around a cylinder were considered, namely flat channel bed and scoured channel bed. The first case was the object of experimental and numerical investigations of the previous study (*Yulistiyanto*, 1997), whereas the second case was experimentally investigated in the present study (see Chapters 2 and 3). In both studies, the experimental investigations were performed by 3D instantaneous velocity measurements using an acoustic Doppler profiler. The experimental data thus obtained allow detailed comparisons of the simulation results to be performed, not only for the velocity fields but also for the turbulence quantities. In the previous numerical work (*Yulistiyanto*, 1997), a 2D model was used thus restricting the comparison to the depth-averaged velocity fields. Nevertheless, the result of this 2D model was promising and encouraged the 3D model development.

The model has various constants, such as those in the k-ε transport equations (c_μ, c_1, c_2, σ_k, and σ_ε) and the ones of the logarithmic velocity law (κ and k_s). In the present model, the k-ε model constants (see Table 4.1 in Chapter 4) and the Karman constant ($\kappa = 0.4$) are invariant and are applied to all flow conditions. The equivalent roughness of the wall, k_s, characterizes the roughness of the physical solid boundaries (the channel wall, the cylinder, and especially the channel bed). It is the only "physical link" of the model to the roughness characteristics of solid boundaries. In order to obtain the correct model-value of k_s, a calibration had to be performed. Using a uniform flow condition (with neither the cylinder nor the scour hole), various k_s-values were tested to obtain the best match between the computed and measured flow fields. In the calibration run, adjustment of the uniform flow depth (which will be the approaching flow depth) was also accordingly needed.

Before performing the simulation of flow around a cylinder, which is a highly complex 3D flow, a series of test runs were carried out for the simple uniform flow case. The test runs were aimed at investigating the basic performance of the model and verifying some computational techniques adopted in the model. This simple well-known flow condition was the best tool to serve this purpose. The experimental data for the comparison were taken from the same preceding work (*Yulistiyanto*, 1997).

The computer code of the model is written in FORTRAN-77. All simulation runs were executed on a personal computer. The computational CPU time of the simulation run is typically 70 to 100 hours.

5.2 Experimental data

5.2.1 Flow around a cylinder on a flat channel bed

The measured data of flow around a cylinder on a flat channel bed are obtained from the previous work (*Yulistiyanto*, 1997). The data were produced from the measurements with and without the cylinder in place. Given below is a brief description of the data; details of the measurements and of the data can be found elsewhere (see *Yulistiyanto*, 1997).

The measurements were conducted in a rectangular *metal-bed* (smooth) tilting flume of an effective length L = 38 [m] and width B = 2 [m]. The uniform approach flow was established by: discharge $Q = 0.250\,[m^3/s]$ $(Q/B = 0.125\,[m^2/s])$, flow depth $h_\infty = 18.5$ [cm] $(B/h_\infty = 10.8)$, cross-sectional-averaged velocity $U_\infty = 0.67$ [m/s] (Re = 123,950 and Fr = 0.5), and bed slope $S_o = 6.25 \times 10^{-4}$. An acoustic Doppler velocity profiler (ADVP), designed and conceived at LRH (see *Lhermitte and Lemmin*, 1994), was used to measure the instantaneous velocity vector. This non-intrusive instrument measures instantaneously three-dimensional velocities at a number of layers (in 5 [mm] intervals) within a water column (flow depth) based on the Doppler shift of the backscattered acoustic signals. The ADVP was fixed at a compartment located below the metal bed, at the center line, $x_L = 16$ [m] from the entrance. A Mylar film, permeable to acoustic waves, was used to separate the instrument compartment and the flow. A PVC circular cylinder of diameter $D_p = 22$ [cm] $(B/D_p = 9)$ was installed vertically with respect to the bed. The cylinder was attached to a movable carriage, allowing it to be positioned at predetermined measurement stations around the ADVP. Vertical distributions of 3D instantaneous velocities were obtained in five planes, α = 0°, 45°, 90°, 157.5°, and 180°. The vertical distributions of the time-averaged velocities, (u,v,w), turbulence intensities, $(\sqrt{\overline{u'u'}}, \sqrt{\overline{v'v'}}, \sqrt{\overline{w'w'}})$, and the Reynolds stresses, $(-\rho\overline{u'w'}, -\rho\overline{v'w'})$, were subsequently deduced.

From the measurement in the uniform flow condition (the flow without the cylinder in place), an equivalent roughness of $k_s = 0.54\,[mm]$ was reported (*Yulistiyanto*, 1997). This value was obtained by using the Colebroke-White equation. A reavaluation of the k_s by imposing a logarithmic distribution to the measured u-velocity profile, u(z), shows an equivalent roughness of $k_s = 0.85\,[mm]$. Since the present mathematical model uses k_s as the input parameter in the wall boundary treatment, its value shall be calibrated to get the suitable model value.

5.2.2 Flow around a cylinder in a scoured channel bed

Measured data of flow around a cylinder in a scoured channel bed are available from the laboratory measurement presented in the previous chapter (see Chapter 2). A brief description of the experimental work is recalled in the following paragraph.

The experiment was conducted in a rectangular channel of length L = 29 [m] and width B = 2.45 [m]. The channel bed is made of *uniform sand* of mean diameter

$d_{50} = 2.1\,[\text{mm}]$. The cylinder, with a diameter of $D_p = 15$ [cm] ($B/D_p = 16.3$), was vertically installed at $x_L = 11$ [m] downstream of the entrance. A nearly uniform approach flow ($Q = 0.2\,[\text{m}^3/\text{s}]$, $U_\infty = 0.45\,[\text{m/s}]$, and $h_\infty = 18\,[\text{cm}]$) was established and can be considered to be two-dimensional ($B/h_\infty = 13.6$), turbulent (Re = 81,000), and subcritical (Fr = 0.34). The velocity measurements were performed at the equilibrium scour hole ($d_s = 25\,[\text{cm}]$, $d_s/D_p = 1.67$) under a clear-water scour condition. The scour hole had been previously established by performing a continuous run of 5 days. The scour geometry was mapped by point gauge measurements. The new version of the ADVP instrument (see *Hurther et al.*, 1996), which has a finer spatial resolution than the one previously used in the flat-bed case, was utilized to get the vertical distribution of the instantaneous velocity vector. In all measurements the ADVP was placed at the water surface, attached on a moveable carriage.

5.3 Model calibration of k_s and h_∞

The model has various constants, such as the ones of the k-ε transport equations (c_μ, c_1, c_2, σ_k, and σ_ε) and of the logarithmic law of the wall (κ and k_s). Except k_s, all model constants are kept the same as the standard model values for any flow conditions. The equivalent roughness, k_s, characterizes the roughness of the solid boundary (wall, cylinder, bed). Its value depends on the roughness size of this solid boundary. A series of preliminary runs using uniform flow conditions, based on the data of measurements without the cylinder in place, indicated that the measured values of the equivalent bed roughness (k_s = 0.54 [mm] for Yulistiyanto data and $k_s = d_{50}$ = 2.1 [mm] for the present measurement) did not result in a satisfactory agreement between the computed and measured flow fields. For this reason, calibration runs were performed by varying the values of k_s in the model. The calibrated k_s value was selected by matching the vertical distributions of the velocity, $u(z)$, eddy viscosity, $\nu_t(z)$, and the shear stress per unit mass, $\tau_{zx}(z)/\rho$, obtained from the computation and the measurements.

It was found during the runs that the flow depth (h_∞ [cm] = 18.5 and 18.0 for Yulistiyanto and the present data, respectively) should also be adjusted accordingly.

5.3.1 Computational domain

The flow, being essentially 2D, is simulated by a computational domain that represents only a slice of the channel (see Fig. 5.1). The quasi 2D computational domain is created by taking a 1-cell grid in the *y* (cross flow) direction representing a 4-[cm] portion (2%) of the channel width. The discharge entering the domain is accordingly adjusted to maintain the discharge per unit width (Q/B [m²/s] = 0.125 and 0.0816 for Yulistiyanto and the present data, respectively). The computational domain in the *x* (streamwise) direction is uniformly divided into 500 cells with a step size of $\Delta x = 4$ [cm]. This represents a 20-[m] long channel reach, which is about one half of the channel length. In the *z* direction, the flow depth is divided into 22 cells whose heights vary from 4% to 8% of the local depth. This discretisation results in 36,144 nodes, of which 1,000 are

computational nodes. The other nodes are either boundary (23,044) or dummy (2,100) ones (see the definition of node and cell in the preceding chapter). The relatively large number of boundary nodes is inevitable for all cell are boundary ones and they can have multiple nodes (see inset in Fig. 5.1).

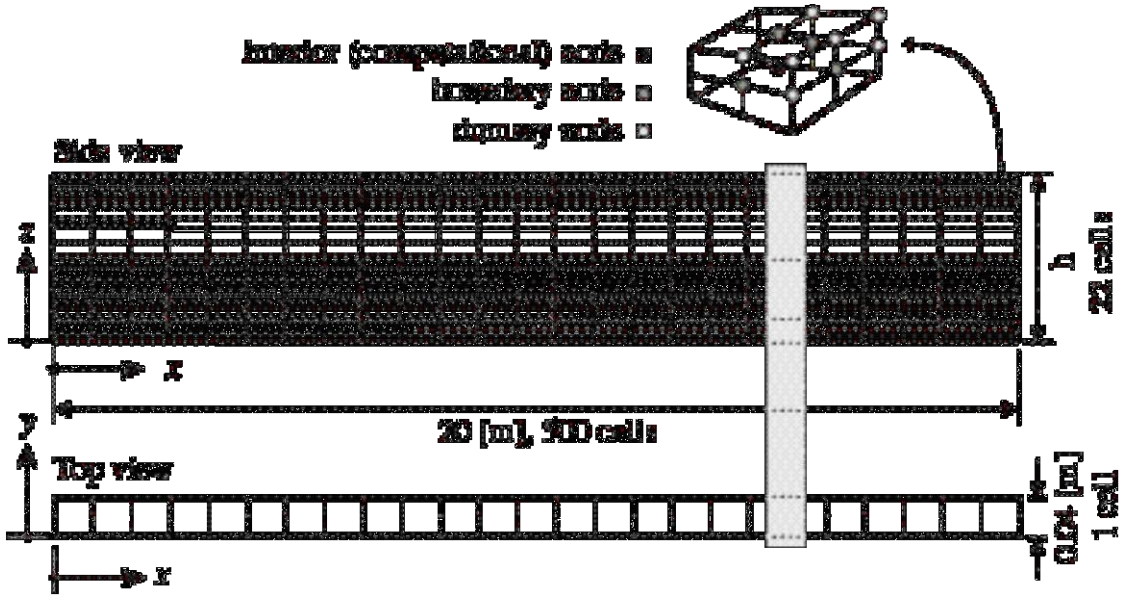

Fig. 5.1 Computational mesh ($500 \times 1 \times 22$) for the model calibration.

5.3.2 Boundary and initial conditions

In the calibration runs, both for Yulistiyanto and the present measurements, a *cyclic inflow-outflow* boundary specification was employed. This works by replacing the values of the inflow variables (u, v, w, k and ε) with those of the outflow variables of the preceding iteration, i.e. $\phi_{\text{inf low}}^{n+1} = \phi_{\text{outflow}}^{n}$ for $\phi = u, v, w, k, \varepsilon$, within the quasi-time iteration (the $n \rightarrow n+1$ iteration, see the preceding chapter). In each replacement, the inflow velocities were adjusted in order to maintain the specified discharge ($Q/B\,[m^2/s] = 0.125$ for Yulistiyanto data and 0.0816 for the present measurements). The pressure is not included in this cyclic inflow-outflow boundary since the pressure in the vicinity of the inflow boundary becomes redundant otherwise. In all calibration runs the flow depth in the entire computational domain was kept constant ($h = h_\infty$), the water surface was assumed as a frictionless (free-slip) boundary, and the side walls were considered as symmetry planes.

The first estimation (initial condition) for the velocity was a uniform distribution, being equal to the average velocity, U = q/h. For the pressure fields a hydrostatic distribution was assumed. For the turbulence parameters, k and ε, their initial distributions were defined according to $k = 1.5(0.06U)^2$ and $\varepsilon = c_\mu^{3/4} k^{3/2} / (0.09h)$ (see *Versteeg and Malalasekera*, 1995, p. 72) where $c_\mu = 0.09$ is a model constant.

5.3.3 Calibration results

The computed flows with different values of the bed equivalent-roughness and the flow depth are depicted in Fig. 5.2. Shown are the computed distributions of the velocity, eddy viscosity, and the shear stress. The corresponding measured data are also plotted in the same figures. Presented in the first figures (Fig. 5.2a-f) are the computed values obtained for Yulistiyanto data and in the second figures (Fig. 5.2g-l) are those for the present measurements. Note that for the eddy viscosity and the shear stress, different expressions were applied to the computed and measured values. For the computed ones, the following relations were used:

$$\left[\nu_t\right]_{\text{computed}} = c_\mu \frac{k^2}{\varepsilon}, \quad \text{with } c_\mu = 0.09 \text{ is the model constant, and}$$
$$\left[\tau_{zx}/\rho\right]_{\text{computed}} = \nu_t\left(\frac{\partial u}{\partial z} + \frac{\partial w}{\partial x}\right) \tag{5.1}$$

where k, ε, and the velocity gradients (computed by using finite volume techniques) are directly obtained from the mathematical model. For the measured data, the corresponding values were obtained by:

$$\left[\nu_t\right]_{\text{measured}} = \frac{-\overline{u'w'}}{\partial u/\partial z + \partial w/\partial x} \approx \frac{-\overline{u'w'}}{\partial u/\partial z}, \quad \text{since } \partial w/\partial x << \partial u/\partial z, \text{ and}$$
$$\left[\tau_{zx}/\rho\right]_{\text{measured}} = -\overline{u'w'} \tag{5.2}$$

where $-\overline{u'w'}$ and $\partial u/\partial z$ are available from the measurements.

The computation results using Yulistiyanto data show that the various k_s values tested hardly shift the velocity (Fig. 5.2a), but they significantly alter the eddy viscosity and the shear stress (Fig. 5.2b,c). With the k_s values tested, the velocity profiles vary by less than 10%. On the other hand, the ν_t obtained with different k_s values can vary as much as 0.0002 [m²/s], which is about 40% of the maximum computed ν_τ. For the bed shear stress (per unit mass, τ_{zx}/ρ), the variation can reach 0.00025 [m²/s²], which is 25% of the maximum computed value. Both eddy viscosity and shear stress increase with k_s. Unlike varying k_s, the consequence of varying h_∞ is seen more on the velocity (Fig. 5.2d) then either on the eddy viscosity (Fig. 5.2e) or on the shear stress (Fig. 5.2f). The velocity increases with decreasing h_∞. The eddy viscosity hardly changes and the shear stress slightly increases with decreasing h_∞. From these results, the equivalent roughness k_s = 0.22 [mm] ($k_s u_*/\nu$ = 6.6, meaning that the channel bed is hydraulically smooth) and the flow depth h_∞ = 18.3 [cm] were considered suitable for the Yulistiyanto flow data.

The calibration of k_s and h_∞ for the present measurement data (Fig. 5.2g-l) easily found h_∞ = 17.8 [cm] as the flow depth that results in the best agreement of the computed flow field to the measured one. For the bed equivalent roughness, the value of k_s = 4.2 [mm]

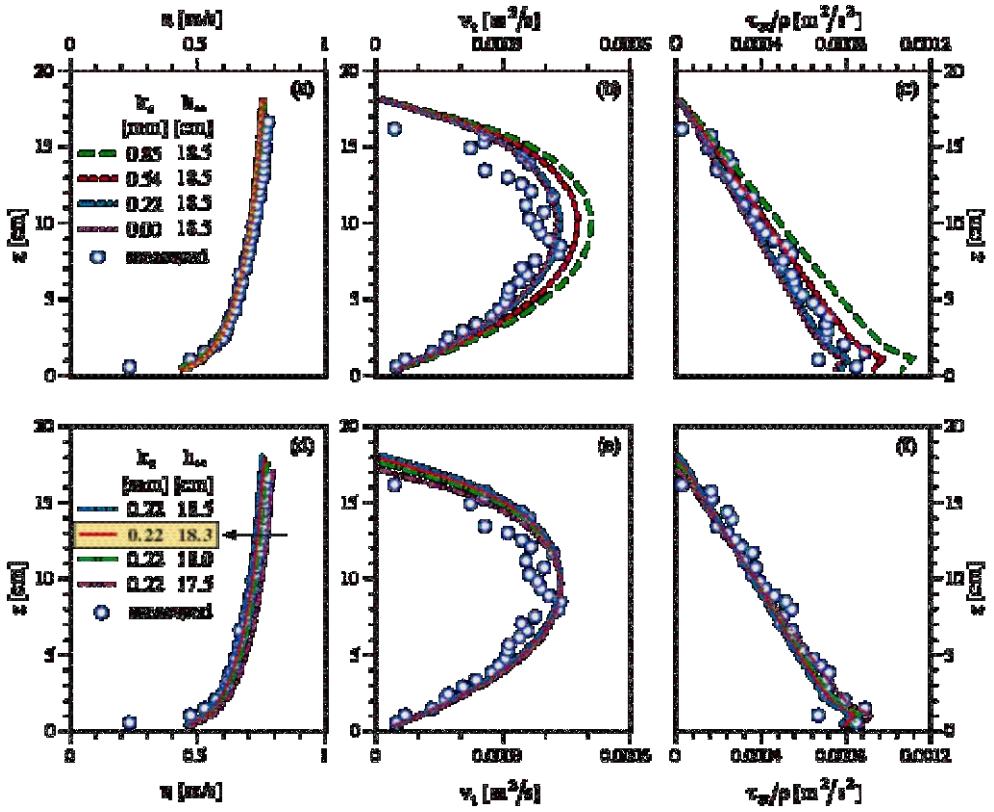

(i) Yulistiyanto data

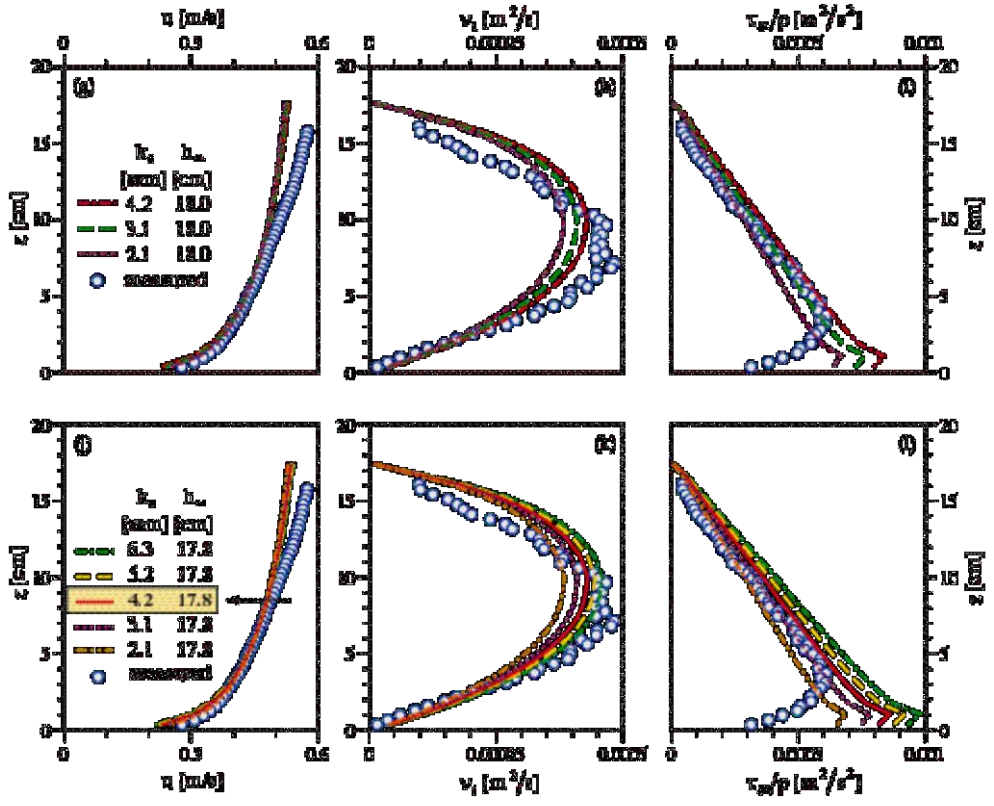

(ii) Present measurements

Fig. 5.2 Computed distributions of the velocity, eddy viscosity, and the shear stress obtained using various values of k_s and h_∞ of the calibration run.
The selected values of k_s and h_∞ are indicated by the frame.

($= 2 \times d_{50}$) was considered as the one suitable as the model k_s-value after evaluating the model results using several different k_s values. This corresponds to $k_s u_* / \nu = 118$, which signifies that the channel bed is hydraulically rough.

The calibrated k_s and h_∞ were subsequently used as the model values for the test runs using uniform flow (Sect. 5.4) and also for the simulation of the flow around a cylinder on a flat channel bed (Sect. 5.5) and in a scoured channel bed (Sect. 5.6).

5.4 Test run using uniform flow condition

5.4.1 Boundary and initial conditions

Having found the k_s and h_∞ values for the model, test runs were carried out in which the basic performance of the model under uniform flow conditions was examined. The uniform flow condition according to Yulistiyanto measurement data was selected as the test case. The same quasi 2D flow as in the calibration runs was considered (see Sect. 5.3.1).

Using the calibrated values of k_s = 0.22 [mm] and h_∞ = 18.3 [cm], three test runs using different initial and boundary conditions were performed:

- ***Test A***: the initial flow depth along the channel varies linearly between the inflow depth, h_{inflow} = 17.3 [cm], and the outflow depth, $h_{outflow}$ = 18.3 [cm]. The initial conditions for the other variables were taken from the results of the calibration run, which were linearly adjusted according to the ratio of the local flow-depth. The same spatial discretisation as used for the calibration run ($500 \times 1 \times 22$) as shown in Fig. 5.1 was used. This test run is aimed at validating the method of the surface computation. Given a variable depth along the channel, the model shall find the uniform depth when it converges to the steady-state condition.

- ***Test B***: uniformly distributed velocity and turbulence parameters were specified at the inflow boundary. These values were also used as the initial conditions along the entire domain. The initial flow depth was $h = h_\infty$ = 18.3 [cm] everywhere. The computational domain covers the entire channel reach (38 [m]), but the number of cells was kept the same as that of Test A ($500 \times 1 \times 22$). The coordinate system was oriented such that the *z*-axis was vertical. This is different from that of Test A where the *z*-axis was normal to the channel bed. This test run is aimed at verifying the wall function implementation. Given a uniformly distributed velocity at the upstream boundary, the model shall produce the logarithmic velocity distribution after a certain distance away from the entrance. This can be considered as a developing flow condition.

- ***Test C***: this is a run identical to Test B, except that the surface boundary is not necessarily updated at every time step (the n-iteration), but only after several time steps. The pressure convergence criterion in the time-step iteration was set to 10 [Pa]

($p/\gamma \approx 1$ [mm]), but the surface was updated only when the pressure computation converges within 0.01 [Pa] ($p/\gamma \approx 0.001$ [mm]) maximum limit. Note that the time step in the model is a pseudo time, which is used as iteration step marking the progress of the surface computation (see Chapter 4). This test was performed since the pressure computation in the previous runs, Test A and B, took a large number of iterations to converge while the other variables had not changed considerably within these iterations. In such case, it might be beneficial to relax the pressure convergence criterion (thus reduces the number of pressure iterations) and let the n-iteration continue, but without changing the surface boundary. The surface update was done only when the maximum pressure-correction reduces to 0.01 [Pa].

5.4.2 Results of the test runs

Comparison with the experimental data

To assess the model, the test results were compared to the experimental data, which was done for the water surface profile along the channel and the vertical distributions of the velocity, eddy viscosity, and shear stress (see Fig. 5.3 and Fig. 5.4). The computed flow of Test C is quite similar to that of Test B and thus the comparison with the experimental data is not presented. Further evaluation of the computational performance was made by inspecting the computational history of some selected variables as the model iterative computation marches towards the steady-state solution (see Fig. 5.5 to Fig. 5.7).

The computed water surface profile for Test A (see Fig. 5.3a) satisfactorily results in a uniform flow depth along the channel. For Test B (see Fig. 5.4a), the water surface profile shows a decreasing flow depth in the first 7.5-meter reach. Further downstream the flow depth gradually increases towards the specified depth of h = 18.30 [cm] at the outlet boundary. Within the downstream half channel-reach, $x \geq 20$ [m], a nearly uniform flow-depth is observed, showing less than 1 [mm] difference between the two ends of this channel reach. This proves that the method of the water surface computation is applicable.

The model produces the logarithmic velocity distribution as expected for uniform flows (see Fig. 5.3b and Fig. 5.4b). In Test A the logarithmic velocity distribution prevails consistently along the computational domain (see Fig. 5.3b). When a uniformly distributed velocity is maintained at the inlet boundary (Test B), it gradually develops into the logarithmic distribution with increasing distance from the inlet (see Fig. 5.4b). After a half reach of the computational domain, $x \geq 19.04$ [m], the velocity distribution is logarithmic.

The above results show the applicability of the model. To further validate the model, the simulation results are compared to the experimental data. The comparison between the simulation and the measurement are made for the vertical distributions of the velocity, eddy viscosity, and the shear stress. The computed profiles at $x = 19.8$ [m] for Test A and at $x = 19.04$ [m] for Test B are compared to the measured ones as shown in Fig. 5.3c and Fig. 5.4c, respectively. The following is to be observed:

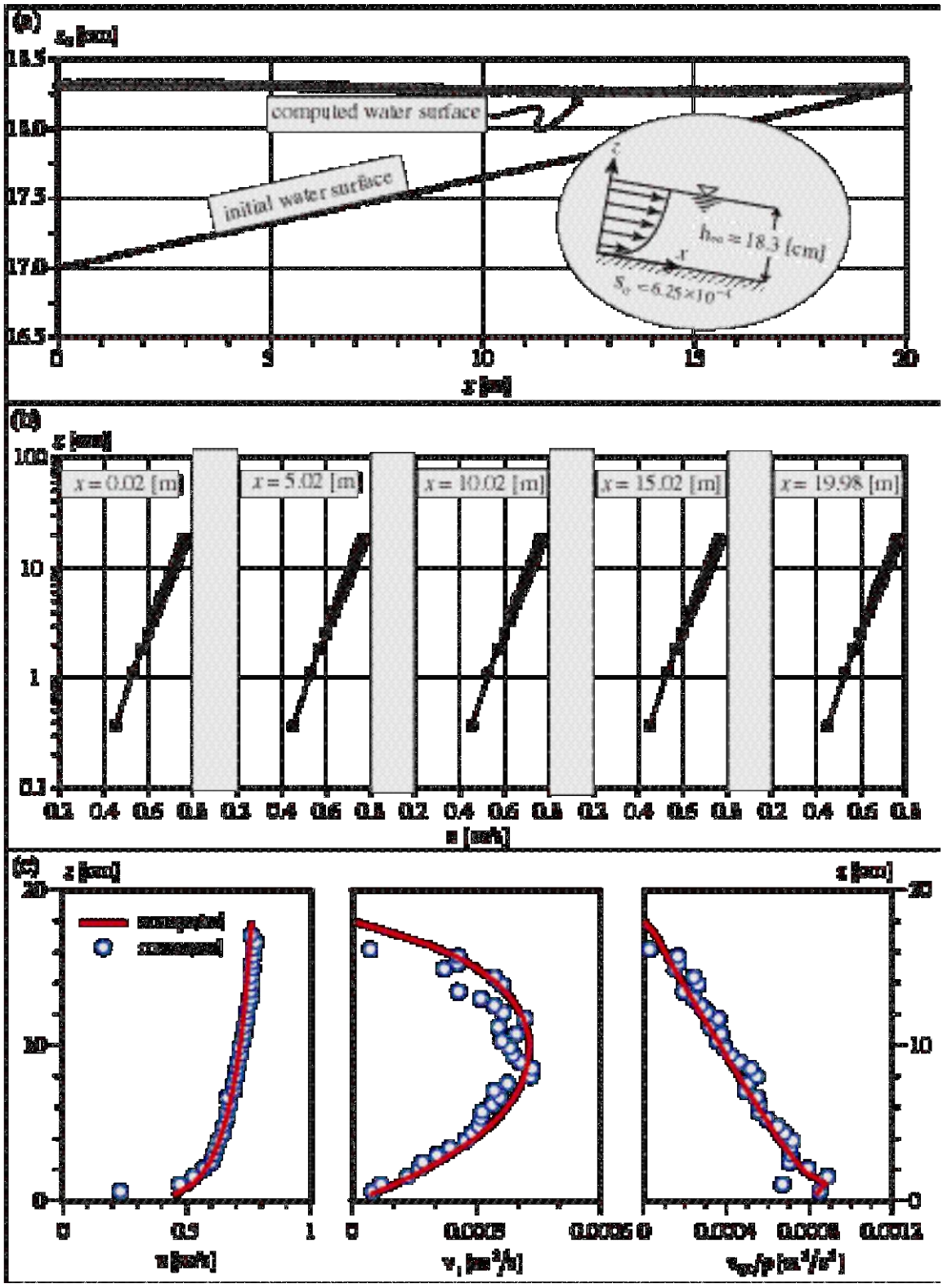

Fig. 5.3 Model test results for **Test A** (uniform flow with $Q/B = 0.125\,[m^2/s]$, h_∞ = 18.3 [cm], L = 20 [m], and a logarithmic velocity distribution at the inlet boundary): **(a)** computed water surface along the channel, **(b)** computed distributions of the velocity at selected sections, and **(c)** comparison between computed and measured distributions of the velocity, the eddy viscosity, and the shear stress at the downstream section, x = 19.8 [m].

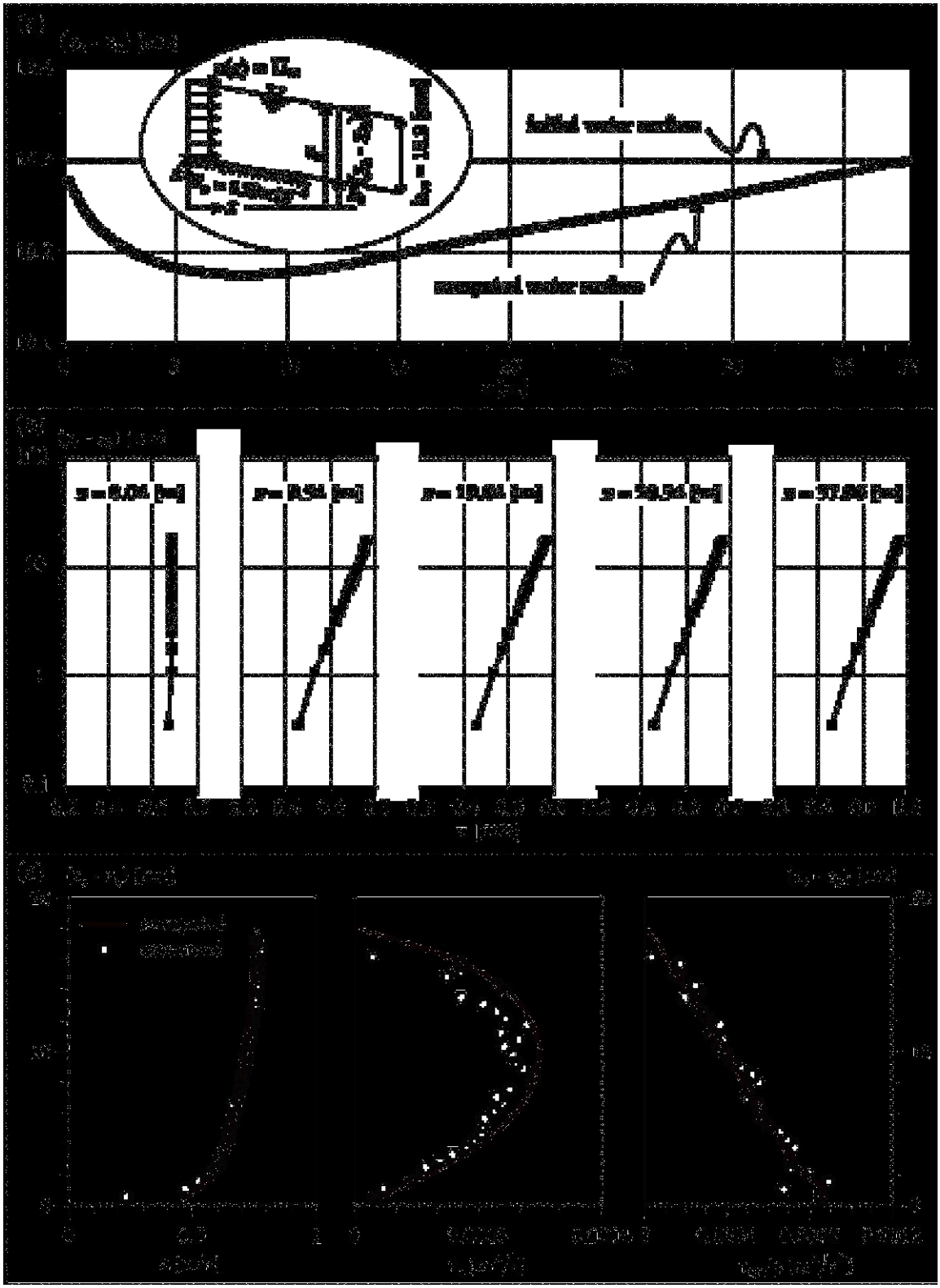

Fig. 5.4 Model test results for **Test B** (developing flow with $Q/B = 0.125\,[m^2/s]$, h_∞ = 18.3 [cm], L = 38 [m], and a uniform velocity distribution at the inlet boundary, $u = Q/B/h$): **(a)** computed water surface along the channel, **(b)** computed distributions of the velocity at selected sections, and **(c)** comparison between computed and measured distributions of the velocity, the eddy viscosity, and the shear stress at half reach of the channel, x = 19.04 [m].

- The two test runs, Test A and B, achieve a near perfect agreement between the computed and measured velocity distributions. In Test A, the logarithmic velocity distribution prevails along the channel. In Test B the development of the velocity profile, from a uniform distribution to the logarithmic one, is achieved after half reach of the computational domain. The agreement between this computed velocity profile and the measured one has confirmed that the wall boundary treatment is appropriately implemented in the model.

- The computed eddy-viscosity profile compares favorably with the measured one. The eddy viscosity is zero at the surface, increases with the depth until a maximum value at around mid-depth, and decreases towards zero at the bed.

- The computed shear-stress profiles in Test A and B well agree with the measurements. The shear stress is linearly distributed with the depth, being zero at the surface and maximum at the bed.

Computational history of the model variables

Having obtained a good agreement with the experimental data, the evolution of the flow variables during the iterative computation of the model is investigated. This evolution of flow variables, as the computation marches towards the steady-state solution, is plotted in Fig. 5.5, Fig. 5.6, and Fig. 5.7 for Tests A, B, and C, respectively. Shown are some selected flow variables ($z_{surface}$, p, u, k, and ε) at 5 computational nodes (inlet and outlet boundary cells, and at x/L = 0.25, 0.5, 0.75). The plots show that stable computations towards the converged solution are observed in all test runs.

The computational history plots of Test A and B (see Fig. 5.5 and Fig. 5.6), however, reveal an interesting behavior of the iteration (the ℓ or m iteration, see Chapter 4) in the model. These figures clearly show that the iterations are devoted almost uniquely to the pressure computation. When the velocity and the k-ε have already converged, i.e. their values have no longer changed appreciably, the pressure is still changing. This leads to a conclusion that the pressure convergence criterion in the ℓ-iteration may be loosened. However, since the pressure is used as the basis for the water surface computation, this strategy would endanger the stability of the latter. To circumvent this problem, two different criteria are used for the pressure convergence. The first criterion is loose ($p^c_{max} \leq$ 10 [Pa], which is equivalent to $p^c_{max}/\gamma \leq 1$ [mm]) for the ℓ-iteration and the second one is much smaller ($p^c_{max} \leq$ 0.01 [Pa] or $p^c_{max}/\gamma \leq 0.001$ [mm]) for the water surface computation. Consequently, the water surface may not be necessarily updated every time step.

With the above strategy, the run of Test B was repeated in Test C. It was found that the final result of Test C does not show a significant difference from that of Test B. The computational history in these two test runs, of course, is not the same. Fig. 5.7 depicts the computational history of certain variables in Test C; this is to be compared to that of Test B, Fig. 5.6. Compared to Test B, the computation in Test C, as expected, converges

within a greater number of time steps (n iterations) but within a smaller number of ℓ- and m-iterations. The total number of iterations in Test C (see Fig. 5.7) is considerably less than that in Test B (see Fig. 5.6). The two strategies can be equally used for uniform flow cases, but as can be seen later for flows around a cylinder, the strategy B does not always converge whereas the strategy C does.

5.4.3 Conclusions

The numerical model developed previously (see Chapter 4) was tested to simulate a simple flow case obtained from the experimental data of approaching uniform flow on a smooth bed channel (*Yulistiyanto*, 1997). The test was done in order to validate the model against a simple and well-known flow case. Three test runs using different boundary conditions were performed. In Tests A and B, two distinct inlet boundary conditions were used, i.e. a logarithmic and a uniform velocity distribution over the depth. In both tests, the model performs quite satisfactorily. Comparison to the experimental data shows that the agreement between the computed and the measured flow fields are quite satisfactory.

In Test C, the same boundary conditions as in Test B were used, but the pressure convergence criterion and the surface positioning were changed. The convergence criterion for the pressure computation was loosened, from 0.1 to 10 [Pa], but the surface positioning was done only when the pressure computation shows a maximum pressure correction of 0.01 [Pa]. The result of this test shows that this method can speed up the computational time compared to Test B.

In all three runs, a stable computation is observed in the entire computation and a convergence towards the steady-state solution is guaranteed.

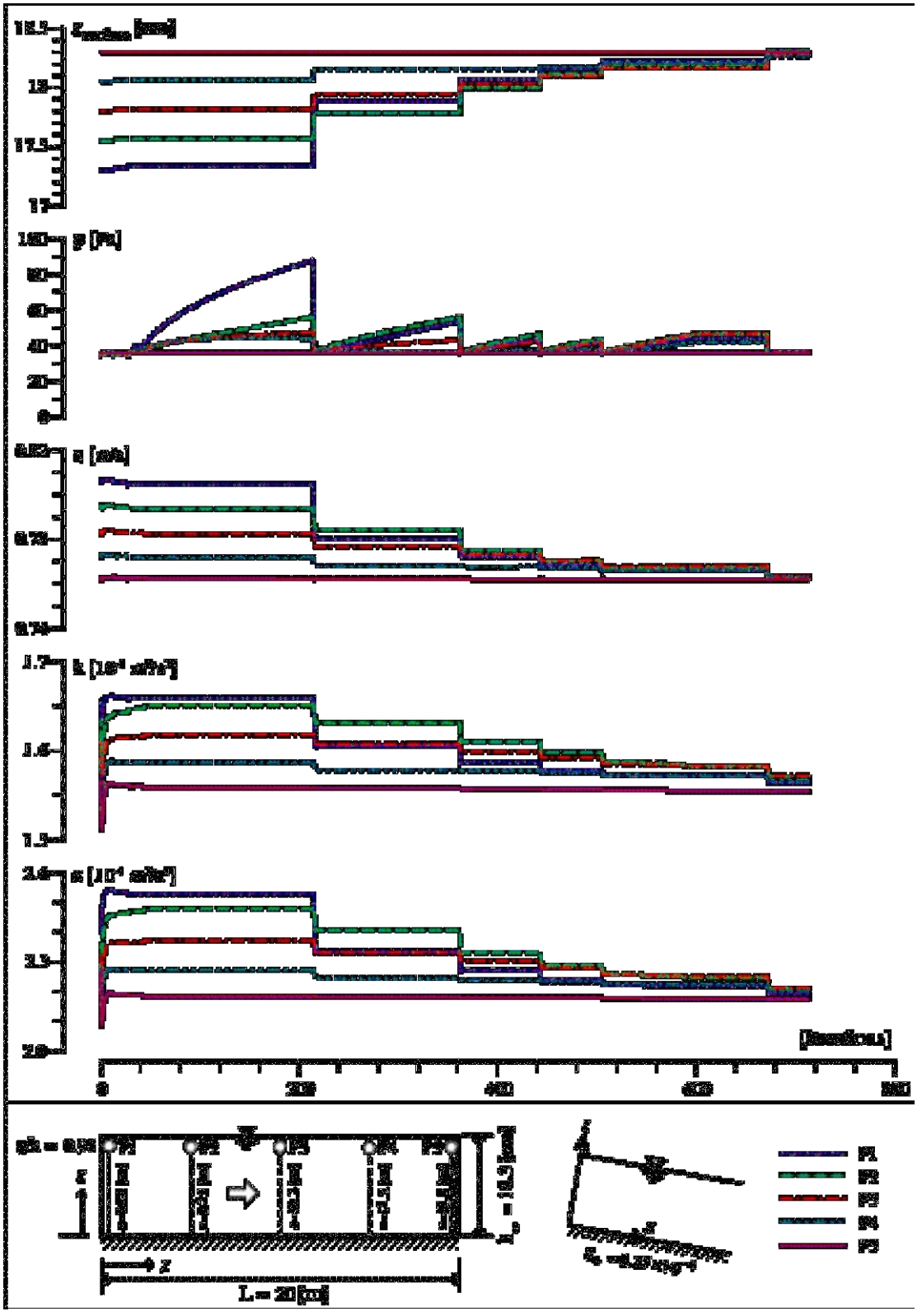

Fig. 5.5 Computational history of some selected variables during the iterative computation of the model. **Test A**: uniform flow with $Q/B = 0.125\,[m^2/s]$, h_∞ = 18.3 [cm], L = 20 [m], and a logarithmic velocity distribution is maintained at the inlet boundary.

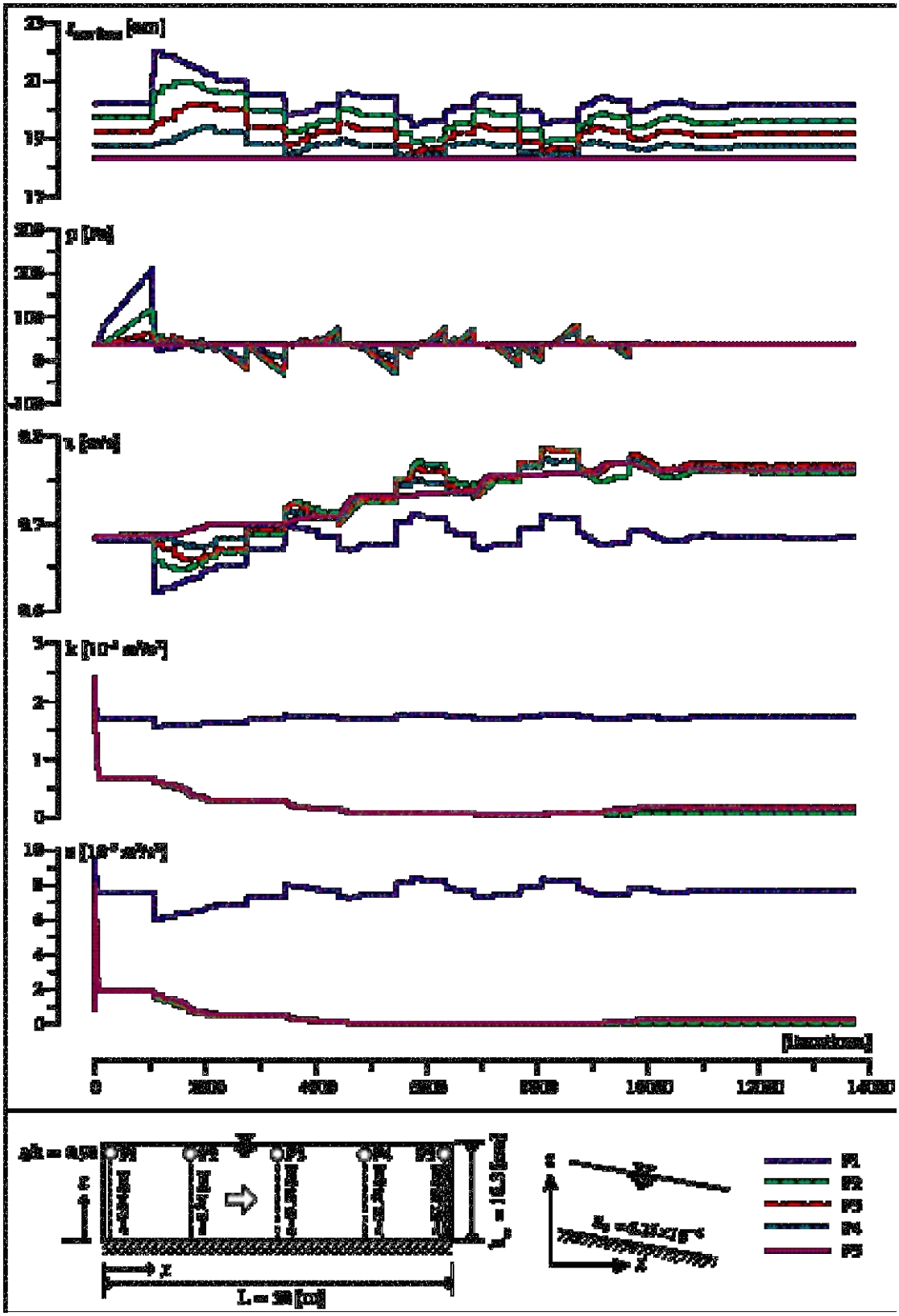

Fig. 5.6 Computational history of some selected variables during the iterative computation of the model. **Test B**: developing flow with $Q/B = 0.125\ [m^2/s]$, $h_\infty = 18.3$ [cm], L = 38 [m], and a uniform velocity distribution is maintained at the inlet boundary, $u(z) = Q/B/h$.

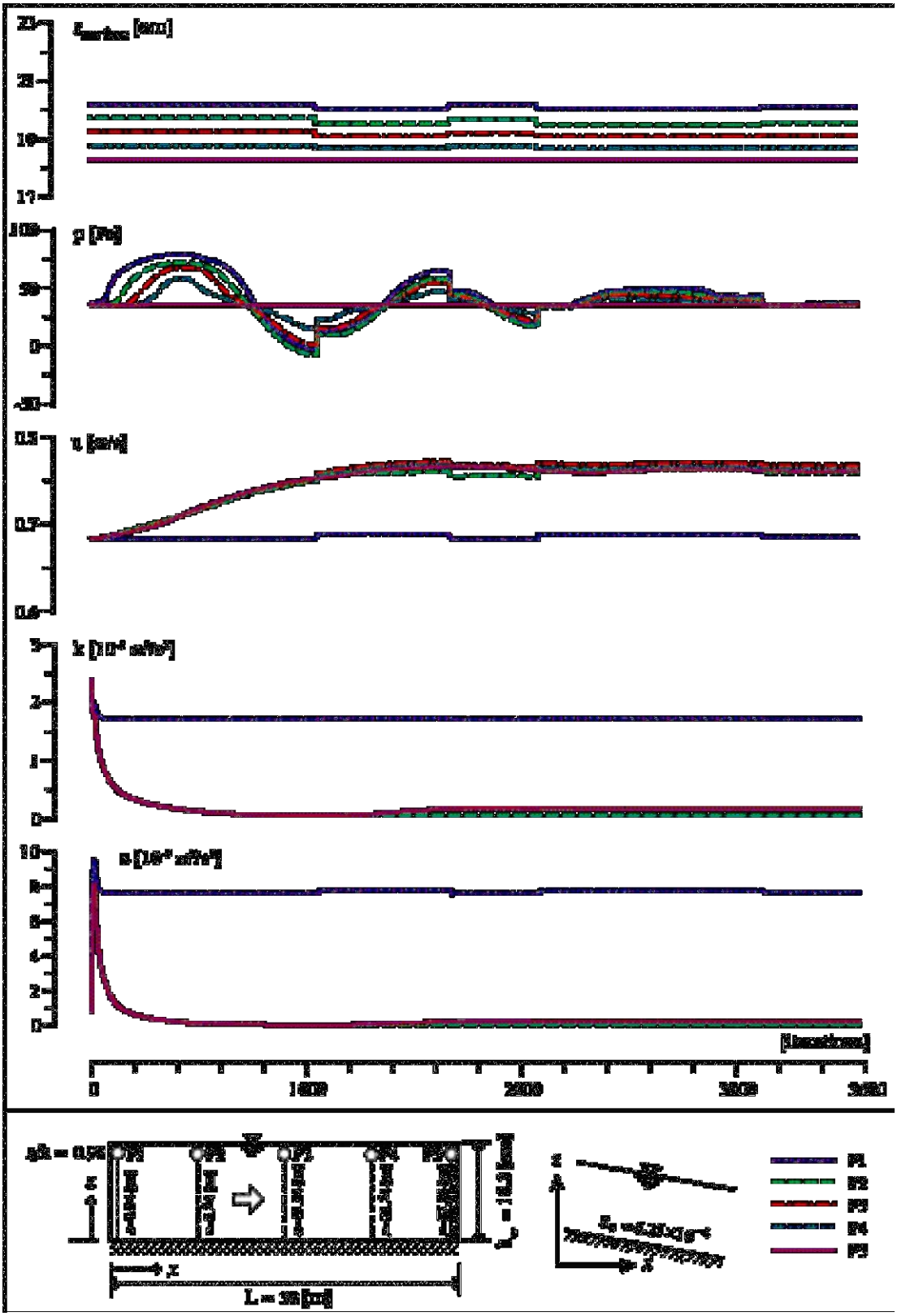

Fig. 5.7 Computational history of some selected variables during the iterative computation of the model. **Test C**: developing flow with $Q/B = 0.125\,[m^2/s]$, h_∞ = 18.3 [cm], L = 38 [m], a uniform velocity distribution is maintained at the inlet boundary, u(*z*) = Q/B/h, and the water surface is not necessarily updated at every time step.

5.5 Simulation of flow around a cylinder on a flat channel bed

5.5.1 Computational domain

The computational domain covers a longitudinal section of 4 [m] with the cylinder at its center. The grid was generated in two steps. Firstly, the Joukowski conformal mapping was used to generate an orthogonal horizontal (*xy* plane) grid. Finer grids are concentrated around the cylinder. Secondly, the horizontal grid was repeated in the *z* direction according to a pre-determined interval to cover the entire flow depth. This is known as a "sigma stretching" method. The number of cells in the *x*, *y* and *z* directions is $99 \times 49 \times 22$ (see Fig. 5.8). The cylinder is represented as a $31 \times 1 \times 22$-cell out-blocked region. There are thus 106,040 computational nodes, 16,834 boundary nodes, and 750 dummy nodes. The *z* distribution of the grid is identical to that of Test A (uniform flow simulation) to enable the use of the computed velocity and turbulence profiles of that test run as the inflow boundary conditions of this simulation.

In presenting the results of the simulation and the comparison to the experimental data, cylindrical and Cartesian coordinate systems are frequently used together. The origin of both coordinates is defined at the center of the cylinder, at the original bed level (see Fig. 5.9).

5.5.2 Boundary and initial conditions

The boundary conditions are as follows:

- Upstream inflow: Q = 0.250 [m^3/s] and prescribed distributions of u,v,w, k, ε which are taken from the results of Test A.
- Downstream outflow: h_∞ = 18.3 [cm].
- Left and right channel (glass) walls: wall boundary with k_s = 0 [mm] (hydraulically smooth).
- Channel (metal) bed and cylinder (PVC) boundaries: wall boundary with k_s = 0.22 [mm] ($u_* k_s / \nu = 6.6$, hydraulically smooth solid boundaries).
- Top boundary: water surface.

The initial conditions over the computational domain are uniform flow depth corresponding to the known downstream depth, h_∞ = 18.3 [cm], hydrostatic pressure, $p = -\rho g_z (z_{surface} - z)$ [Pa], velocity and k-ε according to the known distributions at the inlet section. At early time steps, the water surface was kept constant until the flow field was more or less stable. The simulation was then restarted by letting the water surface move according to the surface boundary treatment. A similar method of surface updating as of Test C in the preceding test run was used. There are two different criteria for the pressure computation, namely the one for terminating the pressure computation in the ℓ-iteration ($p^c_{max} \le 10$ [Pa], which is equivalent to $p^c_{max}/\gamma \le 1$ [mm]) and the other for updating the surface boundary ($p^c_{max} \le 0.01$ [Pa] or $p^c_{max}/\gamma \le 0.001$ [mm]).

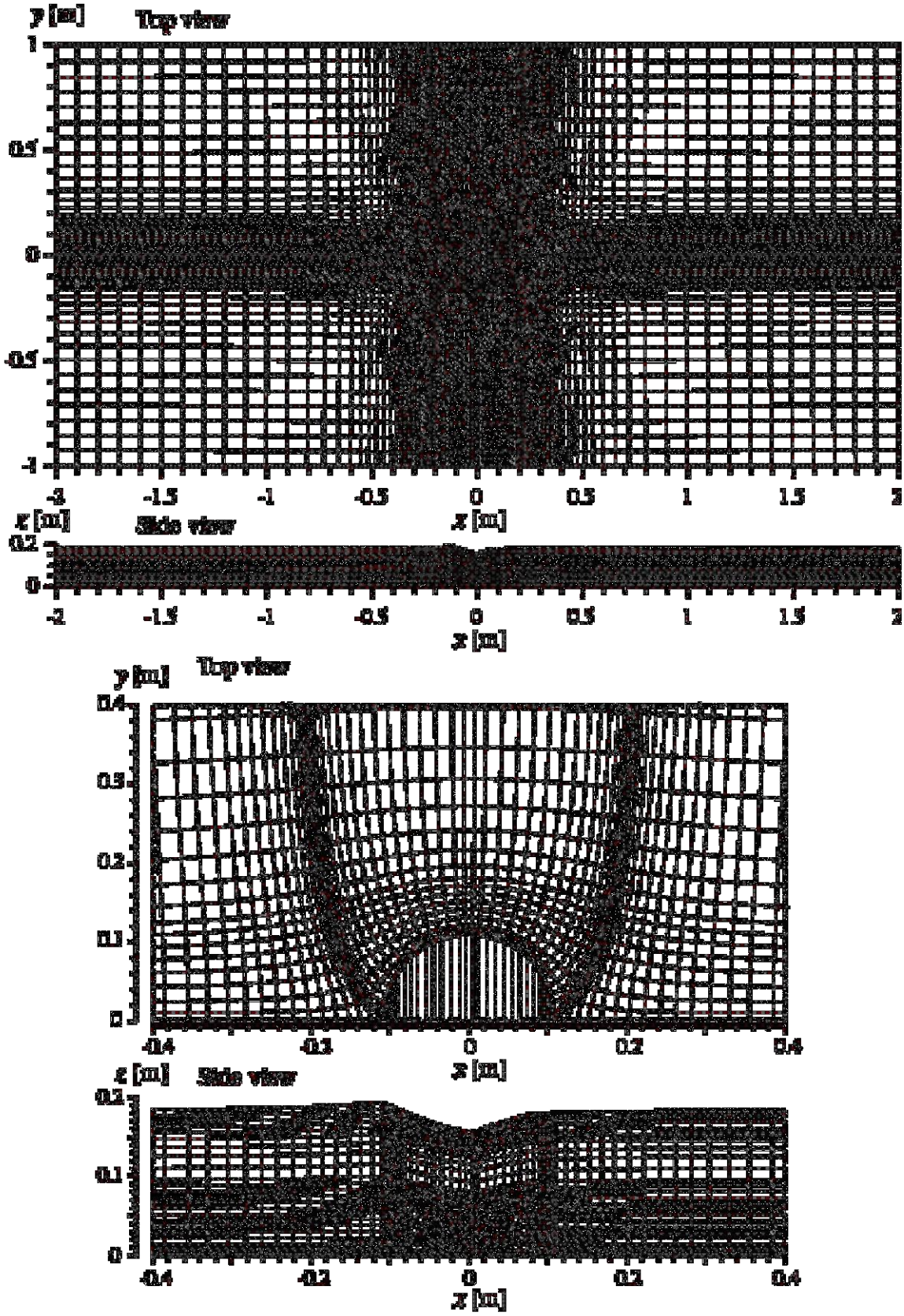

Fig. 5.8 Top view (*xy* plane) and side view (*xz*-plane) of the computational mesh ($99 \times 49 \times 22$ cells) for the simulation of flow around a cylinder on a flat channel bed. An enlargement is shown for region around the cylinder.

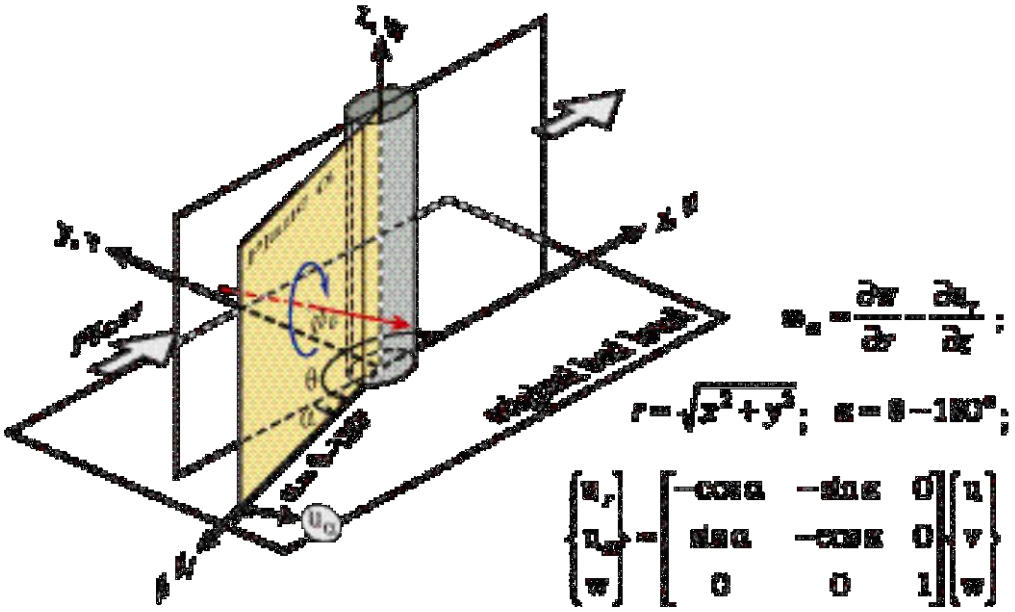

Fig. 5.9 Definition sketch of the coordinate system and the vorticity, ω_α.

5.5.3 Results of the simulation and comparison to the experimental data

The evaluation of the results of the numerical simulation (see Chapter 4) is made for the velocity fields and the water surface. Herewith they are compared to the experimental data (see Chapter 2). Detailed comparison of the 3D velocity profiles in the planes where the experimental data are available is first presented (Fig. 5.10). The velocity fields, resulted from the simulation and the measurement, are then presented by vector plots (Fig. 5.11) and contour plots (Fig. 5.12) in three selected planes, $\alpha = 0°$, 90°, and 180°, to show the general pattern of the flow. Next, the prediction of the flow pattern at the bottom corner of the cylinder is highlighted by contour plots of the computed and the measured vorticity fields (Fig. 5.13), obtainable from the corresponding 2D velocity components in those three planes. Finally, an evaluation is made on the computed water surface profile along the longitudinal section of the symmetry plane and along the cylinder circumference (Fig. 5.14).

Vertical distribution of the 3D velocity components

The comparison between the computed and the measured vertical distributions of the 3D velocity components are done for some selected profiles. Shown in Fig. 5.10 are 20 distributions of the 3D velocity components, u(z), v(z), and w(z), in the planes where measurements data are available, $\alpha = 0°$, 45°, 90°, 157.5°, and 180°. Four stations at r/D_p = 1.5, 1, 0.75, and 0.55, being considered representative ones, are selected from each plane. It can be seen from the comparison in Fig. 5.10 that the computed velocity distributions are in a good agreement with the measured ones, notably in the upstream region, $\alpha = 0°$, 45°, and 90°. The agreement, however, is less evident in the wake region,

$\alpha = 157.5°$ and 180°. Observing the comparison in each plane, the following is to be remarked:

- In the plane $\alpha = 0°$, the good agreement is shown by all velocity components. It is particularly interesting to remark that close to the cylinder, $r/D_p = 0.55$, the negative values of u-velocity near the bed and w-velocity in the entire depth can be well reproduced by the model. This shows that the model is able to simulate the reversed flow upstream of the cylinder, eventhough in this particular region and flow condition the method of computation adopted in the model is very much approximative (see Chapter 4, Sect. 4.5.4, notably that describes the assumptions taken in the wall boundary computation).

- In the plane $\alpha = 45°$, the good agreement is also shown by all velocity components, as in the plane $\alpha = 0°$. The non-zero (negative) v-velocity component, which indicates the flow alteration by the cylinder, can be satisfactorily reproduced by the model. The agreement can also be seen in the negative w-velocity (the downward flow).

- In the plane $\alpha = 90°$, the computed velocities compare with the measured ones. Approching the cylinder, the increasing u-velocity component can also be satatisfactorily reproduced by the model. The negative values of v-velocity (flow leaving the cylinder) and of w-velocity (downward flow) are in a good agreement.

- In the plane $\alpha = 157.5°$, discrepancies are observed showing an under estimation of the measured velocities, notably the u- and v-velocity components. The computed and measured u-velocity profiles, nevertheless, have a similar pattern: both exhibit a positive under current in the lower half-depth and an opposite current in the upper half-depth. In addition, it could be that the discrepancy is more in the flow direction than in its magnitude. If one considers the resultant of the u- and v-velocity components, the difference between the computed and measured values may not be too far.

- In the plane $\alpha = 180°$, a similar picture as in the plane $\alpha = 157.5°$, but with a smaller discrepancy, is observed. Nonetheless, the computed and measured u-velocity profiles, notably at $r/D_p = 3$ and 1, exhibit a similar pattern showing positive values in the lower depth (leaving the cylinder) and negative values (towards the cylinder) in the upper depth. Moreover, the model and the measurements show similar non-zero v-velocities at these two stations, indicating a horizontal momentum exchange across the plane.

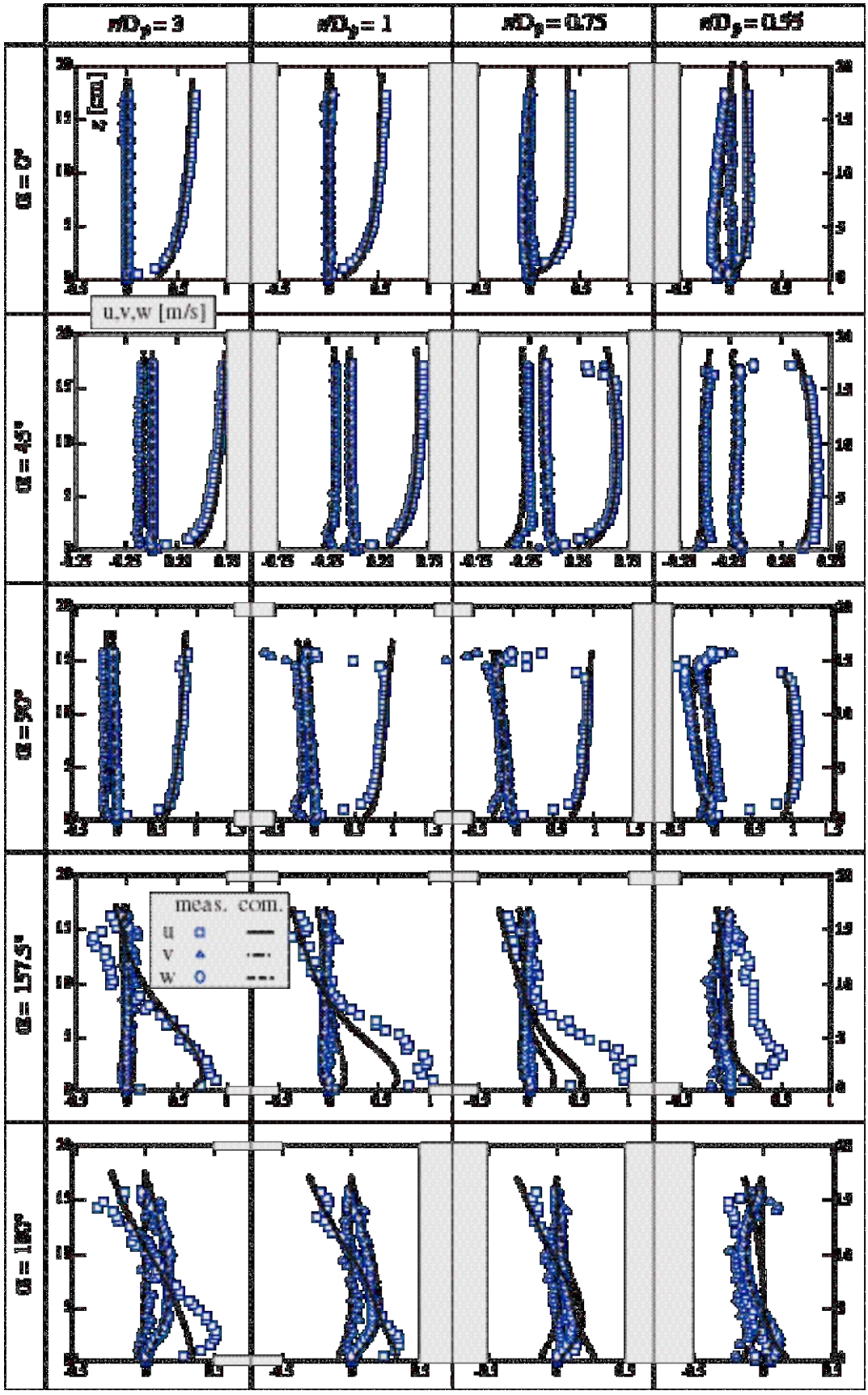

Fig. 5.10 Computed (lines) and measured (symbols) velocity distributions, u(z), v(z), w(z), at some selected stations around the cylinder. Flow around a cylinder on a flat channel bed.

Velocity fields around the cylinder

Further evaluation of the simulation results can be made by presenting the computed velocity fields in a vector form projected on vertical planes around the cylinder. Fig. 5.11 shows these velocity vector plots, $\vec{\mathbf{V}}_\alpha(u_r, w)$, in the planes $\alpha = 0°$, 90°, and 180°. Note that for clarity purpose, only selected computed velocity vectors are drawn. Shown also in the same figure are the ones obtained from the experimental data. The radial velocity component, u_r, can be obtained from the u and v components according to the geometrical relation given in Fig. 5.9.

The comparison shown in Fig. 5.11 has demonstrated the good reproduction of the flow field by the model. A good agreement of the computed and measured flow patterns, at least qualitatively, is clearly ascertained. A good quantitative agreement, to some extent, is also achieved. This is demonstrated in the following figure (Fig. 5.12). The figure shows the contour plot of the flow intensity in the same planes, $\alpha = 0°$, 90°, and 180°, as in the preceding figure (Fig. 5.11). The flow intensity is expressed by $V/U_\infty = \sqrt{u^2 + v^2 + w^2}/U_\infty$, where $U_\infty = 0.68\,[m/s]$ is the approach flow velocity. The resemblance of the computed and the measured flow intensities is observed, except at close to the surface in the plane $\alpha = 90°$. The discrepancy at this region, however, is likely due to the scattered measured data, as seen also in the vector plots (Fig. 5.11). In the plane $\alpha = 180°$, where the flow is typically complex, a good agreement between the computed and measured flow intensity plots can be achieved.

The vector and isoline contour plots of the flow pattern given in Fig. 5.11 and Fig. 5.12 allow one to observe the flow behavior as it interacts with the cylinder. This is described as follows:

- In the plane $\alpha = 0°$, the unidirectional flow coming towards the cylinder becomes increasingly two-directional (Fig. 5.11a,b) and its intensity decreases (Fig. 5.12a,b). Close to the cylinder, a downward velocity develops whose intensity increases with the depth and reaches a maximum value of $0.3U_\infty$ at $z \approx 2$ [cm]. At the bed, this downward velocity is deflected toward upstream (Fig. 5.11a,b), forming a reversed flow with an intensity of $0.2U_\infty$ (Fig. 5.12a,b). This reversed flow encounters the incoming flow and a separation takes place. A visual observation to Fig. 5.11a,b indicate that the separation starts at $r \approx 17$ [cm] according to the model and at $r = 19.7$ [cm] according to the measurements (see *Graf and Yulistiyanto*, 1998).

- In the plane $\alpha = 90°$, the velocity vector, $\vec{\mathbf{V}}_\alpha(u_r, w)$, is directed away from the cylinder, particularly at the surface (Fig. 5.11c,d), with a decreasing intensity as one moves away from the cylinder (Fig. 5.12c,d). The radiating flow represents the skewness of the approaching flow when it passes the cylinder. The flow intensity close to the cylinder is $1.4U_\infty$ from the simulation and is slightly higher, $1.6U_\infty$, from the measurement. On the other hand, at the upper corner between the cylinder and the surface, the simulation indicates a slightly higher intensity, being $1.4U_\infty$ compared to

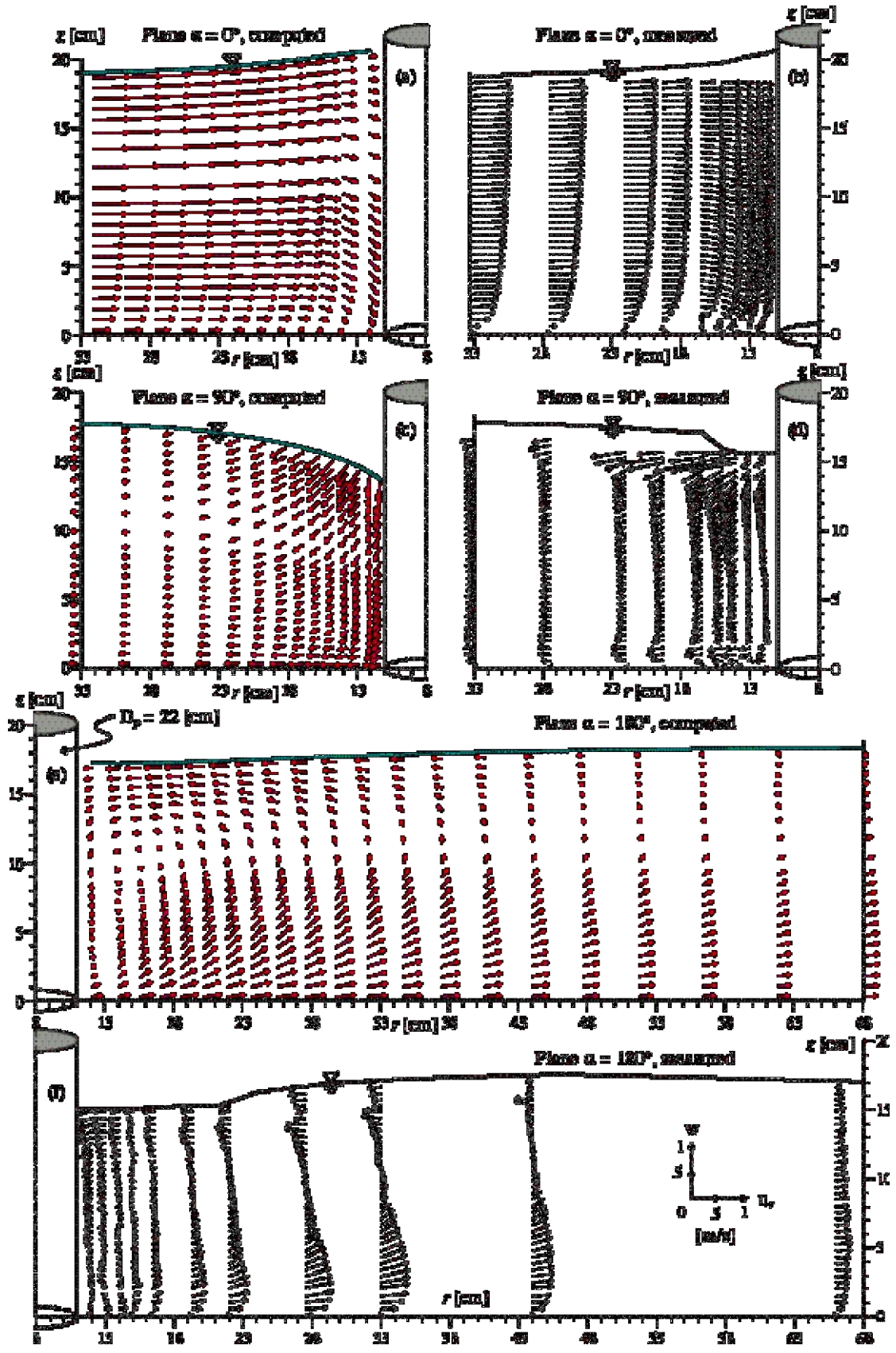

Fig. 5.11 Computed and measured velocity vectors, $\vec{\mathbf{V}}_{\alpha}(u_r, w)$,
in the planes $\alpha = 0°, 90°, 180°$.
Flow around a cylinder on a flat channel bed.

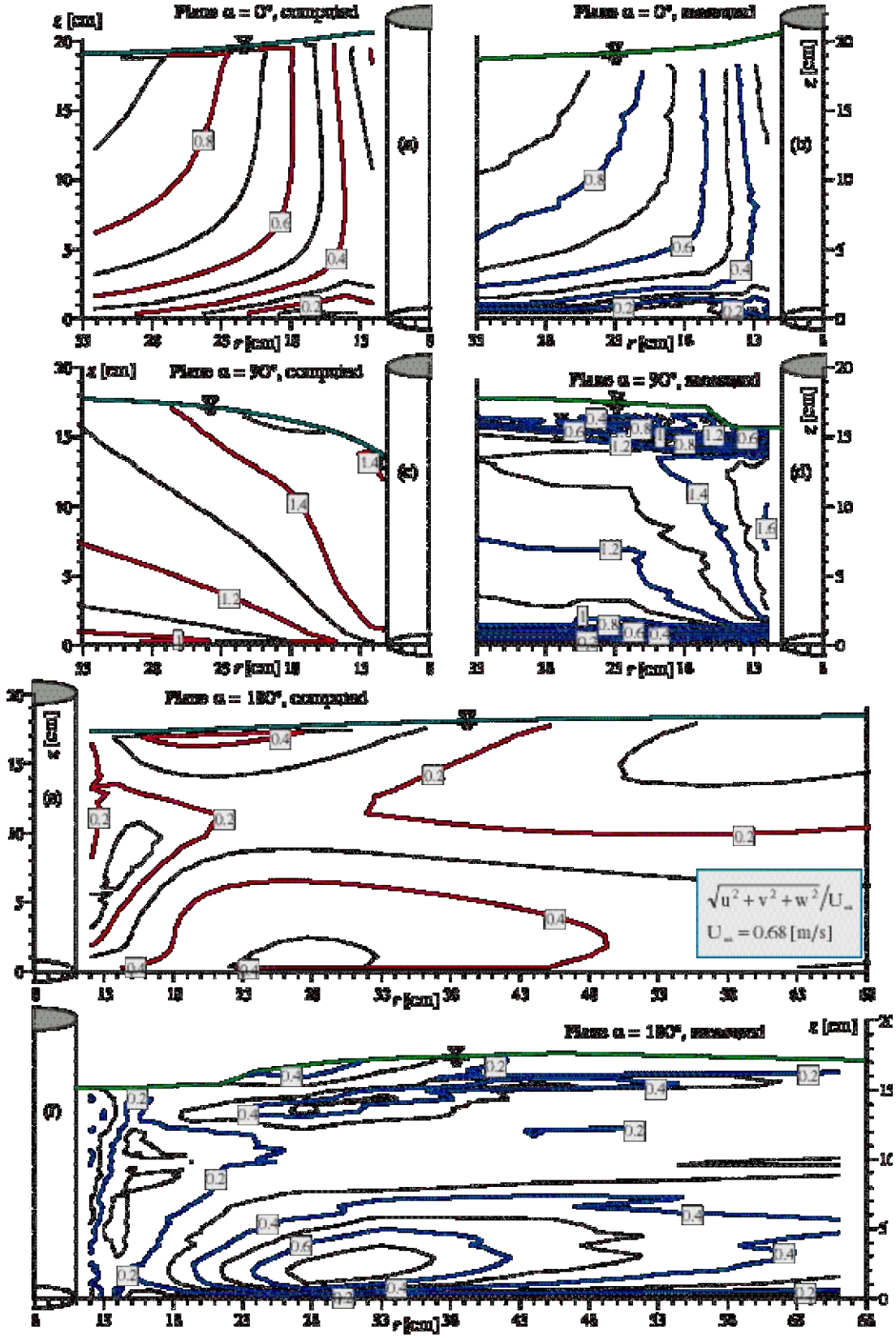

Fig. 5.12 Computed and measured velocity contours, in the planes $\alpha = 0°, 90°, 180°$. The data are normalized by the velocity in the approach flow, V/U_∞, where $V = \sqrt{u^2 + v^2 + w^2}$ and $U_\infty = 0.45$ [m/s]. Flow around a cylinder on a flat channel bed.

$1.2U_\infty$ of the measurement. Note that the vector plot of the measured velocity at this corner indicates some scattered data as has also been mentioned in the preceding section.

- In the plane $\alpha = 180°$, both the simulation and the measurement exhibit a counter rotating flow towards the surface (Fig. 5.11e,f). Except close to the bed, the intensities of the rotating flow obtained by the simulation and measurement are quite comparable (Fig. 5.12e,f). Immediately behind the cylinder, the agreement is quite satisfactory. Leaving the cylinder, the rotating flow diminishes and the flow returns back to the unidirectional flow condition.

Vorticity fields in the bottom corner around the cylinder

Another way of observing the flow around a cylinder is to use the vorticity fields whose component in a vertical plane α is defined by (*Graf and Yulistiyanto*, 1998):

$$\omega_\alpha = \frac{\partial w}{\partial r} - \frac{\partial u_r}{\partial z} \tag{5.3}$$

in which the velocity gradients are obtained by using finite volume techniques (see Chapter 4) for the computed data and by using central finite difference for the measured data. It must be emphasized, however, that the vorticity is highly sensitive to the quality and quantity of the measured data points. The measured vorticity fields thus have to be interpreted with caution.

Shown in Fig. 5.13 are the contour plots of the vorticity fields in the planes $\alpha = 0°$, 90°, and 180° obtained from the simulation and the measurement. Only the bottom corner region, where the vorticity is of importance, is presented. The following is to be remarked:

- Upstream of the cylinder, in the plane $\alpha = 0°$, a qualitative agreement is observed between the computed and measured vorticity fields, notably the negative vorticities formed by the downward flow close to the cylinder. A qualitative, bot not quantitative, agreement is also observed by the positive vorticity fields in the bottom corner of the cylinder formed by the downward flow and the reversed flow. The strong concentrated vorticity shown by the measurements, however, cannot be captured.

- On the side of the cylinder, in the plane $\alpha = 90°$, the agreement is less evident, apart from the negative vorticity region close to the bed. This negative vorticity is formed by the radiating flow away from the cylinder as has been mentioned in the preceding section. There is also a negative vorticity region along the cylinder, produced by the downward flow. The strong positive vorticity at $z = 2$ [cm], which is shown by the measured fields, cannot be reproduced by the simulation.

- Downstream of the cylinder, in the plane $\alpha = 180°$, a similar observation as in the plane $\alpha = 90°$ can be observed. The agreement between the computed and measured vorticities is only shown by the negative fields along the bottom. Above the bed, $z > 1$ [cm], there is almost nothing can be observed. Some scattered positive vorticities shown by the measured values are certainly due to the velocitiy data irregularities as can be seen in the vector plot (see Fig. 5.11).

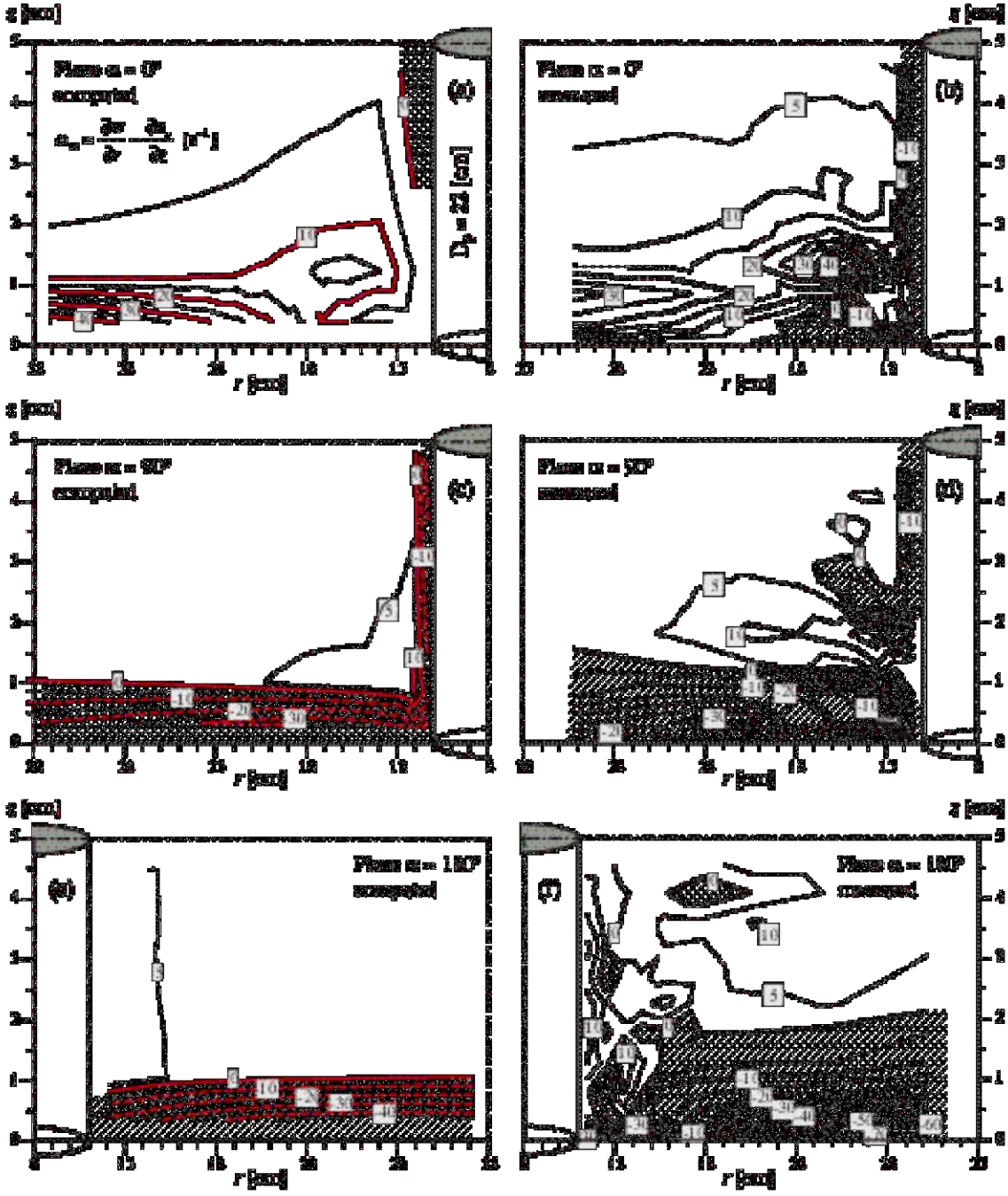

Fig. 5.13 Computed and measured vorticity fields, ω_α, in the planes $\alpha = 0°$, 90°, 180°.
The shaded area indicates regions of negative vorticity fields.
Flow around a cylinder on a flat channel bed.

Water-surface profile

The computed and the measured water surface profiles along the longitudinal section and along the cylinder circumference are shown in Fig. 5.14. The profiles are made dimensionless using the approach flow depth, h_∞, and the cylinder diameter, D_p, as the scaling factors for the z and x directions, respectively. The following remarks are put forward on the comparison of the water surface:

- Upstream of the cylinder the computed water surface tends to be slightly above the measured profile. However, the bow wave in front of the cylinder, due to the stagnation pressure, is quite well reproduced. The simulation gives a relative increase, $(h - h_\infty)/h_\infty$, of 12.2% compared to 12.7% obtained from the measurement.

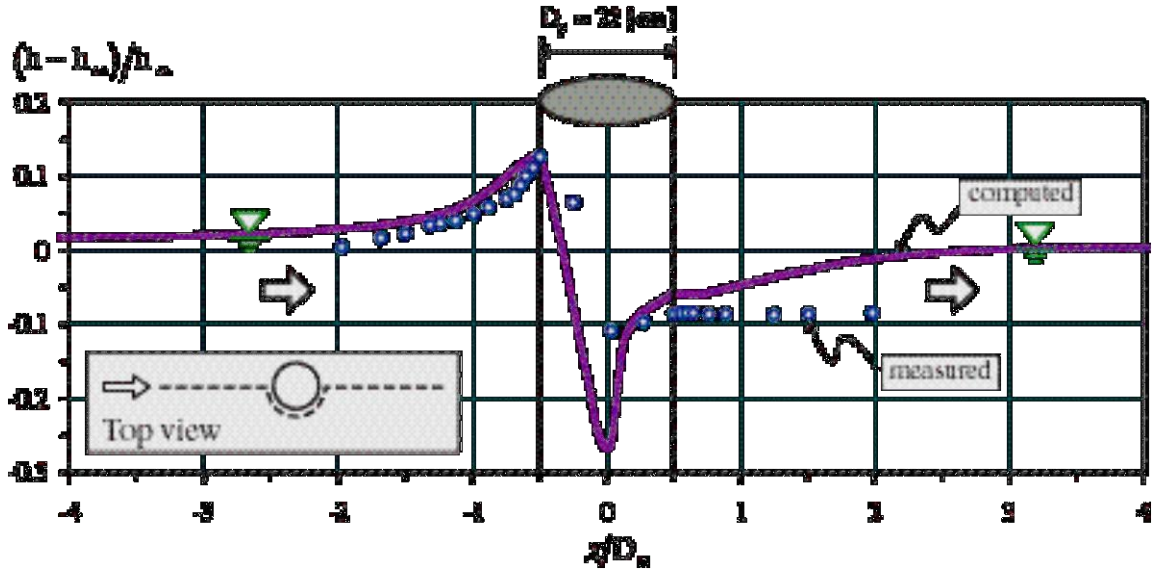

Fig. 5.14 Computed (line) and measured (symbols) water-surface profiles along the longitudinal section and the cylinder circumference.
Flow around a cylinder on a flat channel bed.

- Along the upstream circumference of the cylinder, an under-estimation of the water surface is observed; the maximum depression, $(h - h_\infty)/h_\infty$, is computed as 23% while it is measured as 11%. This rather strong is most likely due to the presence of a strong pressure-gradient along the cylinder circumference. The high (stagnation) pressure upstream of the cylinder, $\alpha = 0°$, is accelerating the flow not only towards the bed (the downward flow), but also towards the downstream along the cylinder circumference (in the angular direction, α). Consequently, there is a steep water surface along this circumference. The method of the surface boundary positioning, which is based on the pressure (see Chapter 4), evidently becomes less accurate when being confronted with such situation. The inaccuracy can be explained by the fact that: (1) the surface pressure is not directly obtained from the computation but from an extrapolation (by assuming a hydrostatic distribution) of the pressure at the cell center just below the surface, and (2) this surface pressure, defined at the center of the top face, is linearly distributed to the vertices of the top face with which the vertices

are moved to define the surface position. These procedures clearly imply computational simplification and approximation. Another method of surface positioning, which is based on the application of kinematic boundary condition along the surface, is discussed in Sect. 5.8.

- Downstream of the cylinder, an over-estimation of the computed water surface is observed. Here also, a rather steep surface profile prevails, in which the high velocity (low flow-depth) in the plane $\alpha = 90°$ is readapting to the lower velocity (higher flow-depth) in the wake of the cylinder. Again, the method of surface positioning has certainly a low accuracy. In the scoured-bed case (see the next section), a similar over-prediction occurs; another interpretation of this problem, which attempts to relate it to the production of the turbulent kinetic-energy, will be discussed (see Sect. 5.6.3). One expects that the disagreement of the water surface should disappear at a distance further downstream away from the cylinder. Unfortunately, the limited measured data do not allow such control. In the scoured channel bed case, it will be seen that the measured water surface further downstream returns back to the one of the approach flow.

5.5.4 Conclusions

The numerical model (see Chapter 4), conclusively, has demonstrated its applicability and ability to simulate flow around a cylinder on a flat channel bed. Detailed comparison of the computed velocity fields to the measured ones (see Fig. 5.10) shows satisfactory agreements. The downward and reversed flows upstream of the cylinder and the rotating flow downstream of the cylinder can be reproduced by the model (see Fig. 5.11 and Fig. 5.12). A qualitative agreement is also seen from the vorticity fields (see Fig. 5.13). The model, however, shows a rather disagreement of the water-surface profile, notably along the cylinder circumference and behind the cylinder. A good agreement, nevertheless, is seen along the upstream water surface, including the bow wave at the cylinder upstream face (see Fig. 5.14). The method of surface boundary positioning, in fact, becomes less accurate in regions of a strong pressure gradient.

5.6 Simulation of flow around a cylinder in a scoured channel bed

5.6.1 Computational domain

The computational domain covers a 5-[m] channel-reach with the cylinder at 2.5 [m] from the upstream boundary (see Fig. 5.15). The origin of the coordinate system is defined at the center of the cylinder, at the original uneroded channel bed. The flow is assumed to be symmetrical about the channel centerline and, therefore, the computational domain represents half of the channel with a symmetry plane on the left (north) boundary, $y = 0$. The grid is formed by $109 \times 43 \times 22$ cells in the x, y and z directions, respectively. There are 103,114 computational nodes, 16,062 boundary nodes, and 704 dummy nodes. The grid was generated by the same method as in the flat-bed case, i.e. by

using a Joukowski transformation to construct the *xy*-grid, and by stretching this grid in the *z* direction to form the *xyz* control-volume grid. The grid sizes in the *x* and *y* directions vary between 0.11 to 12 [cm] and 0.5 to 8 [cm]; in the *z* direction, the grid sizes are 4% to 8% of the local flow-depth. To generate the bed level of the computational domain, the elevations of the bottom cell vertices were interpolated from a 5×5-[mm^2] uniform bed-level grid. This grid was constructed based on the measured bed-level data obtained by point gauge measurements. Fig. 5.15 illustrates the *xy* and *xz* grids at an intermediate solution of the simulation.

5.6.2 Boundary and initial conditions

There are five boundary conditions in this run, i.e. inflow, outflow, symmetry, wall, and surface boundaries. These are all boundary-condition types that can be handled by the present model.

- Upstream inflow, $x = -2.5$ [m]: $Q/2 = 0.1\,[\mathrm{m}^3/\mathrm{s}]$ and u, v, w, k, ε are available from the measurement in the approach flow region (see Chapter 2). The values of ε are obtained by $\varepsilon = c_\mu k^2/\nu_t$ (see Eq. 5.1), where the eddy viscosity, ν_t, and the kinetic energy, k, are obtainable from the measured velocities (see also Eq. 5.2) such as $\nu_t = -\overline{u'w'}/\partial u/\partial z$ and $k = \frac{1}{2}\left(\overline{u'u'} + \overline{v'v'} + \overline{w'w'}\right)$.

- Downstream outflow, $x = 2.5$ [m]: constant surface elevation, which corresponds to the depth of the uniform approach flow, $h_\infty = 17.8$ [cm].

- Left (north) boundary, $y = 0$: wall boundary along the cylinder (persplex glass), $\overline{BCC'B'}$, $(-0.75 \le x\,[\mathrm{m}] \le 0.75)$ with $k_s = 0.22$ [mm] and symmetry plane along the rest, $\overline{ABB'A'}$ and $\overline{CDD'C'}$.

- Right (south) boundary, $y = -1.225$ [m]: wall boundary along the channel glass side-wall with $k_s = 0$ [mm].

- Bottom boundary: wall boundary along the channel uniform-sand bed with $k_s = 2d_{50} = 4.2$ [mm] (see Sect. 5.3.3).

- Top boundary: water surface.

The initial conditions of the simulation are horizontal flow depth corresponding to the known uniform flow depth ($h_\infty = 17.8$ [cm]), hydrostatic pressure distribution, $p = -\rho g_z \left(z_{\mathrm{surface}} - z\right)$ [Pa], velocity and k-ε according to the known distributions at the inlet boundary. Within the initial stage, as in the simulation of the flat-bed case, the water surface was kept constant until the flow field was more or less constant. The simulation was then restarted and the water surface was let to move following the surface boundary treatment, except at the downstream boundary.

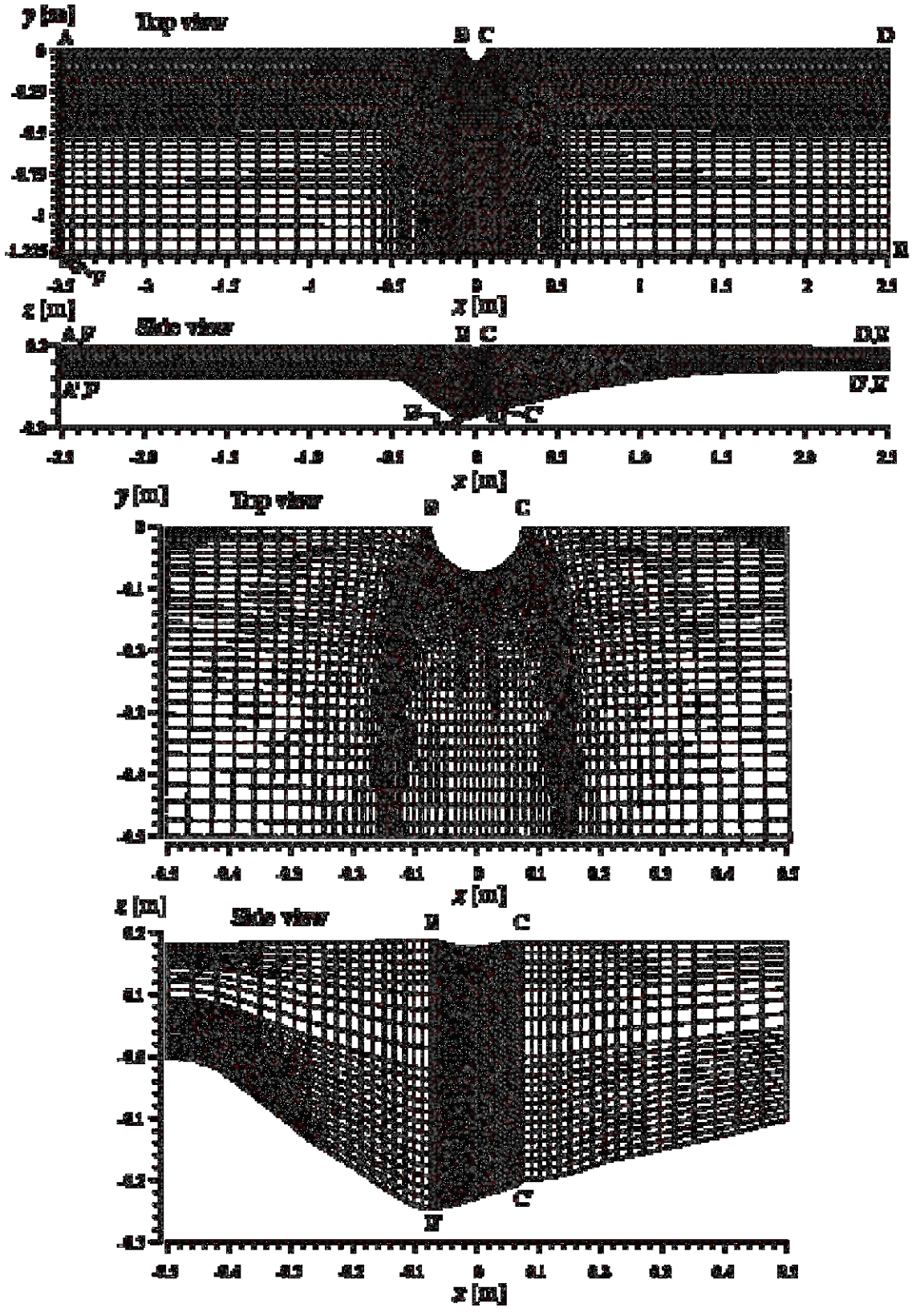

Fig. 5.15 Top view (*xy* plane) and side view (*xz* plane) of the computational mesh ($109 \times 43 \times 22$ cells) for the simulation of flow around a cylinder in a scoured channel bed. An enlargement is shown for the region close to the cylinder.

5.6.3 Results of the simulation and comparison to the experimental data

The results of the simulation, as in the flat-bed case, are evaluated and compared to the experimental data for the velocity fields (see Fig. 5.16 to Fig. 5.19) and the water surface (see Fig. 5.23). In addition, a comparison of the turbulent kinetic energy, k, obtained from the simulation and the measurement, is also presented (see Fig. 5.20). An attempt is also made to evaluate the computed production and dissipation of the turbulence kinetic energy, G and ε (see Fig. 5.21). A comparison with the measured data for these variables, however, is not elaborated since the data density does not allow all terms in the equation of G (see Chapter 4) to be obtained.

Vertical distribution of the 3D velocity components

Detailed comparisons of the computed and measured 3D velocity components are presented in Fig. 5.16 for some selected profiles, being representative ones, at the 5 planes around the cylinder, α = 0°, 45°, 90°, 135°, and 180°. Shown are the vertical distributions of the velocities, u(z), v(z), and w(z), at stations r/D_p = 3, 2, 1, and 0.67. The following is to be observed:

- Outside the scour hole, r/D_p = 3, and still away from the cylinder, the agreement is quite satisfactory for all three velocity components. In the scour hole, $r/D_p < 3$, the agreement is qualitatively good, showing a close trend of the velocity profiles. Some disagreements are observed, but these are rather weak, which are commonly seen as a smoothened out of the profiles.

- The u-velocity component in general is well reproduced, showing a diminishing velocity approaching the cylinder. At r/D_p = 2 and 1, however, the computed u profiles seems to be smoothened out, notably at around z = –5 [cm]. Nevertheless the negative u-velocity at r/D_p = 1 and 0.67 in the planes α = 0° and 45°, which shows a reversed flow, is reasonably reproduced.

- The v-velocity component is in general the smallest component every where, except in the plane α = 45° at $r/D_p \leq 1$ and close to the surface. A reasonably good agreement of this velocity component is observed.

- The w-velocity component manifests itself as a downward flow (negative w) in all planes but α = 180°. A reasonably good agreement of the downward velocity is noticeable, showing an increasing value approaching the cylinder; the maximum downward velocity according to the model, however, is found at a somewhat lower z than according to the measurements. Behind the cylinder, in the plane α = 180°, the upward velocity (positive w) is also reasonably computed.

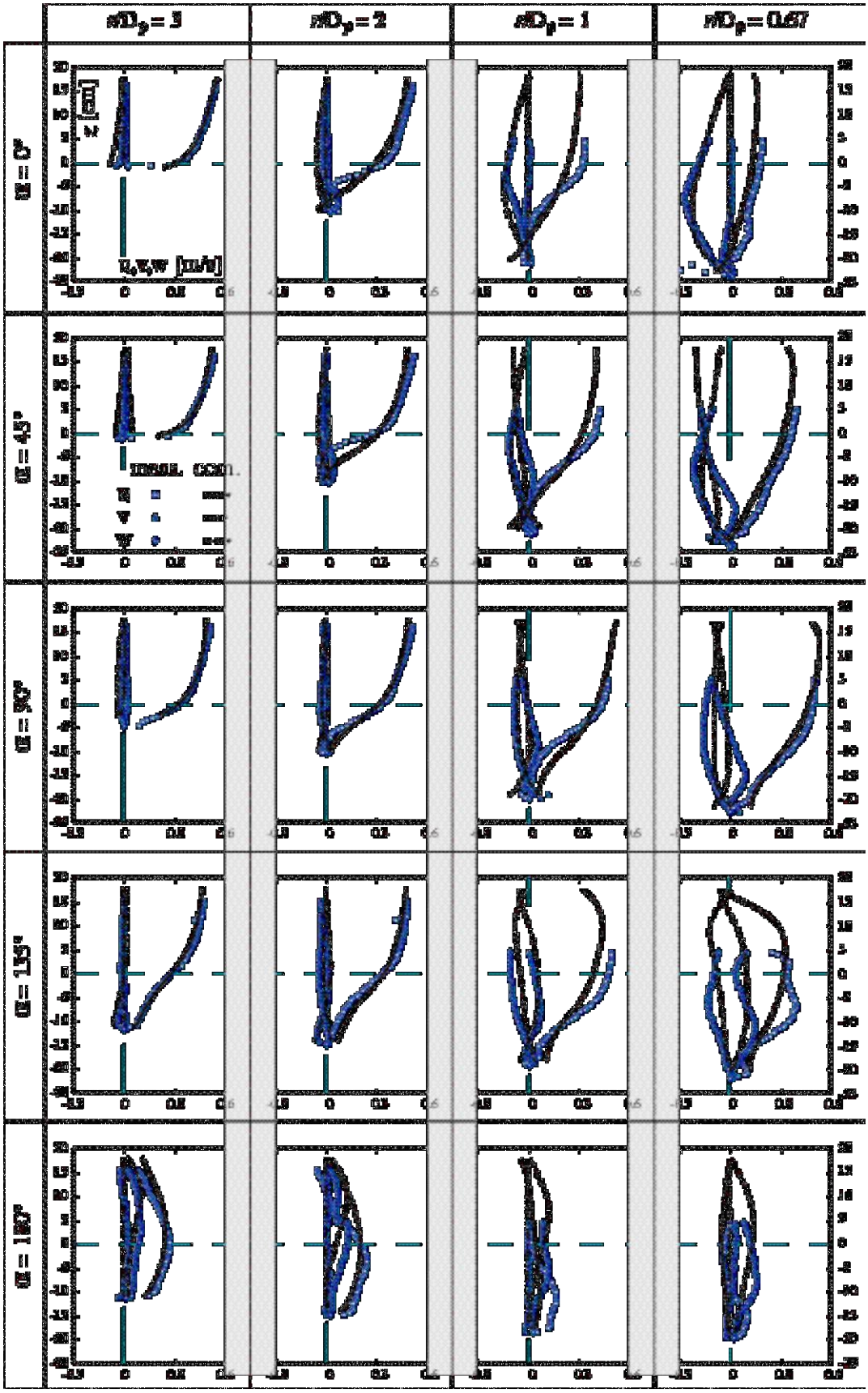

Fig. 5.16 Computed (lines) and measured (symbols) velocity distributions, u(z), v(z), w(z), at some selected stations around the cylinder
Flow around a cylinder in a scoured channel bed.

Velocity fields around the cylinder

A more detailed observation of the flow pattern around the cylinder can be facilitated by plots of velocity vector and flow intensity contour, given in Fig. 5.17 and Fig. 5.18. The plots show the velocity vector, $\vec{\mathbf{V}}_\alpha(u_r, w)$, and the flow intensity, V/U_∞ ($V = \sqrt{u^2 + v^2 + w^2}$ and $U_\infty = 0.45\,[m/s]$), in the planes $\alpha = 0°$, 90°, and 180°. Note that for clarity purposes, not all but only some selected computed velocity vectors, being representative ones, are drawn. Shown also in the same figures are the ones obtained from the experimental data.

Comparing the computed and the measured velocity fields shown in the two plots, it is evident that the two closely resemble. As in the flat-bed case, the model here also has proven its applicability to this highly 3D flow. Further remarks can be put forward from the plots in each of the three planes:

- In the plane $\alpha = 0°$ (Fig. 5.17a,b and Fig. 5.18a,b), the unidirectional incoming flow is decelerating and deflecting towards the bed upon entering the scour hole. Close to the cylinder, the down-deflected flow becomes more pronounced and develops into a downward flow along the cylinder face. The stagnation pressure stimulates the downward flow, which is strengthening with increasing depth (decreasing z) and diminishing close to the bed, where the flow turns to the upstream direction along the bed. This reversed flow diminishes as it moves away from the cylinder and eventually joins the downstream facing upper flow. These downward and the reversed flows can be reasonably well captured by the model; the maximum computed downward flow, $0.5U_\infty$, is slightly weaker than the measured one, $0.6U_\infty$, but the computed reversed flow is comparable with the measured one, being both indicate an intensity of $0.2U_\infty$ (Fig. 5.18a,b). Note that the measurements show a strong reversed flow concentrated in a small region at the bottom corner of the cylinder, which the simulation cannot capture due to the limited spatial resolution of the grid.

- In the plane $\alpha = 90°$ (Fig. 5.17c,d and Fig. 5.18c,d), both simulation and measurement show negligible radial and vertical velocity components as indicated by the vector plot (Fig. 5.17c,d). The contour plot (Fig. 5.18c,d) reveals, on the other hand, a comparable flow intensity as in the plane $\alpha = 0°$. This shows that the flow is mainly directed towards downstream tangentially to the cylinder and that the lateral skewness of the approaching flow is negligible.

- In the plane $\alpha = 180°$ (Fig. 5.17e,f and Fig. 5.18e,f), close to the cylinder the velocity is weak, 0.1 to $0.3U_\infty$, and is directly upward towards the surface, where it turns upstream towards to the cylinder. Further downstream away from the cylinder, the flow is gradually increasing and returning to the approach flow condition. The close resemblance of the computed flow with the measured one is in fact a rather surprising since the flow behind the cylinder is a complex one.

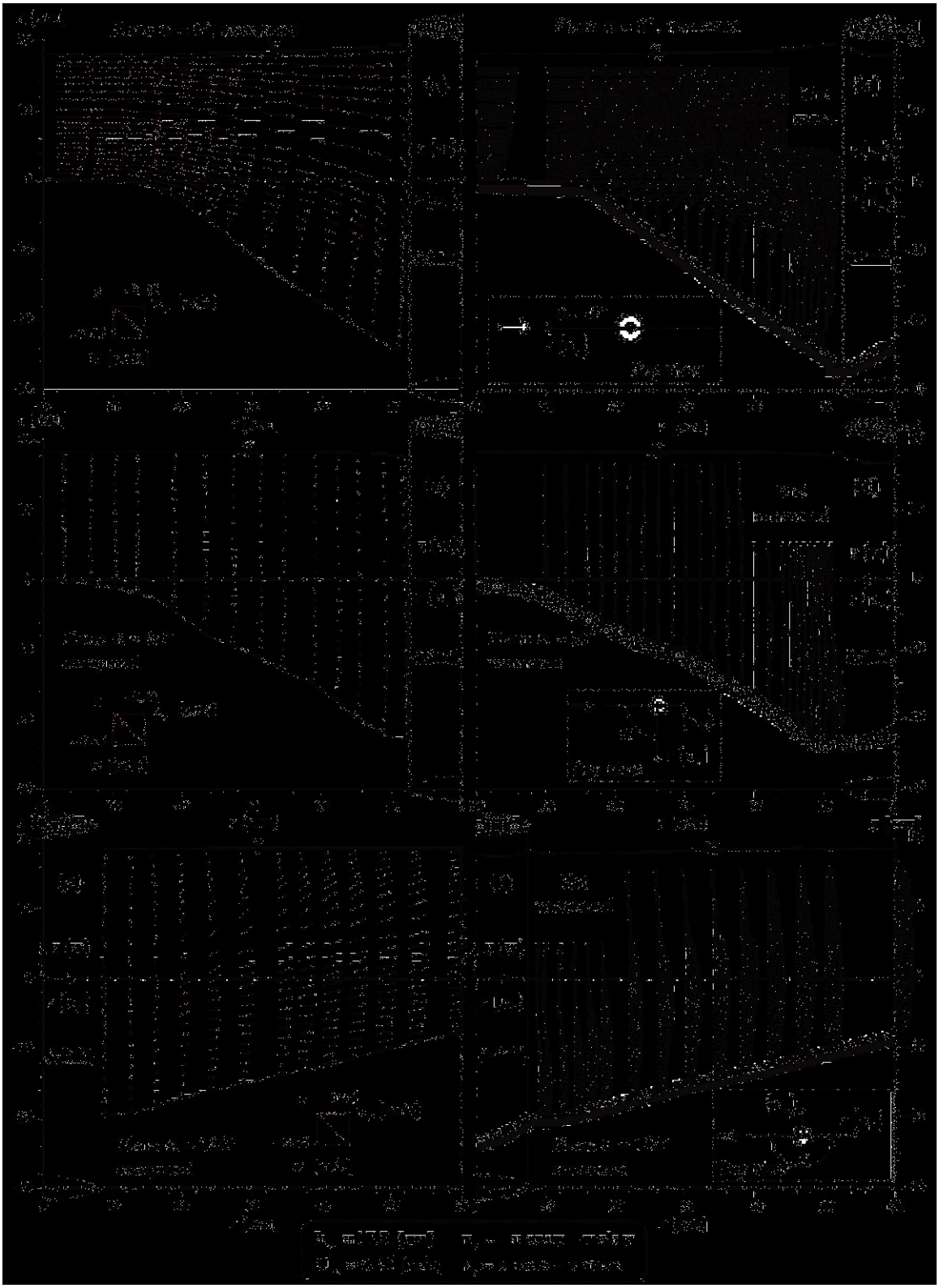

Fig. 5.17 Computed and measured velocity vectors, $\vec{\mathbf{V}}_{\alpha}(u_r, w)$,
in the planes α = 0°, 90°, 180°.
Flow around a cylinder in a scoured channel bed.

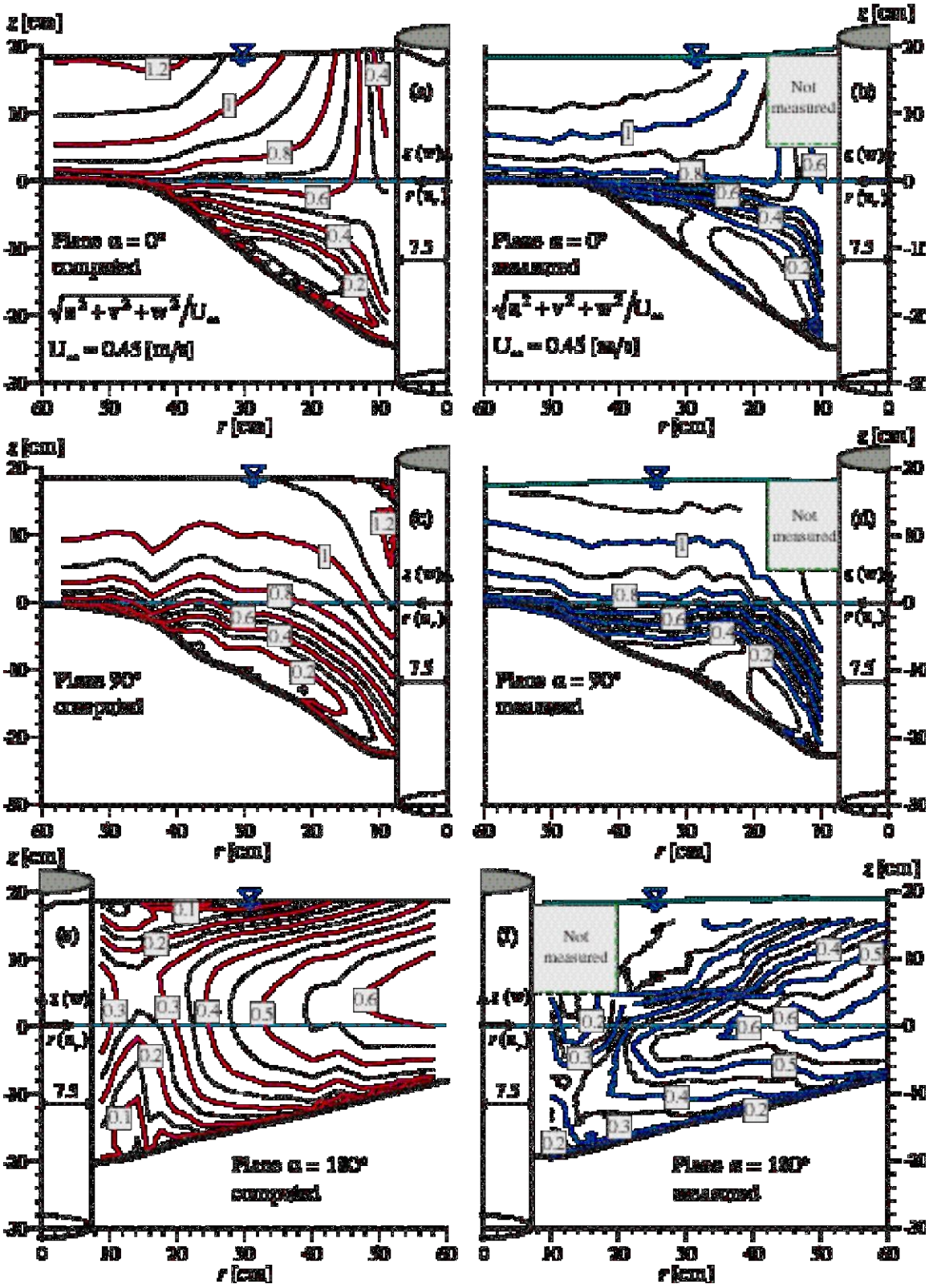

Fig. 5.18 Computed and measured velocity contours in the planes $\alpha = 0°, 90°, 180°$. The data are normalized by the velocity of the approach flow, V/U_∞, where $V = \sqrt{u^2 + v^2 + w^2}$ and $U_\infty = 0.45\,[m/s]$. Flow around a cylinder in a scoured channel bed.

Vorticity fields in the scour hole

As in the flat-bed case, the vorticity fields were computed from the radial and vertical velocity components and are presented in Fig. 5.19. Shown in this figure are the vorticity contours obtained from the simulation and the measurement. While the vorticity was computed using all data points, shown here are the contours in the region of important vorticity, $r \leq 60$ [cm] and $z \leq 5$ [cm]. The following is to be remarked:

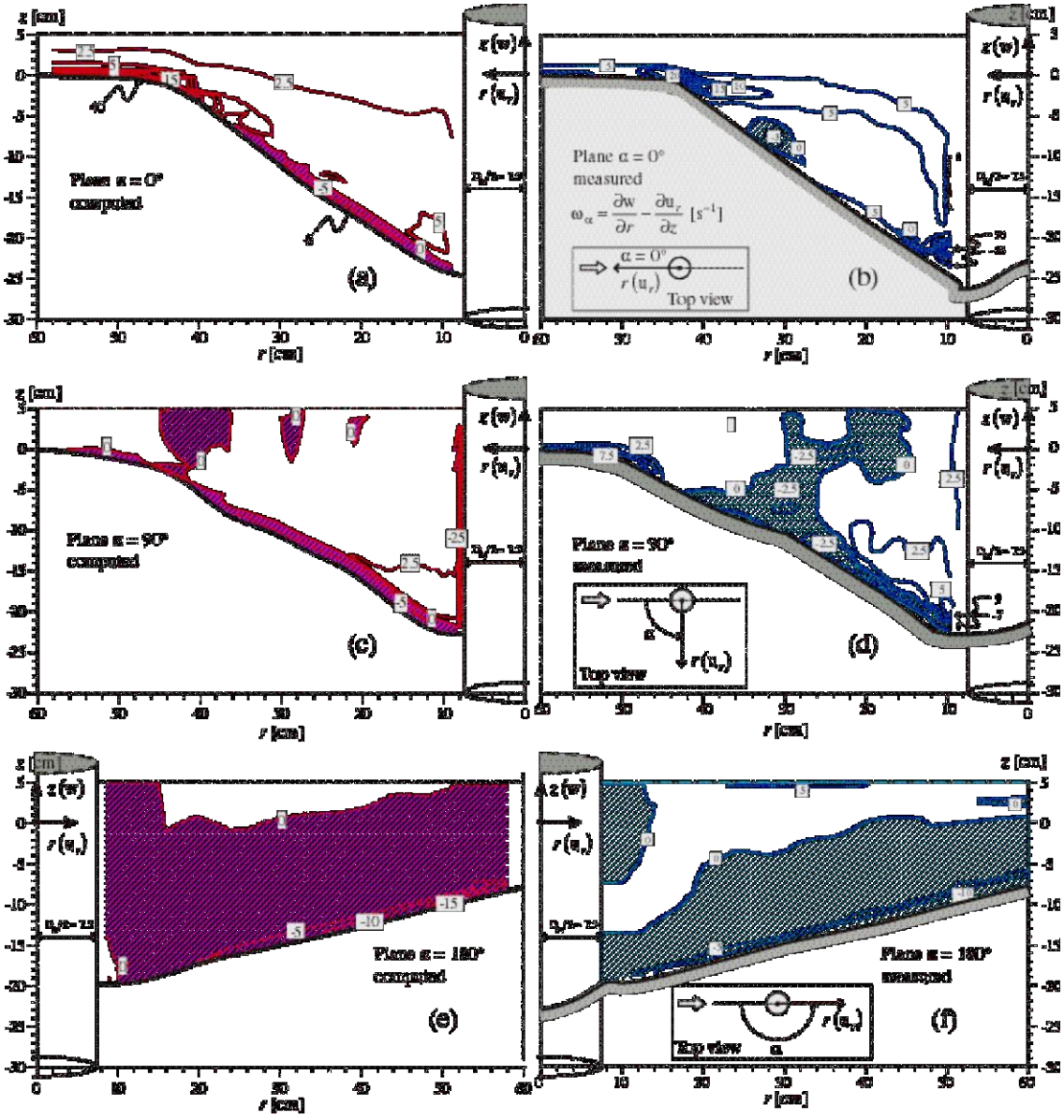

Fig. 5.19 Computed and measured vorticity fields, ω_α, in the planes $\alpha = 0°$, 90°, 180°. The shaded area indicates regions of negative vorticity fields. Flow around a cylinder in a scoured channel bed.

- In the plane $\alpha = 0°$ (Fig. 5.19a,b), a qualitative agreement on the general patterns of the vorticity field in the scour hole is achieved, being the characterized by a strong positive vorticities in the upstream inclined bed and a negative ones at about $r = 30$ [cm]. Quantitatively, though, the computed vorticity everywhere is weaker

than the measured one. The strong vorticity peaks (positive and negative ones) in the bottom corner of the cylinder are missed by the simulation. This is due, as has been mentioned in the preceding section, to the inability of the simulation to reproduce the strong reversed flow at this location, which is caused by the limited spatial resolution of the grid.

- In the plane $\alpha = 90°$ (Fig. 5.19c,d), the vorticity fields show small activity since the velocity components on this plane are very small as shown in the preceding section. Nevertheless, the contour plot near the bed indicates a reasonable agreement between the simulation and the measurement.

- In the plane $\alpha = 180°$ (Fig. 5.19e,f), the simulation and the measurement exhibit surprisingly a good agreement. The vorticity, being rather small, is distributed more or less evenly over the plane and there is no region of concentrated vorticity.

Turbulent kinetic energy around the cylinder

Discussed in this section is the turbulent kinetic energy computed by the model. The computed turbulent kinetic energy is presented as an equivalent height (energy per unit weight), k/g [mm], as shown in Fig. 5.20. For the sake of comparison, plotted also in the same figure are the values obtained from the experimental data; here the turbulent kinetic energy is obtained by $k = \frac{1}{2}\left(\overline{u'u'} + \overline{v'v'} + \overline{w'w'}\right)$ (see Chapter 3). The figures allow the following remarks:

- The plots show that the comparison of the computed and measured turbulent kinetic energy can be considered good. The simulation results in a lower energy than the measurement, but the tendency of the overall distributions is rather well predicted.

- In the plane $\alpha = 0°$ (Fig. 5.20a,b), both simulation and measurement show high energy concentrations in the bottom corner of the cylinder. The computed maximum value shown at the corner vicinity of the cylinder, however, is considerably lower than the measured one. This is consistent with the difference observed between the computed and the measured velocities (and vorticities) at this particular location as discussed in the preceding sections. From the simulation, the high energy is also observed almost along the entire depth at close vicinity of the cylinder. Unfortunately, measurements in this region are not available along the entire depth.

- In the plane $\alpha = 90°$ (Fig. 5.20c,d) similar observations as in the plane $\alpha = 0°$ can be made, but the simulation at the bottom corner of the cylinder is better, showing a close comparison to the measured data.

- In the plane $\alpha = 180°$ (Fig. 5.20e,f) the simulation and the measurement show a similar pattern, but the under-estimation of the kinetic energy is also considerable as in the plane $\alpha = 0°$.

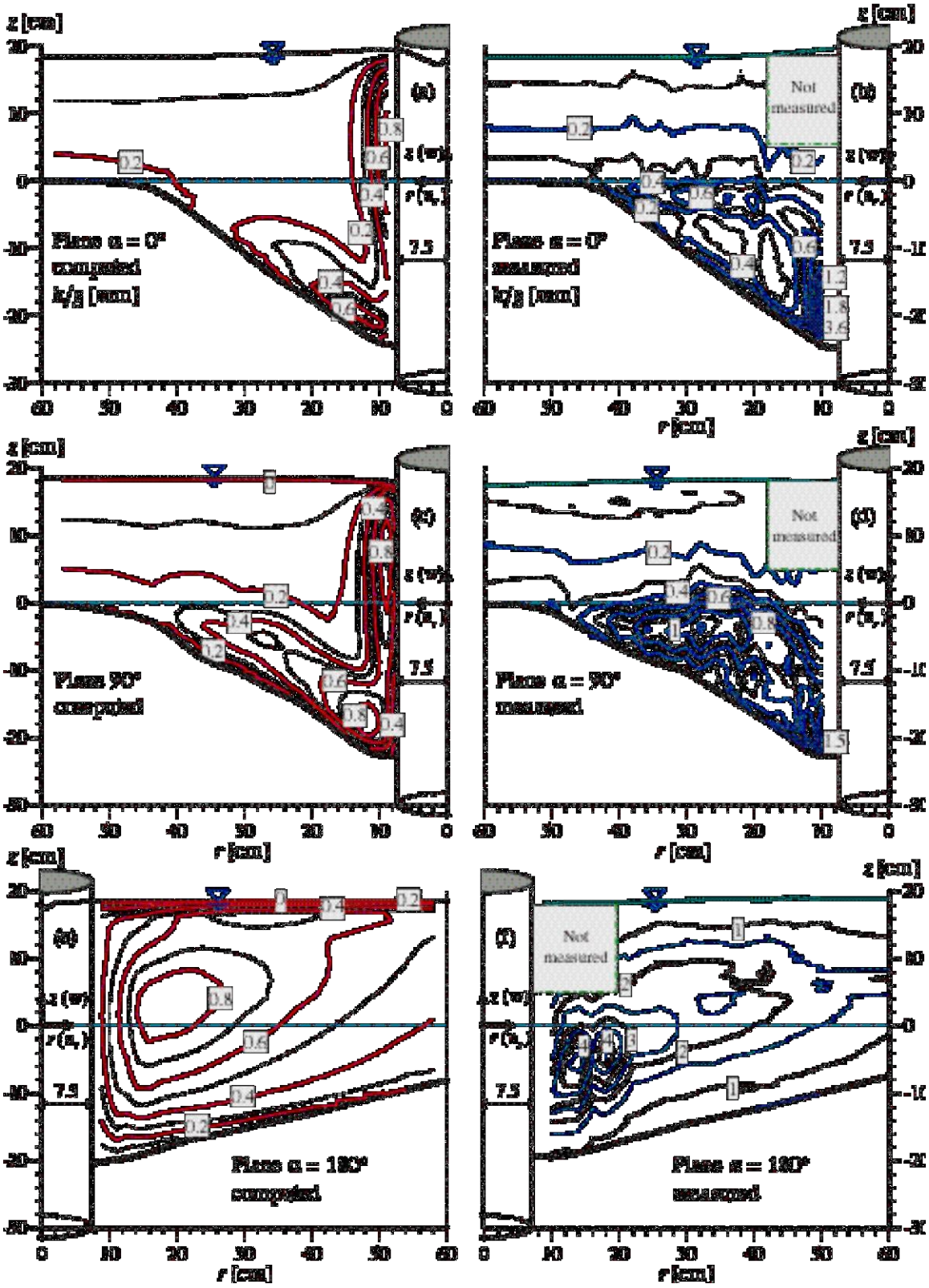

Fig. 5.20 Computed and measured turbulent kinetic energy, k/g ,
in the planes $\alpha = 0°, 90°, 180°$.
Flow around a cylinder in a scoured channel bed.

Production and dissipation of the turbulent kinetic energy around the cylinder

Turbulent kinetic energy, k, is extracted from the mean flow through the interaction of the turbulent shear (Reynolds stress, $-\overline{u_i' u_j'}$) and the mean shear, $\partial u_i / \partial x_j$. This process is represented by the turbulent kinetic-energy production term, G (see Chapter 4). Due to the effect of viscosity, the turbulent kinetic energy is dissipated, which is quantified by the dissipation rate, ε. The turbulent kinetic energy is transported by the flow through convective-diffusive mechanisms. To render the observation of this turbulent kinetic energy possible, contour plots of G and ε in the planes $\alpha = 0°$, 90°, and 180° are drawn and presented in Fig. 5.21. Only the computed results are evaluated since the data from the measurements do not allow all terms of the G expression (see Chapter 4) to be obtained. This figure reveals some interesting points as follow:

- Large production of the turbulent kinetic energy is always accompanied by a large dissipation (Fig. 5.21). This is expected since the source terms of the ε-equation are closely linked (and proportional) to the production and dissipation terms (the source terms) of the k-equation (see Chapter 4). The situation is also true in the opposite direction; diminishing production will be accompanied by diminishing destruction.

- In the upstream planes, $\alpha = 0°$ and 90° (Fig. 5.21a,b,c,d), a large production of the turbulent kinetic energy takes place close to the cylinder, at an elevation of about $z = 10$ [cm]. This production diminishes with the depth and it remains 20% of the maximum value at the bottom corner of the cylinder. From the plot of the turbulent kinetic energy presented in the preceding section (see Fig. 5.20), it can be seen that the zone of large production corresponds to the high turbulent kinetic energy. However, at the bottom corner, the turbulent kinetic energy is still high, whereas the production (and of course the dissipation) has become small. This means that the turbulent kinetic energy produced at the upper layer is transported towards the bed, here by the downward flow.

- Downstream of the cylinder, in the plane $\alpha = 180°$ (Fig. 5.21e,f), the production of the turbulent kinetic energy is smaller than that in the upstream planes. The turbulent kinetic energy, however, is comparable with that in the upstream planes, $\alpha = 0°$ and 90° (see Fig. 5.20). Again, it can be implied that this energy, besides from the local production, receives a contribution from other places, presumably from the upstream planes.

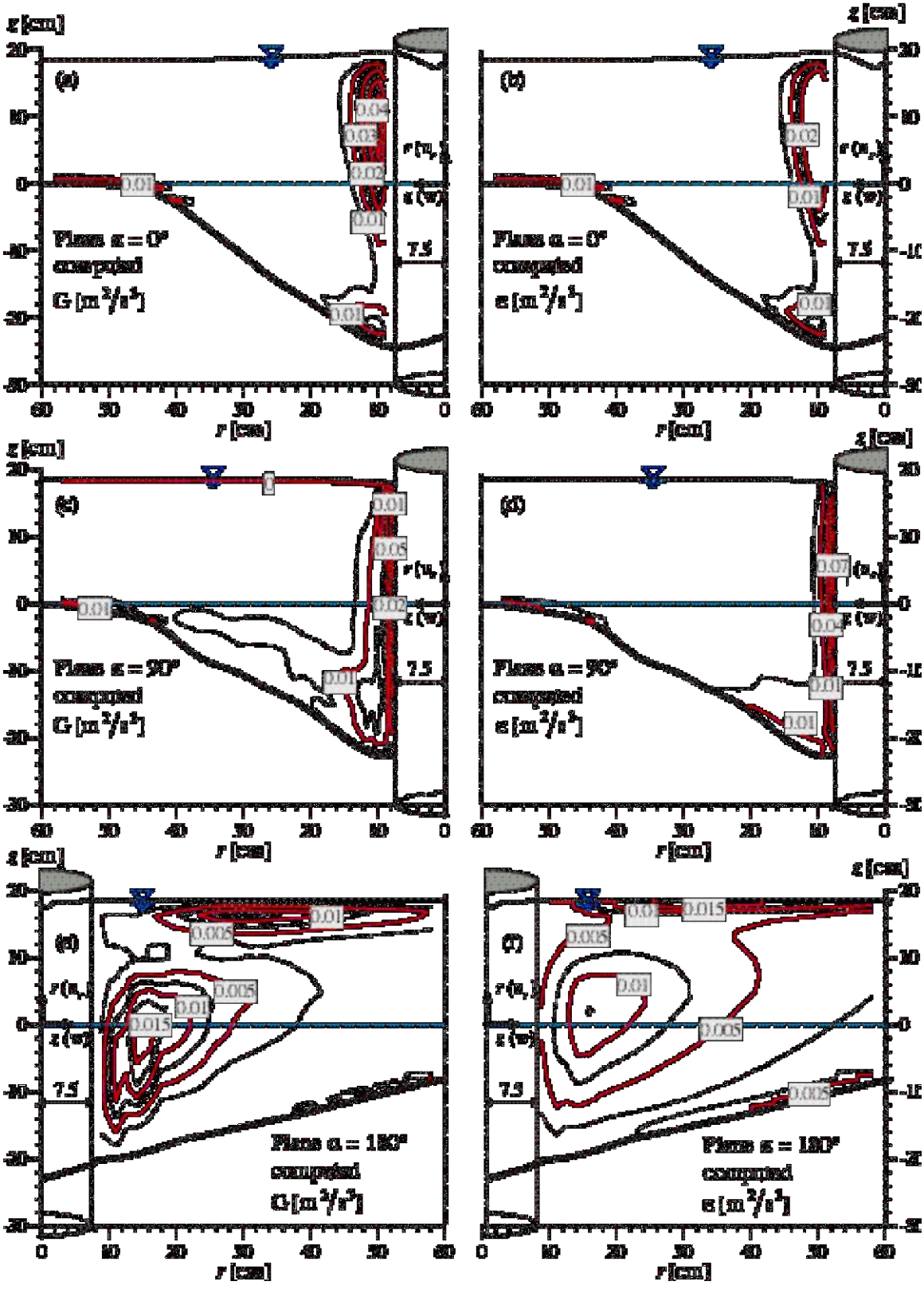

Fig. 5.21 Computed production and dissipation of the turbulent kinetic energy, G and ε , in the planes α = 0°, 90°, 180°.
Flow around a cylinder in a scoured channel bed.

Production of turbulent kinetic energy along cylinder boundaries

It has been observed that the computed turbulent kinetic-energy close to the cylinder is below the measured values. This might be caused by a computational inaccuracy of its production, due to an inherent difficulty related to the method of wall boundary treatment. The computation of the production of turbulent kinetic energy along the cylinder (wall) boundaries is done with a simplification, in which, among others, the production due to the normal stress is neglected (see Eqs. 4.75a,b in Chapter 4). This simplification is in conjunction with the wall function method applied to wall boundaries. This method assumes that the velocity at nodes adjacent to the boundary is parallel to the wall and is, between the wall and the adjacent node, distributed logarithmically. It has been pointed out in the previous chapter that this is a rather rough approximation at the cylinder boundaries. At such boundaries, the measured tangential and normal velocities, notably in front of the cylinder, have the same order of magnitude. This is observed also by the simulation (see Fig. 5.17a,e).

To render further insight into this problem, the computation of the production of turbulent kinetic energy upstream and downstream of the cylinder is elaborated and presented in Fig. 5.22. Shown in the figure are the computed tangential and normal velocity components (Fig. 5.22a,b,c). Obviously, the normal velocities are not negligible. Accordingly, neither the normal stresses are negligible compared to the tangential components (Fig. 5.22d,e). The equation of the production of turbulent kinetic energy written for wall boundaries is (see Eq. 4.75a in Chapter 4):

$$G = \frac{\tau_{nt}}{\rho}\frac{\partial V_t}{\partial n} + \frac{\tau_{nn}}{\rho}\frac{\partial V_n}{\partial n} \qquad (4.75a)$$

where subscripts n and t are the normal and tangential directions, respectively. In the wall function, the universal logarithmic velocity distribution is applied to the tangential velocity. The tangential velocity gradient in Eq. 4.75a is obtained from this logarithmic distribution. The production of turbulent kinetic energy due to the normal stress is simply neglected. The production, G, is therefore computed by (see Eqs. 4.75b in Chapter 4):

$$G = \frac{\tau_{nt}}{\rho}\frac{\partial V_t}{\partial n} \qquad (4.75b)$$

which is plotted by solid lines in Fig. 5.22f,g. It was mentioned previously that this production was not sufficient to generate the turbulent kinetic energy. The simulation under-estimates the experimental values.

Now suppose that, in the absence of knowledge on the normal velocity distribution, we assume a linear distribution of the normal velocities between the wall and the adjacent node. We subsequently use this linear distribution to obtain the normal velocity gradient and the normal stress in Eq. 4.75a. The production term thus obtained is shown by point-dashed lines in Fig. 5.22f,g. Evidently the production increases notably in front of the cylinder (Fig. 5.22f). There is also an increase, although not much, of the production of turbulent kinetic energy downstream of the cylinder (Fig. 5.22g).

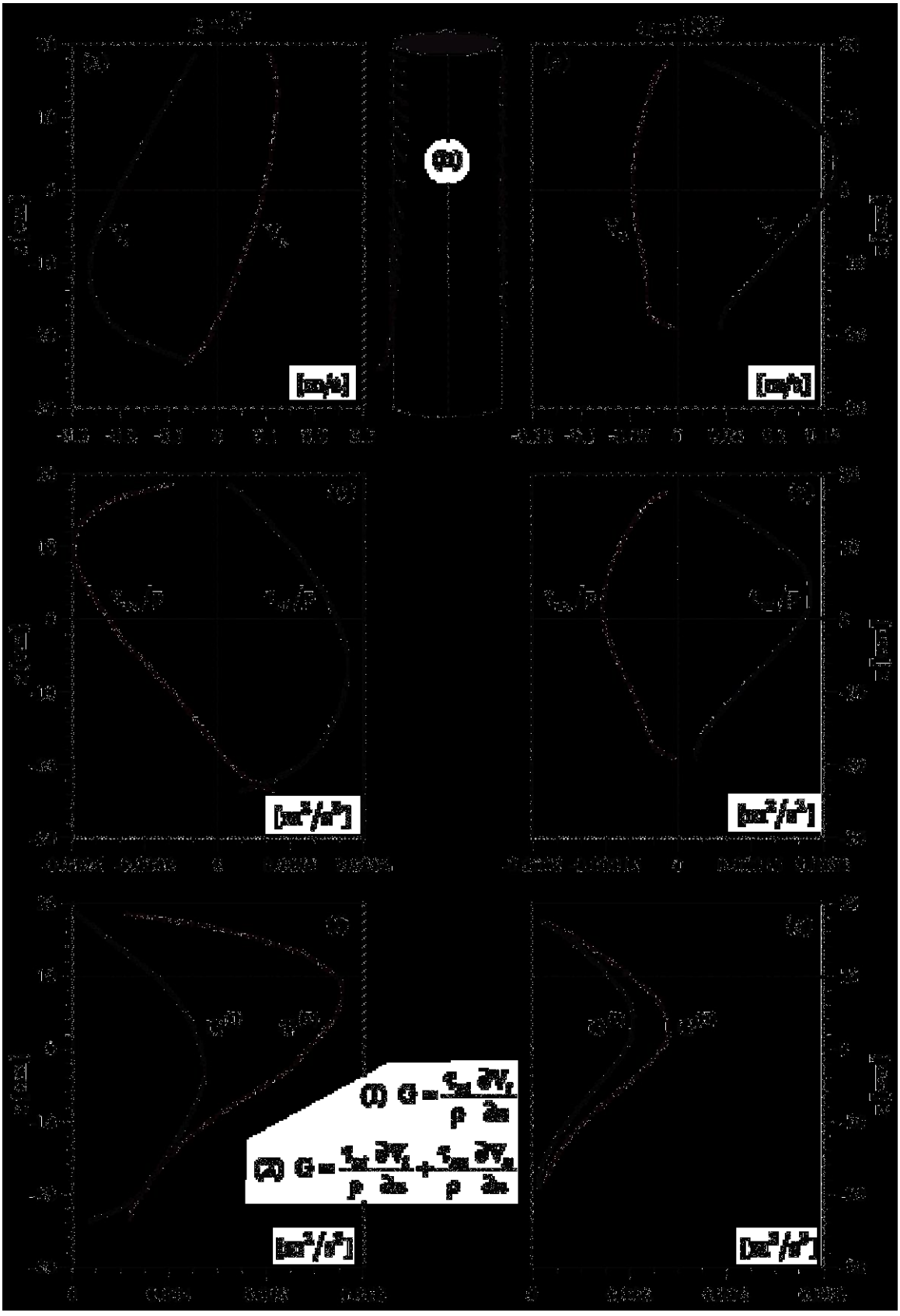

Fig. 5.22 Computation of the production of turbulent kinetic energy along the upstream and downstream faces of the cylinder.

If the above approach were used, the kinetic energy would likely increase that could make up its deficiency shown by the present model. It should be noted, however, that the method presented here is not yet readily compatible with the wall function method used in the model. If the normal velocity was to be taken into account in the production term, it would have also to be incorporated in the wall function method. This is not a straight forward task and, therefore, is not elaborated further in the present work.

Water surface profile

The computed and the measured water surface profiles are plotted together in Fig. 5.23. Shown in the figure are the surface profiles along the longitudinal section through the cylinder and along the cylinder circumference. From this comparison, the following can be observed:

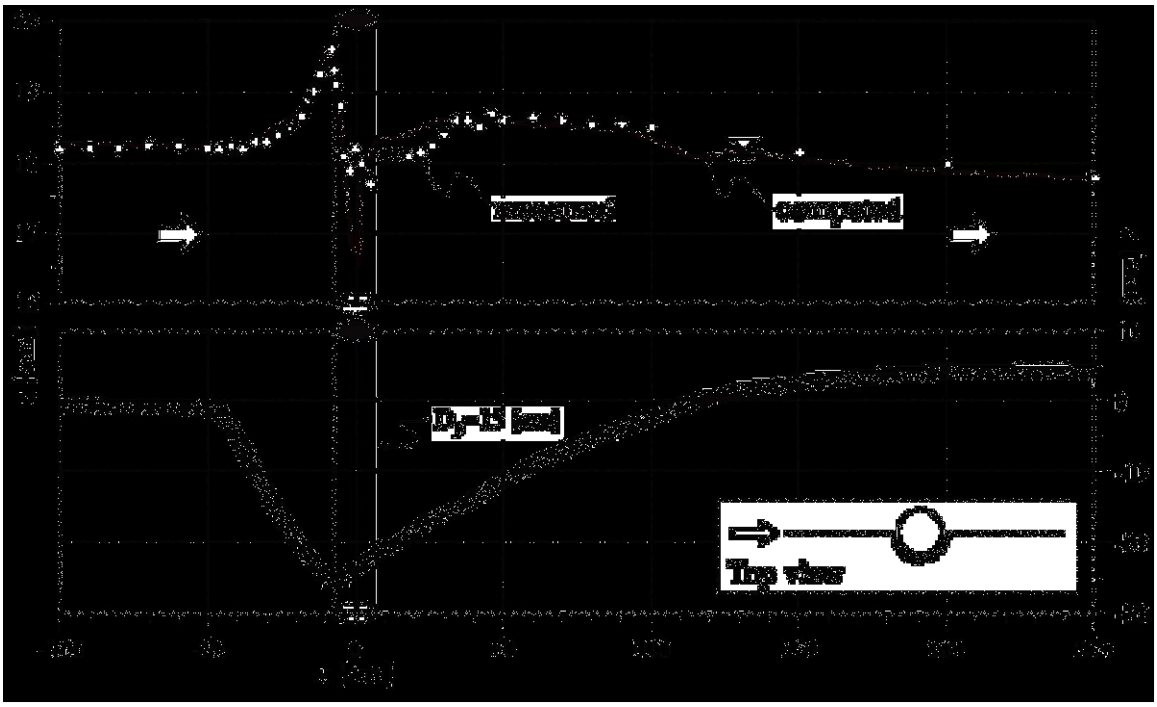

Fig. 5.23 Computed (line) and measured (symbols) water surface profiles along the longitudinal section and the cylinder circumference.
Flow around a cylinder in a scoured channel bed.

- Upstream of the cylinder, a reasonable agreement is visible between the simulation and the measurement. The computed water surface is closely follow the measured one and the bow wave in front of the cylinder is closely matched.

- Along the cylinder upstream circumference, the simulation closely reproduces the water surface obtained from the measurement. For the rest of the circumference until behind the cylinder, the agreement between the simulation and the measurement becomes less good. The problem of obtaining a satisfactory simulation result is again can be explained by the reduced accuracy of the surface computation in the region of strong pressure (surface) gradient such as in the cylinder circumference.

- Downstream and immediately behind the cylinder, the computed water surface is above the measured one; this was also found in the case of the flat channel bed simulation. The same explanation as in the flat-bed case can be put forward. Along the downstream circumference of the cylinder, from $\alpha = 90°$ to 180°, one is moving from the region of low water surface (high velocity) towards the wake region and is experiencing a strong surface gradient. This condition makes the surface computation less reliable. Moving away from the cylinder, however, the surface gradient becomes favorable and the simulation result closely approaches the experimental data.

5.6.4 Conclusions

The applicability of the numerical model presented in Chapter 4 to simulate flow around a cylinder has been again confirmed. The model successfully simulates the flow field around the cylinder installed in a scoured channel bed. Comparison shows that the computed velocity fields expressed in different forms (see Fig. 5.16 to Fig. 5.19) agree qualitatively with the measured ones. Further evaluation of the computed velocities was carried out by observing the turbulent kinetic energy: its distribution, production, and dissipation (see Fig. 5.20 and Fig. 5.21). The distribution of the kinetic energy can be considered reasonable, showing a similar pattern as the experimental data. Its magnitude, though, is lower than the one obtained from the measurement. The computation of the water surface (see Fig. 5.23) is reasonably good, but a problem remains in the downstream circumference of the cylinder as in the flat-bed case.

5.7 Summary and conclusions

The numerical model presented in the preceding chapter (see Chapter 4) was tested and applied. A simple case of uniform flow was selected to test and validate the model. The model was subsequently applied to simulate flow around a cylinder. Two cases of flow around a cylinder were considered, namely the flat channel bed investigated in the previous work (see *Yulistiyanto*, 1997) and the scoured channel bed of the present work (see Chapter 2).

The test runs using the uniform flow condition prove that the model performs satisfactorily. The model produces the uniform flow condition under different inflow and initial conditions. Comparison of the computed flow was made to the experimental data of Yulistiyanto (see *Yulistiyanto*, 1997). After a series of calibration runs to adjust the bed standard-roughness and the flow depth, all flow conditions such as velocity, eddy viscosity, and shear stress are in a good agreement with the experimental data (see Fig. 5.3 and Fig. 5.4).

The applicability of the model to simulate flow around a cylinder has been evidenced. In both flow cases, the flat channel bed and the scoured channel bed, the model has delivered good predictions of the flow fields around the cylinder. Comparisons of the computed flow field to the experimental data were made in different ways, such as profiles of the 3D-velocity components, velocity vectors, flow intensities, 2D-vorticities,

and surface profiles (see Fig. 5.10 to Fig. 5.14 and Fig. 5.16 to Fig. 5.19). In the two flow cases, the comparisons show satisfactory agreements. It was found, however, that the method of locating the surface boundary opted in the model became less accurate in regions of strong pressure gradient. In the scoured channel bed simulation, comparison was also done to the turbulent kinetic energy (see Fig. 5.20). It was shown that reasonable results were obtained, showing a comparable pattern of the distribution of turbulent kinetic energy obtained from the simulation and the measurements.

Conclusively, the numerical model developed in the present work can be considered as being applicable and reliable to simulate flow around a cylinder. It can also be stipulated that this model would also be applicable to other type of flow, such as flows in a channel bend and in a compound channel.

5.8 Recommendations for future works

Judging that the major problem encountered in the simulation is the computation of the surface boundary, below is a proposition to adopt another method that is feasible to be incorporated in the present model.

The approach used in the present model to locate the surface boundary is by imposing a known (zero) flux across the boundary. From the pressure computation, the SIMPLE algorithm, non-zero pressures will be obtained at the surface boundary. Referring to Fig. 5.24a, the surface computation of the present model works as follows:

- Impose zero discharge, $q_t = 0$, at the surface boundaries.
- Obtain the pressure at the cell centers, p_P, from the SIMPLE algorithm.
- Extrapolate the pressure to the surface by assuming a hydrostatic distribution: $p_t = p_P + \rho g_z (z_t - z_P)$.
- Move the surface according to the pressure: $\Delta h = p_t / |\rho g_z|$.
- Distribute the surface to get the coordinate of the cell vertices: $\Delta h_1 = \frac{1}{4} \sum \Delta h_j$, where Δh_j is the surface of the four neighbors.

The proposed alternative approach, on the other hand, imposes a zero pressure at the surface. By assuming a hydrostatic distribution, the pressure at the cell center below the surface can be obtained, $p_P = p_t - \rho g_z (z_t - z_P)$. This pressure is not corrected in the pressure computation of the SIMPLE algorithm. For cells just below the surface, the pressure-correction, p^c, is known (zero). The discharge across the surface, q_t, becomes the unknown. It can be incorporated in the pressure-correction equation (see Eq. 4.67 in Chapter 4) by interchanging those two variables. The q_t is brought to the left-hand side and the p^c is put to the source term on the right-hand side. Once the discharge, q_t, is obtained, the velocity at the surface can be computed and used to move the surface. Introducing a surface function, $Z_t = f(x, y, t)$, to denote the position of the surface and differentiating that function with respect to time, one has:

$$\frac{dZ_t}{dt} = \frac{\partial Z_t}{\partial t} + \frac{\partial Z_t}{\partial x}\frac{dx}{dt} + \frac{\partial Z_t}{\partial y}\frac{dy}{dt} + \frac{\partial Z_t}{\partial z}\frac{dz}{dt} = 0 \quad \Rightarrow \quad \frac{\partial Z_t}{\partial t} + u_t\frac{\partial Z_t}{\partial x} + v_t\frac{\partial Z_t}{\partial y} = w_t \qquad (5.4)$$

which is known as the kinematic condition. The above equation can be solved for Z_t by using a finite-volume technique on the 2D grid (*xy* plane) of the surface boundary. To avoid the excessive computational time, the surface computation can be carried out at the end of each time step. Alternatively, it can also be done after several time steps when the pressure correction has reduced to a sufficiently small number as in the case of the present model.

The surface function, Z_t, is unfortunately given for the surface (top face) center, whereas the cell is defined by its vertices. This in effect necessitates the use of an interpolation to get the *z* values of the cell vertices from this function. The simplest approach will be using a linear interpolation (see Fig. 5.24c). Note that the usual notations PEWNS are used to indicate the center and neighboring nodes on the 2D mesh which constitutes the top boundary of the 3D mesh. Integrating Eq. 5.4 over the 2D cell and writing each term in the discretized finite-volume form, one has:

$$\begin{aligned}
&\frac{\partial}{\partial t}\iint_{S_{t,z}} Z_t \, dS = \frac{Z_{t,P}{}^{n+1} - Z_{t,P}{}^{n}}{\Delta t} S_{t,z} \\
&\oiint_{S_{t,z}} u_t \frac{\partial Z_t}{\partial x} \, dS = (u_t)^{n+1}\left[(Z_t\,\Delta y)_e^{n+1} + (Z_t\,\Delta y)_w^{n+1} + (Z_t\,\Delta y)_n^{n+1} + (Z_t\,\Delta y)_s^{n+1}\right] \\
&\oiint_{S_{t,z}} v_t \frac{\partial Z_t}{\partial y} \, dS = (v_t)^{n+1}\left[(Z_t\,\Delta x)_e^{n+1} + (Z_t\,\Delta x)_w^{n+1} + (Z_t\,\Delta x)_n^{n+1} + (Z_t\,\Delta x)_s^{n+1}\right] \\
&\iint_{S_{t,z}} w_t \, dS = w_t \, S_{t,z}
\end{aligned} \qquad (5.5)$$

where the face values are obtained by interpolation (see Eq. 4.19), for example for the east face: $Z_{t,e} = (1-\beta_e)Z_{t,P} + \beta_e Z_{t,E}$. Using this interpolation to replace the face values in Eq. 5.5, the discretized finite-volume form of Eq. 5.4 is:

$$a_P \, Z_{t,P}{}^{n+1} + \sum_{nb=EWNS} a_{nb} \, Z_{t,nb}{}^{n+1} = b \qquad (5.6)$$

where the coefficients consist of the following terms:

$$a_P = \frac{S_{t,z}}{\Delta t} - \sum_{nb} a_{nb} + (\Delta y_e + \Delta y_w + \Delta y_n + \Delta y_s)u_t + (\Delta x_e + \Delta x_w + \Delta x_n + \Delta x_s)v_t,$$

$$a_E = \beta_e(\Delta y_e \, u_t + \Delta x_e \, v_t),$$

$$a_W = \beta_w(\Delta y_w \, u_t + \Delta x_w \, v_t),$$

$$a_N = \beta_n(\Delta y_n \, u_t + \Delta x_n \, v_t),$$

$$a_S = \beta_s(\Delta y_s \, u_t + \Delta x_s \, v_t),$$

$$b = w_t \, S_{t,z} + \frac{S_{t,z}}{\Delta t}.$$

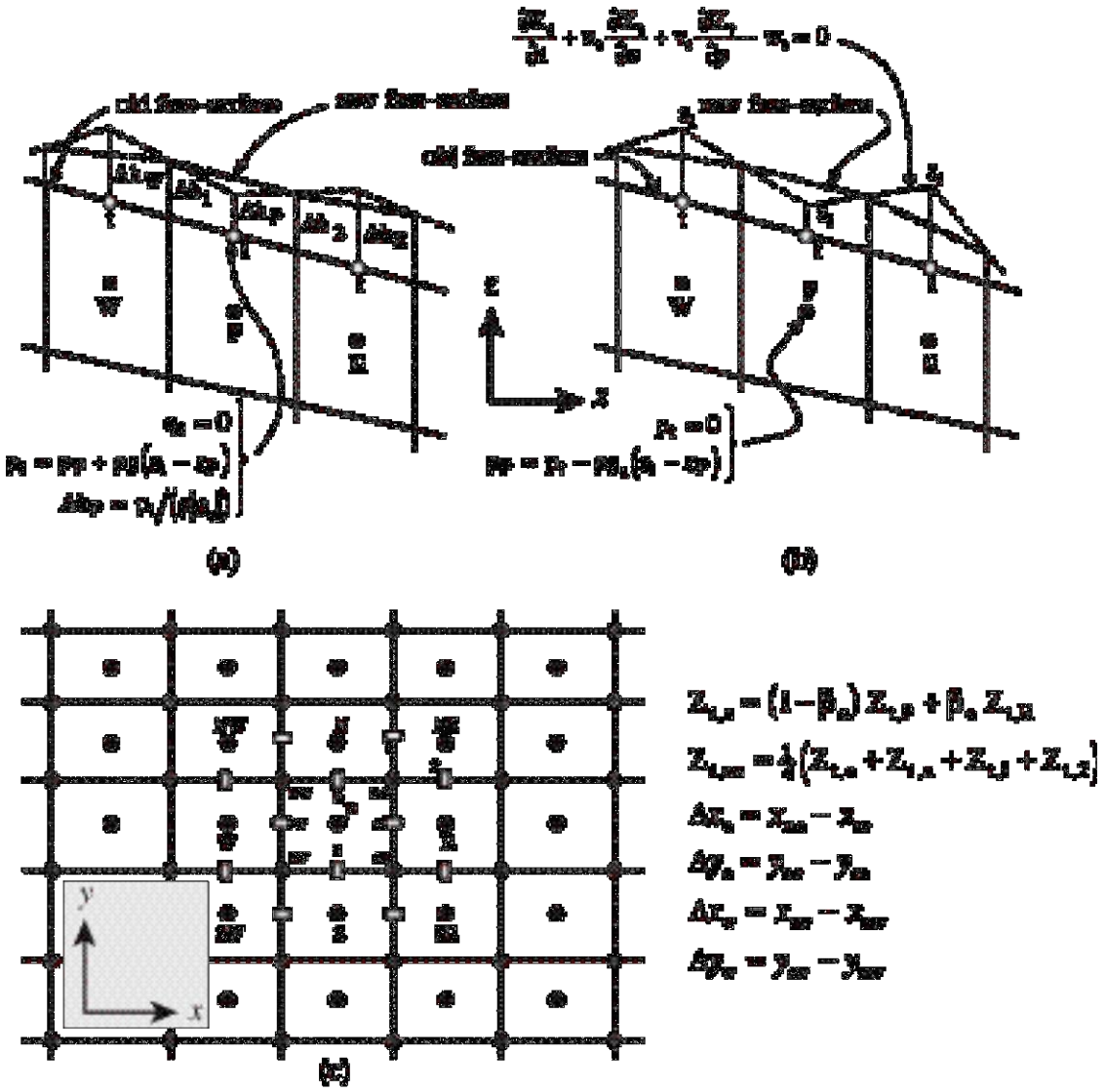

Fig. 5.24 Surface boundary computation: (a) present approach, (b) proposed modification, and (c) 2D mesh of the surface boundary.

Referring to Fig. 5.24b, the proposed approach works as follows:

- Impose zero pressure at the surface, $p_t = 0$, and obtain the pressure at the cell center by assuming a hydrostatic distribution: $p_P = p_t - \rho g_z (z_t - z_P)$.
- Interchange p^c and q_t in the pressure-correction equation for cells neighboring the surface; at those cells, the pressure-correction equation (see Eq. 4.68) reads: $q_t + \sum_{nb} a_{nb}^p p_{nb}^c = b^p$ where the source term b^p does not contain q_t any more.
- Obtain the surface velocity based on the computed discharge: $V_t = q_t / S_t$, whose components are $u_t = \vec{V}_t \cdot \vec{e}_{t,x}$ and $v_t = \vec{V}_t \cdot \vec{e}_{t,y}$.
- Solve Eq. 5.6, at the end of each time step or after the p^c has reduced to sufficiently small numbers, to get the surface position, Z_t.

- Distribute the surface to get the coordinate of the cell vertices, for example by using a simple relation (see Fig. 5.24c): $Z_{t,ne} = \frac{1}{4}\left(Z_{t,e} + Z_{t,n} + Z_{t,1} + Z_{t,2}\right)$.

The cost of the proposed approach, compared to the present one, is the additional equation to be solved at each time step. The iterative matrix solver, similar to the existing matrix solver of the present model but written for a 2D case, can be used to solve Eq. 5.6.

References

Graf, W. H., and Yulistiyanto, B. (1998). "Experiments on flow around a cylinder; the velocity and vorticity fields." *IAHR, J. Hydr. Res.*, 36(4), 637-653.

Hurther, D., Lemmin, U., and Arditi, M. (1996). "Using an annular curved array transducer for bistatic ADVP application." *Rapport Annuel, Laboratoire de recherches hydrauliques, EPFL*, 1996, B.201.1-B.201.19.

Lhermitte, R., and Lemmin, U. (1994). "Open-channel flow and turbulence measurement by high-resolution Doppler sonar." *J. Atm. Ocean. Tech.*, 11, 1295-1308.

Versteeg, H. K., and Malalasekera, W. (1995). *An Introduction to Computational Fluid Dynamics: The Finite Volume Method*., Longman Group, Essex, England.

Yulistiyanto, B. (1997). *Flow around a cylinder installed in a fixed-bed open channel*., *Doctoral Dissertation*, No. 1631, EPFL, Lausanne, Switzerland.

Notations

a_{nb}	[m^2/s]	variable coefficients of the surface function equation.
b	[m^3/s]	source term of the surface function equation.
a_{nb}^p	[$m^3/s/Pa$]	variable coefficients of the pressure-correction equation.
b^p	[m^3/s]	source term of the pressure-correction equation.
c_μ	[–]	k-ε model constant.
D_p	[m]	diameter of cylinder.
d_{50}	[m]	mean diameter of sediment.
G	[m^2/s^3]	production of turbulent kinetic energy.
g	[m/s^2]	gravitational acceleration.
h, h_∞	[m]	flow depth, uniform-flow depth.
k	[m^2/s^2]	turbulent kinetic energy.
k_s	[m]	equivalent roughness.
n	[–]	normal direction.
p, p^c	[Pa]	pressure, pressure correction.
Q	[m^3/s]	discharge.
q	[m^2/s]	discharge per unit width.
Re	[–]	Reynolds number.
r	[m]	radial direction.

S	[m^2]	surface area.
S_o, S_w	[–]	bed and surface slopes.
t	[–]	tangential direction.
U, U_∞	[m/s]	sectional average velocity, average velocity of uniform flow.
u, v, w	[m/s]	Cartesian velocity components.
u_r, u_α	[m/s]	cylindrical (radial and tangential) velocity components.
u_*	[m/s]	friction velocity.
V, V_α	[m/s]	velocity, velocity projection on a plane α.
x, y, z	[m]	Cartesian coordinate directions.
Z_t	[m]	surface function.
α	[°]	angular direction.
β_e	[–]	interpolation factor.
ε	[m^2/s^3]	kinetic energy dissipation.
κ	[–]	Karman constant.
ν, ν_t	[m^2/s]	kinematic viscosity, turbulent eddy viscosity.
ω	[1/s]	vorticity.
θ	[°]	angular direction.
ρ	[kg/m^3]	density of water.
τ, τ_o	[N/m^2]	shear stress, bed shear-stress.

Chapter 6

6 Summary and Conclusions

6.1 The work

The work is about an investigation on flow around a vertical cylinder installed on a mobile channel bed. When passing around a cylinder, a uni-directional flow undergoes different processes as it interacts with the cylinder and the mobile bed. The flow becomes three-dimensional and highly turbulent. At the same time, it erodes the mobile bed around the cylinder base and a local scouring takes place. These two particular physical processes, the flow and the scouring, are the main interests in the study of flow around a cylinder. The present work deals only with the first aspect, in which the flow takes place in an equilibrium scour-depth condition (the scouring has ceased), under a clear-water regime (the transport capacity in and out the scour hole is not exceeded). The objective of the investigation is to get a better understanding on the flow as it is altered by the cylinder and the scour hole.

Two approaches were adopted in the investigation, namely laboratory measurements and numerical simulations. This is a continuation of the work conducted previously at the LRH EPFL by *Yulistiyanto* (1997)[1], in which a scoured channel bed replaces the flat channel bed one of the previous work and a 3D hydrodynamic model substitutes the 2D depth-averaged one.

6.2 Results

6.2.1 Laboratory measurements

Detailed measured velocities were obtained using a non-intrusive acoustic Doppler velocity profiler (ADVP), conceived and developed at the LRH EPFL. The instrument measures instantaneously the vertical distribution of the velocity vectors in the far-field approach flow and scour hole. Two ADVP configurations were used; each one was suited for different flow-depths. The focalized ADVP having a cylindrical measuring volume of diameter $\Delta\phi = 6$ [mm] and height $\Delta d = 3$ [mm] was employed for flow depths $h \leq 18$ [cm]. For deeper flow depths, $h > 18$ [cm], the non-focalized ADVP having a measuring volume of diameter $9 \leq \Delta\phi$ [mm] ≤ 26 and height $\Delta d = 4.5$ [mm] was used.

[1] Yulistiyanto, B. (1997). "Flow around a cylinder installed in a fixed-bed open channel." *Doctoral Dissertation*, No. 1631, EPFL, Lausanne, Switzerland.

The experiments were conducted in a 29 [m] long, 2.45 [m] wide, and 5.5×10^{-4} inclined rectangular channel having a uniform sand bed of mean diameter $d_{50} = 2.1\,[\mathrm{mm}]$. The cylinder with a diameter of $D_p = 15$ [cm], was vertically installed at $x_L = 11$ [m] downstream of the channel entrance. The uniform approach flow ($Q = 0.2\,[\mathrm{m^3/s}]$, $U_\infty = 0.45\,[\mathrm{m/s}]$, and $h_\infty = 18\,[\mathrm{cm}]$) was established and can be considered to be two-dimensional ($B/h_\infty = 13.6$), turbulent (Re = 81,000), and subcritical (Fr = 0.34). The shear velocity was obtained from the measured velocity and shear stress distributions, as being $u_{*,\infty} = 2.65\,[\mathrm{cm/s}]$. The velocity measurements were performed at the equilibrium scour hole ($d_s = 25\,[\mathrm{cm}]$) under a clear-water scour condition, which had been previously established by performing a continuous run of 5 days.

The measured (time-averaged) velocity field confirms that a 3D flow establishes itself around the cylinder, being characterized principally by a clockwise circulating flow inside the scour hole. The circulating flow is formed by the downward flow along the cylinder face and the reversed flow along the scour bed. This structure was detected particularly in the plane of symmetry upstream of the cylinder. Another but smaller and weaker circulating flow was seen at the leading edge of the scour hole. Moving around the cylinder towards downstream, the circulating flow diminishes and becomes practically undetected on the side plane. This circulating flow is here designated as the horseshoe vortex.

The vertical velocity component, which primarily manifests itself as a downward velocity notably along the cylinder face, was separately investigated. The radial distributions of the downward velocity show that they collapse for a distance of $r/D_p \leq 1.8$. Along the cylinder face, the locus of the maximum downward velocities for $\alpha \leq 90°$ fall at 40% of the local flow depth irrespective of the angular direction.

The notion that the vertical velocity component is largely downward —except behind the cylinder— suggests that the scour hole attracts the flow. Inside the scour hole, the flow may undergo a circulating mechanism; this circulating feature yet takes place and remains inside the scour hole. It seems that the flow exits from the scour hole through the wake behind the cylinder, where the vertical velocity component has positive values.

Downstream of the cylinder, a flow reversal towards the surface was observed, being pronounced in the close vicinity of the cylinder. It gradually disappears as the flow moves away from the cylinder and is returning back towards the uni-directional flow condition.

Outside the scour hole, i.e. in the upper layer above the original bed, the longitudinal velocity components dominate; only in the close vicinity of the cylinder the transverse and notably the vertical velocity components are important. The flow direction of the approach flow when passing the cylinder thus remains much the same. The effect of the cylinder in deflecting the approach flow is limited to regions close to the cylinder and inside the scour hole.

The spatial distributions of the turbulence intensities and the Reynolds stresses were also evaluated. The intensity of turbulence inside the scour hole is strong; an increasing turbulence was detected approaching the cylinder and moving around the cylinder towards the downstream (wake) region. In the wake region, where a separation evidenced by a flow reversal takes place, the turbulence attains its strongest intensity. The kinetic energy of the flow inside the scour hole, where a circulating flow is eminent, consists of high turbulent energy, ranging from 10% to 90% of the total kinetic energy. The profiles of the turbulent kinetic energy are characterized by distinguishable bulges along the presumed separation line. Approaching and moving around the cylinder, those bulges move downwards, increase, and enlarge.

The longitudinal distribution of the bed shear-stresses along the plane of symmetry shows that the bed shear-stress is reduced upon entering the scour hole when compared to its value in the approach flow. The shear stress along the upstream scour bed has negative values, corresponding to the flow reversal in that region. These observations are supported by the numerical simulation.

6.2.2 Numerical simulations

The flow simulations were performed by using a 3D numerical model, which is developed based on the approximate solution of the Reynolds-averaged Navier-Stokes equations for incompressible flows by using finite-volume method. The model uses the k-ε turbulence closure model to compute the turbulence stresses and the SIMPLE (Semi-Implicit Method for Pressure-Linked Equations) method of *Patankar and Spalding* (1972)[2] to link the velocity to the pressure. The water surface position is determined according to the pressure along the surface boundary. The model solves the transient flow equations, but is applicable only for steady flow problems.

The core of the present model is relatively standard and can be found in classical textbooks. However, some detailed derivations and clarifications were elucidated about the boundary conditions and the pressure-velocity coupling. These are seldom presented in detail.

Preliminary simulation tests were carried out to ascertain the methods and modeling techniques opted in the model; these serve as the calibration and verification of the model. A simple and well-known uniform flow was selected. The model value of the equivalent standard roughness of the bed was calibrated against the measurements. Verification of the model was done by simulating the flow under different boundary and initial conditions; the model could produce the uniform flow field and the agreement with the measured one was nearly perfect.

[2] Patankar, S.V., and Spalding, D.B. (1972). "A calculation procedure for heat, mass and momentum transfer in three-dimensional parabolic flows." *Int. J. Heat Mass Transfer*, 15, 1787-1806.

The tested model was subsequently applied to simulate two cases of flow around a cylinde, namely the flat channel bed of the previous study and the scoured channel bed of the present measurements.

In both cases, the model has delivered good predictions of the flow fields around the cylinder. Comparisons of the computed flow field to the experimental data were made in different ways, such as profiles of the 3D-velocity components, velocity vectors, flow intensities, vorticities, and water surface position. In both cases, the comparisons show satisfactory agreements. It was found, however, that the method of locating the surface boundary opted in the model became less accurate in regions of strong pressure gradient.

In the scoured channel bed simulation, a comparison to the measured data was also done for the turbulent kinetic energy. While the general trend of the turbulent kinetic-energy distribution could be well predicted, its magnitude was under estimated by the simulation. It appears that the model cannot sufficiently generate the turbulent kinetic energy. From the evaluation of the production and dissipation of the turbulent kinetic energy, it was found that the production is not appropriately computed in the vicinity of solid boundaries. At such boundaries, the assumption used in the derivation of the method is violated. This problem stems from the difficulty in evaluating gradients of the normal velocity, which are not well defined at solid boundaries. The problem has been identified and put forward, but the solution of this problem is not elaborated in the present work.

6.3 Conclusions

The laboratory measurements and the numerical simulations have provided the detail picture of the 3D flow pattern resulted from a uni-directional flow passing around a cylinder. Thanks to the powerful ADVP, the measurements give the detail information not only of the mean (time-averaged) velocities, but also the turbulence structure. The vortex formed by the downward and reversal flow in the scour hole could be detected; this vortex can be designated as the horseshoe vortex. The numerical model developed in the present work has proven also its capability to simulate this highly 3D flow pattern. Comparisons of its results to the measured flow show reasonably good agreements. The model may serve as a predictive tool for other flows of different hydraulic conditions, such as flows in a channel bend and in a compound channel.

The flow pattern upstream and downstream of the cylinder, obtained by the measurements and the numerical simulations, are presented in Fig. 6.1 (for the flat channel bed) and Fig. 6.2 (for the scoured channel bed). These figures may well illustrate the results of the present work.

6.4 Recommendations for future works

From the experience gained during the present work, the following suggestions are proposed in conducting investigative works on the flow around the cylinder:

- Laboratory measurements: completing the measurements with flow visualizations and pressure measurements

- Numerical simulation: refining the boundary treatments, notably the solid boundaries and water surface computation as discussed in Sect. 5.6 and 5.8, respectively

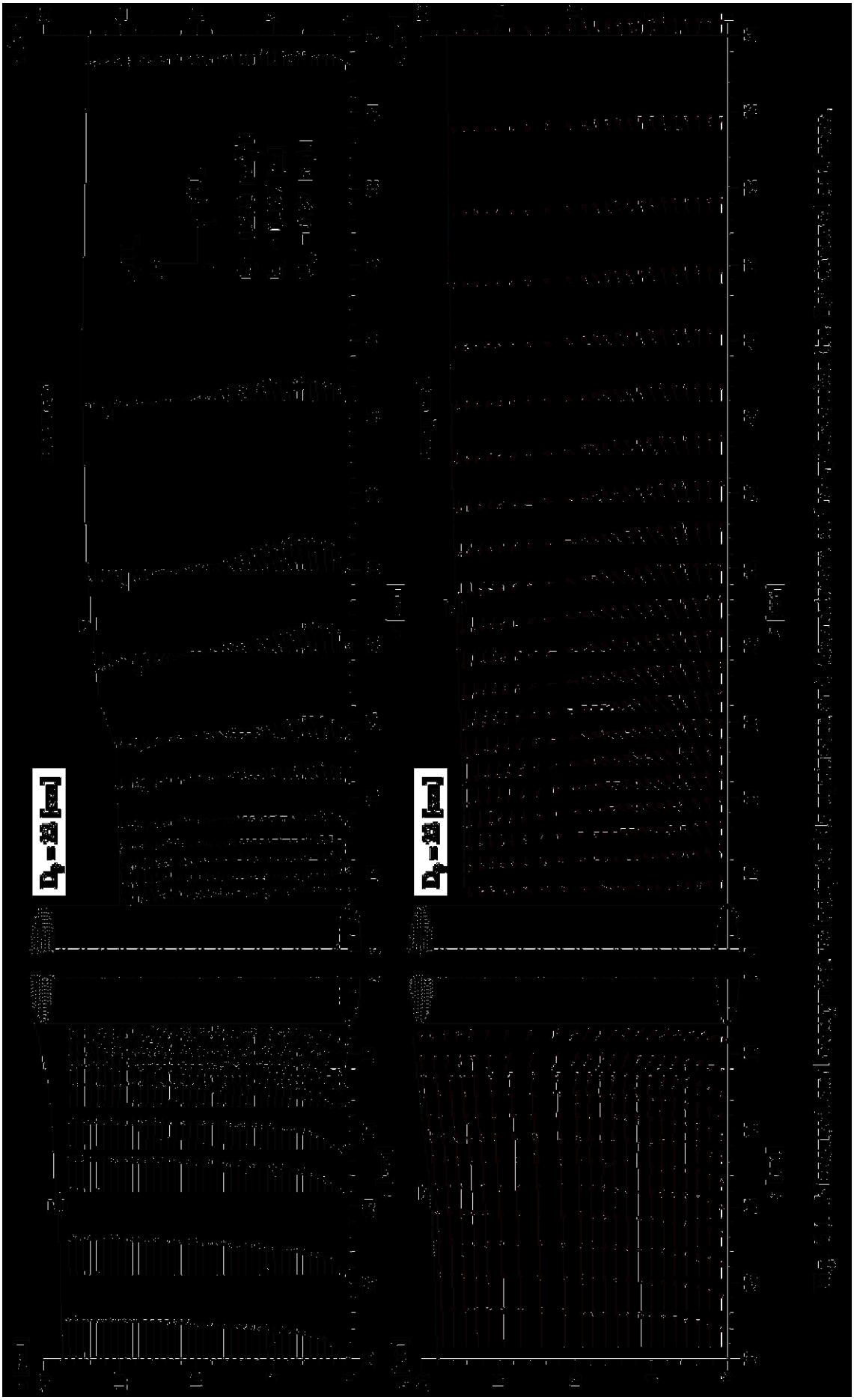

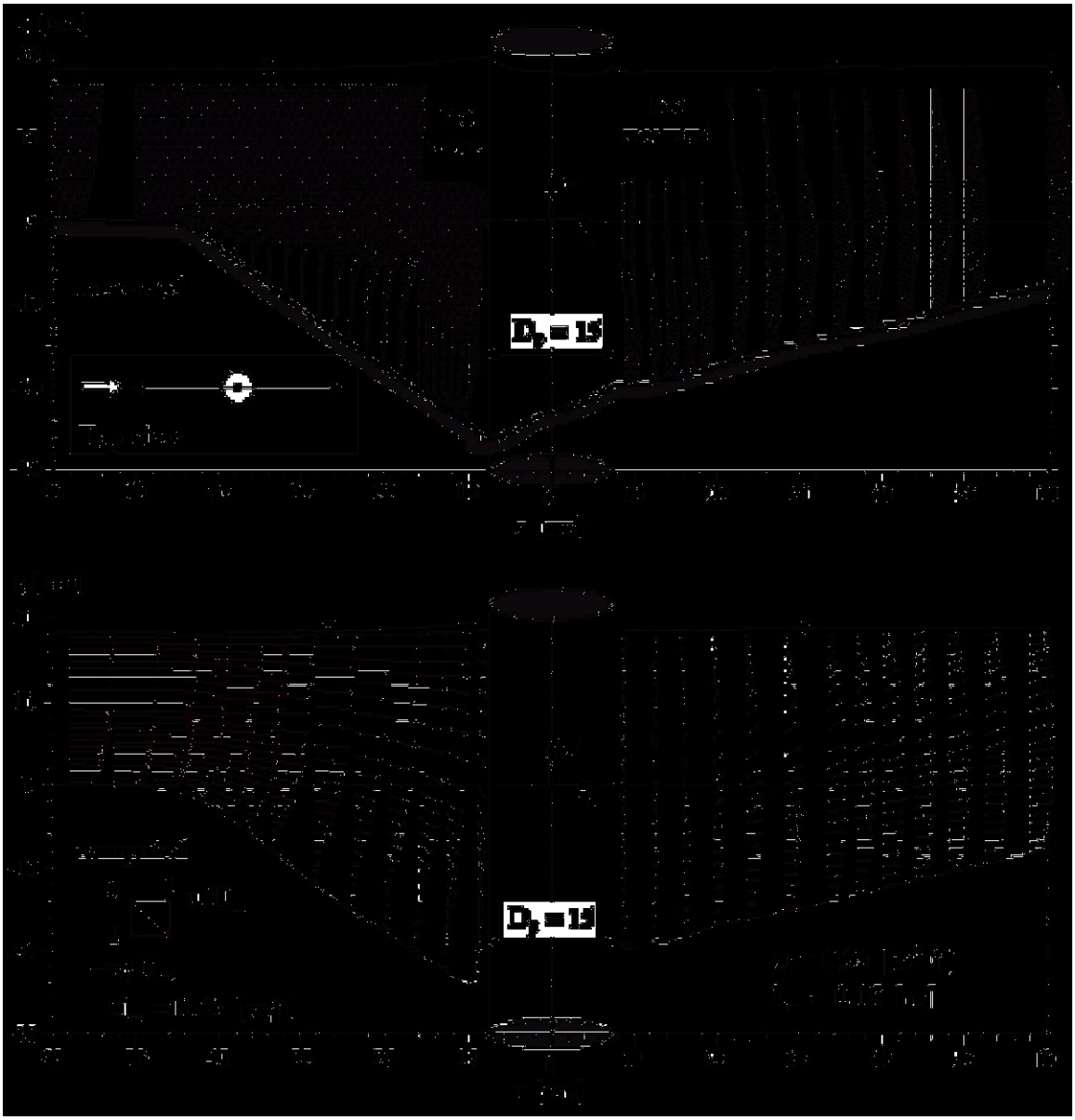

Fig. 6.2 Measured and computed velocity fields upstream and downstream of the cylinder for the scoured channel-bed case.

Curriculum Vitæ

IDENTITE

Nom	**ISTIARTO**
Prénom	**Istiarto**
Date de naissance	11 février 1962 à Yogyakarta, Indonésie
Nationalité	indonésienne
État civil	marié, 2 enfants

FORMATION

1986	Obtention du diplôme d'ingénieur (Insinyur) en génie civil de l'Université Gadjah Mada, à Yogyakarta, Indonésie.
1989	Obtention du diplôme de Master of Engineering in water resources engineering de l'Asian Institute of Technology à Bangkok, Thaïlande. Travail de fin d'études intitulé : « Modelling of Solute Transport in Saturated-unsaturated Conditions ».
1996-2001	Travail de doctorat à l'École Polytechnique Fédérale de Lausanne, Suisse. Titre de la thèse : « Flow around a Cylinder in a scoured Channel Bed ».

FONCTIONS EXERCEES

1987	Assistant du Département de Génie Civil de l'Université Gadjah Mada à Yogyakarta, Indonésie.
1989-1995	Attaché d'enseignement du Département de Génie Civil de l'Université Gadjah Mada à Yogyakarta, Indonésie.
1996-2001	Assistant et doctorant au Laboratoire de Recherches Hydrauliques de l'École Polytechnique Fédérale de Lausanne, Suisse.

LANGUES

Indonésien	langue maternelle
Anglais	bonne connaissances théoriques et pratiques
Français	connaissances théoriques et pratiques.

ACTIVITE PROFESSIONELLE

1990-1995	Responsable ou collaborateur dans plusieurs travaux d'études hydrauliques, notamment dans les modélisations numériques d'écoulement dans un canal du système de refroidissement de central thermique.
1994-1995	Travail de ‘‘detailed design for small scale irrigation projects’’ à Java, Indonésie.

PUBLICATIONS

W.H. Graf et I. Istiarto, *Flow pattern in the scour hole around a cylinder*, accepted for publication.

I. Istiarto, Y. Zech, M.S. Altinakar, W.H. Graf, *3D modeling of flow around a cylinder*, submitted for publication.

I. Istiarto et W.H. Graf, *Experiments on flow around a cylinder in a scoured channel bed*, submitted for publication.

The experimental data and the numerical model source code are available on a CD format, obtainable at the Laboratoire de Recherches Hydrauliques, EPFL, CH-1015 Lausanne, Switzerland.

FLOW AROUND A CYLINDER IN A SCOURED CHANNEL BED

APPENDICES: EXPERIMENTAL DATA NUMERICAL MODEL

THÈSE N^{O} 2368 (2001)

PRÉSENTÉE AU DÉPARTEMENT DE GÉNIE CIVIL

ÉCOLE POLYTECHNIQUE FÉDÉRALE DE LAUSANNE

POUR L'OBTENTION DU GRADE DE DOCTEUR ÈS SCIENCES TECHNIQUES

PAR

Istiarto ISTIARTO

Insinyur (civil), Gadjah Mada University, Yogyakarta, Indonésie
M.Eng., Asian Institute of Technology, Bangkok, Thaïlande
de nationalité indonésienne

acceptée sur proposition du jury :

Prof. W.H. Graf, Directeur de thèse
Dr. M.S. Altinakar, rapporteur
Dr. M. Cellino, rapporteur
Dr. R. Monti, rapporteur
Prof. Y. Zech, rapporteur

Lausanne, EPFL
2001

Appendices

A Experimental Data

The experimental data are stored in the following files:

1. DataSheet_000 — measured data for $\alpha = 0°$.
2. DataSheet_015 — measured data for $\alpha = 15°$.
3. DataSheet_030 — measured data for $\alpha = 30°$.
4. DataSheet_045 — measured data for $\alpha = 45°$.
5. DataSheet_060 — measured data for $\alpha = 60°$.
6. DataSheet_075 — measured data for $\alpha = 75°$.
7. DataSheet_090 — measured data for $\alpha = 90°$.
8. DataSheet_105 — measured data for $\alpha = 105°$.
9. DataSheet_120 — measured data for $\alpha = 120°$.
10. DataSheet_135 — measured data for $\alpha = 135°$.
11. DataSheet_180 — measured data for $\alpha = 180°$.

and

12. DataSheet_Uniform — measured data for uniform flow (without cylinder).
13. DataSheet_zbed&zsur — measured bed and surface elevations.

All files can be found in the accompanying CD.

B Numerical Model

B.1 Program structure

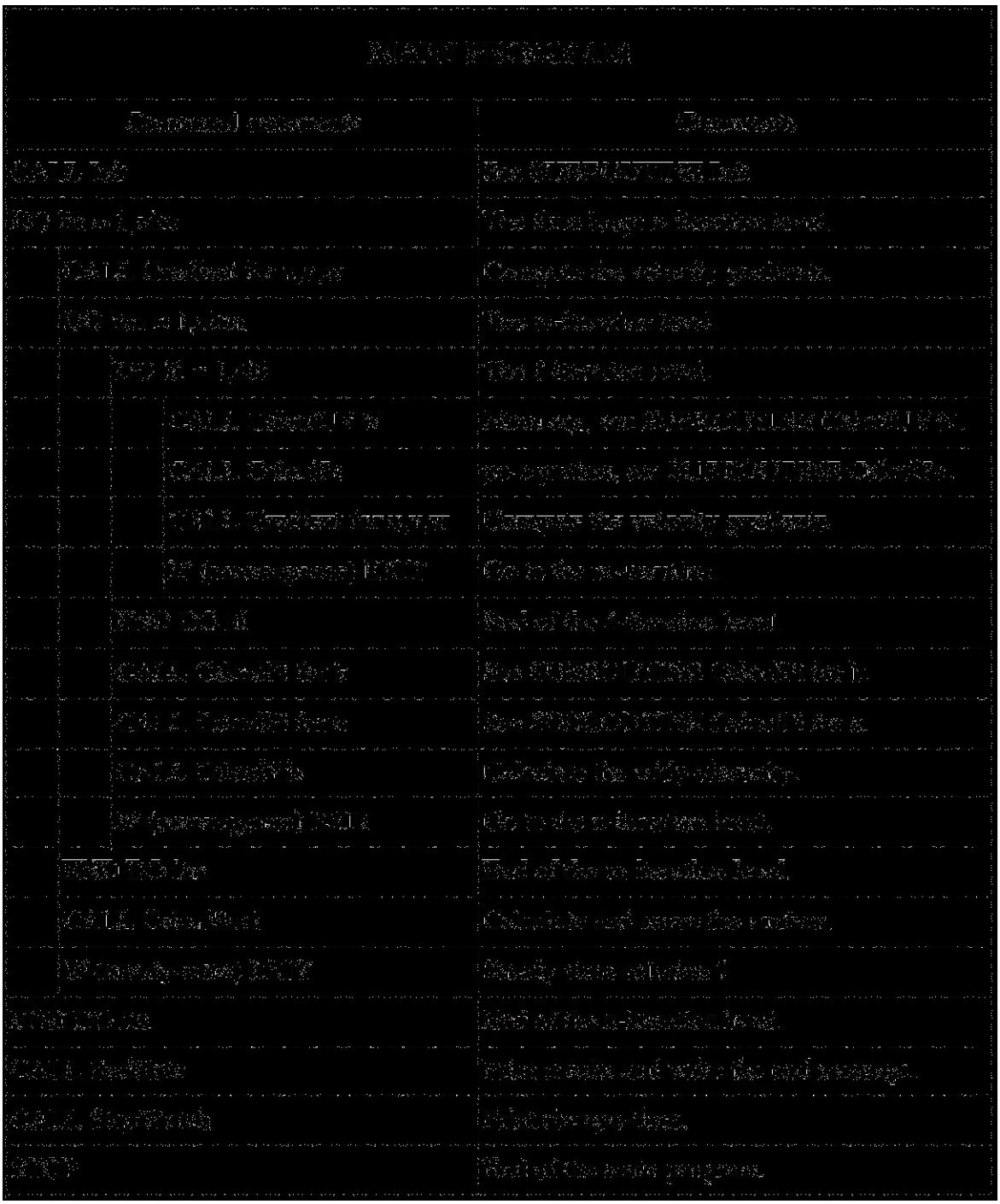

[illegible]	
[illegible]	[illegible]
[illegible]	[illegible]
[illegible]	[illegible]
[illegible]	[illegible]
[illegible]	[illegible]
[illegible]	[illegible]
[illegible]	[illegible]
[illegible]	[illegible]
[illegible]	[illegible]

[illegible]	
[illegible]	[illegible]
[illegible]	
[illegible]	
[illegible]	[illegible]
[illegible]	[illegible]
[illegible]	[illegible]
[illegible]	[illegible]
[illegible]	[illegible]
[illegible]	[illegible]
[illegible]	[illegible]
[illegible]	[illegible]
[illegible]	[illegible]

[illegible]	[illegible]
[illegible]	[illegible]
[illegible]	[illegible]
[illegible]	[illegible]
[illegible]	[illegible]
[illegible]	[illegible]
[illegible]	[illegible]
[illegible]	[illegible]
[illegible]	[illegible]

[illegible]	[illegible]
[illegible]	[illegible]
[illegible]	[illegible]
[illegible]	[illegible]
[illegible]	[illegible]
[illegible]	[illegible]
[illegible]	[illegible]
[illegible]	[illegible]
[illegible]	[illegible]

[illegible]	
[illegible]	
[illegible]	[illegible]
[illegible]	[illegible]
[illegible]	[illegible]
[illegible]	[illegible]
[illegible]	[illegible]
[illegible]	[illegible]
[illegible]	[illegible]
[illegible]	[illegible]
[illegible]	[illegible]
[illegible]	[illegible]
[illegible]	[illegible]
[illegible]	[illegible]
[illegible]	[illegible]
[illegible]	[illegible]
[illegible]	[illegible]
[illegible]	[illegible]
[illegible]	[illegible]
[illegible]	[illegible]
[illegible]	[illegible]
[illegible]	[illegible]
[illegible]	[illegible]
[illegible]	[illegible]

B.2 Input data file

The input data files are the KECONTROL that defines the main control parameters of the computation and the KECOORDINA that specifies the coordinates of the cell vertices. The following sections explain these two data files; examples can be found in the accompanying CD.

B.2.1 KECONTROL

#1 **title**
A string of 100 characters.

#2 **lcont, lreset, lwinit, ltest**
four logical characters used to define a continuation run, to reset the time-level index to zero, to ask for a print out of the initial conditions (into the KERESINI file), and to a debugging process in a test run, respectively.

#3 **lgrav, lcyclic, lsurface**
three logical characters: the gravitational acceleration is specified, cyclic inlet-outlet boundary conditions are used, and the surface update is active.

#4 **lunsteady, ldtvar**
two logical characters: the time level is active and the time step varies.

#5 **lzunif, lvinit, lnewinl, lnewcoor**
four logical characters: a uniform grid size in the vertical direction is used, the velocity throughout the computational domain is specified, new inlet values are specified, and a new geometry is imposed, respectively.

#6 **lpcout**
one logical character: a zero pressure is enforced at the top cells of the outlet.

#7 **lcal(i), i=1,nfi (nfi=6)**
six logical characters: do the computation for each of the ϕ (u,v,w,p,k,ε) variables.

#8 **modke:**
integer number: [1] standard k-ε [2] non-equlibrium k-ε.

#9 **nsol(i), i=1,nfi (nfi=6)**
six integer numbers: which matrix solver is used for each of the ϕ-equations [1]=SIPSOL, [2]=CGStab.

#10 **nit(i), i=1,nfi (nfi=6)**
six integer numbers: the number of the inner iterations in the matrix solver for each of the ϕ-equations.

#11 **clamda1(i), i=1,nfi (nfi=6)**
six real numbers: the first convergence criteria in the matrix solver for each of the ϕ-equations.

#12 **clamda2(i), i=1,nfi (nfi=6)**
six real numbers: the second convergence criteria in the matrix solver for each of the ϕ-equations.

#13 **nsc(i), i=1,nfi (nfi=6)**
six integer numbers: the discretisation methods for each of the ϕ-equations [1] upwind, [2] hybrid, or [3] power law.

#14 **dcf(i), i=1,nfi (nfi=6)**
six real numbers: the deferred-correction factors for each of the ϕ-equations.

#15 **urf(i), i=1,nfi (nfi=6)**
six real numbers: the under-relaxation factors for each of the ϕ-equations.

#16 **urfvis,urfdhp,urfdhz**
three real: the under-relaxation factors for the eddy-viscosity, for the surface movement according to the grid size criterion, and for the surface movement according to the pressure defect criterion.

#17 **tol(i), i=1,nfi (nfi=6)**
six real numbers: the error tolerances for each of the ϕ-equations.

#18 **pctol**
one real number: the error tolerance for the pressure correction.

#19 **resmin, resmax**
two real numbers: the minimum and maximum errors, if these limits are exceeded, the program will stop.

#20 **npcor**
one integer number: the method of the pressure correction: [1] SIMPLE or [2] SIMPLEC.

#21 **nipcor**
one integer number: the number of iterations in the pressure correction [1] without or [2] with correction due to non-orthogonal terms.

#22 **nigrad**
one integer number: the number of iterations in the gradient computation [1] without or [2] with correction due to non-orthogonal terms.

#23 **dt, edt**
two real numbers: the time step and the E factor in case of varying Δt.

#24 **nitl, nitm, nitn, nitprn**
four integer numbers: the number of iterations for the ℓ-, m-, n-iterations, and for the printing interval, respectively.

#25 **density, viscosity, gravity**
three real numbers: the water density, the kinematic viscosity, and the gravitational acceleration, respectively.

#26 **disch**
one real number: the discharge through the inlet boundary.

#27 **axisrot**
one real number: the angle of the axis rotation in degrees, a counter-clockwise convention is used.

#28 **nx, ny, nz**
three integers numbers: the number of vertices (the number of divisions + 1) in the *x*, *y*, and *z* directions, respectively (see example).

#29 **ipcr, jpcr, kpcr**
three integers numbers: the (i,j,k) indices of the cell used for the reference of the pressure correction.

#30 **ipr, jpr, kpr**
three integer numbers: the (i,j,k) indices of the cell used for the reference of the pressure.

#31 **imon1, jmon1, kmon1**
three integer numbers: the (i,j,k) indices of the first monitoring cell.
#32 **imon2, jmon2, kmon2**
three integer numbers: the (i,j,k) indices of the second monitoring cell.
#33 **imon3, jmon3, kmon3**
three integer numbers: the (i,j,k) indices of the third monitoring cell.
#34 **imon4, jmon4, kmon4**
three integer numbers: the (i,j,k) indices of the fourth monitoring cell.
#35 **imon5, jmon5, kmon5**
three integer numbers: the (i,j,k) indices of the fifth monitoring cell.
#36 **nrbnd**
one integer number: the number of the boundary specifications (see example).

#37 **cbnd 1,cbnd 2**
two 3-character strings, put in the columns 1-3 and 5-7: the boundary type and the position of the boundary node with respect to the interior node, respectively.
#38 **istart, iend, jstart, jend, kstart, kend**
six integer numbers: the position of the boundary nodes, from istart to iend, from jstart to jend, and from kstart to kend (see example).
#39 **rks**
one real number: the equivalent roughness of the wall boundary; a zero value is given to boundaries other than the wall and the block boundaries (see example).

The above 3 lines (#37, #38, #39) are to be specified to each boundary specification, nrbnd.

#40 **zper**
one real number: the vertical location of the cell vertices, in percent of the depth.

The above input line (#40) is to be specified for each vertical vertices, nz, starting from the top (the surface, zper = 100.0) to the bottom (the bed, zper = 0.0). If a uniform vertical grid size is specified, i.e. when lzunif is true (see #5), this input is not needed.

#41 **uin, vin, win, kin, epsin**
five real numbers: the inlet values for u, v, w, k, and ε.

The above input line (#41) is to be specified for each cells in a vertical, nk = nz+1, starting from the top (the surface, k = nk) to the bottom (the bed, k = 1). This is done for one vertical (one profile) only and is assumed to be valid for all verticals in the inlet boundaries.

EXAMPLE: BOUNDARY SPECIFICATION

An example is here given to demonstrate the specification of the boundary specification in the KECONTROL input file.

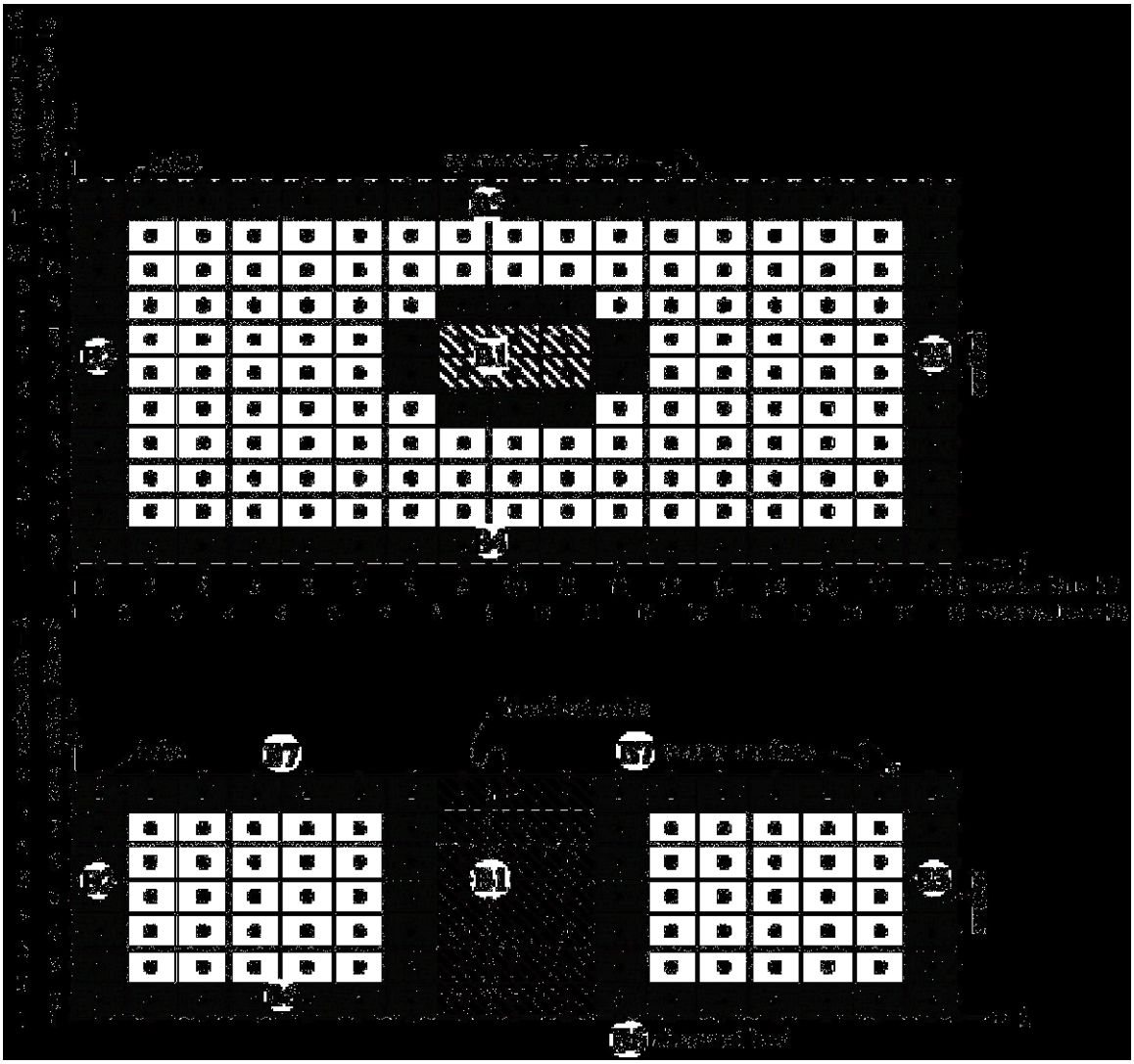

Fig. B.1 Example of a computational domain having $(17 \times 11 \times 7)$ cells and 7 boundary specifications.

Consider a computational domain shown in Fig. B.1. There are $17 \times 11 \times 7$ cells in the *x*, *y*, and *z* directions, respectively. The corresponding number of cell vertices is thus $18 \times 12 \times 8$ and of nodes is $19 \times 13 \times 9$. In data **#28 (nx, ny, nz)** of the KECONTROL, the following values are specified:

#28: **18 12 8**

There are 7 boundary types: B1 (blocked cells), B2 (inlet), B3 (outlet), B4 (channel side wall), B5 (symmetry plane), B6 (channel bed), and B7 (water surface). In data **#36 (nrbnd)** of the KECONTROL, the following is specified:

#36: **7**

This input is then followed by 3-lines boundary specifications, **#37 (cbnd 1, cbnd 2)**, **#38 (istart, iend, jstart, jend, kstart, kend)**, and **#39 (rks)**, to be inputted for each boundaries. The boundary type (cbnd 1) is either:

BLO for blocked cells,
INL for inlet,
OUT for outlet,
WAL for wall boundaries,
SYM for symmetry planes, or
FRE for free surfaces.

The boundary position (cbnd 2) is either:

EAS for east face,
WEA for west face,
NOR for north face,
SOU for south face,
TOP for top face, or
BOT for bottom face.

Note that the cbnd must be written in either upper case or lower case letters, but not mixed ones. For the boundary specifications shown in Fig. B.1, the following data must be inputted:

#37: **blo blo**
#38: **9 11 7 8 2 8**
#39: **0.22E-3**
#37: **inl wea**
#38: **2 2 2 12 2 8**
#39: **0.0**
#37: **out eas**
#38: **18 18 2 12 2 8**
#39: **0.0**
#37: **wal sou**
#38: **2 18 2 2 2 8**
#39: **0.22E-3**
#37: **sym nor**
#38: **2 18 12 12 2 8**
#39: **0.0**
#37: **wal bot**
#38: **2 18 2 12 2 2**
#39: **4.2E-3**
#37: **fre top**
#38: **2 18 2 12 8 8**
#39: **0.0**

B.2.2 KECOORDINA

#1 **title**
A string of 100 characters.

#2 **dummy text**
A string of any number of characters; this line is not read.

#3 **i, j, x, y, zb, zs**
2 integer numbers: the (i,j) cell indices and
4 real numbers: the (x, y) coordinates of the bed vertices, and the bed (z_b) and the surface (z_s) coordinates.

The above input is to be repeated according to the number of vertices, (nx,ny), of the computational domain.

B.3 Source code

The source code of the program consists of 6 program files and 11 variable-declaration files:

1. ke.f — the main program.
2. keflow.f — the flow model.
3. keturb.f — the k-ε model.
4. keinit.f — the initialization routines.
5. keread.f — the routines that read the data from or write the results to a file.
6. kegeom.f — the routines that construct the geometry of the computational domain.

7. ke_bound.inc — variable declarations: boundary conditions.
8. ke_calcon.inc — variable declarations: computational control-parameters.
9. ke_coef.inc — variable declarations: variable coefficients.
10. ke_geo.inc — variable declarations: geometry.
11. ke_grad.inc — variable declarations: gradients.
12. ke_index.inc — variable declarations: cell indices.
13. ke_logic.inc — variable declarations: logical variables.
14. ke_param.inc — variable declarations: space (memory) allocations.
15. ke_varflo.inc — variable declarations: flow variables.
16. ke_varold.inc — variable declarations: variables at the n time level.
17. ke_vartur.inc — variable declarations: k-ε variables.

The program is written in the FORTRAN77 language and is suited for the MPW Absoft Version 6.2 compiler.

The print out of all files is given in the next pages. The files can also be found in the accompanying CD.

FLOW AROUND A CYLINDER IN A SCOURED CHANNEL BED

3D Hydrodynamic Model
Program Source Code

Istiarto ISTIARTO

Laboratoire de recherches hydrauliques
Département de Génie Civil
Ecole Polytechnique Fédérale de Lausanne

Lausanne, EPFL
2001